

# ACCOMPLISHMENTS AND OPPORTUNITIES

NIST CENTER FOR NEUTRON RESEARCH

# 2020



## ON THE COVER

The NCNR's neutron source provides a valuable research tool for a wide variety of scientific fields from biological systems, engineering materials, to magnetic structures, and more. The cover features data from only a few of the experiments highlighted in this report.

NIST Special Publication 1257

# 2020 NIST Center for Neutron Research Accomplishments and Opportunities

*Robert M. Dimeo*, Director

*Steven R. Kline*, Editor

This publication is available free of charge from:  
<https://doi.org/10.6028/NIST.SP.1257>

December 2020



U.S. Department of Commerce  
*Wilbur L. Ross, Jr.*, Secretary

National Institute of Standards and Technology  
*Walter Copan*, NIST Director and Undersecretary of  
Commerce for Standards and Technology

## DISCLAIMER

Certain commercial entities, equipment, or materials may be identified in this document in order to describe an experimental procedure or concept adequately. Such identification is not intended to imply recommendation or endorsement by the National Institute of Standards and Technology, nor is it intended to imply that the entities, materials, or equipment are necessarily the best available for the purpose. Throughout the text, unless otherwise stated,  $q$  (or  $Q$ ) refers to the momentum transfer. Error bars in figures and uncertainties in the text represent one standard deviation unless otherwise stated.

National Institute of Standards and Technology Special  
Publication 1257, 94 pages (December 2020)  
CODEN: NSPUE2

This publication is available free of charge from:  
<https://doi.org/10.6028/NIST.SP.1257>

# Table of Contents

## II FOREWORD

### 1 THE NIST CENTER FOR NEUTRON RESEARCH

### 2 NIST CENTER FOR NEUTRON RESEARCH INSTRUMENTS

## BIOSCIENCES

- 4 Characterization of a dynamic membrane-bound molecular switch: the oncoprotein KRas-4B, F. Heinrich, et al.
- 6 Measuring the rigidity of heterogeneous lipid membranes, E. G. Kelley, et al. (CHRNA)

## CHEMICAL PHYSICS

- 8 Hibonite blue: A new class of inorganic blue colorants, B. A. Duell, et al.
- 10 Cation orientation dependent charge separation in a hybrid perovskite, E. M. Mozur, et al. (CHRNA)
- 12 Stability and microheterogeneity in concentrated nonaqueous electrolyte solutions, L. A. Robertson, et al. (CHRNA)
- 14 Quantification of sub-nanometer chloride layer on the surface of PbS nanocrystals, S.W. Winslow, et al.

## CONDENSED MATTER

- 16 Field-tunable quantum disordered ground state in the triangular-lattice antiferromagnet  $\text{NaYbO}_2$ , M. M. Bordelon, et al.
- 18 Magnetic phase transitions and spin-density distribution in the molecular multiferroic  $\text{GaV}_4\text{S}_8$  system, R. L. Dally, et al.
- 20 Three-dimensional magnetism in a kagome staircase lattice, J. S. Helton, et al.
- 22 Anisotropic effect of a magnetic field on the neutron spin resonance in  $\text{FeSe}$ , T. Chen, et al. (CHRNA)
- 24 Realization of magnon spin valves utilizing unexpected antiferromagnetic coupling on Si, Y. Fan, et al.

## ENGINEERING PHYSICS

- 26 Benchmarking residual stress and dimensional fidelity in additive manufacturing, T. Gnaupel-Herold, et al.
- 28 Changes in lithiation of battery materials *in operando* during electrochemical discharge, Z. Nie, et al.

## GEOLOGY

- 30 SANS pore structure studies for a better understanding of tight oil production, Y. Zhang, et al. (CHRNA)

## NEUTRON PHYSICS

- 32 Precision measurement of the neutron scattering length of  $^4\text{He}$  using neutron interferometry, R. Haun, et al.

## SOFT MATTER

- 34 Polymer dynamics in block copolymer electrolytes detected by neutron spin echo, W. S. Loo, et al. (CHRNA)
- 36 Color, structure, and rheology of a diblock bottlebrush copolymer solution, M. A. Wade, et al. (CHRNA)
- 38 Bottlebrush polymers in the melt and polyelectrolytes in solution share common structural features, J. M. Sarapas, et al. (nSoft)
- 40 Rigid rod polymer construction through peptide computational design and hierarchical solution assembly, N. Sinha, et al. (CHRNA)
- 42 Accelerated local dynamics in matrix-free polymer grafted nanoparticles, M. Jhalaria, et al. (CHRNA)
- 44 Evolution of local and global chain conformation of polymer melts during extensional flow: what happens inside the "tube"?, C. R. López-Barrón, et al.
- 46 Neutron probe for mass transport mechanisms in oil-in-water emulsions, Y.-T. Lee, et al. (CHRNA)

## ADVANCES IN MEASUREMENT

- 48 Techniques for time-resolved SANS measurements, C. Glinka, et al.
- 49 Measuring structure and viscosity of complex fluids at extreme shear rates, R. P. Murphy, et al.
- 50 An autonomous liquid-handling platform for industrial formulation discovery, P. A. Beaucage, et al.
- 51 Annealing and etching away machining damage in a neutron interferometer, B. Heacock, et al.
- 52 An RF neutron spin flipper for controlling the polarization in large beams with high efficiency, W. C. Chen, et al.
- 53 Restraining molecular simulations with neutron reflection data, B. W. Treece, et al.

## 54 NEUTRON SOURCE OPERATIONS

## 56 FACILITY DEVELOPMENTS 2020

## 60 SERVING THE SCIENCE AND TECHNOLOGY COMMUNITY

## 63 THE CENTER FOR HIGH RESOLUTION NEUTRON SCATTERING (CHRNA)

## 68 2020 AWARDS

## 71 PUBLICATIONS: AUGUST 1, 2019 TO JULY 31, 2020

## 92 INSTRUMENTS AND CONTACTS

## 94 NIST CENTER FOR NEUTRON RESEARCH CONTACTS

# Foreword

It is my pleasure to present this year's Accomplishments and Opportunities for the NIST Center for Neutron Research.

The global pandemic caused an unplanned suspension of scientific operations from March 17 – July 14. We resumed scientific operations on July 15, but in a mode limited to internal (NIST programmatic) experiments and mail-in experiments. As of this writing, scientific operations remain limited. The reactor operated for 160 days and, excluding the impact of the pandemic on scientific operations, operational reliability exceeded 98%.

Despite the significant impact to scientific operations by the global pandemic, it has been a remarkably productive year. The NSF/NIST partnership, CHRNS (Center for High Resolution Neutron Scattering), was renewed for another five years and includes the new reflectometer, CANDOR, in the CHRNS suite. You can read more about CHRNS, our most important interagency partnership, in this report. Planning continues for the 2023 outage when the H<sub>2</sub> cold source will be replaced with a liquid D<sub>2</sub> cold source, resulting in a doubling of the cold neutron flux at long wavelengths. Major procurements, including the cold source cryostat, were awarded this year for long lead-time items that are on the critical path. The neutron guide system will be upgraded during the outage. All guides required to reestablish reactor confinement at the end of the outage have been ordered. The NSE performance upgrade project is underway and the major, long lead-time items have been ordered. Major upgrades have also been made to the reactor's cooling tower systems and electrical infrastructure which will contribute to increased operational reliability.



The result of NIST's neutron facility development and operations is in the research carried out by you, the scientific community. This report contains a collection of these research highlights. I invite you to read through the report and see for yourself the fascinating work that took place here in the last year. I believe that these highlights speak for themselves.

A handwritten signature in black ink, reading "Paul D. Smith".



# The NIST Center for Neutron Research

**N**eutrons provide a uniquely effective probe of the structure and dynamics of materials ranging from water moving near the surface of proteins to magnetic domains in memory storage materials. The properties of neutrons (outlined below) can be exploited using a variety of measurement techniques to provide information not otherwise available. The positions of atomic nuclei in crystals, especially of those of light atoms, can be determined precisely. Atomic motion can be directly measured and monitored as a function of temperature or pressure. Neutrons are especially sensitive to hydrogen, so that hydrogen motion can be followed in H-storage materials and water flow in fuel cells can be imaged. Residual stresses such as those deep within oil pipelines or in highway trusses can be mapped. Neutron-based measurements contribute to a broad spectrum of activities including engineering, materials development, polymer dynamics, chemical technology, medicine, and physics.

The NCNR's neutron source provides the intense, conditioned beams of neutrons required for these types of measurements. In addition to the thermal neutron beams from the heavy water moderator, the NCNR has two liquid hydrogen moderators, or cold sources which supply neutrons to three-fourths of the instruments. One is a large area moderator and the other is smaller, but with high brightness. These moderators provide long wavelength guided neutron beams for industrial, government, and academic researchers.

## Why Neutrons?

Neutrons reveal properties not readily probed by photons or electrons. They are electrically neutral and therefore easily penetrate ordinary matter. They behave like microscopic magnets, propagate as waves, can set particles into motion, losing or gaining energy and momentum in the process, and they can be absorbed with subsequent emission of radiation to uniquely fingerprint chemical elements.

**WAVELENGTHS** – in practice range from  $\approx 0.01$  nm (thermal) to  $\approx 1.5$  nm (cold) ( $1 \text{ nm} = 10 \text{ \AA}$ ), allowing the formation of observable interference patterns when scattered from structures as small as atoms to as large as biological cells.

**ENERGIES** – of millielectronvolts, the same magnitude as atomic motions. Exchanges of energy as small as nanoelectronvolts and as large as tenths of electronvolts can be detected between samples and neutrons, allowing motions in folding proteins, melting glasses and diffusing hydrogen to be measured.

There are currently 30 experiment stations: 12 are used for neutron physics, analytical chemistry, or imaging, and 18 are beam facilities for neutron scattering research. The subsequent pages provide a schematic description of our instruments. More complete descriptions can be found at <https://www.nist.gov/ncnr/neutron-instruments>. The newest instrument, a quasi-white beam neutron reflectometer (CANDOR) is currently in the commissioning stage.

The Center supports important NIST measurement needs but is also operated as a major national user facility with merit-based access made available to the entire U.S. technological community. Each year, approximately 2000 research participants from government, industry, and academia from all areas of the country are served by the facility (see p. 60). Beam time for research to be published in the open literature is without cost to the user, but full operating costs are recovered for proprietary research. Access is gained mainly through a web-based, peer-reviewed proposal system with user time allotted by a beamtime allocation committee twice a year. For details see <https://www.nist.gov/ncnr/obtaining-beam-time>. The National Science Foundation and NIST co-fund the Center for High Resolution Neutron Scattering (CHRNS) that currently operates six of the world's most advanced instruments (see p. 63). Time on CHRNS instruments is made available through the proposal system. Some access to beam time for collaborative measurements with the NIST science staff can also be arranged on other instruments.

**SELECTIVITY** – in scattering power varies from nucleus to nucleus somewhat randomly. Specific isotopes can stand out from other isotopes of the same kind of atom. Specific light atoms, difficult to observe with x-rays, are revealed by neutrons. Hydrogen, especially, can be distinguished from chemically equivalent deuterium, allowing a variety of powerful contrast techniques.

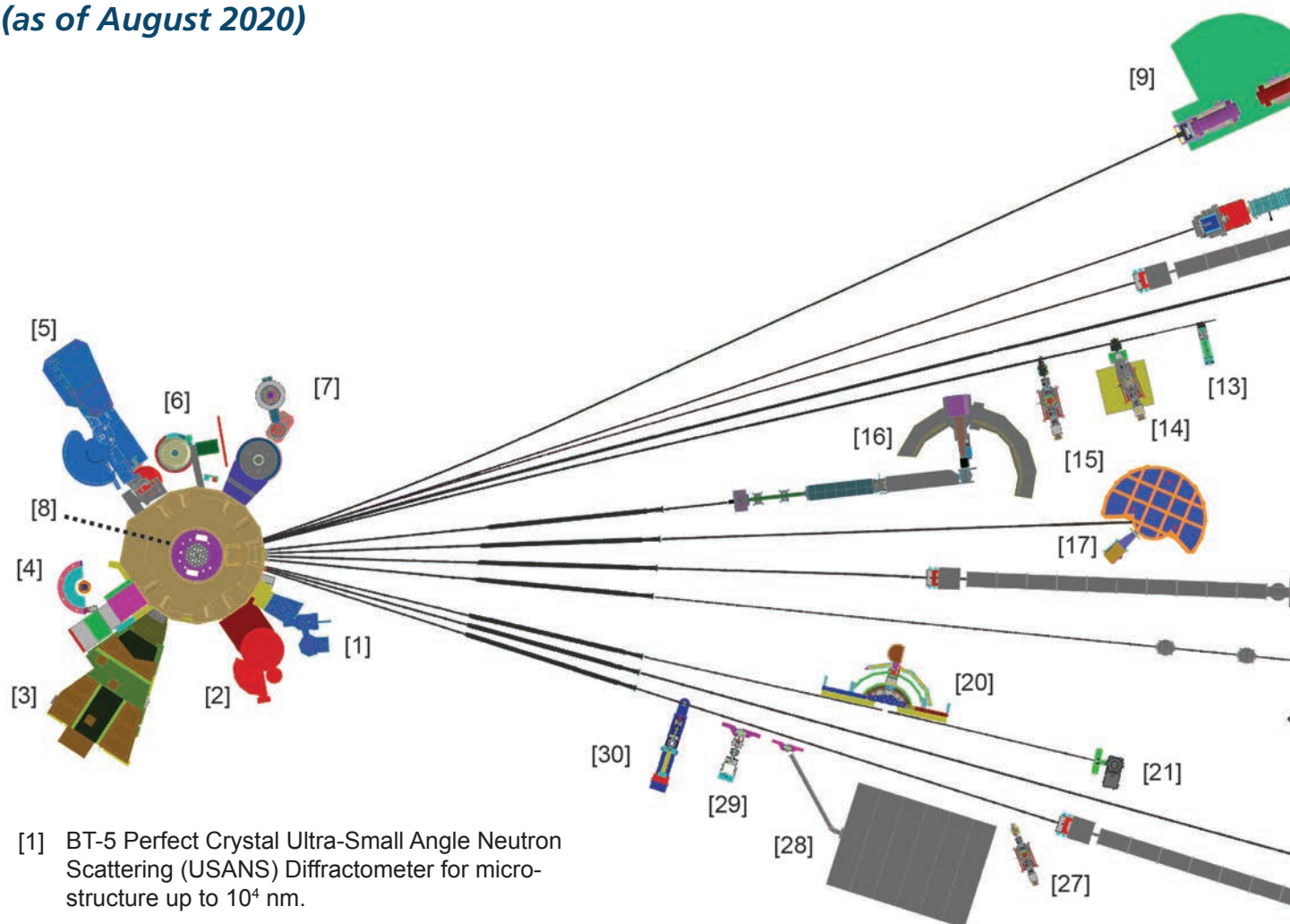
**MAGNETISM** – makes the neutron sensitive to the magnetic moments of both nuclei and electrons, allowing the structure and behavior of ordinary and exotic magnetic materials to be detailed precisely.

**NEUTRALITY** – of the uncharged neutrons allows them to penetrate deeply without destroying samples, passing through walls that condition a sample's environment, permitting measurements under extreme conditions of temperature and pressure.

**CAPTURE** – characteristic radiation emanating from specific nuclei capturing incident neutrons can be used to identify and quantify minute amounts of elements in samples as diverse as ancient pottery shards and lake water pollutants.

# NIST Center for Neutron Research Instruments

(as of August 2020)

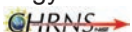


[1] BT-5 Perfect Crystal Ultra-Small Angle Neutron Scattering (USANS) Diffractometer for micro-structure up to  $10^4$  nm.

[2] BT-4 Filter Analyzer Neutron Spectrometer with cooled Be/Graphite filter analyzer for chemical spectroscopy and thermal triple axis spectrometer.

[3] BT-2 Neutron Imaging Facility for imaging hydrogenous matter in large components such as water in fuel cells and lubricants in engines, in partnership with General Motors and DOE.

[4] BT-1 Powder Diffractometer with 32 detectors; incident wavelengths of 0.208 nm, 0.154 nm, and 0.120 nm, with resolution up to  $\Delta d/d \approx 8 \times 10^{-4}$ .

[5] BT-9 Multi Axis Crystal Spectrometer (MACS II), a cold neutron spectrometer for ultra high sensitivity access to dynamic correlations in condensed matter on length scales from 0.1 nm to 50 nm and energy scales from 2.2 meV to 20 meV. 


[6] BT-8 Engineering Diffractometer optimized for depth profiling of residual stresses in large components.

[7] BT-7 Thermal Triple Axis Spectrometer with large double focusing monochromator and interchangeable analyzer/detectors systems.

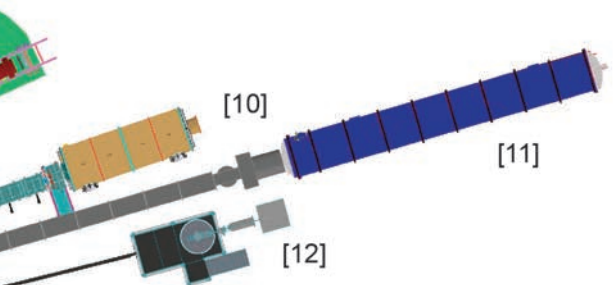
[8] VT-5 Thermal Neutron Capture Prompt Gamma-ray Activation Analysis Instrument used for quantitative elemental analysis of bulk materials including highly hydrogenous materials ( $\approx 1\%$  H) such as foods, oils, and biological materials.

[9] NG-A Neutron Spin-Echo Spectrometer (NSE) for measuring dynamics from 5 ps to 100 ns.

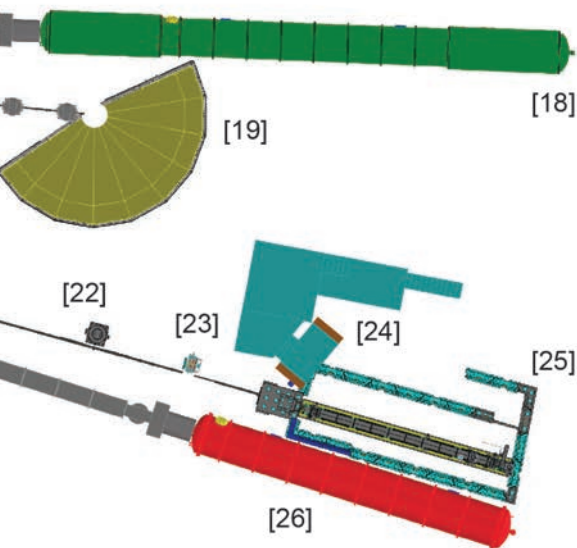





[10] NG-B 10 m SANS for macromolecular structure measurements. 





The Center for High Resolution Neutron Scattering (CHRNA) is a partnership between NIST and the National Science Foundation that develops and operates neutron scattering instrumentation for use by the scientific community. The following instruments are part of the Center: 1 (USANS), 5 (MACS II), 9 (NSE), 16 (CANDOR), 17 (HFBS), and 18 (vSANS).



- [16] NG-1 CANDOR Chromatic Analysis Diffractometer or Reflectometer, capable of high throughput measurements (commissioning). 
- [17] NG-2 Backscattering Spectrometer (HFBS), high intensity inelastic scattering instrument with energy resolution  $< 1 \mu\text{eV}$  for studies of motion in molecular and biological systems. 
- [18] NG-3 VSANS for single measurement investigation of lengths from 1 nm to 2 micron. 
- [19] NG-4 Disk Chopper Time-of-Flight Spectrometer for diffusive motions and low energy dynamics. Wavelengths from  $\approx 0.18 \text{ nm}$  to  $2.0 \text{ nm}$  and energy resolutions from  $\approx 2 \text{ meV}$  to  $< 10 \mu\text{eV}$ .
- [20] NG-5 Spin-Polarized Triple Axis Spectrometer (SPINS) using cold neutrons with position sensitive detector capability for high-resolution studies.
- [21] NG-5 Cold Neutron Depth Profiling for profiling of subsurface elemental composition.
- [22] NG-6 Precision measurement of the magnetic dipole moment of the neutron.
- [23] NG-6 Precision measurement of neutron flux.
- [24] NG-6 LAND detector development, neutron source calibration, and neutron cross section measurement
- [25] NG-6 Cold Neutron Imaging Facility for imaging hydrogenous matter in large components such as water in fuel cells and lubricants in engines.
- [26] NG-7 30 m SANS for microstructure measurements, in partnership with ExxonMobil and University of Minnesota's IPrime.
- [27] NG-7 PHADES Cold neutron test station.
- [28] NG-7 Neutron Interferometry and Optics Station with perfect crystal silicon interferometer. A vibration isolation system provides exceptional phase stability and fringe visibility.
- [29] NG-7 Neutron Physics Interferometry Test Bed for quantum information science.
- [30] NG-7 Horizontal Sample Reflectometer allows reflectivity measurements of free surfaces, liquid/vapor interfaces, as well as polymer coatings.

- [11] NG-B 30 m SANS for microstructure measurements.
- [12] NG-C Neutron lifetime experiment.
- [13] NG-D Cold neutron capture Prompt Gamma Activation Analysis, for quantitative elemental analysis of bulk materials
- [14] NG-D MAGIK off-specular reflectometer for studies of thin-film samples with in-plane structure.
- [15] NG-D Polarized Beam Reflectometer (PBR) for measuring reflectivities as low as  $10^{-8}$  to determine subsurface structure.

# Characterization of a dynamic membrane-bound molecular switch: the oncoprotein KRas-4B

F. Heinrich,<sup>1,2</sup> M. Lösche,<sup>1,2</sup> Q. N. Van,<sup>3</sup> and A. G. Stephen<sup>3</sup>

Information processing in biological cells is a fundamental capability of all living systems. It applies to sensory processes, such as vision, hearing, smelling, tasting, and touch, but also to decision-making: bacteria swim toward nutrients in their vicinity and away from harmful substances; and cells in more complex organisms, such as ourselves, regulate proliferation – i.e., growth and division. The communication of cells with each other in these processes is known as cell signaling. On a molecular level, it is realized by groups of proteins organized in complex interaction cascades, in which the activity of one protein has branching downstream effects on others. RAS proteins are cell membrane-bound molecular switches of the Small GTPase protein family, which are at the core of a protein interaction cascade that regulates cell proliferation by translating signals from outside the cell to effector proteins within cell. The KRas-4B GTPase is a critical cellular regulator that, if mutated, can trigger cancers of the pancreas, colon and lung. Certain KRas mutations leave the molecule permanently switched on leading to the characteristic uncontrolled cell proliferation associated with the disease. One line of research focuses on identifying small therapeutic molecules that bind to KRas, thereby inhibiting it and restoring the balance between activated and deactivated KRas; but painful setbacks made it clear that detailed knowledge of the KRas structure at the membrane is essential for finding inhibitors [1].

The general molecular architecture of KRas is well known: The C-terminal bears a disordered, lipidated membrane tether called the hypervariable region (HVR). It connects to the G-domain, a folded protein domain that allows effector proteins to bind and harbors the intrinsic GTPase activity. Despite decades-long efforts, no consensus structural model of KRas at the lipid membrane has emerged. Conventional structural biology tools readily provide high-resolution structures of ordered, well-folded proteins but fail to resolve disordered segments of proteins like KRas, and the association of such proteins with intrinsically disordered membranes or membrane models complicates the situation further. Fortunately, neutron scattering techniques such as reflectometry, while offering lower resolution, do not suffer from those limitations [2]. An interdisciplinary collaboration between NIST, Carnegie Mellon University, and the RAS Initiative at the National Cancer Institute has now established such a model of membrane-bound KRas using a combination of neutron reflectometry (NR),

nuclear magnetic resonance (NMR) and molecular dynamics (MD) simulation, among other techniques.

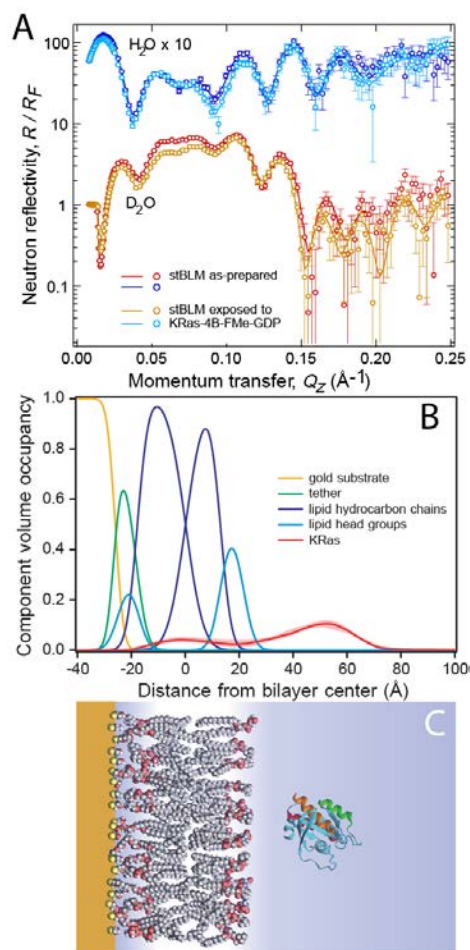


**FIGURE 1:** NR characterization of membrane-associated, fully processed KRas-4B-FMe-GDP. (A) Exemplary data sets before and after adding KRas from solution, measured with  $\text{D}_2\text{O}$  and  $\text{H}_2\text{O}$ -based buffer bathing the lipid membrane. (B) Component volume occupancy (CVO) profiles along the membrane normal. Shaded areas show 68% confidence intervals for the protein component. (C) Real-space representation in agreement with the data, using the crystal structure, PDB 6VC8, of the KRas-4B G-domain.

In past years, substantial MD simulation work consistently predicted that KRas is organized on the membrane such that its G-domain directly associates with the lipid bilayer while

<sup>1</sup> Department of Physics, Carnegie Mellon University, Pittsburgh, PA 15213

<sup>2</sup> NIST Center for Neutron Research, National Institute of Standards and Technology, Gaithersburg, MD 20899

<sup>3</sup> Cancer Research Technology Program, Frederick National Laboratory for Cancer Research (FNLCR), Leidos Biomedical Research, Inc., Frederick, MD 21702

assuming discrete orientations. Transitions between those orientations were observed to occur without prolonged detachment of the G-domain from the membrane surface [3] leading to a model of KRas at the membrane that, similar to a mechanical clock, sequentially switches between functionally distinct states. However, this molecular picture has now been revised by new experimental results of the Ras Initiative using the NCNR infrastructure for membrane protein research. Figure 1A shows a representative example of NR data before and after exposing a sparsely-tethered bilayer lipid membrane (stBLM) to KRas in solution. Panel B shows the distributions of the various molecular components deduced from these data in terms of a component volume occupancy (CVO) profile. Algorithms for rigorous determination of confidence intervals of these CVO profiles (shaded in Fig. 1B) using statistical inference with a Monte-Carlo Markov-Chain global optimizer, provides a realistic measure of the uncertainty on these structural profiles. Finally, Figure 1C shows a to-scale representation of the KRas G-domain crystal structure (PDB 6VC8) positioned on the bilayer in agreement with the experimental data, which convincingly shows that on average the G-domain is detached from the lipid bilayer. Omitted from this representation, because their conformations remain unknown, are the HVR tether and the membrane anchor. A quantitative comparison of panels B and the dimensions of the G-domain shown in panel C indicates that the CVO profile is several Ås broader than expected for a static structure. This shows a substantial conformational flexibility of the membrane-associated KRas GTPase, facilitated by the disordered HVR. These results were corroborated by complementary biophysical methods, including the  $Gd^{3+}$ -induced quenching of NMR signals. Membrane-distant conformations of the G-domain are estimated to represent  $\approx 90\%$  of the full ensemble of states, while membrane-associated conformations are in the minority. We conclude that during membrane-contacts, the G-domain adopts orientations that were previously identified in MD simulations but remains most of the time in configurations conducive to effector protein recruitment.

Further research at the NCNR determined the structure of KRas in a complex with the Ras-Binding Domain of its immediate downstream effector Raf1 (Raf1-RBD), see Figure 2. Utilizing the isotopic sensitivity of neutrons, NR measurements resolved separate CVO profiles for both binding partners, from which the position and orientation of the complex was determined using a rigid body modeling approach with a crystal structure of the G-domain complexed with Raf1-RBD (PDB 6VJJ). We demonstrated that the two proteins form a membrane-bound 1:1 complex. Unlike free KRas, the position and orientation of the complex with respect to the membrane are much more narrowly distributed, indicating a single, specific orientation. Complementary biophysical characterization techniques validated this interpretation.

In this work, a large body of experimental and computational work established a new, experimentally substantiated model of KRas signaling at the plasma membrane, as visualized in Figure 3. The data suggest that the specific architecture of

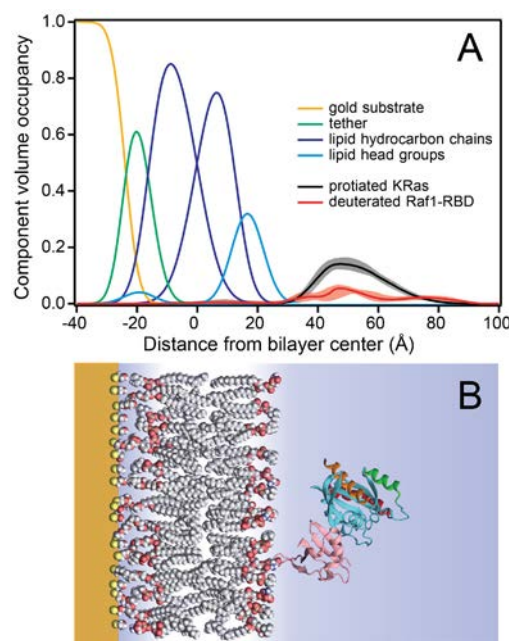


**FIGURE 2:** NR characterization of the membrane-associated KRas / Raf1-RBD protein complex. (A) CVO profiles. Shaded areas show 68% confidence intervals for the protein components. (B) Real-space representation in agreement with the NR data using the structure of the complex from PDB 6VJJ.

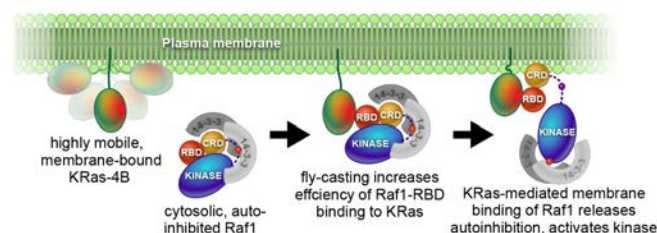


**FIGURE 3:** Model of kinase recruitment by membrane-bound KRas based on this research [4].

the KRas protein enables a directional fly-casting mechanism, in which the G-domain acts as bait to recruit Raf1 to the membrane. Membrane-bound KRas is highly dynamic, and both membrane-bound and membrane-tethered conformations coexist in fast exchange. These dynamics allow the G-domain to sample a larger conformational space, increasing the capture efficiency of the Raf1 effector protein. Once Raf1 has been captured, KRas and its binding partner assume a rigid configuration at the membrane. This insight may prove critical to guiding the development of small-molecule or biopharmaceutical therapeutics for Ras-driven cancers.

## References

- [1] A. G. Stephen, D. Esposito, R. K. Bagni, F. McCormick, *Cancer Cell* **25**, 272 (2014).
- [2] F. Heinrich, M. Lösche, *Biochim. Biophys. Acta* **1838**, 2341 (2014).
- [3] P. Prakash, Y. Zhou, et al., *Biophys. J.* **110**, 1125 (2016).
- [4] Q. N. Van, C. A. López, et al., *Proc. Natl. Acad. Sci. USA*, in press (2020).



# Measuring the rigidity of heterogeneous lipid membranes

E. G. Kelley,<sup>1</sup> P. D. Butler,<sup>1,2,3</sup> and M. Nagao<sup>1,2,4</sup>

**B**iological membranes are highly heterogeneous. They contain thousands of chemically distinct lipids, various sterols and carbohydrates, and diverse proteins that account for upwards of 50% of the membrane mass. Cells also further organize certain lipids, sterols and proteins into transient domains known as rafts to facilitate specific protein-protein interactions. This rich heterogeneity in composition and organization is thought to play an essential role in regulating biological processes such as protein signaling and even pathogen entry into cells, but the detailed mechanisms remain largely unknown. The heterogeneity also inherently causes local variations in the membrane thickness, molecular order, and rigidity that in turn affect membrane physical properties that are essential to different cell processes. Given the intrinsic complexity of biological membranes, one of many questions that arises is – how do local variations in rigidity affect the elastic properties crucial to membrane deformation and rearrangement in processes like cell division?

While the underlying lipid matrix that forms the basis of cell membranes is soft and highly deformable, the other membrane components are much less flexible. Proteins are reported to be 2X to 400X stiffer than the surrounding lipid membrane and rafts at least 3X. More than 30 years of theoretical studies have considered the effects of such rigid bodies, often referred to as additives or inclusions, on the dynamics of soft lipid membranes. The studies suggest that the collective dynamics are governed by an effective rigidity,  $\kappa_{\text{eff}}$ , that is highly sensitive to the inclusion area fraction ( $\phi$ ), shape, and interactions with the surrounding lipids, as well as how the rigid bodies are laterally organized within the membrane. However, there are limited experimental data to compare with these predictions, particularly at high  $\phi$  where the effects of the inclusions and their organization are expected to be most pronounced.

Experimental challenges in measuring the predicted trends of  $\kappa_{\text{eff}}$  in heterogeneous membranes are twofold. First, finding an appropriate technique to measure the effective rigidity is difficult as commonly used methods do not always work for heterogeneous membranes and cannot be used to determine  $\kappa_{\text{eff}}$ . Second, making appropriate model systems and then methodically varying the concentration of rigid inclusions is

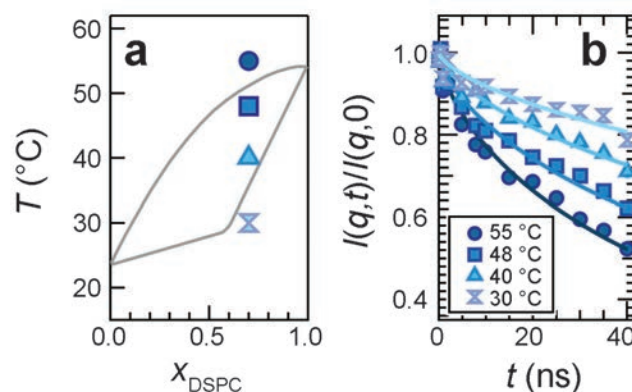


FIGURE 1: (a) Phase diagram for DMPC/DSPC lipid mixtures. The temperature region between the two gray lines corresponds to the two-phase coexistence region. (b) Intermediate scattering function at  $q = 1.1 \text{ nm}^{-1}$  for a membrane containing a DSPC mole fraction ( $x_{\text{DSPC}}$ ) of 0.7 in the fluid (55 °C), gel + fluid (48 °C and 40 °C) and gel (30 °C) regions of the phase diagram as seen in the corresponding points in panel (a). Error bars represent one standard deviation are smaller than the symbols.

labor intensive and often infeasible. Here we overcome both challenges and measure the effective rigidity ( $\kappa_{\text{eff}}$ ) of phase separated lipid membranes as a simple heterogeneous model system using neutron spin echo spectroscopy (NSE) [1].

We take advantage of the well-documented phase behavior of dimyristoylphosphatidylcholine (DMPC) and distearoylphosphatidylcholine (DSPC) lipid membranes, shown in Fig 1a. There is a large temperature region where the membranes phase separate into coexisting soft, fluid domains and rigid, gel domains. We systematically vary the amount of rigid phase ( $\phi$ ) by simply cooling the system from temperatures in the fluid phase, into the two-phase region, and finally the gel phase, allowing us to quantify  $\kappa_{\text{eff}}$  as  $\phi$  varies from 0 to 1.

Shown in Figure 1b are representative NSE data measured for a DMPC/DSPC membrane containing a DSPC mole fraction ( $x_{\text{DSPC}}$ ) of 0.7 as the system is cooled from the fluid phase, into the coexistence region, and then into the gel phase following the temperature points in Fig 1a. The dynamics markedly slow down with decreasing temperature. The

<sup>1</sup> NIST Center for Neutron Research, National Institute of Standards and Technology, Gaithersburg, MD 20899

<sup>2</sup> University of Delaware, Newark, DE 19716

<sup>3</sup> The University of Tennessee, Knoxville, TN 37996

<sup>4</sup> Indiana University, Bloomington, IN 47405

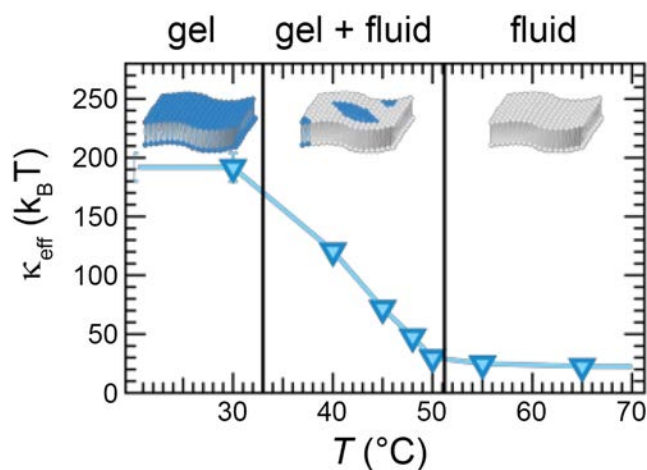


FIGURE 2: Effective bending modulus ( $\kappa_{\text{eff}}$ ) versus temperature for  $x_{\text{DSPC}} = 0.7$ . Error bars represent one standard deviation are smaller than the symbols.

intermediate scattering function data are well described by a stretched exponential as predicted for membrane bending fluctuations, where the relaxation rate is inversely related to  $\kappa_{\text{eff}}$ . Accordingly, the slowing of the dynamics is directly related to an increase in membrane rigidity.

The changes in  $\kappa_{\text{eff}}$  with temperature for  $x_{\text{DSPC}} = 0.7$  are shown in Figure 2.  $\kappa_{\text{eff}}$  is on the order of  $\approx 30 k_B T$  at high temperatures and monotonically increases with decreasing temperature before reaching  $\kappa_{\text{eff}} \approx 200 k_B T$  in the gel phase. These temperature-dependent data, as well as  $\kappa_{\text{eff}}$  measured for different lipid mixing ratios, can be collapsed onto a single master curve shown in Fig 3.

As seen in Fig 3,  $\kappa_{\text{eff}}$  depends only on the rigid domain area fraction ( $\phi$ ). Moreover, the experimental results quantitatively agree with theoretical predictions for heterogeneous membranes with no adjustable parameters. The theoretical predictions by Netz and Pincus are shown as the solid line in Fig. 3, and the NSE data provide the first experimental validation that  $\kappa_{\text{eff}}$  not only scales with  $\phi$ , but also depends on the lateral organization of the rigid phase within the membrane [1, 2].

While the present results are for phase separated lipid membranes, the general methods and theories should extend to any rigid inclusions embedded in a soft surfactant of lipid membrane. In fact, the theoretical studies were first developed to understand how  $\kappa_{\text{eff}}$  scales with the amount of protein in biological membranes. Red blood cells, synaptic vesicles, and viral membranes have transmembrane protein volume occupancies on the order of  $\phi \approx 0.2$  to  $\phi \approx 0.3$ . As seen in Fig. 3, these low  $\phi$  may only have a small effect on

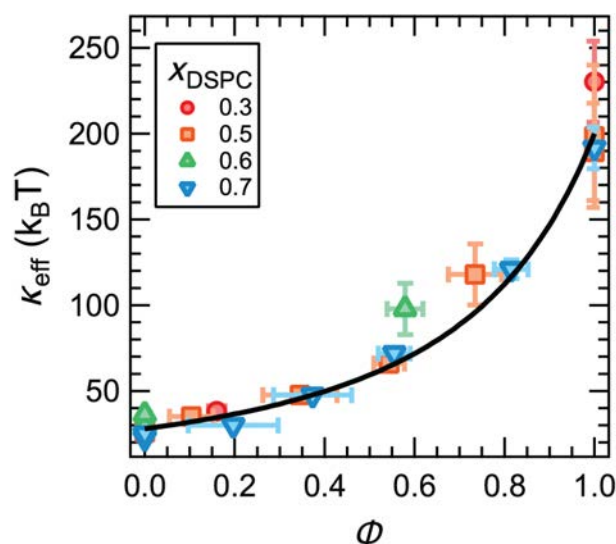


FIGURE 3: Effective bending modulus ( $\kappa_{\text{eff}}$ ) plotted versus area fraction of the gel phase ( $\phi$ ) for DMPC/DSPC lipid mixtures with the compositions given in the legend. The solid line is the predicted scaling calculated from the experimental data with no free parameters.

the membrane elasticity properties, where the protein-filled biological membranes may only be 1.2 to 1.3 times stiffer than a bare lipid matrix.

This work takes a bottom-up approach to understand the rigidity of heterogeneous membranes and was designed to experimentally measure the effective stiffness of a specific type of membrane described in theoretical studies. There are likely other contributions to  $\kappa_{\text{eff}}$  in biological membranes that are considerably more complex than the models used here. For example, asymmetric proteins are predicted to couple to local curvature changes in the membrane which could lead to membrane softening with increasing protein concentrations [3]. Many proteins are not perfectly rigid bodies and undergo their own shape fluctuations and rearrangements that could also couple to the membrane dynamics. Nevertheless, the present results highlight that NSE will be a powerful tool to understand the collective dynamics in membranes as the models continue to build in complexity and we better understand the interplay between membrane mechanics and biological function.

## References

- [1] E. G. Kelley, P. D. Butler, and M. Nagao, *Soft Matter* **15**, 2762 (2019).
- [2] R. R. Netz and P. Pincus, *Phys. Rev. E* **52** (4), 4114 (1995).
- [3] S. Leibler, *J. Physique* **47**, 507 (1986).



# Hibonite blue: A new class of inorganic blue colorants

B. A. Duell,<sup>1</sup> J. Li,<sup>1</sup> J. K. Stalick,<sup>2</sup> and M. A. Subramanian<sup>1</sup>

For thousands of years, civilizations around the world have sought inorganic materials that could be used to paint things blue, with limited success [1,2]. The first blue material discovered was Lapis Lazuli, which was about 6000 years ago. Since that discovery, only a few synthetic inorganic blue pigments have been developed – Prussian Blue ( $\text{Fe}_4[\text{Fe}(\text{CN})_6]_3$ ) in 1706, Cobalt Blue ( $\text{CoAl}_2\text{O}_4$ ) in 1802, Ultramarine Blue ( $\text{Na}_7\text{Al}_6\text{Si}_6\text{O}_{24}\text{S}_3$ , the synthetic form of lapis lazuli) in 1824, and YInMn Blue ( $\text{YIn}_{1-x}\text{Mn}_x\text{O}_3$ ) in 2009. Most of these compounds suffer from stability, cost, color, and toxicity issues. The YInMn Blue family of pigments are durable and possess remarkable heat reflecting properties, which makes them excellent candidates for energy-saving coatings, nonetheless they are not considered cost-effective for widespread general coating applications [2,3]. Co Blue,  $\text{CoAl}_2\text{O}_4$ , has been a dominant commercial blue pigment for the last two hundred years. It contains 33% by mass  $\text{Co}^{2+}$  and thus is expensive and environmentally unfriendly to produce.

The intensity of color generally scales with the chromophore composition, however reducing cobalt content is infeasible in the  $\text{CoAl}_2\text{O}_4$  spinel structure without significant loss in coloration. The search for materials with similar local environments for chromophores has led to the exploration of other crystal structures as color-producing hosts. The hibonite, with general formula  $\text{CaM}_{12}\text{O}_{19}$ , has five distinct crystallographic *M* sites, including three different octahedra, a set of tetrahedra, and a set of trigonal bipyramids (TBPs) (Fig. 1). Hibonites crystallize into a hexagonal crystal structure, with spinel blocks identical to  $\text{CoAl}_2\text{O}_4$  separated by an 'R' block with TBPs, face-sharing octahedral *M* sites, and the  $\text{Ca}^{2+}$  sites. The tetrahedral and TBP sites are of interest because they are non-centrosymmetric and therefore may produce intense transitions as found in  $\text{YIn}_{1-x}\text{Mn}_x\text{O}_3$  and  $\text{CoAl}_2\text{O}_4$ . Previous work has discovered many different colors in hibonite compounds [4,5]; however, the resulting blue colors are less intense than those in  $\text{CoAl}_2\text{O}_4$ .

We have investigated the effects of systematic  $\text{Co}^{2+}/\text{Ti}^{4+}$  substitution into the hibonite structure and have found that  $\text{Co}^{2+}$  gives rise to intense, tunable blue coloration with up to  $x = 1$   $\text{Co}^{2+}$  ( $\text{CaAl}_{12-2x}\text{Co}_x\text{Ti}_x\text{O}_{19}$ , 8 % by mass  $\text{Co}^{2+}$ ) [6]. This coloration at such low  $\text{Co}^{2+}$  concentrations is characteristic due to the unique effect of the co-substituted  $\text{Ti}^{4+}$  within the

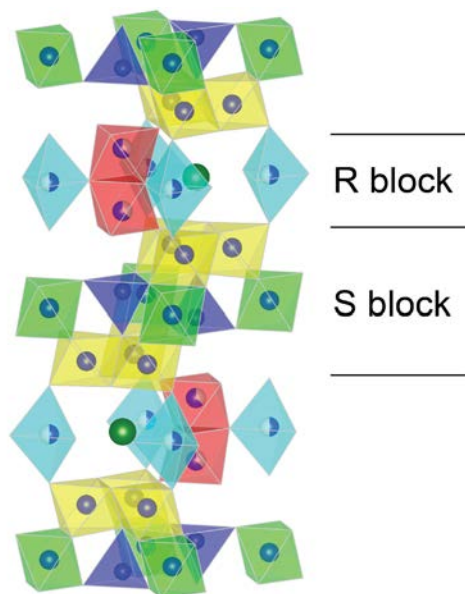


**FIGURE 1:** Unit cell of hibonite,  $\text{CaM}_{12}\text{O}_{19}$ . Dark green spheres are Ca ions, green and yellow polyhedra are edge-sharing  $\text{MO}_6$  octahedra, red are face-sharing  $\text{MO}_6$  octahedra, light blue are  $\text{MO}_5$  trigonal bipyramids (TBP), and blue are  $\text{MO}_4$  tetrahedra.

hibonite structure. This color is tunable by varying the  $\text{Co}^{2+}$  concentration as well as co-substitution with other transition metals, such as  $\text{Ni}^{2+}$ ,  $\text{Mn}^{3+}$ , and  $\text{Cr}^{3+}$ .

In order to understand the origin of the intense blue color of  $\text{CaAl}_{12-2x}\text{Co}_x\text{Ti}_x\text{O}_{19}$ , neutron powder diffraction data were collected using the NIST high resolution powder diffractometer. The structures were refined in hexagonal space group  $\text{P6}_3/\text{mmc}$ . We found that  $\text{Co}^{2+}/\text{Ti}^{4+}$  co-substitution increases the lattice parameters from the parent composition. The deep blue hues seen in hibonites originate in the strong site preference of  $\text{Co}^{2+}$  and  $\text{Ti}^{4+}$  substitution. The face-sharing octahedral sites are the primary occupied sites of  $\text{Ti}^{4+}$ , which is consistent with what has been found in other substituted hibonite systems. At least 70% of  $\text{Co}^{2+}$  distributes into the tetrahedral site and 17% distributes into the TBP site by  $x = 1$  substitution, with no  $\text{Co}^{2+}$  present in the face-sharing octahedral or one set of edge-sharing octahedral sites. Refinement of these numerous sites is enabled by the large difference in neutron scattering lengths of  $\text{Al}^{3+}$ ,  $\text{Co}^{2+}$ , and  $\text{Ti}^{4+}$ .

<sup>1</sup> Oregon State University, Corvallis, OR 97331

<sup>2</sup> NIST Center for Neutron Research, National Institute of Standards and Technology, Gaithersburg, MD 20899

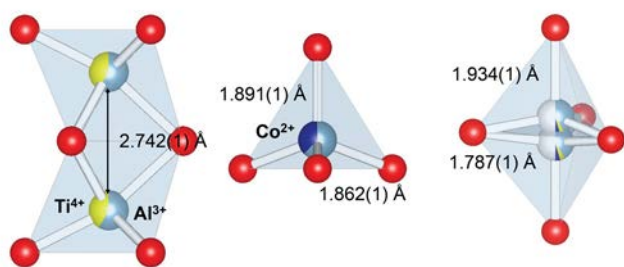


**FIGURE 2:** The face-sharing octahedral, tetrahedral, and TBP sites.  $\text{Ti}^{4+}$ ,  $\text{Al}^{3+}$ , and  $\text{Co}^{2+}$  occupancy is represented by bright yellow, light blue, and dark blue spheres, respectively; red spheres are oxygens. Interatomic distances of interest are shown.

The  $\text{Co}^{2+}$  ion displays a strong preference for the tetrahedral coordination environment even though the crystal field stabilization energy for octahedral  $\text{Co}^{2+}$  is higher. This may be because the  $d^7$  electron configuration of  $\text{Co}^{2+}$  favors a weak Jahn-Teller distortion in octahedral coordination, which is unavailable in the hibanite structure. Neither the TBP nor tetrahedral environments require a Jahn-Teller distortion for  $d^7$ , however, the tetrahedral site has a much higher percent of  $\text{Co}^{2+}$  in refined compositions. This is attributed to the displacement of the metal center of the TBP away from the trigonal plane (Fig. 2). This displacement creates a pseudo-tetrahedral environment that is smaller than the real tetrahedral site and thus less likely to be occupied by the larger  $\text{Co}^{2+}$  ion. The total TBP occupancy in refined compositions is similar, despite the difference in molar percent of cobalt out of all sites. This suggests the TBP site becomes saturated by  $\text{Co}^{2+}$  at low concentrations of  $\text{Co}^{2+}$ .

This site preference is much more pronounced in  $\text{CaAl}_{12-2x}\text{Co}_x\text{Ti}_x\text{O}_{19}$  than in the previously investigated  $\text{CaAl}_{12-2x}\text{Ni}_x\text{Ti}_x\text{O}_{19}$  or  $\text{Ca}_{1-x}\text{La}_x\text{Al}_{12-2x}\text{Ni}_x\text{O}_{19}$ . The high spin  $d^8$  electron configuration of  $\text{Ni}^{2+}$  may contribute to this reduced preference as the octahedral crystal field stabilization energy is much larger than that for  $\text{Co}^{2+}$ .

Diffuse reflectance spectra shown in Figure 3 reveal absorption peaks centered at 580 nm and 1400 nm associated with tetrahedral  $\text{Co}^{2+}$ , similar to that of commercial Cobalt Blue spinel. The hibanite blue spectra are blue-shifted until higher  $\text{Co}^{2+}$  concentration, resulting in a more neutral blue hue than Cobalt Blue. The tetrahedral site in hibanite blue is smaller and able to distort symmetrically away from the apical oxygen (Fig. 2), a feature forbidden in cubic Cobalt Blue. The increased intensity of the visible transition in hibanite is associated with the presence of both distorted tetrahedral  $\text{Co}^{2+}$  and TBP  $\text{Co}^{2+}$ . The TBP site is more accurately described as a disordered pseudo-tetrahedral site, which may contribute to the tetrahedral electronic transitions seen in the diffuse reflectance spectra. Lastly, we have found that due to the reduction in  $\text{Co}^{2+}$  content in hibanite blue compared to Cobalt Blue, the near infrared reflectivity is enhanced in hibanite blue, making hibanite blues more suitable for energy-saving heat-reflective coatings.

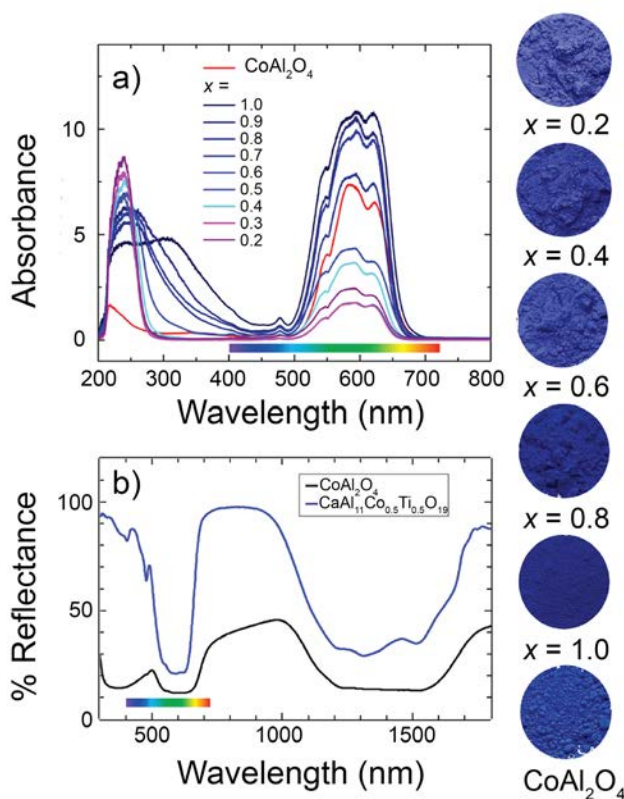


**FIGURE 3:** (a) UV/visible and (b) near infrared diffuse reflectance spectra of hibanite blue and cobalt blue. Representative color comparisons are shown at right.

In conclusion, we have found that hibanite blues exhibit intense, neutral blue coloration with  $\text{Co}^{2+}$  content lower than 8% by mass due to the high site preference of  $\text{Co}^{2+}$  and  $\text{Ti}^{4+}$  within the hibanite structure. This color rivals that of commercial Cobalt Blue pigments with a fraction the amount of  $\text{Co}^{2+}$  of Cobalt Blue while maintaining durability and better near infrared reflectivity.

## References

- [1] P. Ball, *Bright Earth: The Art and Invention of Color*, The Chicago University Press: Chicago (2003).
- [2] K. Kupferschmidt, *Science*. **364**, 424 (2019).
- [3] A. E. Smith, H. Mizoguchi, K. Delaney, N. A. Spaldin, A. W. Sleight, M. A. Subramanian, *J. Am. Chem. Soc.* **131**, 17084 (2009).
- [4] J. Li, E. A. Medina, J. K. Stalick, A. W. Sleight, M. A. Subramanian, *Prog. Solid State Chem.*, **44**, 107 (2016).
- [5] E. A. Medina, J. Li, M. A. Subramanian, *Prog. Solid State Chem.* **45-46**, 9 (2017).
- [6] B. A. Duell, J. Li, M. A. Subramanian, *ACS Omega*. **4** (26), 22114 (2019)

# Cation orientation dependent charge separation in a hybrid perovskite

E. M. Mozur,<sup>1</sup> J. C. Trowbridge,<sup>1</sup> A. E. Maughan,<sup>1</sup> M. J. Gorman,<sup>1</sup> C. M. Brown,<sup>2,3</sup> T. R. Prisk,<sup>2</sup> and J. R. Neilson<sup>1</sup>

Hybrid perovskites have radically transformed photovoltaics research. These materials do not quite “look” like our conventional semiconductors, such as silicon and gallium arsenide. While they all appear as black, light-absorbing materials macroscopically, hybrid perovskites have different atomic structures and atomic *dynamics*, as informed by diffraction and spectroscopy (Figure 1). The presence of an organic cation introduces several dynamic degrees of freedom not present in conventional materials. While these hybrid materials have recently been a focus of intense research, an enigmatic question has remained: does the organic component contribute to the advantageous properties? In other words, how does having a dynamic organic cation embedded into an inorganic semiconductor benefit the photovoltaic performance? A few studies have showed that optical excitation of the material yields transient (e.g.,  $\approx$  ps) responses of the organic cations that relate to the separation of charge carriers [1-3]; however, the relationship to macroscopic and steady-state performance has remained disconnected. Here we describe neutron scattering results which reveal how changes in the cation dynamics directly influence *steady-state* photoconductivity [4].

The hybrid perovskite formamidinium lead bromide,  $(\text{CH}(\text{NH}_2)_2)\text{PbBr}_3$ , exhibits a strong photoconductivity response with a puzzling temperature dependence showing 5 anomalies in the wavelength and amplitude on cooling single-crystal specimens (Figure 2). Only two of these anomalies are

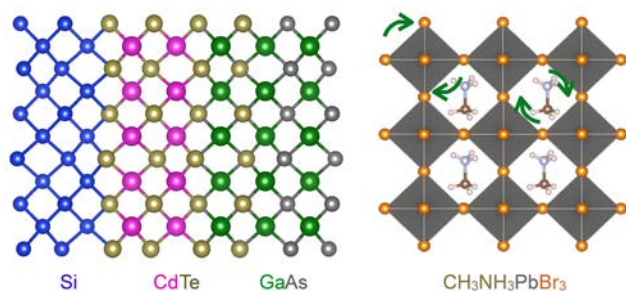


**FIGURE 1:** Comparison of the structures of the conventional inorganic semiconductors silicon, cadmium telluride, and gallium arsenide to the hybrid perovskite methylammonium lead bromide, which has dynamically reorienting molecular cations.

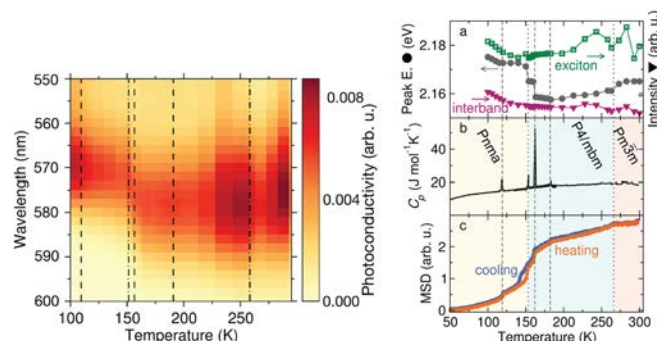


**FIGURE 2:** Left: False-color representation of the temperature-dependent photoconductivity as a function of excitation wavelength of  $(\text{CH}(\text{NH}_2)_2)\text{PbBr}_3$ . Dashed-dotted gray lines indicate crystallographically resolvable phase transition temperatures while transitions indicated by the dashed gray lines are not detected by diffraction. Right: (a) Photoconductivity peak center (left axis, gray circles), photoconductivity peak intensity (right axis, unfilled green triangles), and photoconductivity background intensity (right axis, pink triangles). (b) Heat capacity data for  $(\text{CH}(\text{NH}_2)_2)\text{PbBr}_3$  showing entropy-releasing phase transitions at 118 K, 153 K, 162 K, 182 K and 266 K; only the transitions at 153 K and 266 K result in a change of crystallographic symmetry (dashed-dotted lines). (c) Mean squared displacement (MSD) from fixed window elastic neutron scattering (NIST, HFBS). After [4].

explained by structural phase transitions detected by neutron and synchrotron X-ray diffraction (NIST, BT-1; APS, 11-BM). The remaining anomalies in these properties required an understanding of the dynamics of the material.

Changes in the dynamics and entropy of formamidinium lead bromide correlate with the anomalies in the temperature-dependent photoconductivity. Each of the five anomalies corresponds to an entropy-releasing phase transition detected by calorimetry experiments, including the phase transitions with changes in crystallographic symmetry (Figure 2a, b). Fixed-window elastic neutron scattering (NIST, HFBS) revealed that all five transitions correspond to significant changes in the dynamics of the material (Figure 2c). Given that  $^1\text{H}$  has the largest neutron scattering cross section in the material by nearly an order of magnitude, these changes in dynamics correspond largely to changes in motions of the formamidinium molecules. Therefore, the three anomalies not explained by changes in crystal structure depend on changes in organic cation dynamics.

<sup>1</sup> Colorado State University, Fort Collins, CO 80523

<sup>2</sup> NIST Center for Neutron Research, National Institute of Standards and Technology, Gaithersburg, MD 20899

<sup>3</sup> University of Delaware, Newark, DE 19716



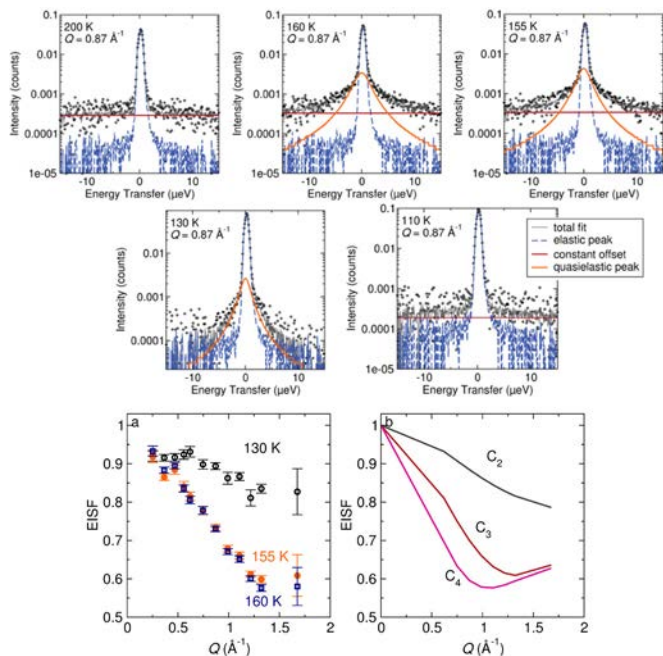


**FIGURE 3:** Top: Representative QENS spectra of  $\text{CH}(\text{NH}_2)_2\text{PbBr}_3$  collected above and below phase transition temperatures. The quasielastic component at the middle temperatures narrows as a temperature decreases, indicative of changes in the molecular dynamics within the energy resolution; the QENS is bandwidth limited at 200 K ( $\pm 15 \mu\text{eV}$ ). Bottom: (a) Elastic incoherent structure factor (EISF) extracted at  $T = 160$  K, 155 K, and 130 K. The smaller slope at  $T = 130$  K indicates that the geometry of the motion has changed to encompass a smaller radius in the extent of motion compared to  $T = 155$  K. For comparison, models constructed based on  $C_2$ ,  $C_3$ , and  $C_4$  molecular rotations are shown in (b). After [4].

The temperature dependence of the quasielastic neutron scattering (QENS) reveals a change in the nature of reorientational dynamics of the formamidinium molecules. Representative QENS data (NIST, HFBS; Figure 3, top) indicate a significant increase in the relaxation time upon cooling from 155 K to 130 K, as observed in the decreasing linewidth of the quasielastic component. By extracting the elastic incoherent structure factor (i.e., the  $Q$ -dependent ratio of incoherent elastic to incoherent total scattering), we reveal changes in the form factor of the formamidinium dynamics (Figure 3, bottom) – at higher temperatures, the molecules are able to undergo many hopping reorientations, consistent with  $120^\circ$  ( $C_3$ ) or  $90^\circ$

( $C_4$ ) rotations about the long molecular axis; however, upon cooling below 155 K, only  $180^\circ$  ( $C_2$ ) rotations about the short molecular axis are observed. This causes a measurable increase in the material's bandgap (Figure 3), indicating that the organic reorientational dynamics are coupled to the inorganic lattice that contributes to the frontier electronic states.

When we consider the observed changes in the photoconductivity of the hybrid perovskite formamidinium lead bromide in the context of the neutron scattering experiments, it shows that the cation dynamics are responsible for hidden, nanosized domains that result in changes to the macroscopic, optoelectronic response. This description is consistent with what others have described as a 'ferroelastic electret' [5] or dynamic, "ferroelectric large polarons" [3] in this family of materials. Our subsequent work studying the solid-solution,  $(\text{CH}(\text{NH}_2)_2)_{1-x}(\text{Cs})_x\text{PbBr}_3$ , using neutron scattering and nuclear spectroscopies ( $^1\text{H}$  and  $^{14}\text{N}$  NMR and  $^{79}\text{Br}$  NQR) revealed the importance of quadrupolar interactions between the organic cation and the anionic cage in dictating this phase behavior [6]. These neutron scattering studies make an important connection between organic cation dynamics and the steady-state photo-response of these materials that is directly relevant for photovoltaic applications.

## Reference

- [1] H. Zhu, K. Miyata, Y. Fu, J. Wang, P. P. Joshi, D. Niesner, K. W. Williams, S. Jin, X.-Y. Zhu. *Science* **353** (6306), 1409 (2016).
- [2] K. Miyata, D. Meggiolaro, M. T. Trinh, P. P. Joshi, E. Mosconi, S. C. Jones, F. De Angelis, X.-Y. Zhu. *Sci. Adv.* **3** (8), e1701217 (2017).
- [3] K. Miyata, X.-Y. Zhu. *Nat. Mater.* **17** (5), 379 (2018).
- [4] E. M. Mozur, J. C. Trowbridge, A. E. Maughan, M. J. Gorman, C. M. Brown, T. R. Prisk, J. R. Neilson. *ACS Mater. Lett.* **1** (2), 260 (2019).
- [5] J. N. Wilson, J. M. Frost, S. K. Wallace, A. Walsh. *APL Mater.* **7**, 010901 (2018).
- [6] E. M. Mozur, M. A. Hope, J. C. Trowbridge, D. M. Halat, L. L. Daemen, A. E. Maughan, T. R. Prisk, C. P. Grey, J. R. Neilson. *Chem. Mater.* **32**, 6266 (2020).

# Stability and microheterogeneity in concentrated nonaqueous electrolyte solutions

L. A. Robertson,<sup>1</sup> Z. Li,<sup>2,3</sup> Y. Cao,<sup>1</sup> I. A. Shkrob,<sup>4</sup> M. Tyagi,<sup>5,6</sup> K. C. Smith,<sup>7</sup> L. Zhang,<sup>4</sup> J. S. Moore,<sup>1,3,8</sup> and Y. Z.<sup>2,3,8,9</sup>

**B**attery technologies typically require high energy densities for economic feasibility. For popular solution-phase batteries (e.g., redox-flow batteries), this requirement translates to high concentrations of active materials. Structural properties, solubility, electrochemical diversity, and low cost make organic molecules promising active material candidates. However, problems, including high viscosities, crystallization, and high cell resistance, occur when the concentrations of redox-active organic molecules (ROMs) are increased in nonaqueous electrolyte solutions. Furthermore, building a reliable model to describe and predict the structure and dynamics of ROMs in nonaqueous electrolyte solutions is challenging, and experimental data are needed to develop the model. In this study, neutron scattering was performed on the CHANS High Flux Backscattering Spectrometer (HFBS) at the NCNR to probe crystallization behavior and microheterogeneity formation in nonaqueous electrolyte solutions. Specifically, we compared two solutions – one contained symmetrical ROMs prone to crystallize, and one contained desymmetrized ROMs preferring disordered states. Calorimetry and neutron data show that the desymmetrized system stays in a disordered liquid state even at very low temperatures and high concentrations. Interestingly, localized cold crystallization occurs during heating, which prompts the system to increase nucleation of microcrystalline solids within liquid phases. These findings suggest molecular clustering, solvation inhomogeneities, and molecular crowding in concentrated solutions [1].

Neutron scattering can easily distinguish between hydrogen and deuterium; this fact makes it a highly useful technique for probing multicomponent electrolyte solutions because it is possible to synthesize selectively deuterated ROMs. While we are interested in the single-particle motions measured by the neutron incoherent scattering, we kept the chemical species of interest protiated while deuterating all other components. In this work, we studied ROM solutions containing acetonitrile solvent, lithium bis(trifluoromethane)sulfonimide (LiTFSI)

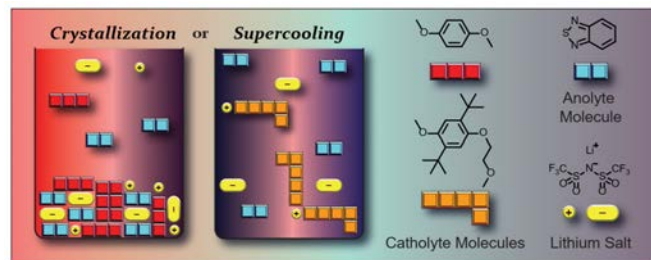


**FIGURE 1:** Crystallization differences in complex fluids

supporting electrolyte, dimethoxybenzene-based catholytes (oxidized species), and 2,1,3-benzothiadiazole anolyte (BzNSN, reduced species). We chose 1,4-dialkoxybenzene (DMB) as the catholyte for the “symmetrized” solutions and 2,5-di-tert-butyl-1-methoxy-4-[2'-methoxyethoxy]benzene (DBMMB) for the “desymmetrized” solutions. The ROMs were studied at 0.5 mol/L, 1.0 mol/L, and 1.5 mol/L concentrations while the LiTFSI was 1.0 mol/L in all cases. Neutron incoherent elastic scattering was measured using a fixed-window temperature scan to probe the temperature dependence of the single-particle dynamics. Differential scanning calorimetry (DSC) was performed to complement these data. Significant differences were observed between DMB-containing solutions and DBMMB-containing solutions. A schematic cartoon explains this phenomenon (Figure 1). DMB solutions prefer to crystallize while DBMMB solutions remain amorphous/supercooled. The LiTFSI was necessary to favor the supercooled state, likely through solvate formation with the functional groups on DBMMB. Interestingly, the supercooled DBMMB solutions also exhibited cold crystallization on heating.

We then performed quasi-elastic neutron scattering (QENS) experiments on DBMMB solutions both after cooling or heating to 250 K to reveal the molecular-level differences of supercooled and post-crystallized states. By analyzing the QENS spectra (see Figure 2), we extracted the  $Q$ -dependence of the relaxation time  $\tau$ . In Figure 3a and 3b,  $1/\tau$  vs.  $Q^2$  was shown.

<sup>1</sup> Department of Chemistry, University of Illinois at Urbana–Champaign, Urbana, IL 61801

<sup>2</sup> Department of Nuclear, Plasma, and Radiological Engineering, University of Illinois at Urbana–Champaign, Urbana, IL 61801

<sup>3</sup> Beckman Institute for Advanced Science and Technology, University of Illinois at Urbana–Champaign, Urbana, IL 61801

<sup>4</sup> Argonne National Laboratory, Argonne, IL 60439

<sup>5</sup> NIST Center for Neutron Research, National Institute of Standards and Technology, Gaithersburg, MD 20899

<sup>6</sup> Department of Material Science and Engineering, University of Maryland, College Park, MD 20742

<sup>7</sup> Department of Mechanical Science and Engineering, University of Illinois at Urbana–Champaign, Urbana, IL 61801

<sup>8</sup> Department of Materials Science and Engineering, University of Illinois at Urbana–Champaign, Urbana, IL 61801

<sup>9</sup> Department of Electrical and Computer Engineering, University of Illinois at Urbana–Champaign, Urbana, IL 61801



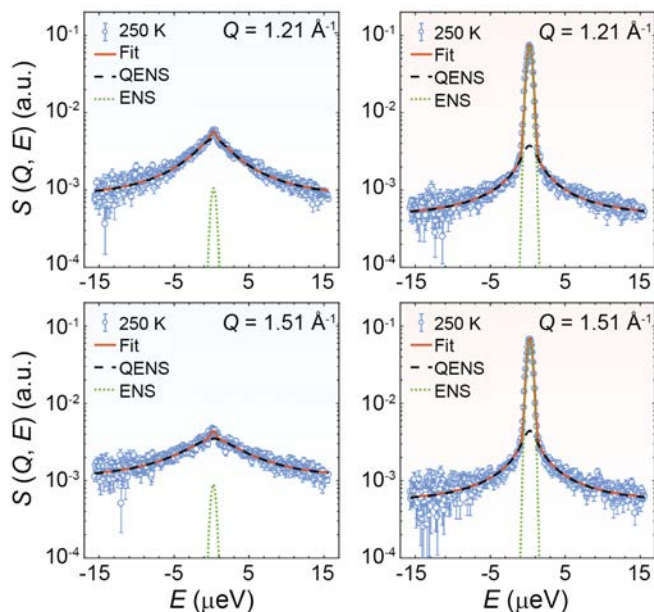


**FIGURE 2:** QENS spectra of 1.0 mol/L DBMMB at 250 K. The overall fit (the orange line) is the sum of the elastic (ENS, green dotted line) and inelastic (QENS, dark purple dashed line) contributions. For cooling curves, the stretching exponent,  $\beta$ , used was  $\beta = 0.65$ , while for heating  $\beta = 0.5$ .

After cooling,  $1/\tau$  increases nearly linearly with  $Q^2$  but deviates slightly from linearity at large  $Q$ . This behavior was fitted with the Singwi-Sjölander jump diffusion model [2], which implies a homogeneous phase (supercooled state). After heating,  $1/\tau$  depends on  $Q^2$  only for  $Q < 0.5 \text{ Å}^{-1}$ . For larger values of  $Q$ ,  $1/\tau$  shows oscillatory behavior (Figure 3b), suggesting a different phase state. This behavior was fitted with the Chudley-Elliott jump diffusion model [3]. In this model, the jump distance is fixed to account for diffusion in liquids with short-range order. The fitted jump length is five times larger than in the supercooled state, suggesting a more-ordered local structure. This result also indicates liquid-like and solid-like microdomains coexist after heating, and that the latter form by burst nucleation after the cold crystallization. These results demonstrate how subtle structural changes in electrolyte design lead to perturbative phase changes and the delicate balance between maintaining an amorphous glassy state vs. unwanted crystallization.

In summary, our work demonstrates how electrolyte design has a major impact on dynamics and phase behavior in ROMs

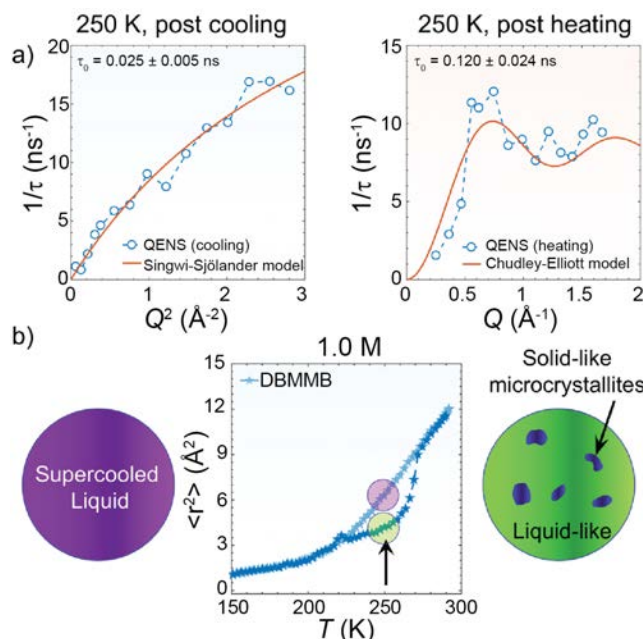


**FIGURE 3:** (a) 1.0 mol/L DBMMB at 250 K follows the Singwi-Sjölander jump diffusion model after cooling, suggesting a more homogeneous phase, and (b) the Chudley-Elliott jump diffusion model after heating, suggesting mixed solid-like microcrystalline and liquid-like domains and cartoons denoting these regimes.

nonaqueous solutions. Specifically, desymmetrized DBMMB-containing solutions show the formation of surprisingly metastable supercooled states on cooling and mixed solid-like and liquid-like states on heating. The coexistence of solid and liquid micro-domains further leads to the slower translational diffusion of the molecule; this result shows that neutron scattering is a powerful technique for understanding early-onset heterogeneity in concentrated flow battery solutions.

## References

- [1] L. A. Robertson, Z. Li, Y. Cao, I. A. Shkrob, M. Tyagi, K. C. Smith, L. Zhang, J. S. Moore, Y. Z., *J. Am. Chem. Soc.*, **141**, 8041 (2019).
- [2] K. S. Singwi, A. Sjölander, *Phys. Rev.*, **120**, 1093 (1960).
- [3] R. J. Chudley, C. T. Elliott, *Proc. Phys. Soc.*, **77**, 353 (1961).

# Quantification of sub-nanometer chloride layer on the surface of PbS nanocrystals

S.W. Winslow,<sup>1</sup> Y. Liu,<sup>2</sup> J.W. Swan,<sup>1</sup> and W.A. Tisdale<sup>1</sup>

**P**bs quantum dots (QDs) are a promising class of nanomaterials that have been proposed for use in many next-generation optoelectronic devices. These semiconductor crystallites – typically less than 8 nm in diameter – exhibit widely tunable absorbance/emission across the near-infrared spectrum. PbS QDs are particularly exciting for use in solar cells, LEDs, thermoelectrics, lasers, photodetectors, and infrared imaging systems. At the nanoscale, the high surface-to-volume ratio in these materials means the surface structure and energetics are critical to determining ensemble properties. However, quantitative chemical characterization of QD surfaces is extraordinarily challenging.

There are multiple synthetic routes for producing PbS QDs using either PbO or PbCl<sub>2</sub> as the lead precursor. However, there are notable differences in the reported materials from each synthesis. A sizing curve for PbO-based PbS QDs yields smaller nanocrystal sizes for a given first exciton absorption peak as compared to a sizing curve for PbS QDs synthesized with a large excess of PbCl<sub>2</sub> [1]. Additionally, the reported Pb-to-S ratio in PbCl<sub>2</sub>-based QDs is higher than that for PbO-based QDs, and residual Cl can be detected even after washing [1]. Circumstantial evidence suggests that PbS QDs prepared from a PbCl<sub>2</sub> precursor may be coated with an insulating PbCl<sub>x</sub> shell [2, 3]. However, direct structural evidence is missing. Transmission electron microscopy (TEM) shows only that PbCl<sub>2</sub>-based QDs are as large as they were originally reported to be. This is because electron scattering techniques are dominated by the heavy lead atoms, which are present in both the PbS core and the hypothesized PbCl<sub>x</sub> shell. Small angle X-ray scattering (SAXS) likewise is dominated by Pb. Moreover, X-ray powder diffraction (XRD) is of limited value since an epitaxial PbCl<sub>x</sub> shell, by definition, will have the same continuous crystal structure as the PbS core.

In a recent paper, we showed that small angle neutron scattering (SANS) provides the elemental contrast needed to quantify the presence of a PbCl<sub>x</sub> shell in oleate-capped PbCl<sub>2</sub>-based PbS QDs [4]. Unlike electron and X-ray scattering probes, neutron scattering cross sections do not scale with the atomic number. SANS is well-suited to resolve all components of a colloidal nanocrystal given the significant contrast between the core, surface layer, ligand-shell, and solvent that results from the different scattering length densities (SLDs) of each of these

components. The ability to shift the contrast with the solvent through deuteration enables robust parameter estimation for a complex model of the nanoparticle form factor.

We used Bayes rule to describe the statistical relationship between the parameters of a piecewise linear form factor model

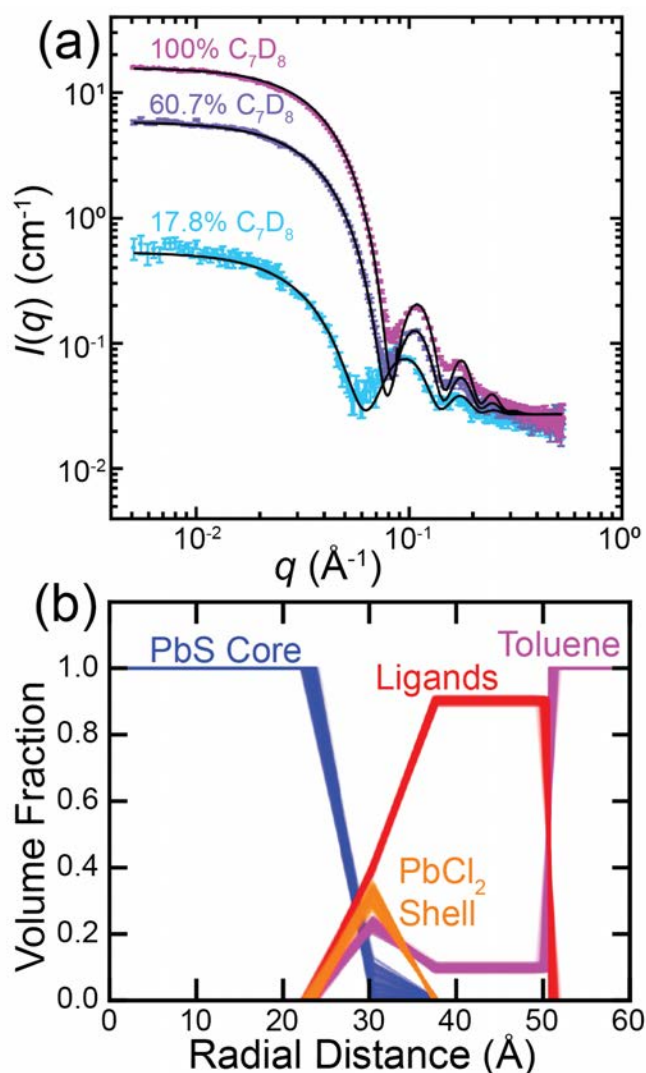


**FIGURE 1:** SANS data fitting of oleate-capped colloidal PbS nanocrystals in toluene. (a) Fit intensity profiles of three selected deuteration fractions. (b) Best-fit radial volume fraction profile corresponding to the data presented in panel (a).

<sup>1</sup> Department of Chemical Engineering, Massachusetts Institute of Technology, Cambridge, MA 02139

<sup>2</sup> NIST Center for Neutron Research, National Institute of Standards and Technology, Gaithersburg, MD 20899

derived from molecular dynamics simulations and the measured scattering intensity in experiments with nanocrystals. We sampled from the distribution of form factor model parameters using an affine invariant Markov Chain Monte Carlo (MCMC) method. This statistical approach to analyzing the scattering data enabled detection and uncertainty quantification for different materials and their amounts within the nanocrystal core and the ligand shell. We found that the ensemble of form factor models sampled by the MCMC method using data drawn from nanocrystals synthesized with and without a chloride precursor were statistically distinct. Samples of the different form factor models were used to compute the expected ratios of lead to sulfur and sulfur to chlorine in the nanocrystals as well as the variance in these ratios. We confirmed that the elemental ratios derived solely from the form factor model and scattering data were consistent with elemental analysis of solutions of nanocrystals synthesized with and without a chloride precursor. These robust statistical methods for analyzing scattering data are far more complex than standard least squares fitting. However, the ability to derive ensembles of form factor models and to analyze directly the correlations among different parameters within the model yield insights that make the additional computational effort worthwhile.

Our SANS experiments were performed at the NG7SANS instrument at the NIST Center for Neutron Research. In order to have enough data sets to determine all the fitting parameters, nine different solvent contrasts were prepared by mixing the protonated and deuterated solvents. The fraction of the deuterated solvent ranges from 17% to 100%. By fitting all the data at different contrasts, our SANS analysis aided with a computer simulation model yields a lead chloride surface layer thickness of  $\approx 0.3$  nm, which is consistent with a monolayer of  $\text{PbCl}_2$  epitaxially bound to the PbS core. The difference in sizing curves is attributed to this surface layer. The ligand coverage and atomic ratios measured with SANS agree with nuclear magnetic resonance (NMR) spectroscopy and energy-dispersive X-ray spectroscopy (EDS) measurements on the same QDs. Finally, we used this information to propose an atomic surface configuration that is charge neutral and consistent with all experimental measurables. This study resolved a scientific discrepancy between reported sizing curves for PbS QDs and further demonstrated the power of SANS in resolving molecular structure in soft and hybrid nanomaterials.

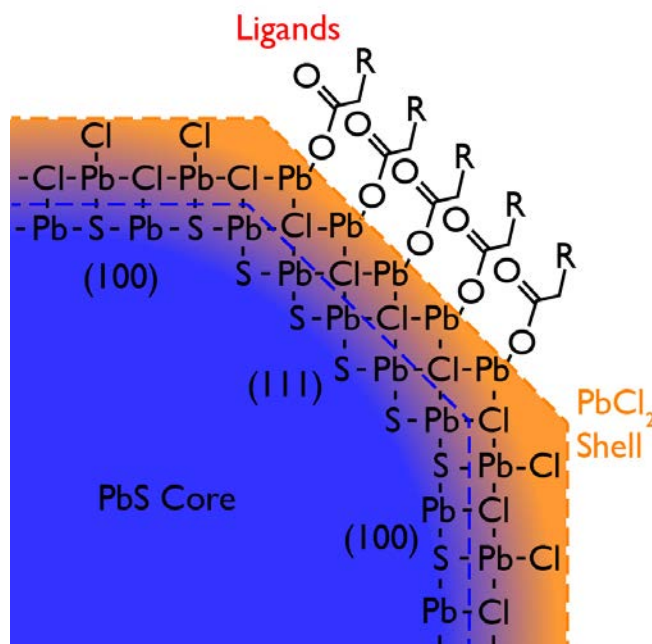


**FIGURE 2:** Proposed structure of the  $\text{PbCl}_x$  shell. A pristine PbS core (blue) is covered in a monolayer of  $\text{PbCl}_2$  (orange) over both (100) and (111) facets. The three-dimensional structure, including oleate ligands bound to the (111) facets, is charge neutral.

## References

- [1] M. C. Weidman, M. E. Beck, R. S. Hoffman, F. Prins, W. A. Tisdale, *ACS Nano* **8**, 6363 (2014).
- [2] S. Brittman, A. E. Colbert, T. H. Brintlinger, P. D. Cunningham, M. H. Stewart, W. B. Heuer, R. M. Stroud, J. G. Tischler, J. E. Boercker, *J. Phys. Chem. Lett.* **10**, 1914 (2019).
- [3] P. B. Green, Z. Li, M. W. B. Wilson, *J. Phys. Chem. Lett.* **10**, 5897 (2019).
- [4] S. W. Winslow, Y. Liu, J. W. Swan, W. A. Tisdale, *bridge* **1**, 209 (2019).



# Field-tunable quantum disordered ground state in the triangular-lattice antiferromagnet $\text{NaYbO}_2$

M. M. Bordelon,<sup>1</sup> E. Kenney,<sup>2</sup> C. Liu,<sup>3</sup> T. Hogan,<sup>4</sup> L. Posthuma,<sup>1</sup> M. Kavand,<sup>5</sup> Y. Lyu,<sup>5</sup> M. Sherwin,<sup>5</sup> N. P. Butch,<sup>6</sup> C. Brown,<sup>6,7</sup> M. J. Graf,<sup>2</sup> L. Balents,<sup>8</sup> and S. D. Wilson<sup>1</sup>

**M**agnetic ground states that are forbidden from ordering due to quantum fluctuations, such as quantum spin liquids, represent enticing new electronic phases of matter that in certain scenarios host long-range entanglement between spins and unconventional quasiparticles. However, experimentally stabilizing and studying quantum spin liquid states predicted from idealized theoretical models is an enduring challenge—one often fraught with the complexities of defects, anisotropies, and symmetry breaking that appear in real materials. Our recent study advances this field by using neutron scattering techniques to identify a chemically ideal material,  $\text{NaYbO}_2$ , that stabilizes a native, quantum-disordered, ground state that can be driven into a classically ordered phase via the application of an external magnetic field. This opens an exciting new frontier for exploring and understanding how quantum disorder arises in a highly frustrated magnetic system and how external perturbations promote the formation of competing magnetic order.

Geometrically frustrated magnetic materials are a rich platform for discovering new electronic phases of matter, and the triangular lattice antiferromagnet is one of the most intensively studied cases. The interplay of quantum effects in the limit of  $S = 1/2$  spins and underlying anisotropies can lead to dynamically disordered, many-body correlated ground states that fundamentally behave differently from a conventionally ordered magnet or a frozen ensemble of disordered spins. Emergent degrees of freedom such as fractionalized spin excitations are endemic to many flavors of these quantum disordered states and are often sought via neutron inelastic scattering experiments. Realizing materials capable of manifesting true quantum disordered ground states born from idealized spin Hamiltonians is often a challenge, as is finding unambiguous evidence of many of the exotic properties predicted from these models. Within triangular lattice systems, chemical defects, lattice distortions, or electronic anisotropies in real materials often break the symmetries of an idealized, frustrated spin Hamiltonian and either promote conventional magnetic order or a static, frozen magnetic ground state.

Rare earth oxides, such as  $\text{YbMgGaO}_4$  [1-4], have recently generated interest in this arena where Yb-moments with a Kramers' crystalline electric field  $J_{\text{eff}} = 1/2$  ground state decorate a geometrically-ideal triangular lattice. While this material exhibits a continuum of spin excitations and no signs of conventional long-range order that could presage a true quantum disordered ground state, intrinsic site disorder (between divalent Mg and trivalent Ga ions) within its crystal structure imparts ambiguity to interpreting these effects as either born from quantum fluctuations or from highly disordered exchange fields. To address this ambiguity, we furthered this notion of harnessing rare earth oxides to create an ideal triangular lattice of  $J_{\text{eff}} = 1/2$  moments and explored the magnetism in the compound  $\text{NaYbO}_2$  [5]. Unlike previous materials studied, in  $\text{NaYbO}_2$ , the triangular layers of Yb moments are not impacted by innate chemical disorder (Figure 1), and this has a resounding effect on the resultant low-temperature physical states observable in the system.

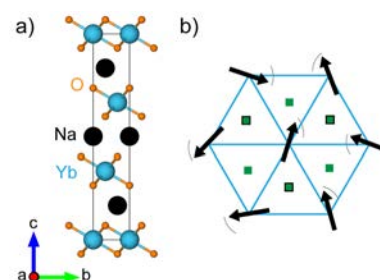


**FIGURE 1:** (a)  $\text{NaYbO}_2$  crystallizes in the  $\alpha\text{-NaFeO}_2$   $R\bar{3}m$  structure with  $D_{3d}\text{YbO}_6$  octahedra generating two-dimensional triangular lattice layers (Yb: blue, O: orange, Na: black). The layers are stacked in an ABC sequence separated by one, fully occupied Na ion layer, within experimental resolution. (b) A simplified depiction of a spin liquid state involves dynamically disordered quantum spins that resist magnetically ordering to zero Kelvin. In  $\text{NaYbO}_2$ , the system does not order in zero field down to 50 mK, as the  $J_{\text{eff}} = 1/2$  spins are frustrated in the triangular lattice. Furthermore, the stacking sequence enhances the geometrical frustration of the system, as the projection of Yb ions into neighboring planes contains three equivalent bonds from the center of a Yb triangle (Yb ions above: black outlined green squares; Yb ions below: green squares).

<sup>1</sup> Materials Department, University of California, Santa Barbara, Santa Barbara, CA 93106

<sup>2</sup> Department of Physics, Boston College, Chestnut Hill, MA 02467

<sup>3</sup> Department of Physics, University of California, Santa Barbara, Santa Barbara, CA 93106

<sup>4</sup> Quantum Design, Inc., San Diego, CA 92121

<sup>5</sup> Department of Physics and Center for Terahertz Science and Technology, University of California, Santa Barbara, Santa Barbara, CA 93106

<sup>6</sup> NIST Center for Neutron Research, National Institute of Standards and Technology, Gaithersburg, MD 20899

<sup>7</sup> Department of Chemical and Biomolecular Engineering, University of Delaware, Newark, DE 19716

<sup>8</sup> Kavli Institute for Theoretical Physics, University of California, Santa Barbara, Santa Barbara, CA 93106

Figure 1 shows the chemical structure of  $\text{NaYbO}_2$ . The  $\text{YbO}_6$  octahedra form in the  $D_{3d}$  point group and generate  $J_{\text{eff}} = 1/2$  spins that decorate a geometrically ideal triangular lattice. Specific heat measurements of the system [5] reveal that this material exhibits a complex series of magnetic phenomena that vary with temperature and magnetic field. In zero magnetic field, no sharp anomaly appears down to 80 mK; this is one indication that the material contains an unconventional, disordered ground state. The data instead only show broad features that account for all the expected magnetic entropy of a  $J_{\text{eff}} = 1/2$  system. However, upon the application of a magnetic field, the features in specific heat shift in temperature and form a sharp peak indicative of the appearance of magnetic order. This provides evidence that the disordered magnetic ground state is innate in this material and can be driven to order under a reasonably small perturbation that breaks the degeneracy of  $\text{NaYbO}_2$ 's quantum disordered magnetic ground state.

The appearance of the sharp heat capacity anomaly coincides with new, long-range ordered, magnetic diffraction peaks, observed at 5 T using the NCNR neutron powder diffractometer BT-1, that are absent at 0 T [5]. Fits to the neutron powder diffraction data show that the ordered magnetic state is a collinear “up-up-down” state represented by two ordering wave vectors of  $k_1 = (1/3, 1/3, 0)$  and  $k_2 = (0, 0, 0)$  with moments aligning nearly parallel to the  $(1, -1, -1)$  direction. The extracted magnetic moment of  $1.36 \pm 0.1 \mu\text{B}$  per Yb ion is slightly lower than the expected  $1.5 \mu\text{B}$  moment and is likely caused by strong remnant quantum fluctuations endemic to this material.

Neutron inelastic scattering measurements performed on DCS at the NCNR on  $\text{NaYbO}_2$  powder were used to explore the dynamics associated with the unconventional ground state of this compound (Figure 2). In zero field, the data in Figure 2 (a) reveal a gapless continuum of excitations centered on the two-dimensional antiferromagnetic  $Q = (1/3, 1/3, 0)$  zone center ( $1.25 \text{ \AA}^{-1}$ ) and spanning a 1 meV bandwidth. Upon increasing magnetic field, these magnetic excitations coalesce into an ordered state, and a new flat band of excitations appears near 1 meV at 5 T. Linear spin wave models of these excitations within the ordered state identify a model XXZ Hamiltonian with a slight easy-plane anisotropy and  $J_z = 0.45$  and  $J_{xy} = 0.51$  meV. However, this classical model fails to capture the inelastic spectrum in zero field and predicts  $120^\circ$  correlations between neighboring moments in an ordered antiferromagnetic ground state. Further theoretical analysis of  $\text{NaYbO}_2$  suggests that the quantum fluctuations and geometrical frustration in this material are enhanced by three-dimensional interlayer frustration that potentially promotes a two-dimensional spin liquid magnetic ground state.  $\text{NaYbO}_2$  therefore shows promise for exploring the behavior of this anomalous new magnetic phase and, more broadly, for helping us to understand how a quantum

disordered phase evolves into a conventionally ordered magnetic state as its degeneracy is lifted via the application of a modest magnetic field.

In summary, our work demonstrates that  $\text{NaYbO}_2$  is a model material for investigating the formation of an intrinsic quantum disordered state formed by  $J_{\text{eff}}=1/2$  Yb-moments on a triangular lattice. The presence of a field-induced transition into a magnetically ordered “up-up-down” state directly demonstrates that this quantum disordered state is innate to the highly frustrated Yb-based triangular lattice and does not arise from extrinsic chemical disorder.  $\text{NaYbO}_2$  thus provides a unique opportunity to investigate the formation of a quantum spin liquid ground state and to test predictions of model Hamiltonians in a chemically ideal setting with an easily field-controllable magnetic phase diagram.

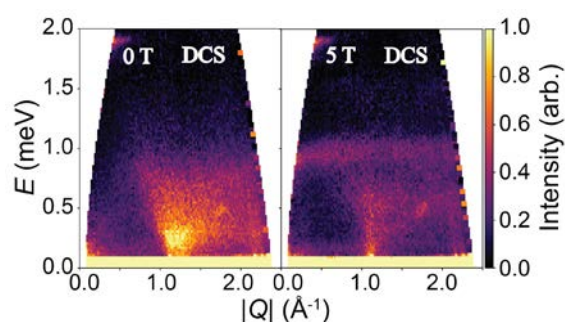


**FIGURE 2:** (a) Neutron inelastic scattering from a powder sample at 67 mK in zero magnetic field in the quantum disordered state of  $\text{NaYbO}_2$ . Scattering intensity is centered near  $Q = (1/3, 1/3, 0)$  ( $1.25 \text{ \AA}^{-1}$ ) and forms a continuum that stretches to roughly 1 meV. (b) At 5 T and 74 mK, the inelastic spectral weight is pushed primarily into the elastic line forming static magnetic order and develops a flat band near 1 meV. The strong, low-energy, quantum fluctuations in  $\text{NaYbO}_2$  become suppressed by the external magnetic field as it enters a conventional long-range ordered phase with an equal moment “up-up-down” structure.

## References

- [1] Y. Li, H. Liao, Z. Zhang, S. Li, F. Jin, L. Ling, L. Zhang, Y. Zou, L. Pi, Z. Yang, J. Wang, Z. Wu, Q. Zhang. *Sci. Rep.* **5**, 16419 (2015).
- [2] Y. Li, D. Adroja, R. I. Bewley, D. Voneshen, A. A. Tsirlin, P. Gegenwart, Q. Zhang. *Phys. Rev. Lett.* **118**, 107202 (2017).
- [3] Y. Shen, Y.-D. Li, H. Wo, Y. Li, S. Shen, B. Pan, Q. Wang, H. C. Walker, P. Steffens, M. Boehm, Y. Hao, D. L. Quintero-Castro, L. W. Harriger, M. D. Frontzek, L. Hao, S. Meng, Q. Zhang, G. Chen, J. Zhao. *Nature* **540**, 599 (2016).
- [4] J. A. M. Paddison, M. Daum, Z. Dun, G. Ehlers, Y. Liu, M. B. Stone, H. Zhou, M. Mourigal. *Nat. Phys.* **13**, 117 (2017).
- [5] M. M. Bordelon, E. Kenney, C. Liu, T. Hogan, L. Posthuma, M. Kavand, Y. Lyu, M. Sherwin, N. P. Butch, C. Brown, M. J. Graf, L. Balents, S. D. Wilson. *Nat. Phys.* **15**, 1058 (2019).



# Magnetic phase transitions and spin-density distribution in the molecular multiferroic $\text{GaV}_4\text{S}_8$ system

R. L. Dally,<sup>1</sup> W. D. Ratcliff II,<sup>1,2</sup> L. Zhang,<sup>3,4</sup> H.-S. Kim,<sup>5,6</sup> M. Bleuel,<sup>1,2</sup> J. W. Kim,<sup>6,7</sup> K. Haule,<sup>6</sup> D. Vanderbilt,<sup>6</sup> S.-W. Cheong,<sup>3,6,7</sup> and J. W. Lynn<sup>1</sup>

It can be very convenient to think of magnetism in terms of localized spins – that is, assigning a valence state to an atom, which determines the magnitude of the moment at that atom. While this picture works well for insulators and even some metals, many materials can't be described in these terms. An example is a molecular magnet, where a group of atoms shares an unpaired electron (or, electrons) and this group is the smallest unit in a compound for which you can assign a moment value.  $\text{GaV}_4\text{S}_8$  is a molecular magnet, where  $\text{V}_4$  tetrahedra share a single electron with  $S = 1/2$ , and all the magnetic properties within the system are driven by this electron within each vanadium cluster. Above 44 K,  $\text{GaV}_4\text{S}_8$  has cubic lattice symmetry, and the electron is known to be equally shared between all vanadium atoms due to equal V-V bonding lengths (Fig. 1(a)). When  $\text{GaV}_4\text{S}_8$  is cooled below 44 K, it undergoes a structural distortion that breaks the equality of the V-V bonds, and an outstanding question has been what happens to the shared nature of the electron? This is a particularly important inquiry because the structural transition displaces one V atom (the apical) in the cluster further from the other three, which induces a robust ferroelectricity, a sought-after material property involving charge ordering. A proper understanding and modeling of the ferroelectricity depends on knowing where the electron resides. Upon further cooling,  $\text{GaV}_4\text{S}_8$  orders magnetically at 13 K, and the dual ordering of charge and spin is what classifies this system as a multiferroic. These two properties can be coupled, where manipulating one type of order can drive the other to undergo changes, thus broadening the ways in which the properties useful to quantum computing and spintronics can be controlled.

Using the triple-axis spectrometer BT7, we carried out neutron-diffraction measurements of the magnetic order as a function of temperature and magnetic field in all the different phases of this multiferroic system [1]. The transition from the high-temperature cubic phase to the low-temperature rhombohedral phase at 44 K can be seen in Fig. 1(b), where the (3,3,3) Bragg peak splits as the symmetry is lowered and ferroelectricity sets in. The focus of this study was to determine the magnetization

density in the ferroelectric phase and the nature of the magnetic ground state, which turns out to be ferromagnetic. The magnetization density, a real-space distribution, is determined by measuring the magnetic form factor, a reciprocal space quantity, which gives information on the location of the unpaired electron within the material. This measurement is particularly challenging in  $\text{GaV}_4\text{S}_8$  given that the magnetic moment is small and that the magnetic Bragg scattering coincides with the nuclear Bragg scattering. Nevertheless, we were able to make these measurements by using the field-induced magnetic scattering and a polarized neutron beam, which maximizes sensitivity to weak magnetic scattering. The magnetic form factor at 20 K obtained from these polarized beam data is shown in Fig. 2(a), where we have assumed in calculating the magnetic structure factor that the average aligned moment on each V ion is the same and aligned along the field direction. The smooth curve is the calculated spherically averaged form factor for a singly ionized V atom. Some deviations from spherical symmetry are not unusual, so we don't expect all the points to be within the statistical uncertainties of the curve, but there is quite good agreement with the overall trend. In contrast, assuming that the unpaired electron is only located on the apical ion produces an unphysical result, as shown in Fig. 2(b) for the same experimental data. Density functional theory (DFT) calculations found that the electron most likely has a slight inhomogeneous distribution among the 4 V, but the results are consistent with the neutron analysis showing that the equal density picture model best fits the data. Analysis of magnetic form factor data requires exact knowledge of the crystal structure. Repeating the form factor measurements at 15 K, which pushes the system closer to the magnetically ordered state, proved difficult due to the coupling between the magnetic and ferroic orders, which was reflected in our measurements by changes to the structure as field was applied.

Exploring the magnetic ground state utilized both polarized and unpolarized neutron diffraction measurements. We found that the field-induced saturated magnetic moment at 20 K – above the long-range ordered state – matched that of the zero-field

<sup>1</sup> NIST Center for Neutron Research, National Institute of Standards and Technology, Gaithersburg, MD 20899

<sup>2</sup> Department of Materials Science and Engineering, University of Maryland, College Park, MD 20742

<sup>3</sup> Laboratory for Pohang Emergent Materials, Pohang Accelerator Laboratory and Max Plank POSTECH Center for Complex Phase Materials, Pohang University of Science and Technology, Pohang 790-784, Korea

<sup>4</sup> School of Materials Science and Engineering, Harbin Institute of Technology, Harbin, 150001, China

<sup>5</sup> Department of Physics, Kangwon National University, Chuncheon 24341, Republic of Korea

<sup>6</sup> Department of Physics and Astronomy, Rutgers University, Piscataway, NJ 08854

<sup>7</sup> Rutgers Center for Emergent Materials, Rutgers University, Piscataway, NJ 08854

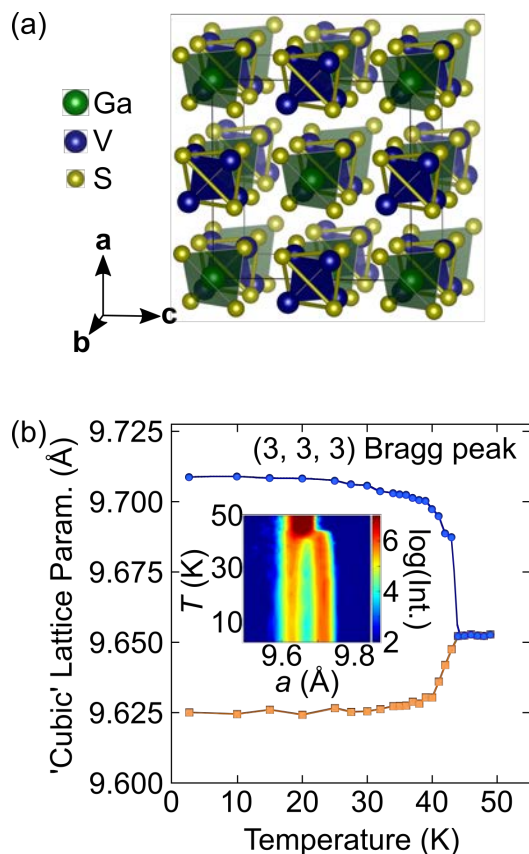


**FIGURE 1:** (a) Crystal structure of GaV<sub>4</sub>S<sub>8</sub> in the cubic phase. (b) The effective "cubic" lattice parameters from neutron-diffraction data. The inset is a contour plot of the neutron diffraction intensity from the (3, 3, 3) Bragg peak as it splits on cooling below the cubic-to-rhombohedral phase transition.

magnetic moment at 2 K. The analysis showed that all the magnetic moment can be accounted for assuming a collinear ferromagnetic model as the ground state. Additionally, we were able to determine that in the ground state, the magnetic anisotropy is particularly strong, such that a 2 T applied field is not large enough to pull the moments away from the preferred ferromagnetic axis.

Measurements performed at the NCNR focused on studying the distribution of the unpaired electron within the V<sub>4</sub> clusters and the magnetic ground state using neutron diffraction. In addition to the diffraction measurements, theoretical calculations using the DFT framework were employed to verify what was observed. The theoretical and experimental results are in close agreement, suggesting that the electron stays distributed among the vanadium clusters upon entering the electrically polarized phase. The study also demonstrated the coupled nature between the magnetic and ferroic ordering, where the

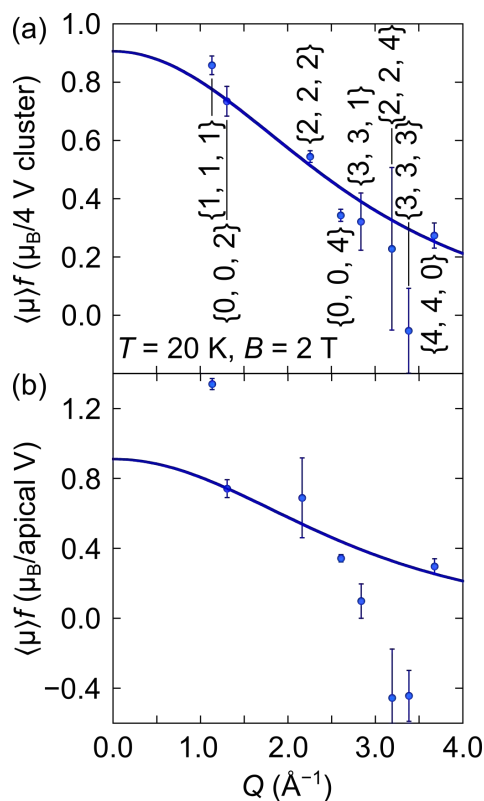


**FIGURE 2:** (a) Magnetic form factor obtained from the polarized beam data, normalized by moment per V<sub>4</sub> cluster and plotted against wavevector, assuming that the electron is equally likely to be found on the 4 V. The solid curve is the spherically averaged form factor for a singly ionized V atom. This function was fit to the data, and both data and function are scaled by the saturated moment at high field. (b) Alternative extracted form factor assuming the electron is localized on the apical V, where the solid curve is the spherical average for a singly ionized V atom. This function provides a poor fit to the data, where both data and function are scaled by the saturated moment at high field.

addition of an applied magnetic field redistributes the structure due to the magnetic moments aligning with the external field. These results answer outstanding questions about GaV<sub>4</sub>S<sub>8</sub>, which has long been studied for its many intriguing properties.

## References

- [1] R. L. Dally, W. D. Ratcliff II, L. Zhang, H.-S. Kim, M. Bleuel, J. W. Kim, K. Haule, D. Vanderbilt, S.-W. Cheong, J. W. Lynn, Phys. Rev. B **102**, 014410 (2020).

# Three-dimensional magnetism in a kagome staircase lattice

J. S. Helton,<sup>1,2</sup> N. P. Butch,<sup>2</sup> D. M. Pajerowski,<sup>2</sup> S. N. Barilo,<sup>3</sup> and J. W. Lynn<sup>2</sup>

**F**rustrated magnetism occurs when a material contains coupled magnetic moments where no ordered state can simultaneously satisfy all magnetic interactions. Geometrical frustration arises from the material's lattice structure, usually from antiferromagnetic interactions (which encourage neighboring spins to point antiparallel) in a material with spins arrayed on triangular plaquettes. The antiferromagnetic kagome lattice, consisting of corner-sharing triangles, is particularly frustrated due to an infinite degeneracy of the classical ground state. Frustration can also arise from disorder or when ferromagnetic and antiferromagnetic interactions compete. Magnetic frustration weakens the energetic favorability of the ordered state, which often allows for unique magnetic phases to arise due to quantum or thermal fluctuations.  $\text{Co}_3\text{V}_2\text{O}_8$  features spin-3/2 magnetic moments arranged on a kagome staircase lattice of corner-sharing triangles (Fig. 1). While competing interactions yield a complex magnetic phase diagram, previous work had treated the compound as quasi-two-dimensional with only weak interactions between the buckled kagome planes. In contrast, our extensive spin-wave measurements using the DCS spectrometer at the NCNR show that a fundamentally three-dimensional magnetic model is necessary to describe this material [1]. Further, the spin-wave spectra point to an unusually large Dzyaloshinskii-Moriya antisymmetric exchange interaction on the nearest-neighbor bond.

$\text{Co}_3\text{V}_2\text{O}_8$  belongs to a family of compounds featuring a divalent transition metal ion decorating the kagome-staircase structure. Like the planar-kagome lattice, magnetic ions lie on corner-sharing triangles. In the kagome-staircase structure there are two crystallographically distinct sites: the Co1 sites, referred to as the cross-ties, and the Co2 sites, referred to as the spines. Previous powder and single-crystal-diffraction experiments [2] revealed a complex series of magnetically ordered phases. Below  $T_C = 6.2$  K all magnetic moments align ferromagnetically along the  $a$ -axis. Above  $T_C$  diffraction experiments show antiferromagnetic Bragg peaks with a propagation vector  $\vec{k} = (0, \delta, 0)$ , where  $\delta$  evolves continuously with temperature from  $\delta = 1/3$  just above  $T_C$  to  $\delta = 0.55$  at  $T_N = 11.3$  K with commensurate lock-ins at  $1/3$  and  $1/2$  persisting over a range of temperatures. These diffraction data indicate a transversely polarized spin-density-wave structure, where the changing value of  $\delta$  with temperature

is driven by competition between various ferromagnetic and antiferromagnetic interactions.

A previous work [3] had measured the spin-wave spectra of  $\text{Co}_3\text{V}_2\text{O}_8$  along the  $[H\ 0\ 0]$  and  $[0\ 0\ L]$  directions and found that they could be modeled fairly accurately using only the nearest-neighbor-ferromagnetic interaction  $J_1$  between a cross-tie and spine site. Because of this the literature had, for a decade, treated  $\text{Co}_3\text{V}_2\text{O}_8$  as quasi-two-dimensional with the out-of-plane magnetic interactions being quite small compared to those within a buckled-kagome plane. Using the DCS spectrometer, we measured the spin-wave spectra of  $\text{Co}_3\text{V}_2\text{O}_8$  in the ferromagnetic phase in multiple orientations that could probe along the  $[0\ K\ 0]$  direction (perpendicular to the buckled-kagome planes). We found that the spin waves along this direction, shown in Fig. 2(a), are highly dispersive with a bandwidth comparable to that measured along directions within the planes. This indicates fully three-dimensional magnetism, with interactions between planes that are comparable in strength to those within them.

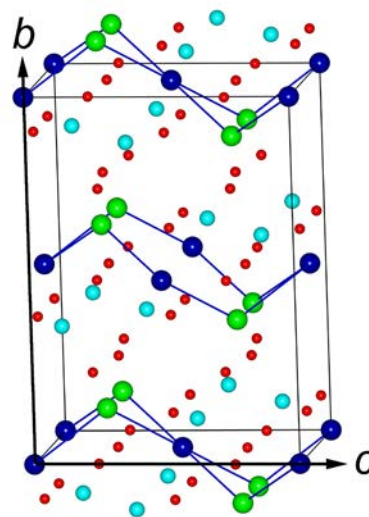


**FIGURE 1:** Structure of  $\text{Co}_3\text{V}_2\text{O}_8$ . The two crystallographically distinct cobalt sites are shown in blue (Co1 cross-tie sites) and green (Co2 spine sites). Vanadium ions are cyan and oxygen ions are red.

<sup>1</sup> United States Naval Academy, Annapolis, MD 21402

<sup>2</sup> NIST Center for Neutron Research, National Institute of Standards and Technology, Gaithersburg, MD 20899

<sup>3</sup> Institute of Solid State and Semiconductor Physics, Academy of Sciences, Minsk 220072, Belarus



Our spin-wave spectra along these directions reveal two distinct modes that are split from each other by about 0.3 meV near high-symmetry points, indicating an avoided crossing between these two modes. One possible cause of this avoided crossing is the Dzyaloshinskii-Moriya (DM) interaction, an antisymmetric exchange interaction that is possible for bonds with low symmetry but that is typically fairly weak. We performed a fit of all of our measured spin-wave data to a spin Hamiltonian featuring multiple Heisenberg exchange terms, a DM interaction on the nearest-neighbor bond, and single-ion anisotropy on each site. Figure 2 displays both the data and simulations using the best fit Hamiltonian, showing very good agreement. As expected, the fit values support a three-dimensional magnetic model where the out-of-plane couplings between a spine and cross-tie site ( $J_3 = -0.14 \text{ meV} \pm 0.02 \text{ meV}$ ) or between spine sites ( $J_4 = -0.12 \text{ meV} \pm 0.03 \text{ meV}$ ) on adjacent planes are only slightly weaker than the ferromagnetic interaction between spine and cross-tie sites within the same plane ( $J_1 = -0.21 \text{ meV} \pm 0.02 \text{ meV}$ ). It is expected that there must also be at least one weaker antiferromagnetic coupling between planes in order to lead to the antiferromagnetic spin-density-wave phase observed between 6.2 K and 11.3 K [2]. The structure of the  $\delta = 1/2$  spin-density wave features spins connected by these three dominant ferromagnetic interactions that are aligned with each, suggesting that antiferromagnetic perturbations too small to be deduced from spin-wave measurements could be sufficient to drive the spin-density wave phase.

The measured spin-wave spectra are best fit by a model that includes a DM interaction on the nearest-neighbor bond with  $D_{1,x} = 0.12 \text{ meV} \pm 0.03 \text{ meV}$ . This is an unexpectedly large value, with  $D_1/J_1 \geq 0.5$ . Other frustrated magnets with very large DM interactions display unique physics like topological excitations, nonreciprocal spin waves, or the magnon Hall effect.  $\text{Ni}_3\text{V}_2\text{O}_8$  features spin-1 moments on a kagome-staircase structure that is very similar to that of  $\text{Co}_3\text{V}_2\text{O}_8$ .

The related  $\text{Ni}_3\text{V}_2\text{O}_8$  compound is a multiferroic material, with combined magnetic and electrically polarized domains that can be controlled with an applied electric field [4]. The magnetic order in the multiferroic phase exhibits a helical-spin-density wave that might be stabilized by a DM interaction. In this way a full understanding of the magnetic Hamilton of  $\text{Co}_3\text{V}_2\text{O}_8$  might shed new light on the multiferroic behavior of the related material.

We also performed neutron spectroscopy measurements at 9.2 K, in the spin-density-wave phase. Well-defined spin waves were not observed. Instead, we found that most of the spectral weight was in broad, diffuse scattering centered on antiferromagnetic Bragg positions, which may be a characteristic of the spin-density wave that would be interesting to explore further experimentally.

$\text{Co}_3\text{V}_2\text{O}_8$  is a prime example of classical frustrated magnetism driven by competing ferromagnetic and antiferromagnetic interactions. Extensive spin-wave measurements at the NCNR have shown that the magnetic interactions are more complex than previously assumed, with strong magnetic interactions between buckled-kagome planes yielding an essentially three-dimensional spin Hamiltonian. This enables future work to probe the effects of subtle antiferromagnetic interactions between the planes in driving the spin-density-wave phase. An unusually strong Dzyaloshinskii-Moriya interaction on the nearest-neighbor bond is also required to explain the spin waves. Such a strong DM term suggests that  $\text{Co}_3\text{V}_2\text{O}_8$  might be close to a more exotic ordered structure, possibly including an inversion-symmetry-breaking-helical order of the type that is found in the multiferroic phase of the structurally similar compound  $\text{Ni}_3\text{V}_2\text{O}_8$ .

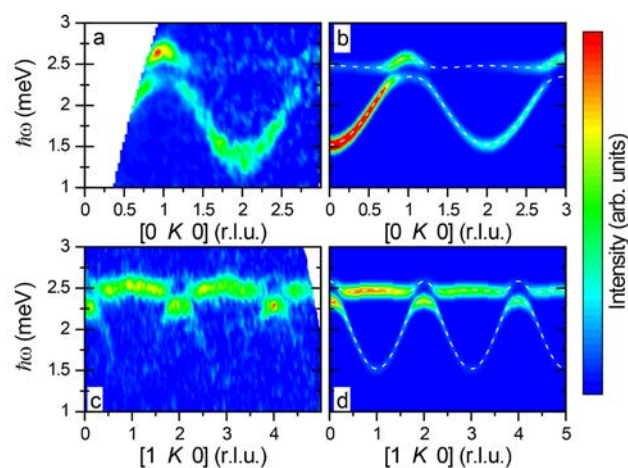


**FIGURE 2:** Measured and calculated spin-wave spectra of  $\text{Co}_3\text{V}_2\text{O}_8$  in the ferromagnetic phase at 2.8 K. Top: Measured (a) and modeled (b) spectra along the  $[0\ K\ 0]$  direction, expressed as reciprocal lattice units (r.l.u.). Bottom: Measured (c) and modeled (d) spectra along the  $[1\ K\ 0]$  direction. The dashed white lines are the dispersions of the two spin-wave modes where the splittings are caused by the very large Dzyaloshinskii-Moriya interaction.

## References

- [1] J. S. Helton, N. P. Butch, D. M. Pajerowski, S. N. Barilo, J. W. Lynn, *Science Advances* **6**, eaay9709 (2020).
- [2] Y. Chen, J. W. Lynn, Q. Huang, F. M. Woodward, T. Yildirim, G. Lawes, A. P. Ramirez, N. Rogado, R. J. Cava, A. Aharony, O. Entin-Wohlman, A. B. Harris, *Phys. Rev. B* **74**, 014430 (2006).
- [3] M. Ramazanoglu, C. P. Adams, J. P. Clancy, A. J. Berlinsky, Z. Yamani, R. Szymczak, H. Szymczak, J. Fink-Finowicki, B. D. Gaulin, *Phys. Rev. B* **79**, 024417 (2009).
- [4] I. Cabrera, M. Kenzelmann, G. Lawes, Y. Chen, W. C. Chen, R. Erwin, T. R. Gentile, J. B. Leão, J. W. Lynn, N. Rogado, R. J. Cava, C. Broholm, *Phys. Rev. Lett.* **103**, 087201 (2009).

# Anisotropic effect of a magnetic field on the neutron spin resonance in FeSe

*T. Chen,<sup>1</sup> Y. Chen,<sup>2</sup> D. W. Tam,<sup>1</sup> B. Gao,<sup>1</sup> Y. Qiu,<sup>3</sup> A. Schneidewind,<sup>4</sup> I. Radelytskyi,<sup>4</sup> K. Prokes,<sup>5</sup> S. Chi,<sup>6</sup> M. Matsuda,<sup>6</sup> C. Broholm,<sup>2,3</sup> and P. Dai<sup>1</sup>*

**H**igh-transition-temperature (high- $T_c$ ) superconductivity in copper- and iron-based materials, derived from their antiferromagnetic (AF) ordered parent compounds [1, 2], is believed to arise from interactions between itinerant electrons mediated by spin fluctuations [3]. One of the key signatures is the appearance of a neutron spin resonance mode, a collective spin excitation with an intensity tracking the superconducting order parameter below  $T_c$ . In the case of iron-based superconductors, the spin resonance can have more than one component in energy and be anisotropic in spin space due to the multi-orbital nature and spin orbital coupling (SOC). Here we study iron selenide (FeSe), a clean material among iron-based superconductors with relatively low  $T_c$  and a sharp resonance in energy, on MACS at the NIST Center for Neutron Research. We show that a c-axis aligned magnetic field suppresses the intensity of the spin resonance mode much more efficiently than for an in-plane field, which is consistent with lower upper critical fields required to suppress superconductivity in c-axis aligned fields, suggesting that the intensity of the resonance is a measure of superconducting electron pairing density.

FeSe, which undergoes a tetragonal-to-orthorhombic structural transition at  $T_s = 90$  K, forms a nematic phase below  $T_s$ , and becomes superconducting at  $T_c = 9$  K, is an excellent choice to test if the resonance in iron-based superconductors is a spin exciton and associated with singlet-triplet or singlet-doublet transition for several reasons. First, the compound is known to be extremely clean and has a relatively low resonance energy of  $E_r = 3.6$  meV. Second, the resonance in FeSe only occurs at the in-plane AF wave vector  $Q_{AF} = (1, 0)$ . Third, neutron polarization analysis of the resonance reveals that the mode is anisotropic in spin space and essentially c-axis polarized due to SOC. Finally, the upper critical fields to suppress superconductivity in FeSe are around 16 T and 28 T for the c-axis and in-plane aligned fields, respectively, meaning that an applied magnetic field will have a larger impact on superconductivity compared with that of optimally doped iron pnictides.

The effect of an 8.5 T in-plane magnetic field on the resonance and low-energy spin excitations is shown using data obtained on MACS. Figures 1(a-d) show constant-energy scans along the  $[1, 0]$  direction at different energies with 8.5 T and zero

magnetic fields in the superconducting state ( $T = 2$  K). At  $E = 2.5$  meV, an 8.5 T field induces magnetic scattering near  $Q_{AF} = (1, 0)$  above the flat background, indicating a reduction in spin gap energy [Fig. 1(a)]. Near the resonance around

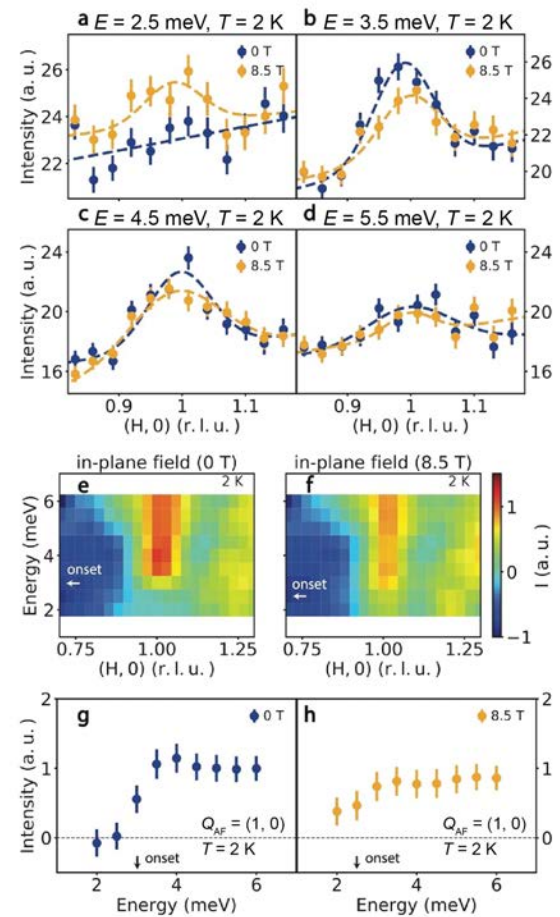


**FIGURE 1:** (a)-(d) Constant-energy scans along the  $[1, 0]$  direction, expressed as reciprocal lattice units (r.l.u.), at  $E = 2.5$  meV, 3.5 meV, 4.5 meV and 5.5 meV in zero field and 8.5 T in-plane magnetic fields at  $T = 2$  K. (e) and (f) 2D images of wave-vector and energy dependence of the spin fluctuations in 0 T and 8.5 T in-plane magnetic fields at  $T = 2$  K. (g) and (h) are constant- $Q$  cuts at the  $Q_{AF}$  position from (e) and (f), respectively. The error bars indicate statistical errors of one standard deviation.

<sup>1</sup> Rice University, Houston, TX 77005

<sup>2</sup> Johns Hopkins University, Baltimore, MD 21218

<sup>3</sup> NIST Center for Neutron Research, National Institute of Standards and Technology, Gaithersburg, MD 20899

<sup>4</sup> Jülich Center for Neutron Sciences, Forschungszentrum Jülich GmbH, Outstation at MLZ, D-85747 Garching, Germany

<sup>5</sup> Helmholtz Zentrum Berlin für Materialien und Energie, 14109 Berlin, Germany

<sup>6</sup> Oak Ridge National Laboratory, Oak Ridge, TN 37831



$E = 3.5$  meV [Fig. 1(b)], the field suppresses the resonance as expected. Above the resonance energy at  $E = 4.5$  meV and 5.5 meV, the applied field has little effect on the magnetic scattering [Figs. 1(c), and 1(d)]. Figures 1(e) and 1(f) show the two-dimensional (2D) wave vector-energy images of the resonance above background scattering at zero field and 8.5 T field, respectively. The effect of an 8.5 T in-plane magnetic field is to weaken and broaden the resonance, with no convincing evidence for the splitting of the mode. Figure 1(g) is a cut along the energy direction at  $Q_{AF} = (1, 0)$ , which reveals the resonance at 0 T field. The net effect of a magnetic field is to push the spectral weight of the resonance to lower energies [Fig. 1(h)].

Figure 2 illustrates the effect of a 5 T c-axis aligned magnetic field on the resonance. Figure 2(a-d) show constant-energy scans along the  $[1, 0]$  direction with different energies in 5 T and zero magnetic fields in the superconducting state ( $T = 2$  K). At  $E = 2$  meV, a 5 T c-axis aligned field induces magnetic scattering near  $Q_{AF}$ , which is 1.6 meV below the spin resonance energy  $E_r$ . Off the resonance energy at  $E = 3$  meV and 4 meV and above the resonance energy at  $E = 5$  meV, the applied field has slight effect on the resonance. Figures 3(e) and 2(f) compare the 2D images of the wave-vector and energy dependence of the spin resonance in 0 T and 5 T, respectively. For a c-axis aligned magnetic field, the upper critical field  $B_{c2}(\perp)$  is around 16 T, meaning that a 5 T field is already  $\approx 31\%$  of  $B_{c2}$ , which is similar to the fraction of 30 % achieved for the 8.5 T in-plane oriented field given the 28 T critical field. Although qualitatively the broadening in energy is similar to that of the in-plane field, the amplitude of the broadening is more significant. Figures 2(g) and 2(h) show the constant- $Q$  cuts at the  $Q_{AF}$  position from (e) and (f), respectively. We see that an applied field shifts the magnetic spectral weight to lower energies. By comparing Figs. 1(g), 1(f), 2(g) and 2(f), we conclude that a 5 T c-axis aligned field has a larger impact on the resonance than that of an 8.5 T in-plane field.

The effects of c-axis and in-plane magnetic fields on the neutron spin resonance of FeSe, are determined. An in-plane magnetic field increases the width of the resonance following the field-induced Zeeman effect, while a c-axis aligned field suppresses and broadens the resonance much more effectively than the in-plane field, clearly related to the orbital effect and vortex currents induced by the c-axis field. The data indicates that rather than the absolute applied field, it is the ratio of the applied field to the upper critical field that controls changes in the magnetic excitation spectrum. The results are consistent with the hypothesis that the resonance is associated with electron pairing density in FeSe superconductor.

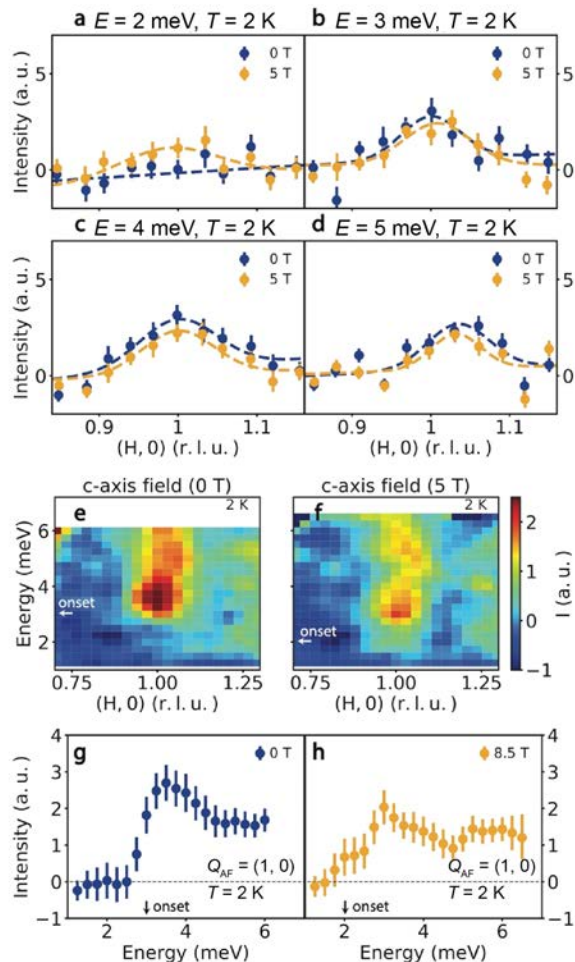


**FIGURE 2:** (a)-(d) Constant-energy scans along the  $[1, 0]$  direction at  $E = 2$  meV, 3 meV, 4 meV and 5 meV in zero field and 5 T c-axis aligned magnetic fields at  $T = 2$  K. (e) and (f) 2D images of wave- vector and energy dependence of the resonance in zero field and 5 T magnetic fields at 2 K. (g) and (h) are constant- $Q$  cuts at the  $Q_{AF}$  position from (e) and (f), respectively. The error bars indicate statistical errors of one standard deviation.

## References

- [1] M. R. Norman, *Science* **322**, 196 (2011).
- [2] B. Keimer, S. A. Kivelson, M. R. Norman, S. Uchida, J. Zaanen, *Nature* **518**, 179 (2015).
- [3] D. J. Scalapino, *Rev. Mod. Phys.* **84**, 1383 (2012).
- [4] T. Chen, Y. Chen, D. W. Tam, B. Gao, Y. Qiu, A. Schneidewind, I. Radelytskyi, K. Prokes, S. Chi, M. Matsuda, C. Broholm, P. Dai, *Phys. Rev. B* **101**, 140504 (2020).

# Realization of magnon spin valves utilizing unexpected antiferromagnetic coupling on Si

Y. Fan,<sup>1</sup> P. Quarterman,<sup>2</sup> J. Finley,<sup>1</sup> J. Han,<sup>1</sup> P. Zhang,<sup>1</sup> J. T. Hou,<sup>1</sup> M. D. Stiles,<sup>3</sup> A. J. Grutter,<sup>2</sup> and L. Liu<sup>1</sup>

**T**raditional spin valves built around a nonmagnetic (NM) layer sandwiched by two metallic ferromagnetic (FM) layers have found applications in hard disk drives as well as spintronic memories and logic schemes. The key concept of a spin valve is that the efficiency of spin-polarized electrons able to travel across the FM/NM/FM structure is dependent on the relative orientation of the magnetization of the two ferromagnetic layers (i.e. parallel vs. antiparallel). Thus, the state of the valve is 'written' by setting the relative magnetization direction by a variety of methods such as external fields, spin-transfer torques, and spin-orbit torques and is 'read-out' by the resistance across the structure due to the efficiency of spin-polarized electrons transmitted from one end to the other, known as magnetoresistance.

Magnons, also known as spin waves, transmit spin without the need for electron currents. A magnon is the magnetic analog of a photon or phonon, and is a quantized quasiparticle associated with coherent magnetic excitations of precessing spins that form a standing wave. Transmission of spins using only magnons, and not spin polarized electron currents, is potentially advantageous in that magnons allow for long-distance signal propagation (not limited by spin diffusion lengths) while avoiding the energy dissipation associated with Joule heating. A magnon spin valve is conceptually similar to a traditional spin valve, except in this case the relative orientation of the magnetic layers does not modulate the flow of spin-polarized currents, but instead regulates the magnon transmission coefficient. In particular, because insulators block charge currents, hybrid systems which integrate magnetic insulators (MIs) with metallic FMs show promise for realizing a highly efficient magnon spin valve.

Yttrium iron garnet ( $\text{Y}_3\text{Fe}_5\text{O}_{12}$ , YIG) is a ferrimagnetic insulator that efficiently propagates magnons and possesses other favorable magnetic properties that make it a promising material for use in spintronic technologies. The magnon spin valve effect has been realized in YIG/Au/YIG/Pt and YIG/CoO/Co samples, where the spacer layers (Au and CoO) allow for the realization of parallel and antiparallel magnetic configurations between the YIG layers. In these systems, the metallic Pt and Co layers serve as a read-out of the magnon transmission from the YIG as a charge current via the inverse spin Hall effect, a phenomenon where a spin polarized current is converted into a conventional electric charge current [1, 2]. As is common for obtaining high

quality YIG, these works relied on growing the structures on  $\text{Gd}_3\text{Ga}_5\text{O}_{12}$  (GGG) substrates which results in non-homogenous magnetization profiles due to interdiffusion between the YIG films and the substrate. More importantly, structures reliant on GGG substrates are not compatible with semiconductor industry techniques for mass production.

In an effort to realize magnon spin transport in YIG hybrid structures grown on industry compatible Si, we have used sputtering to grow Pt(10 nm)/YIG(40 nm)/Py(20 nm)/Ru(3 nm) (where Py denotes the popular alloy permalloy,  $\text{Ni}_{80}\text{Fe}_{20}$ ) thin films on Si substrates [3]. Initial magnetic characterization of the samples was completed using common laboratory scale magnetometry (Figure 1), where it was found that the switching of the magnetization differs dramatically depending on whether YIG and Py are in direct contact or separated by a thin insulating barrier. However, laboratory scale magnetometry can lead to ambiguous understanding when the total magnetic moment is non-trivial—such as in cases including, but not limited to complex interlayer coupling, multiple domains, magnetic dead layers, and magnetic proximity effects.

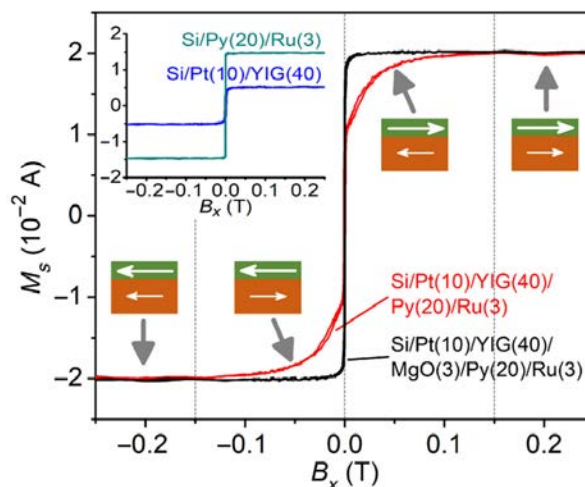


**FIGURE 1:** Magnetometry measurements of the Si/Pt(10)/YIG(40)/Py(20)/Ru(3) and Si/Pt(10)/YIG(40)/MgO(3)/Py(20)/Ru(3) samples (thickness denoted in nm). When the external field is less than 150 mT, pronounced differences in the switching process were observed. Inset shows control samples with individual magnetic layers to demonstrate magnetic moment conservation.

<sup>1</sup> Microsystems Technology Laboratories, Massachusetts Institute of Technology, Cambridge, MA 02139

<sup>2</sup> NIST Center for Neutron Research, National Institute of Standards and Technology, Gaithersburg, MD 20899

<sup>3</sup> Physical Measurement Laboratory, National Institute of Standards and Technology, Gaithersburg, MD 20899

To thoroughly characterize the depth resolved chemical composition and in-plane magnetization for the Si/Pt/YIG/Py/Ru hybrid structure, we carried out polarized neutron reflectometry measurements using the PBR instrument with varied *in situ* magnetic field (Figure 2a). We found that the sample contained sharp interfaces, near theoretical composition for each layer and at an applied field of 700 mT had magnetizations in strong agreement with expected values (indicative of magnetic moments fully aligned to the field). The depth profiles of the nuclear and magnetic scattering length densities are shown in Fig. 2b. When the field was lowered to 4 mT, we surprisingly found that the polarized neutron reflectometry (PNR) data (Figure 2a) could only be fit to a model in which the magnetization of the YIG layer is antiparallel to the field and Py magnetization direction. We then carried out a series of field dependent measurements to map out the reversal mechanism, including collecting reflectivity in the spin flip cross-sections to search for signatures of magnetic domains perpendicular to the field direction—which we did not observe. From these field dependent measurements, we found that the YIG and Py layers aligned along the same direction only when the external field was in excess of 150 mT. In order to confirm that this unexpected antiparallel coupling is caused by exchange coupling, and not dipolar effects, a similar control sample was measured with a thin 3 nm insulating layer of MgO separating the YIG and Py (data not shown). In this sample, we observed that the YIG and Py remain aligned in parallel both at high field (700 mT) and low field (4 mT)—indicative that direct contact (i.e. exchange coupling) is the necessary for this antiferromagnetic coupling in our Si/Pt/YIG/Py/Ru samples.

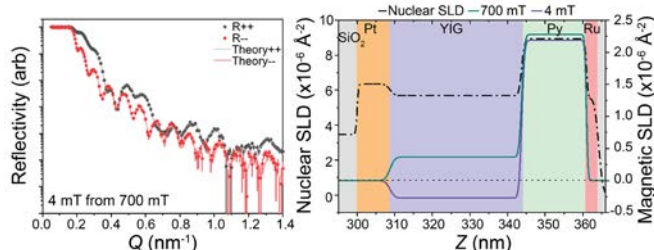


**FIGURE 2:** (a) PNR data for the Si/Pt/YIG/Py/Ru hybrid structure for an applied field of 4 mT. The depth profiles of the nuclear (dashed, left axis) and magnetic (solid, right axis) scattering length densities for an external field of 700 mT and 4 mT. A positive/negative magnetic scattering length density corresponds to a magnetization applied parallel/anti-parallel to the magnetic field.

Given that our Si based Pt/YIG/Py hybrid samples showed pronounced and unambiguous antiferromagnetic and ferromagnetic coupling, when in direct contact, depending on the external field, the samples were patterned into spin-pumping devices to look for signatures of the magnon spin valve effect. Patterning was carried out such that the electrodes were placed only on the Pt layer, and the whole device was then mounted onto a RF waveguide, which was used to set the Py into ferromagnetic resonance and generate the magnon current in the YIG by spin injection. The two DC electrodes

were attached to the Pt layer as a ‘read-out’ of the magnon spin current injected into Pt via the inverse spin Hall effect. A cartoon schematic of this setup can be seen in Figure 3a.

The spin pumping signal, in the Pt layer, as a function of field with varied driving radio frequency is shown in Figure 3b. Based on the relationship between the resonance field vs. radio frequency input, the signal detected in the Pt originated from the Py layer. This was further confirmed by control measurements that found no clear resonance peaks associated with the YIG layer, and the DC resistance between the Pt and Py layers was found to be as large as a one-hundred mega-Ohm. From these combined results, we were able to conclude that the magnetic excitation in the Py is transmitted to the Pt as a DC voltage through magnon transmission in the YIG and spin to charge conversion from the inverse spin Hall effect. Further, the field dependence shows that the detected voltage in the Pt is largest when the external field corresponds to the YIG and Py aligning in parallel, and smallest when they are antiparallel. And so, by taking the ratio of these spin pumping voltages, we estimated the ON/OFF ratio of our magnon spin valve to be 130%.

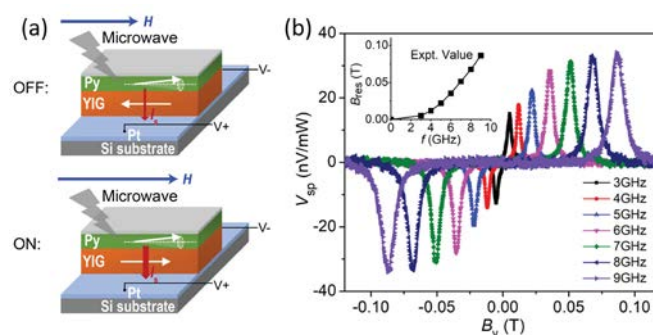


**FIGURE 3:** (a) a schematic of the spin valve structure and ferromagnetic resonance setup. (b) Spin pumping voltage induced in the underlying Pt layer as a function of field  $B_y$  (T) differing applied radio frequency.

This work demonstrated that new magnetic coupling mechanisms can be found even in thin film materials that have been thought to be well understood. Using PNR, we have shown that YIG grown on Si substrates directly couples antiparallel to Py, without the need for an additional spacer layer, when the applied field is less than 150 mT. This novel coupling has been used as the building block for a magnon spin valve that operates at room temperature with an efficient ON/OFF ratio of 130 %, which is comparable to low temperature achievements on GGG samples reported by other groups. Thus, we have demonstrated that magnon spintronics may be industry compatible and not simply an exciting physics playground.

## References

- [1] H. Wu et al., Physical Review Letters **120**, 097205 (2018).
- [2] J. Cramer et al., Nature Communications **9**, 1089 (2018).
- [3] Y. Fan et al., Physical Review Applied **13**, 061002 (2020).



# Benchmarking residual stress and dimensional fidelity in additive manufacturing

T. H. Gnaupel-Herold,<sup>1</sup> T. Q. Phan,<sup>2</sup> J. Heigel,<sup>2</sup> and L. E. Levine<sup>3</sup>

There is a growing expectation that additive manufacturing (AM) will lift manufacturing to a new level not just through a new fabrication technology, but also by fabricating parts that could not have been made any other way. At the core of the technology is highly localized and rapid melting followed by fast cooling, resulting in significant levels of residual stresses/strains at various length scales. Such stresses and their effect on the performance of AM parts represent one of the main obstacles for a broad dissemination of the technology. It is therefore crucial to accurately predict the residual stresses either to aid decision making for mitigation (heat treatment) or to make stress induced distortions part of the design. In response, NIST initiated the AM bench program in which a series of controlled measurements would provide customers with stress/strain data for a well characterized bridge shape part. The beneficiaries of this program are simulation software developers, companies that both manufacture parts using AM and AM machines, and end users.

The bridge shape part investigated here [1] was produced by the laser powder bed fusion process (LPBF) using nickel based super alloy feed stock (IN625) and 15-5 stainless steel as materials. Metallic AM materials possess high strength which, together with the high cooling rates of the laser melt pool, leads to high multi length-scale residual stresses in the as-built part. Stress levels are such that dimensional fidelity is affected after the part is separated from the build plate. In severe cases, it is possible that separation from the build plate occurs spontaneously during the build process. Other concerns are related to the effect of stresses on fatigue and part life. Besides their magnitude, residual stresses in AM parts are also characterized by high gradients in excess of  $> 100$  MPa/mm which pose a challenge for the spatial resolution capabilities in measuring stress/strains. The neutron stress/strain measurements reported here are part of the Benchmark Challenge CHAL-AMB2018-01-RS that also included the application of synchrotron X-ray diffraction and the contour method on the bridge shape part. Four identical bridge structures were fabricated (Figure 1) which were cut for separate measurements using electro discharge machining. In order for stresses to be truly representative of the as-built state, each structure had their base of the build plate still attached.

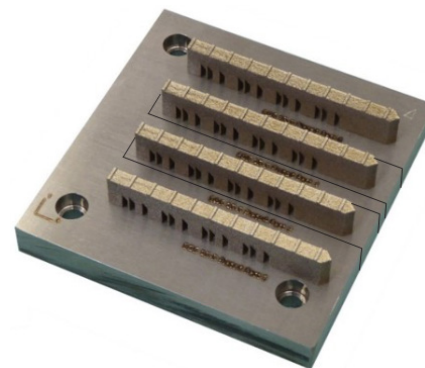


**FIGURE 1:** Build plate with four bridge shapes attached. The lines indicate cuts for extraction of parts used in the residual strain measurements.

The build parameter set consisted of 20  $\mu\text{m}$  layer height, 100 W contour laser power and scan speed of 900 mm/s; 195 W infill laser power and 800 mm/s scan speed. The laser spot size was estimated as a Gaussian distribution with full width at half maximum of 50  $\mu\text{m}$ . Each bridge structure consisted of 625 layers.

The neutron measurements were conducted using a (1.5 mm)<sup>3</sup> cube gage volume for specimen orientations and locations indicated in Figure 2. Since the gage volume is more than one order of magnitude larger than the layer height and the laser spot size, the strain variations on the length scales of the latter cannot be resolved and will be averaged.

The AM Bench program defined the residual strain as the target quantity in order to allow comparisons to synchrotron X-ray diffraction which cannot measure the  $\epsilon_{yy}$  component due to absorption limitations that arise from small Bragg angles and very large pathlengths for this orientation of the scattering vector. In this context it is instructive to compare strains and stresses because, without additional boundary conditions, the tensorial relationship between these quantities generally prohibits a direct inference between single components of stress and strain.

Diffraction measures lattice spacings which relate to strain through  $\epsilon = \frac{(d-d_0)}{d_0}$  where  $d_0$  is the unstressed lattice spacing. In the procedure applied here, near surface measurements (Figure 2, red line) were used to obtain an average  $d_0$  from the 43 near surface locations such that the average stress  $\sigma_{zz}=0$  at these

<sup>1</sup> NIST Center for Neutron Research, National Institute of Standards and Technology, Gaithersburg, MD 20899

<sup>2</sup> Engineering Lab, National Institute of Standards and Technology, Gaithersburg, MD 20899

<sup>3</sup> Materials Measurement Lab, National Institute of Standards and Technology, Gaithersburg, MD 20899



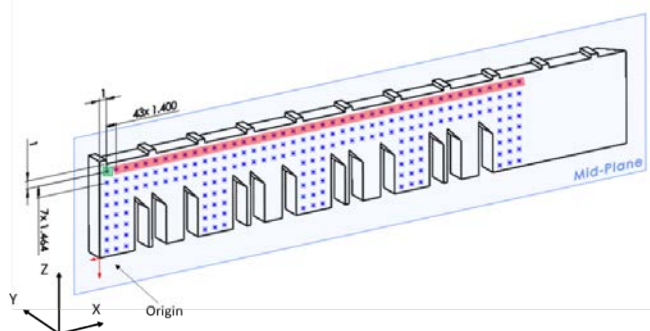


**FIGURE 2:** Specimen directions and measurement locations for neutron strain measurements.

locations. The strains and stresses for each direction obtained for IN625 are shown in Figure 3. It is clear from the location specific comparison of stress and strain that one stress component depends on all strain components and vice versa. As a consequence, no simplifying assumptions can be made to obtain stresses from only two strain components. More to the point, despite the slenderness of the specimen with 5 mm thickness in the y-direction the  $\sigma_{yy}$ -stresses are sufficiently large to prohibit the plane stress assumption  $\sigma_{yy}=0$ .

The aforementioned effects of stresses on dimensional fidelity are best illustrated by the distortions caused by a partial EDM cut from the build plate shown in Figure 4. The deflection is caused primarily by stresses in the top part of the bridge. This is illustrated by the average stresses in the longitudinal direction  $\sigma_{xx}$  which are tensile in the top layer and compressive underneath (Figure 3) with a resulting bending moment that forces an upward deflection. The maximum separation bridge to build plate is  $\approx 1.3$  mm; there is a corresponding curvature on the top which, if unmitigated, would render the part useless. One of the possible mitigation strategies is to incorporate the stresses/strains – such as the data presented here – into the design process in such a way that the part, on separation from the build plate, distorts into the desired, nominal, shape. The same design principle is employed in sheet metal forming where it is used to account for spring back.

The AM Bench made a great effort to collect strain data through independent methods, and good agreement in the results was found between all methods. The direct comparison of strains measured by X-ray and neutron diffraction (Figure 5) shows good consistency between both, with the expected blur of the neutron results due to higher spatial averaging (spatial resolution 0.25 mm for X-ray vs. 1.5 mm for neutrons). The results show that key demands of the AM Bench are met in that the data provided are consistent and accurate. However, each of the methods employed has different strengths. The evaluation of triaxial stresses is only possible by neutron diffraction but at the expense of reduced spatial resolution. Length scales substantially smaller than the neutron gage volume are accessible to synchrotron diffraction which is best suited to resolve localized strains and

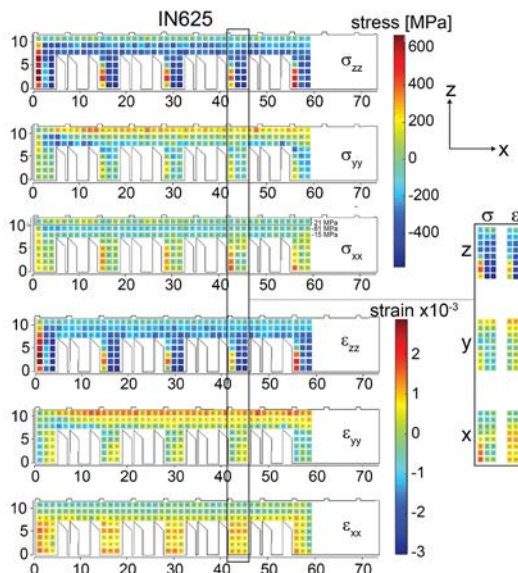


**FIGURE 3:** Stresses and strains in the as-built IN625 sample with a close-up comparison shown on the right.

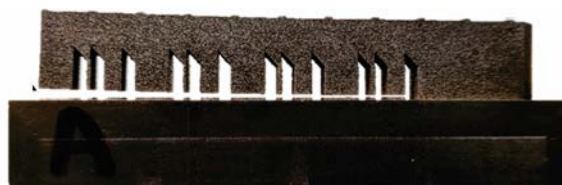


**FIGURE 4:** Stress induced deflection after partial separation by EDM cutting from the build plate [1].

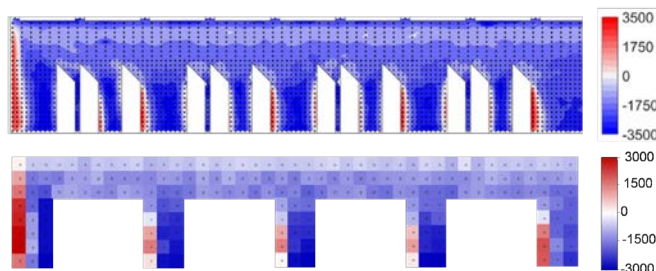


**FIGURE 5:** Comparison of strains  $\epsilon_{zz}$  from synchrotron (top) and neutron measurements (bottom).

strain gradients of the type shown in Figure 5. It can be concluded that there is no one method of strain measurement that meets all demands of resolution, accuracy, and completeness (as in all strain components). The most desirable approach is therefore to use multiple measurement techniques for the complete understanding of the residual strain/stress states within the AM parts.

## Reference

- [1] T. Q. Phan et al., Integrating Materials and Manufacturing Innovation **8** (3), 318 (2019).

# Changes in lithiation of battery materials *in operando* during electrochemical discharge

Z. Nie,<sup>1</sup> S. Ong,<sup>1</sup> D. S. Hussey,<sup>2</sup> J. M. LaManna,<sup>2</sup> D. L. Jacobson,<sup>2</sup> and G. M. Koenig<sup>1</sup>

**B**ecause of their high volumetric and gravimetric energy density, lithium (Li)-ion batteries are the predominant energy storage technology for consumer electronics and electric vehicles [1]. While the materials chemistry of these batteries has been the primary research and development focus, other factors such as processing and electrode geometry are also important. For example, increasing the thickness of a battery electrode will result in higher energy density at the cell level because less mass and space is needed for inactive components (e.g., separators, current collectors), however, the tradeoff is that thicker electrodes become limited in their power or high rate capabilities due to ion transport limitations [2-5]. Additionally, reducing the inactive components (e.g., binders and conductive additives) within the electrodes themselves also increases energy density, although care must be taken to accommodate the functions of those inactive components, namely the mechanical and electronic conductivity properties of the electrodes.

Recently, a system has been reported which holds promise for using very thick electrodes, eliminating inactive materials and moving towards the goal of creating Li-ion batteries with higher energy density than those currently on the market. These electrodes only contain electroactive material and can be very thick ( $> 1$  mm) [3]. During processing, they undergo a mild thermal treatment or sintering step and thus will be referred to as “sintered electrodes” [3-5]. Scanning electron micrographs of examples of fabricated sintered anode  $\text{Li}_4\text{Ti}_5\text{O}_{12}$  (LTO) and cathode  $\text{LiCoO}_2$  (LCO) cross-sections can be found in Fig. 1. The electrodes only contain the solid electroactive material (LTO or LCO) and can be processed into discs with diameters determined by the size of the hydraulic die used to press the pellets and thicknesses dependent on the amount of powder added. The pellets are porous (typically  $\approx 40\%$  by volume pores). When processed into electrochemical cells these pores are filled with electrolyte. Materials for the sintered electrodes must have sufficient electronic conductivity and minimal volume change during cycling to avoid excessive cell polarization and electrode pulverization, respectively [3].

While sintered electrodes with large thicknesses can result in very high energy densities at the cell level, much like

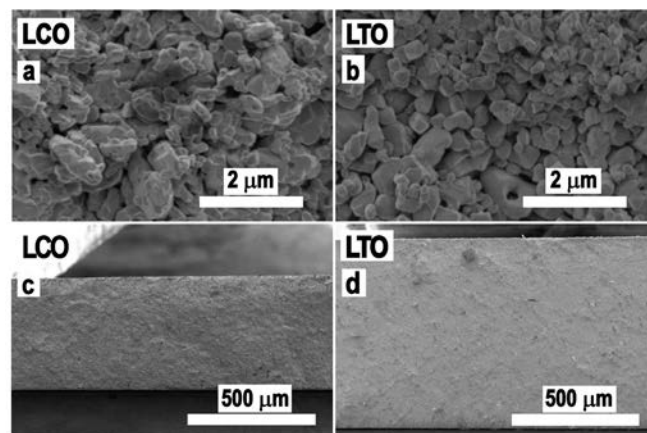


**FIGURE 1:** SEM micrographs of (a)  $\text{LiCoO}_2$  (LCO) and (b)  $\text{Li}_4\text{Ti}_5\text{O}_{12}$  (LTO) sintered electrode surfaces. (c) LCO and (d) LTO cross-sectional SEMs at lower magnification showing the full electrode thickness [3].

other thick electrode systems they are limited in delivering high capacity at increasing charge/discharge rates or current densities [3, 5]. Quantitative assessment of the capacity of a Li-ion battery cell is routinely done in using standard electrochemical equipment such as potentiostats, though other techniques must be employed to understand the root cause of the electrochemical properties of the battery materials. For the thick sintered electrodes, the hypothesis was that the limitations in the capacity at increasing charge/discharge rates was due to limited ion transport through the microstructure of the thick electrodes. Support for this hypothesis would require insights into where the  $\text{Li}^+$  moves in the cell during charge/discharge as a function of the electrochemical rate or current density. In particular, an observation that  $\text{Li}^+$  in the electrodes become more concentrated near the separator at increasing rates would support the hypothesis that ion transport through the microstructure was indeed limiting the capacity because the ions could not traverse the deeper regions of the electrodes fast enough and/or with low enough polarization to accommodate a given current density, thus prematurely ending an electrochemical cycle.

In order to access information about how  $\text{Li}^+$  redistributes during electrochemical charge and/or discharge of a Li-ion cell, a technique is needed which is nondestructive to the cell, capable of providing *in operando*  $\text{Li}^+$  concentration

<sup>1</sup> Department of Chemical Engineering, University of Virginia, Charlottesville, VA 22904

<sup>2</sup> Physical Measurements Laboratory, National Institute of Standards and Technology, Gaithersburg, MD 20899

information during cell operation at the appropriate time and length scales, and ideally does not require custom cell fabrication. Neutron imaging experiments were ideally suited to achieving these goals because 1)  $\text{Li}^+$  ( $^6\text{Li}^+$  in particular) is highly attenuating to neutrons, and thus there is a large change in neutron transmission depending on the concentration of  $\text{Li}^+$  encountered for a given location of the beam path through the cell, 2) the other cell components are highly transparent to neutrons, meaning that conventional cell processing and components can be used, and 3) the resolution of the neutron imaging conditions used in time (30 seconds) and space ( $6.5\text{ }\mu\text{m}$  pixel pitch) were sufficient to give information on  $\text{Li}^+$  redistribution in the electrodes relative to the total time (30 min to 800 min) and thickness ( $468\text{ }\mu\text{m}$  to  $691\text{ }\mu\text{m}$ ) of interest. The battery cell could be aligned and mounted in front of the neutron detector with external leads going to a potentiostat such that images could be collected *in operando* during charge/discharge (Fig. 2a). Many of the battery cell features can be found in the raw radiographs (Fig. 2b), although for determining the changes in  $\text{Li}^+$  concentration in the cell the desired information is the changes in neutron transmission throughout the electrodes during cell operation (Fig. 2c).

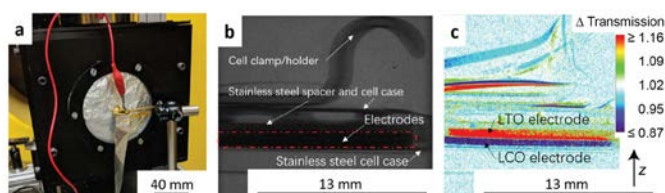


**FIGURE 2:** (a) Photograph of experimental setup used for neutron imaging. (b) Example of a raw radiograph image of the coin cell region, (c) example of the change in transmission for a radiograph of the cell after normalizing relative to the “no current” image. The color scale shows the relative change in neutron transmission. The black arrow depicts the z-direction the cell (thickness/depth dimension) [5].

After aligning the electrochemical cell containing a sintered LTO anode and sintered LCO cathode with the neutron beam, the cell was electrochemically charged/discharged while continuously collecting neutron images (Fig. 3). For cell cycling, “C rate” is a measure of the rate at which a cell is charged or discharged, with 1C typically corresponding to the rate where a fully charged cell is discharged in 1 hour, thus increased C rate is an increased rate of charge/discharge. Charging profiles are not shown, although the cell was always charged at the relatively low rate of C/20, and then discharged at increasing rates of C/20, C/10, C/5, and C/2.5. The discharge polarization curves can be found in Fig. 3a, which are measures of the voltage as a function of time during discharge of the cell at the constant rate indicated. There are eight points on Fig. 3a at the beginning and end of each discharge, and the relative transmission for the neutron radiographs collected at that point can be found in Fig. 3b. There are two main outcomes to note in the neutron radiographs. First, for each radiograph at the beginning of discharge, the images look very similar, indicating

the relatively slow charge rate resulted in the  $\text{Li}^+$  distribution in the electrodes being approximately the same before discharge. Second, as the discharge rate increased, the changes in neutron transmission (and thus changes in  $\text{Li}^+$  redistribution and electrochemical activity) were focused near the middle of the electrodes where the separator region is located. This observation was consistent with the initial hypothesis of ion transport through the microstructure limiting the achievable capacity or rate capability at increasing rates of discharge.

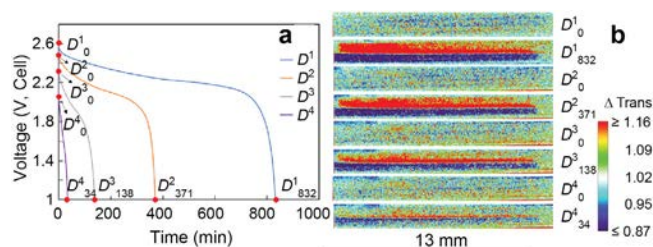


**FIGURE 3:** (a) Discharge profiles at C/20 (blue), C/10 (orange), C/5 (grey), and C/2.5 (purple). The points labeled  $D_i^j$  represent the  $x^{\text{th}}$  minute in the  $i^{\text{th}}$  discharge process. (b) The neutron imaging radiographs corresponding to the points noted in (a) [5].

While not discussed in detail in this highlight, the neutron images were collected at many time points beyond the beginning and end of discharge. Analysis of this information coupled with an electrochemical model of the system allows more detailed insights for the system, and it was determined that the neutron imaging results were consistent with a random-packed distribution of particles and their corresponding pore architecture. We expect that neutron imaging will provide further validation of the impacts of how modifications to cell chemistry and processing influence transport behavior within the electrodes, to provide insights into the fundamental properties of sintered electrode Li-ion batteries and eventually improvements in their design and performance.

## Reference

- [1] J.-M. Tarascon, M. Armand, *Nature* **414**, 359 (2001).
- [2] K. G. Gallagher, et. al, *The Journal of the Electrochemical Society* **163**, A138 (2016).
- [3] J. P. Robinson, J. J. Ruppert, H. Dong, G. M. Koenig Jr., *Journal of Applied Electrochemistry* **48**, 1297 (2018).
- [4] Z. Nie, P. M. McCormack, H. Z. Bilheux, J. C. Bilheux, J. P. Robinson, J. Nanda, G. M. Koenig Jr., *Journal of Power Sources* **419**, 127 (2019).
- [5] Z. Nie, S. Ong, D. S. Hussey, J. M. LaManna, D. L. Jacobson, G. M. Koenig Jr., *Molecular Systems Design & Engineering* **5**, 245 (2020).



# SANS pore structure studies for a better understanding of tight oil production

Y. Zhang,<sup>1</sup> Q. Hu,<sup>1</sup> T. J. Barber,<sup>1</sup> M. Bleuel,<sup>2,3</sup> and H. F. El-Sobky<sup>4</sup>

**K**nowledge of the nanometer-micrometer (nm to  $\mu\text{m}$ ) pore structure of shales and other fine-grained rocks (which make up unconventional reservoirs) is critical to understanding production decline. In particular, the presence and proportion of isolated pores which hinder petroleum flow and production are of critical importance. We have studied the Bakken Formation in the Williston Basin of North Dakota which in 2019 produced about 7.7 million barrels of crude oil per day ( $\approx 1/3$  of the shale oil produced in the U. S.). The Bakken Formation itself is divided into lower, middle, and upper members. The lower and upper members are organic-rich shales considered to be the sources of petroleum for the entire Bakken unconventional system. The middle Bakken member contains calcareous siltstones, which are somewhat more porous reservoir rocks (with slightly larger pore throats), and this is the main target for horizontal drilling and hydraulic fracturing. However, the predominantly nano-scale pore geometries (with about 2/3 pore space controlled by  $< 100$  nm pore throats) of these low porosity rocks (both source and reservoir) are linked to the steep initial decline and low overall recovery even after fracturing [1-2]. Our work focuses on the integrated methodologies of (Ultra-) Small Angle Neutron Scattering (U)SANS and mercury intrusion porosimetry (MIP) analysis, aided by field emission- scanning electron microscopy (FE-SEM) imaging, to characterize and differentiate the pore structures of source and reservoir rocks [3].

FE-SEM images provide a direct observation of pore types in both source and reservoir samples. Mineral pores, including inter-particle and intra-particle pores, are widely distributed in the rock matrix and easy to identify (Fig. 1a-b). Pores in organic matter (OM) are well developed in the OM-rich shales (e.g., Fig. 1a), and these can be classified into the following OM pore types [4]: primary pores (formed during deposition) ( $> 1 \mu\text{m}$ ), large bubble pores (round-shaped secondary pores related to thermal maturation) (200 nm to  $1 \mu\text{m}$ ), or (to a much larger extent) small spongy pores (nm in scales; homogeneously distributed secondary pores; rounded, sub-rounded, and sub-angularly shaped) ( $< 200$  nm). The OM-hosted pores, especially the nm-scale pores, can contribute significantly to the total porosity despite being so small, because of the relatively large mass of OM (as high as 22 % by weight) in the shale,

compared to  $< 1$  % typically for the middle member which only have mineral-associated pores (Fig. 1b).

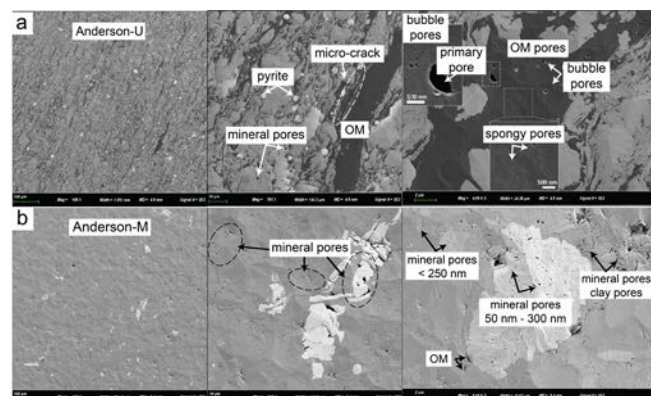


**FIGURE 1:** FE-SEM images of (a) upper Bakken shale (U), and (b) middle Bakken shale (M) of the Anderson well. Organic matter: dark grey; pores: black; quartz, feldspar, carbonates, and clays: light grey; pyrite: white.

While SEM provides visual and qualitative assessment of pore types, (U)SANS and MIP measure the porosity and pore size distribution using different principles. MIP is an invasive method and hence only measures pores connected to the edges of a sample (i.e., surface-accessible pore space). Neutrons scatter at the pore-mineral interface for both connected and unconnected (isolated) pores, and therefore, (U)SANS measures the entire pore space in the pore size range of 1 nm to  $20 \mu\text{m}$ . Mineralogical data and total organic carbon (TOC) contents were used to calculate the average neutron scattering length density (SLD - a measure of the scattering power of a material) of the rock matrix. The intensity of scattered neutrons [ $I(Q)$  in Fig. 2 where  $Q$  is the momentum transferred in the scattering process] is proportional to the square of the difference between the averaged SLD values of a scattering object and its surrounding medium (i.e., pore space) [3].

Scattering profiles of combined SANS and USANS are presented in Fig. 2. (U)SANS porosities were obtained using the polydisperse spherical pore (PDSP) model and Porod-invariant (model-independent) analysis. The PDSP model generates the

<sup>1</sup> The University of Texas at Arlington, 500 Yates Street, Arlington, TX 76019

<sup>2</sup> NIST Center for Neutron Research, National Institute of Standards and Technology, Gaithersburg, MD 20899

<sup>3</sup> University of Maryland College Park, MD 20742

<sup>4</sup> Petrophysics & Reservoir Quality, Exploration, Subsurface & Other International, ConocoPhillips, Houston, TX 77079



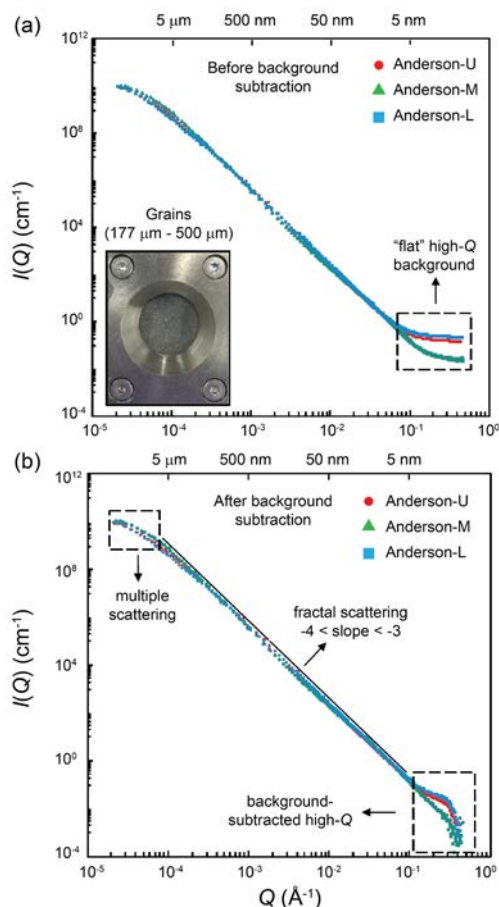


**FIGURE 2:** Combined (U)SANS scattering profile before (a) and after (b) background subtraction for Anderson well samples (L: lower member).

fractal porosity (described by a power law relationship) and pore size distribution in the (U)SANS pore size measurement range, while Porod invariant analysis yields the volume of all pore space regardless of the pore shapes. MIP porosities and pore-throat size distributions were obtained using methodologies documented in Hu et al. (2017) [5].

The PDSP and the Porod analysis methods give porosities that are quite close, indicating that (1) the assumption of a spherical pore shape is adequate for quantifying the porosity; and (2) the amount of non-fractal pores at sub-nm sizes is small. In addition, the MIP results indicate that the middle Bakken siltstones have a larger measured porosity than the lower/upper Bakken shales. In contrast, the (U)SANS results generally show lower porosity in the middle member. There are at least two possible reasons for the disparity. First, the larger samples (1 cm cube) used for MIP lead to a smaller pore connectivity (a higher proportion of isolated pores) when measured with MIP. This effect is expected to be more pronounced for fine-grained tight rocks such as lower/upper Bakken shales than for the middle Bakken sample, as its dominant pore-throat size (10 nm to 50 nm) is larger than for the upper and lower members (< 10 nm). It might also be that the volume proportion of closed pores, especially OM pores, is higher in the lower/upper Bakken than the middle Bakken. This closed porosity is not observable using the MIP method. Neutron

scattering on the other hand is sensitive to all porosity in the system, both connected and isolated. We also note that to avoid multiple scattering, the thickness of the SANS samples is limited to 500  $\mu\text{m}$ . This restriction only allows us to validate the sample-size-dependent effective porosity observed by other approaches such as MIP, at this sample length.

The proportion of non-connected pore space as measured by MIP is a function of sample size because as the sample gets larger the sample, fewer pores will be connected directly to the surface increasing the proportion of isolated pores relative to the total porosity. In general, the measured effective porosity by MIP is relatively low ( $\approx 1\%$  to  $4\%$ ) when using a larger-sized cubic sample, even though MIP has a slightly larger upper size detection limit (i.e., pore-throat size of  $50\ \mu\text{m}$ ) compared to (U)SANS, which gives a measured porosity of  $9\%$  to  $15\%$  for small-sized samples using either grains ( $177\ \mu\text{m}$  to  $500\ \mu\text{m}$ ) or  $150\ \mu\text{m}$ -thick thin sections.

In conclusion, the combination of (U)SANS and MIP techniques, aided by SEM imaging, provides a comprehensive way to characterize and differentiate shale pore systems over a broad measurable range of pore and pore-throat sizes from  $1.25\ \text{nm}$  to  $50\ \mu\text{m}$ , and for different sample sizes. The results show that the lower/upper Bakken samples (source rocks) and the middle Bakken samples (reservoir rocks) have distinct pore structures in terms of throat-size and connectivity, which are in turn a function of different mineral compositions and organic matter contents related to deposition and diagenesis. The porosities measured by the MIP method (which is only sensitive to connected pores) is related to sample size due to the limited pore accessibility of tight rocks. As the sample size gets smaller, the porosities measure by MIP and (U)SANS techniques tend to converge as more of the pores become connected to the surface of the sample. As sample size increases, results diverge as more of the pores become disconnected and are not measured by MIP. As a result, (U)SANS gives higher porosities than MIP at larger sample sizes, but at the SANS-measurable sample size of  $< 500\ \mu\text{m}$ , the proportion of pores isolated from the surface is small, yielding similar SANS and MIP porosities. The proportion of unconnected pores for any given sample size is related to the mineralogy and TOC content. A very large sample size (such as a subsurface reservoir) will possess a higher proportion of isolated pores, which could limit the rock drainage volume even after fracturing and lead to lower overall recovery during production.

## References

- [1] Q. H. Hu, May 10, 2013. DOI: 10.1038/494307a.
- [2] Q. H. Hu, R. P. Ewing, and H. D. Rowe, *J. Geophys. Res. – Solid Earth* **120**(12), 8073 (2015).
- [3] Y. X. Zhang, T. J. Barber, Q. H. Hu, M. K. Bleuel, H. F. El-Sobky, *Intern. J. Coal Geol.* **212**, 103252 (2019).
- [4] L. Ko, R. G. Loucks, S. C. Ruppel, T. W. Zhang, S. Peng, *AAPG Bulletin*. **101**(3), 387 (2017).
- [5] Q. H. Hu, Y. X. Zhang, X. H. Meng, Z. Li, Z. H. Xie, M. W. Li, *Pet. Explor. Dev.* **44**(5), 720 (2017).

# Precision measurement of the neutron scattering length of $^4\text{He}$ using neutron interferometry

*R. Haun,<sup>1</sup> F. E. Wietfeldt,<sup>1</sup> M. Arif,<sup>2</sup> M. G. Huber,<sup>2</sup> T. C. Black,<sup>3</sup> B. Heacock,<sup>4,5</sup> D. A. Pushin,<sup>6,7</sup> and C. B. Shahi<sup>8</sup>*

Neutron scattering from a nucleus can be described using a single parameter known as the scattering length ( $b$ ). It has dimensions of unit length and varies uniquely across different isotopes. For instance, for two of hydrogen's isotopes  $b(^1\text{H}) = -3.74$  fm and  $b(^2\text{H}) = 6.67$  fm. The value of  $b$  can be complex, in which case the imaginary part describes absorption, and can also be spin dependent. Neutron scattering lengths are fundamental in neutron scattering applications and are widely used in neutron science and nuclear engineering. Our aim is to measure the scattering lengths of low-mass isotopes precisely to inform nuclear theory.

In nuclear theory, the forces within a nucleus holding the protons and neutrons in confinement are far too strong to be directly calculated using the Standard Model of physics. Instead, two alternative approaches have emerged to provide insight into nuclear structure. The first uses realistic nucleon-nucleon (NN) potentials to model nucleon behavior. A variety of such models exists with names such as Nijmegen, CD Bonn, and AV18. These models do successfully predict several few-nucleon scattering amplitudes but fail to reproduce three and four-body binding energies and do not accurately predict the vector-analyzing power in several few-nucleon systems. A number of 3N potential models [1] have been created (Tucson-Melbourne, Brazilian, and Urbana-Illinois) that can be adjusted to match the  $^3\text{H}$  and  $^3\text{He}$  binding energies, but they do not resolve the discrepancies between theory and scattering experiments and have trouble reproducing the binding energy of helium-4.

Another approach to understanding nuclear structure is chiral effective field theory ( $\chi\text{EFT}$ ), which use the symmetries of QCD in a perturbative expansion of the particle momenta [2]. In  $\chi\text{EFT}$  short-range behavior is accounted for in a different manner than it is for intermediate and long-range regimes where the interaction is calculated explicitly. Instead, short-range behavior is accounted for through use of low-energy constants (LECs) that are adjusted to match experimental data including scattering lengths. Calculations in  $\chi\text{EFT}$  are done to a specific

order of expansion with current state-of-the-art calculations to order  $N = 3$  (abbreviated N3LO).

A significant motivation for making more precise measurements of the neutron scattering lengths of light nuclei, and in particular this measurement, is to provide high-quality "set-point" data to test effective-range expansions of  $N$ -nucleus systems. These expansions can help generate more realistic 3N and 4N potential models and constrain the LECs used in building models at higher orders in chiral effective field theory. It is hoped that these improved models will bring few-nucleon theory and experiment into better agreement. A high-precision neutron interferometry measurement, previously performed at NIST, of the  $n$ - $^3\text{H}$  scattering length [3] has already been used to help correct the LECs for the N3LO 3N force interaction.

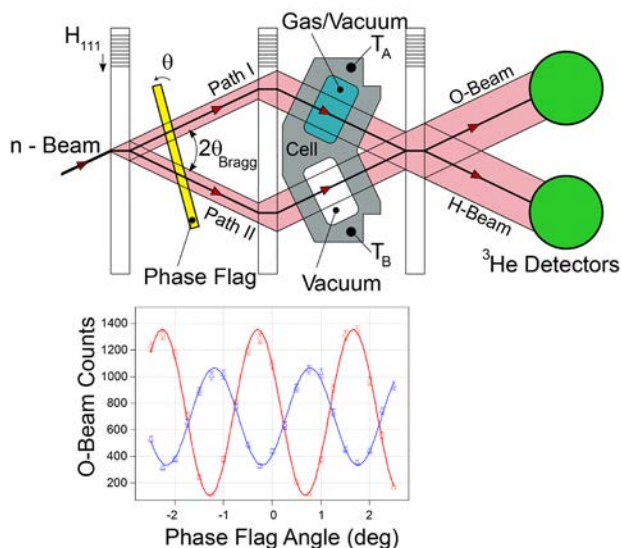


**FIGURE 1:** Overhead view of the experimental setup. The phase difference between the gas (blue) and an empty interferometer (red) is shown in the interferogram below.

<sup>1</sup> Tulane University, New Orleans, LA 70118

<sup>2</sup> National Institute of Standards and Technology, Gaithersburg, MD 20899

<sup>3</sup> University of North Carolina-Wilmington, Wilmington, NC 28403

<sup>4</sup> North Carolina State University, Raleigh, NC 27695

<sup>5</sup> Triangle Universities Nuclear Laboratory, Durham, NC 27708

<sup>6</sup> University of Waterloo, Waterloo, Ontario N2L 3G1, Canada

<sup>7</sup> Institute for Quantum Computing, Waterloo, Ontario N2L 3G1, Canada

<sup>8</sup> University of Maryland, College Park, MD 20742

This experiment uses a single-crystal neutron interferometer that splits the wavefunction of a neutron into two spatially coherent paths using Bragg diffraction. Exiting the interferometer, the two wavefunctions interfere with one another, and any difference along the paths manifests as a phase shift. For a physical target of thickness  $D$  placed in only one path of the interferometer a relative phase shift of  $\phi = -N\lambda Db$  is created. Here,  $N$  is the atomic density of the target and  $\lambda$  is the neutron wavelength. Here, an incident monochromatic neutron beam  $\lambda = (2.70913 \pm 0.00016 \text{ (stat.)} \pm 0.00023 \text{ (syst.)}) \text{ \AA}$  was incident on the first blade of the interferometer. The wavelength was determined using a pressed-silicon monochromator placed behind the interferometer and rotated around the Bragg angle. A phase flag made of 1.5 mm thick fused silica inserted inside the interferometer provided a controllable phase shift. The target was a double cell constructed of 6061 alloy aluminum (see Fig. 1). To eliminate air-scattering corrections, one cell was kept evacuated. The neutron path length  $D$  through the cell target was measured at the NIST Precision Engineering Division Coordinate Measuring Machine to be  $D = (1.0016 \pm 0.0001) \text{ cm}$  at 20 °C. Adjustments to  $D$  were made using the thermal expansion of aluminum. The other cell was filled with helium-4 gas at pressures ranging from 7 bar to 13 bar. Different pressures were used as a systematic check. To account for the phase shift caused by the aluminum walls both cells were evacuated, and phase shift of just the aluminum ( $\phi_{\text{cell}}$ ) was measured. The density of the gas was measured using a high-precision pressure gauge and temperature probes attached to the cell. Both the temperature and pressure gauges were calibrated by NIST.

The intrinsic phase ( $\phi_0$ ), i.e. when no sample is present, of the interferometer is known to drift with time due to the interferometer's coupling with the surrounding environment. To minimize drift the interferometer at the NCNR is housed in a unique enclosure with both active and passive vibration damping. Further, the interferometer is kept at a constant temperature using a feedback control loop. Despite these facility features, phase drifts are still present at the interferometer. To account for this, the double cell is periodically removed from the apparatus every 44 mins to measure  $\phi_0$  directly. All movement of the cell, phase flag, and gas manipulation was done remotely to minimize interactions with the interferometer.

A systematic problem arose from the fact that the target slowly warmed over the course of measuring a data set, as it is translated in and out by a motor-driven stage. This created a thermal gradient between the sample and the interferometer crystal, which effectively caused a time-dependent drift in  $\phi_{\text{cell}}$ . This thermal gradient issue derailed several early attempts

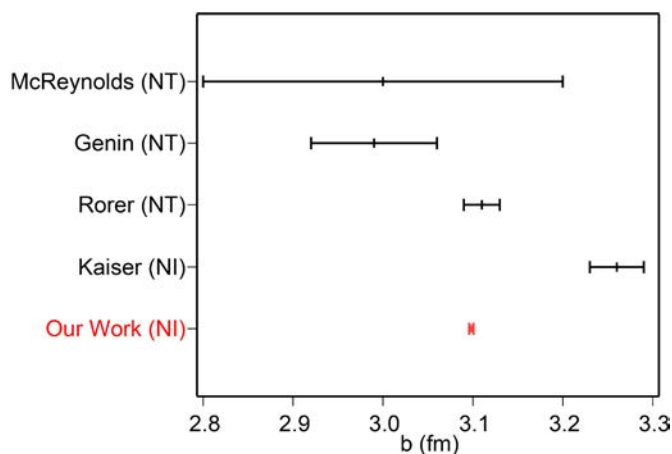


**FIGURE 2:** Our result vs previous measurements using neutron transmission (NT) and neutron interferometry (NI) techniques.

to measure  $b(^4\text{He})$ . This challenge was overcome using a combination of techniques. First, the motor driving the double cell was attached to a glycol-cooled copper block, and its effectiveness was checked using a specialized variation on the double cell. Secondly, a pattern of repeatedly measuring  $\phi_{\text{cell}}$  throughout the experiment was adopted. This had not been done in previous measurements. In total, we measured 1456 separate interferograms corresponding to 23 days of continuous phase data.

Our current measurement of the phase shift caused by helium-4 gas inside a neutron interferometer yields a value of  $b = (3.0982 \pm 0.0021 \text{ (stat.)} \pm 0.0014 \text{ (syst.)}) \text{ fm}$  [4]. Our largest systematic error is caused by the deformation of the cell under pressure, which is on the order of only 100 nm. The magnitude of this effect was calculated using finite-element analysis. The value of  $b$  was found by subtracting the measured  $\phi_0$  and  $\phi_{\text{cell}}$  values from measurements using the helium target. Our result is in disagreement with the often-quoted previous neutron interferometric measurement of Kaiser et al. [5]. However, it is in good agreement with earlier measurements that used neutron transmission (see Fig. 2). Our measurement is the most precise evaluation of this quantity, at 0.08 % relative uncertainty. It shifts the world average for  $b$  by 2 % lower and reduces the net uncertainty by a factor of more than six.

## Reference

- [1] S. C. Pieper et al., Phys. Rev. C **64**, 014001 (2001).
- [2] R. Machleidt and D. R. Entem, Phys. Rep. **503**, 1 (2011).
- [3] K. Schoen et al., Phys. Rev. C **67**, 044005 (2003).
- [4] R. Haun et al., PRL **124**, 012501 (2020).
- [5] H. Kaiser et al., Zeit. Phys. A **291**, 231 (1979).



# Polymer dynamics in block copolymer electrolytes detected by neutron spin echo

W. S. Loo,<sup>1</sup> A. Faraone,<sup>2</sup> L. S. Grundy,<sup>1</sup> K. W. Gao,<sup>1</sup> and N. P. Balsara<sup>1,3</sup>

The liquid electrolytes currently used in lithium-ion batteries unfortunately pose safety concerns due to their flammability. One promising approach for creating safer, solid electrolytes is through the microphase separation of block copolymers, which decouple the  $\text{Li}^+$  ion conducting and mechanically reinforcing properties of the electrolyte through the self-assembly into nanoscale structures. Under the potentials applied to these electrolytes in a battery, the competition between diffusion and migration leads to significant Li salt concentration gradients. Since the salt and polymer concentration in the electrolyte must be uniform at equilibrium, polymer chains must compensate by diffusing away from regions of high salt concentration toward those of low salt concentration. Using neutron spin echo (NSE) spectroscopy, we have elucidated the molecular underpinnings of this process by quantifying segmental motion and polymer dynamics in a series of block copolymer electrolytes.

The block copolymer electrolyte of interest is a well-studied model system: polystyrene-*block*-poly(ethylene oxide) (SEO) mixed with lithium trifluoromethanesulfonate (LiTFSI) salt. Our experiments covered time scales from 0.1 ns to 100 ns corresponding to polymer dynamics on the Å to nm length scales. We synthesized two SEO copolymers with similar compositions by living anionic polymerization: deuterated PS-*b*-deuterated PEO (ddSEO) and deuterated PS-*b*-hydrogenated PEO (dhSEO). The average PEO volume fraction of both copolymers is 0.78. The samples used were blends of 20% dhSEO and 80% ddSEO by volume and LiTFSI was added to the copolymer blends such that the final molar salt ratios,  $r = \frac{[\text{Li}]}{[\text{EO}]}$ , were 0, 0.025, 0.075, and 0.10. The sample design was chosen so that the NSE data are dominated by relaxation of the PEO segments as they interact with salt ions.

Small angle neutron scattering (SANS) data for SEO/LiTFSI at 90 °C are shown in Figure 1. All profiles contain a primary peak at  $Q = Q^*$  and a higher order peak at  $Q = \sqrt{3}Q^*$ . At  $r \geq 0.075$ , an additional higher order peak at  $Q = \sqrt{7}Q^*$  is seen. The SANS data indicate that SEO/LiTFSI self-assembles into hexagonally packed PS cylinders in a salt-containing PEO matrix at all salt concentrations. These data also show that the blends are macroscopically homogeneous at all salt concentrations and that at high- $Q$  the scattering intensity scales with  $Q^{-2}$

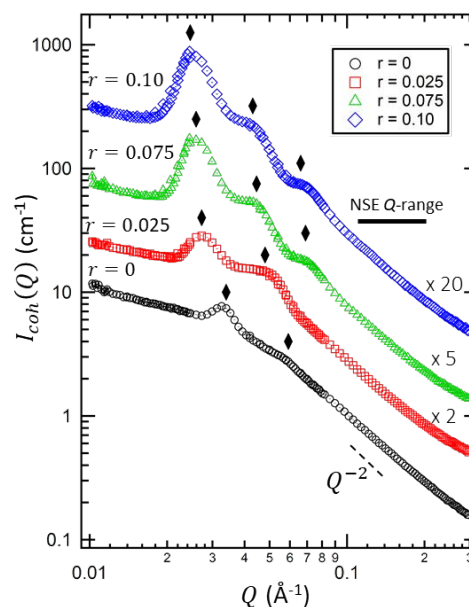


**FIGURE 1:** SANS profiles,  $I_{\text{coh}}(Q)$ , of SEO/LiTFSI mixtures at different salt concentrations,  $0 \leq r \leq 0.10$ , at 90 °C. Curves are offset vertically for clarity. Diamonds represent the primary scattering peak,  $Q^*$ , and the higher order scattering peaks. An example of the scaling for a Gaussian chain,  $Q^{-2}$ , is shown in the high- $Q$  regime.

indicative of scattering from polymer chains obeying random walk statistics. The bar at high- $Q$  in Fig. 1 shows the range of scattering vectors covered by the NSE experiments, which corresponds to length-scales where the intra-domain scattering dominates ensuring that the NSE experiments selectively probe the PEO/LiTFSI matrix phase.

The normalized intermediate scattering function measured by NSE,  $\frac{S(Q,t)}{S(Q,0)}$ , is shown in Figure 2 at two temperatures for a salt concentration:  $r = 0.025$ . The NSE data for the remaining salt concentrations are provided in Ref. [1]. At short times,  $t \leq 10$  ns, the data are consistent with the Rouse model, wherein the polymer segmental motion is quantified by an effective friction coefficient,  $\zeta$ , of the monomer units. The solid and dashed curves through the short time data in Fig. 2 represent fits to an approximation of the Rouse model. The data show deviations from Rouse dynamics at  $t \geq 20$  ns for all salt concentrations

<sup>1</sup> Department of Chemical and Biomolecular Engineering, University of California Berkeley, Berkeley, CA 94720

<sup>2</sup> NIST Center for Neutron Research, National Institute of Standards and Technology, Gaithersburg, MD 20899

<sup>3</sup> Materials Sciences Division and Joint Center for Energy Storage Research (JCESR), Lawrence Berkeley National Lab, Berkeley, CA 94720



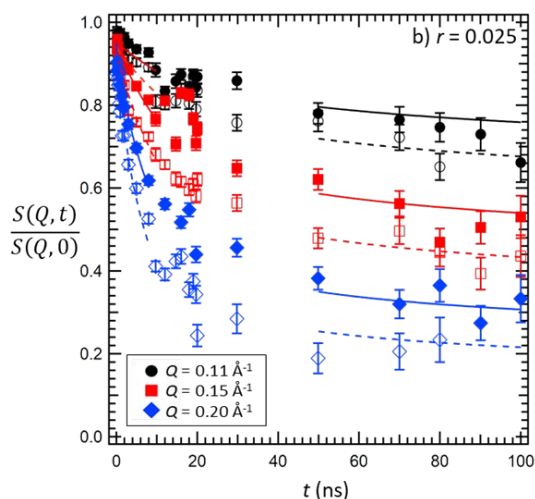


**FIGURE 2:** The normalized intermediate scattering function,  $\frac{S(Q,t)}{S(Q,0)}$ , for SEO at 90 °C (filled symbols) and 120 °C (open symbols) for  $r = 0.025$ . At  $t \leq 10$  ns, the curves correspond to the Rouse model. At  $t \geq 50$  ns, the curves correspond to the tube model for reptation. Solid curves correspond to the fits of 90 °C data and dashed curves to the fits of 120 °C data.

signaling the slowing down of segmental motion due to constraints imposed by the presence of other chains. The tube diameter,  $d$ , quantifies these constraints. At long times,  $t \geq 50$  ns, the data in Fig. 2 were fit to the tube model proposed by de Gennes and are represented by the solid and dashed curves in the long-time regime.

Figure 3 shows the parameters obtained from fitting the NSE data. The dependence of  $\zeta$  on salt concentration is shown in Fig. 3a at 90 °C and 120 °C. The monomeric friction coefficient increases with increasing salt concentration at a similar rate for both temperatures. At 90 °C, this rate matches that seen in homopolymer PEO/LiTFSI systems [2]. The segmental dynamics on short-time scales,  $t \leq 10$  ns, in a microphase separated block copolymer electrolyte is indistinguishable from that of the homopolymer electrolyte. The dependence of tube diameter,  $d$ , on salt concentration is shown in Figure 3b. Our measured values of  $d$  increase with increasing temperature as typically seen in homopolymers due to increased chain mobility. In addition, the tube diameter decreases with increasing salt concentration. As salt concentration increases, the coordination between  $\text{Li}^+$  ions and the ether oxygens on the PEO backbone increases, leading to a decrease in  $d$ . In a melt of entangled homopolymers, the longest molecular relaxation time,  $\tau_d$ , quantifies the time needed for a confined chain to escape the tube created by neighboring chains and scales with  $\zeta/d^2$ . We define a normalized relaxation time,  $\tau_{d,n} = \tau_d(r)/\tau_d(r=0)$ , to quantify the effect of salt concentration on chain dynamics (Fig. 3c).  $\tau_{d,n}$  increases by a factor of 1.7 across our salt concentration window at 90 °C. The effect of salt concentration of chain diffusion is less pronounced at 120 °C. These factors are the lower bounds on the effect of added salt on the longest relaxation time of block copolymer electrolytes as we have neglected contributions arising from the presence of the PS block. To our knowledge, these results provide the first

measurements of the entanglement constraints, represented by tube diameters, in polymer electrolytes as well as block copolymers.

When a large enough current is applied to a polymer-electrolyte-based battery, the volume fraction of the salt near the cathode will approach zero due to concentration polarization. In this case, the electrolyte volume that was originally occupied by salt must be replaced by polymer due to the incompressibility constraint. Similarly, the salt concentration at the anode will increase, displacing polymer chains. The NSE data suggest that relaxation processes at the anode will be about 1.7 times slower than those at the cathode. While further work is necessary to substantiate this effect, the NSE results provide the first insights into factors that may limit the performance of polymer-electrolyte-based batteries operating at high currents.

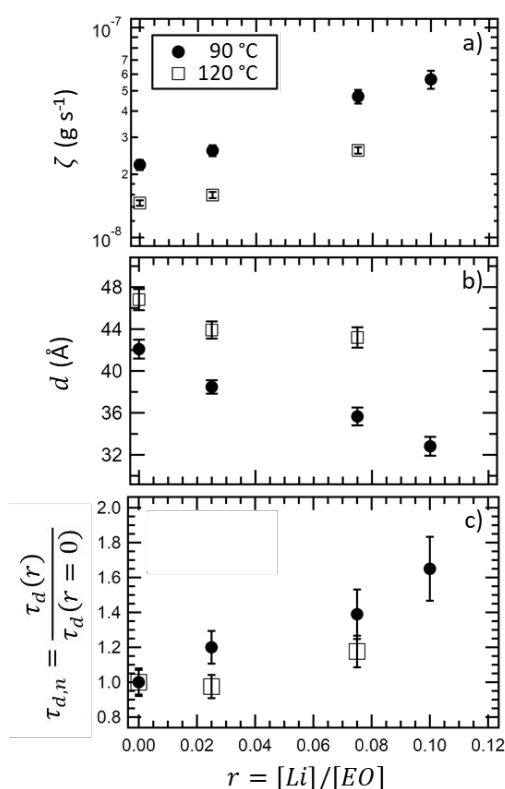


**FIGURE 3:** Results from NSE data: (a) monomeric friction coefficient,  $\zeta$ , (b) tube diameter,  $d$ , and (c) normalized longest molecular relaxation time,  $\tau_{d,n} = \tau_d(r)/\tau_d(r=0)$ , as a function of salt concentration,  $r$ , at 90 °C (filled circles) and 120 °C (open squares).

## References

- [1] W. S. Loo, A. Faraone, L. S. Grundy, K. W. Gao, N. P. Balsara, ACS Macro Lett. **9**, 639 (2020).
- [2] K. I. S. Mongcopa, M. Tyagi, J. P. Mailoa, G. Samsonidze, B. Kozinsky, S. A. Mullin, D. A. Gribble, H. Watanabe, N. P. Balsara, ACS Macro Lett. **7**, 504 (2018).

# Color, structure, and rheology of a diblock bottlebrush copolymer solution

M. A. Wade,<sup>1</sup> D. Walsh,<sup>1</sup> J. Ching-Wei Lee,<sup>1</sup> E. Kelley,<sup>2</sup> K. Weigandt,<sup>2</sup> D. Guirounet,<sup>1</sup> and S. A. Rogers<sup>1</sup>

To understand how the microstructure of inks used in 3D printing develops during the printing process, we studied the non-equilibrium behavior of a lamellar phase made of diblock bottlebrush copolymer across a wide range of shear rates. The effects of the steady flow conditions on the self-assembled microstructure are shown using imaging, bulk rheology, and rheo-VSANS. We show that we can control the color of the solution by shearing alone, taking the fluid from green at low shear rates, to cyan and indigo at higher rates. By considering the structure of the bottlebrush polymers within the solution in tandem with the rheological response, we develop a structure-property-process relation that connects the applied shear rate to the self-assembled microstructure, which dictates the color of the sample. This relation can be used to rationally design new generations of smart materials for printing applications [1].

Bottlebrush polymers are a class of high molecular weight polymers consisting of a single linear backbone with a series of side chains densely grafted along the length of a linear backbone. These materials display a wide range of physical properties that can be accessed by adjusting the polymer's chemistry, backbone length, side chain length, and graft density [2]. In particular, diblock bottlebrush block copolymers rapidly self-assemble into highly uniform lamellae with a domain spacing similar to the wavelength of visible light making them promising photonic materials [3]. Prior studies with diblock bottlebrush polymers have focused on the impact of backbone length and the inclusion of additives on the reflected color under quiescent conditions [4, 5]. However, in the case of practical applications such as melt extrusion or direct-ink-writing, the out-of-equilibrium processing conditions experienced by a soft material can have a significant impact on the microstructure and macroscopic properties [6].

We investigated a polylactic acid-*b*-polystyrene diblock bottlebrush polymer dispersed in toluene with a concentration of 175 mg/ml. Images of this sample collected through the use of a rheo-microscope setup positioned perpendicular to the flow vorticity direction and a camera position at  $\approx 45^\circ$  from axis of rotation are presented in Figure 1 for a select set of shear rates. At low shear rates the solution appears green when viewed perpendicular to the flow gradient direction. The color of the sample transitions from green to cyan and eventually indigo

with increasing shear rate. Higher shear rates result in the sample appearing colorless and are not shown. When viewed off axis, the sample appears blue at quiescence and very low shear rates. A green band can be observed at the front of the geometry at higher shear rates.

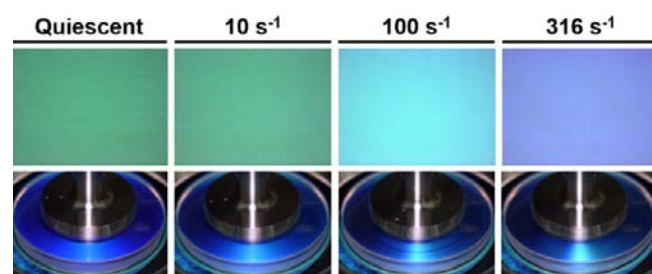


**FIGURE 1:** Microscopy and imaging data collected using a microscope positioned perpendicular to the velocity gradient direction and a camera positioned at an angle of  $\approx 45^\circ$  from the velocity gradient axis.

We identified the structural changes that give rise to color variation as a function of shear with *in-situ* rheo-VSANS. One dimensional scattering data along the velocity gradient and vorticity directions are shown in Figure 2 for a representative set of shear rates. At shear rates below  $1000 \text{ s}^{-1}$ , peaks are observed at integer multiples of a primary peak,  $q_p$ , along the velocity gradient direction, indicating that the diblock bottlebrush copolymer has self-assembled into a lamellar structure. An additional peak is observed at very low  $q$ , corresponding to the inter-backbone interactions of the bottlebrush polymer. With increasing shear rates, the 3<sup>rd</sup> and 4<sup>th</sup> order peaks along the velocity gradient direction are observed to widen and lose definition, indicating a loss of long-range order. At shear rates of  $1000 \text{ s}^{-1}$  and greater, all higher order peaks become indistinguishable from the primary peak. Azimuthal smearing is observed between the vorticity and velocity gradient at starting low shear rates. This feature suggests that the lamellae are not uniformly aligned in the 'face-on' configuration with the geometry wall but are instead distorting and buckling during flow.

By fitting a series of gaussian curves to the scattering data, we identified the location of the primary lamellar peak and thus the characteristic length scale of the self-assembled lamellae. Along the velocity gradient direction, this peak is observed to shift to higher  $q$  as a function of shear rate. This change

<sup>1</sup> University of Illinois at Urbana-Champaign, IL 61801

<sup>2</sup> NIST Center for Neutron Research, National Institute of Standards and Technology, Gaithersburg, MD 20899

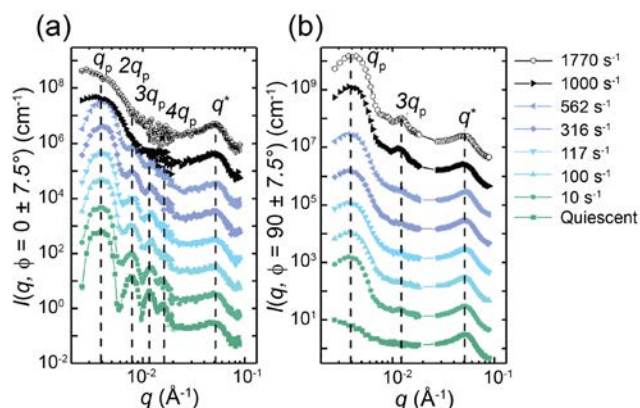


**FIGURE 2:** (a) Sector averages for select shear rates along the velocity gradient direction. Dotted lines serve as guides to the eye, highlighting the initial peak positions under quiescence. (b) Sector averages for select shear rates along the vorticity direction. Error bars represent the standard deviation of scattering intensities over the averaged area. Data have been offset to aid in the comparison of peak position and width.

in the scattering corresponds to a compression of the self-assembled lamellae, which accounts for the shift in sample color from green to cyan as shown in Figure 1. Along the vorticity direction, the location of the peak shifts to lower  $q$  accounting for the change in color from deep blue to green. In the velocity gradient direction, the changes in the domain size of the lamellae are not significant enough to induce a color change from cyan to indigo on their own. Therefore, we also consider the width of the peak as a function of shear rate. Increases in the peak widths indicate a loss of coherence in the undulations of the lamellae as shown in Figure 3. This greater dispersity in the primary peak points towards the existence of many scatterers with smaller length scales than indicated by the primary peak position alone. The presence of these smaller spacings contributes to the cyan to indigo color transition observed at shear rates from  $100 \text{ s}^{-1}$  to  $316 \text{ s}^{-1}$ .

Above a shear rate of  $316 \text{ s}^{-1}$ , we observe a complete rotation of the lamellae from a face-on configuration to an edge-on configuration. This transition is indicated by the disappearance of the repeated lamellae peaks along the velocity gradient direction coupled with the appearance of a peak located at  $3q_p$  along the vorticity direction. The reorientation of the lamellae results in an effectively infinite path length through the material when viewed along the velocity gradient direction, thus leaving the sample colorless.

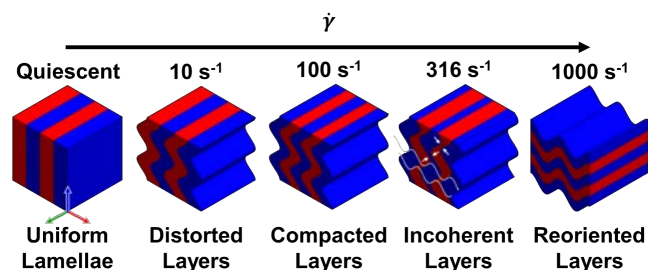


**FIGURE 3:** A schematic representation of the structural transitions undergone at different shear rates, supported by the data shown elsewhere in this paper. Arrows at  $\dot{\gamma} = 316 \text{ s}^{-1}$  serve as guides to the eye, highlighting pinch points that develop between the incoherent layers. White lines at the same shear rate indicate layers that could develop due to these pinch points.

In summary, we have shown how the microstructure and photonic properties of a diblock bottlebrush solution change across a broad range of flow rates. From this information we establish a comprehensive structure-property-processing relation, providing a basis for the rational design of new materials. This relation highlights how the complex flow environment in printing processes, such as additive manufacturing and solution printing, can impact the self-assembled microstructure. A single ink of diblock bottlebrush polymers can therefore be used to print a wide range of colors by controlling the printing conditions.

## References

- [1] M. A. Wade, J. Ching-Wei Lee, D. Walsh, E. G. Kelley, K. M. Weigandt, D. Guirionnet, S. A. Rogers, *Soft Matter* **16**, 4919 (2020).
- [2] J. Rzayev, *ACS Macro Lett.* **1**, 9 (2012).
- [3] A. L. Liberman-Martin, C. K. Chu, R. H. Grubbs, *Macromol. Rapid Commun.* **38**, 13 (2017).
- [4] G. M. Miyake, R. A. Weitekamp, V. A. Piunova, R. H. Grubbs, *J. Am. Chem. Soc.* **134**, 34 (2012).
- [5] R. J. Macfarlane, B. Kim, B. Lee, R. A. Weitekamp, C. M. Bates, S. F. Lee, A. B. Chang, K. T. Delaney, G. H. Fredrickson, H. A. Atwater, R. H. Grubbs, *J. Am. Chem. Soc.*, **136**, 50 (2014).
- [6] R. C. Hayward, D. J. Pochan, *Macromolecules*, **43**, 8 (2010).



# Bottlebrush polymers in the melt and polyelectrolytes in solution share common structural features

J. M. Sarapas, T. B. Martin, A. Chremos, J. F. Douglas, and K. L. Beers

The tunable architecture of bottlebrush polymers promises a wide array of potential application including adhesives, biomaterials, photonics, and beyond [1-6]. These materials are made up of linear backbones with densely grafted sidechains as shown in Figure 1a. For bottlebrush polymers, the properties of the grafted sidechain (e.g., grafting density, graft length, and graft chemistry) and backbone (e.g., backbone length, chemistry) determine the overall conformation, or shape, that the polymer adopts. For example, longer and more densely grafted sidechains are commonly thought to cause the polymer to adopt more extended conformations in solution due to the steric hindrances introduced by the crowding of sidechains. Despite this simple picture, bottlebrush studies still seek to further elucidate the relationship between the molecular design of the polymer and its conformation in order to create design rules that can be leveraged in the development of new bottlebrush-based materials. Here, we combine polymer synthesis, neutron characterization, and molecular simulation to show that backbones of uncharged bottlebrush polymers in bulk adopt similar conformational statistics to charged, linear chain polymers in solution [7].

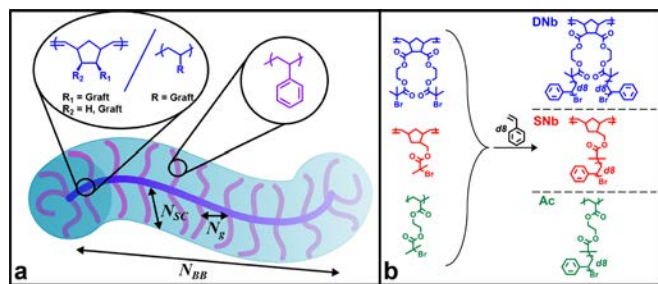


**FIGURE 1:** (a) Schematic of bottlebrush polymers with relevant physical parameters labeled. (b) General synthetic approach to three chemically distinct families of partially deuterated bottlebrush polymers.

Our goal was to produce broad insight into bottlebrush materials and decouple our observations from the unique behavior of a single bottlebrush chemistry or architecture. To achieve this, we synthesized a large library of polymers with varying backbone degree of polymerization ( $N_{BB}$ ), sidechain degree of polymerization ( $N_{SC}$ ), graft spacing ( $N_g$ ) and backbone chemistry. Moreover, molecular dynamics simulations provided guidelines on which molecular parameters would be of most interest. As shown in Figure 1b, we denote the three

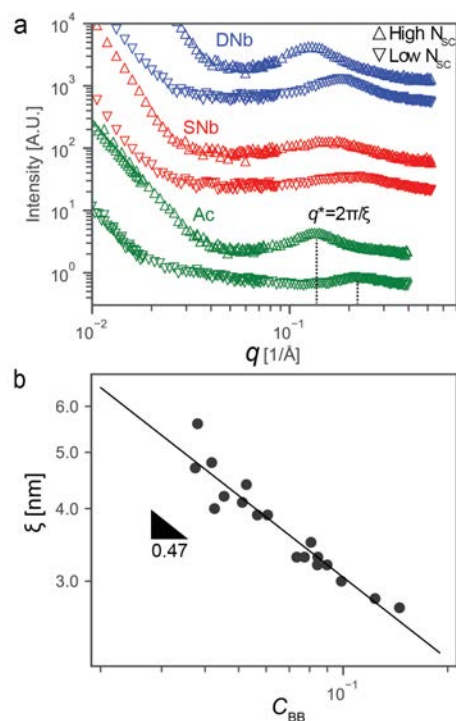
backbone chemistries considered as double-graft norbornene (DNb), single-graft norbornene (SNb), or acrylate (Ac). These chemistries represent variation in both  $N_g$  and intrinsic backbone stiffness due to the size, number of graft points, and conformational restrictions of the backbone monomers. Each polymer was synthesized with deuterated polystyrene sidechains in order to provide neutron contrast with the hydrogenated backbone. All samples were prepared from toluene solutions by casting approximately 20  $\mu\text{m}$  thick films onto quartz windows and removing all residual solvent using applied vacuum.

Figure 2a shows the small-angle neutron scattering (SANS) data from 6 polymers in our synthetic library. With the deuteration scheme described above, these data can be interpreted as describing the *backbone* packing and conformational statistics of bottlebrushes in the cast films. This study focused on the peak that appears at wavenumbers  $q > 0.1 \text{ \AA}^{-1}$  for each system. The position of the peak,  $q^*$ , is related to the average distance between bottlebrush backbones via the correlation length  $\xi = 2\pi/q^*$  and the breadth of the peak is related to the dispersity in this spacing. With increasing  $N_{SC}$  we see that  $q^*$  shifts to lower values indicating that the backbones show increased separation due to the longer sidechains. We also observe that the DNb and Ac bottlebrushes show sharper, more well-defined correlation peaks compared to SNb. This indicates that packing is less random and more ordered for higher grafting densities. Similarly, within each bottlebrush chemistry, the bottlebrushes with longer sidechains display sharper correlation peaks. All of these trends in  $\xi$  are reproduced in structure factors calculated from coarse-grained molecular dynamics simulations from this study and previous ones [7-9].

Unexpectedly, we observed that the data in Figure 2a superficially resemble SANS from polyelectrolyte solutions. To explore this observation further, we plot the intermolecular correlation length  $\xi$  against the backbone monomer concentration  $c_{BB}$ . This way of treating our data is based on a physical picture of the bottlebrush melt being a “mesh” of linear backbone chains within a sea of sidechain monomers. For uncharged, linear chain polymers in semi-dilute good-solvent solutions, we would expect from a simple model that the scaling exponent  $\mu = 3/4$  while linear chain polyelectrolytes in semi-dilute solution should have  $\mu = 1/2$ . Despite the bottlebrushes in this study being uncharged, their backbone



scaling statistics show near quantitative agreement with polyelectrolytes rather than neutral polymers at  $\mu = 0.47$ . This trend, also seen in our coarse-grained simulations, indicates that the backbones adopt similar conformational statistics whether they repel each other *via* sidechain excluded volume or long-range Coulombic repulsion. We can further support this comparison by comparing the scaling of  $\xi$  with  $N_{SC}$  (shown in Reference 7). Here, we find that the low grafting density system SNb shows particle like scaling ( $\mu \approx 0.35$ ) while DNb and Ac show more mesh-like scaling (0.43 and 0.44 respectively). This behavior is also similar to what is observed for polyelectrolyte solutions with wider variation in polymer concentration.



**FIGURE 2:** (a) SANS data for bottlebrush melts of two sidechain lengths and three backbone chemistries and (b) log-log scaling diagram of the correlation length  $\xi$  (nm) as a function of backbone monomer concentration  $C_{BB}$ .

Taken together, these results strongly indicate that uncharged bottlebrush polymers exhibit similar interchain correlations to

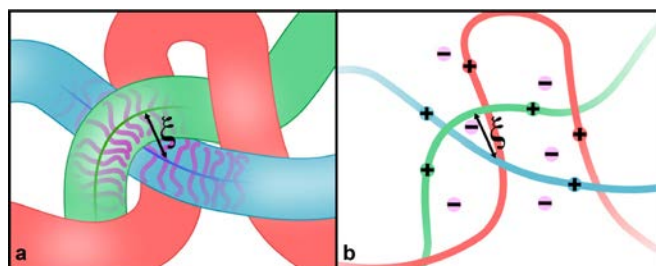


**FIGURE 3:** Schematic depiction of the packing of bulk brush polymers (a) and polyelectrolyte solutions (b).

solutions of linear polyelectrolyte chains, as shown as shown schematically in Figure 3. With the great promise of bottlebrush polymers across many applications, it is essential that we have a rational understanding of how their molecular design relates to microstructure and finally macroscopic material properties. While our data does not explain the origin of this behavior, it indicates that past studies of polyelectrolyte solutions may provide unique insight into bulk bottlebrush behavior. This provides a potentially powerful new avenue towards material design in leveraging a bottlebrush-polyelectrolyte analogy.

## References

- [1] K. L. Beers, S. G. Gaynor, K. Matyjaszewski, S. S. Sheiko, M. Moeller, *Macromolecules* **31**, 9413 (1998).
- [2] Y. Xia, J. A. Kornfield, R. H. Grubbs, *Macromolecules* **42**, 3761 (2009).
- [3] M. Vatankeh-Varnosfaderani et al., *Nature* **549**, 497 (2017).
- [4] B. R. Sveinbjörnsson et al., *Proc. Natl. Acad. Sci. USA* **109**, 14332 (2012).
- [5] S. Onbulak, J. Rzaev, *J. Polym. Sci. Part A Polym. Chem.*, **55**, 3868 (2017).
- [6] R. Verduzco, X. Li, S. L. Pesek, G. E. Chem. Soc. Rev. **44**, 2405 (2015).
- [7] J.M. Sarapas, T.B. Martin, A. Chremos, J.F. Douglas, K.L. Beers, *Proc Natl. Acad of Sci.* **117** (10), 5168 (2020).
- [8] A. Chremos, J. F. Douglas, *Polymers (Basel)*. **11**, 1045 (2019).
- [9] A. Chremos, J. F. Douglas, *J. Chem. Phys.* **149**, 163305 (2018).

# Rigid rod polymer construction through peptide computational design and hierarchical solution assembly

*N. Sinha,<sup>1</sup> D. Wu,<sup>1</sup> J. Lee,<sup>1</sup> H. Zhang,<sup>2</sup> J. G. Saven,<sup>2</sup> C. J. Kloxin,<sup>1,3</sup> and D. J. Pochan<sup>1</sup>*

Nature achieves complex molecular structures and exquisite functionality using biopolymers, the most versatile of which are polypeptides and proteins. The information for structure and function is encoded in sequences of amino acids that direct molecular folding and intermolecular assembly. A protein possesses a well-defined shape and size, and its structure determines both internal and external presentation of chemical functional groups. This specificity in protein structure and consequent function has motivated the engineering of proteins and protein assemblies to produce new materials not observed in nature. While there have been many successes in the design of protein assemblies, primarily through the modification of the exterior of natural proteins [1], the design and manipulation of complex protein interactions remains challenging. Thus, a new, simplified scheme of materials design is needed to further the adoption of amino acid-based molecules into materials and nanotechnology.

Large proteins can be aggregation prone, and their use is often limited to narrow ranges of environmental conditions, such as temperature and pH. At the high concentrations typically required for materials assembly, the folding and assembly of protein systems tend to be irreversible upon cycling temperature or pH, forming amorphous aggregates. Structural variation of the building block protein is desirable in tuning the structures and properties of material assemblies but is limited by what nature has provided. To develop stable, robust material assemblies, it is of interest to introduce covalent cross-links between residues; however, the chemistries for achieving this with natural proteins are limited. Advances in assembly, covalent crosslinking, and material functionality can potentially be achieved by incorporating nonbiological amino acids, but it is difficult to introduce non-natural amino acids into overexpressed proteins at more than just a few residue positions without the protein losing its inherent folded structure.

To overcome the limitations of using natural proteins to build materials, we use computational design of non-biological peptide sequences that include both natural and non-natural amino acids to provide new physical and covalent interactions for hierarchical solution assembly into designed nanomaterials. The use of natural and non-natural amino acid side groups on a polyamide backbone allows us to create new assemblies that constitute modular, functional building blocks (Figure 1), which become

the basis of an entirely new method of materials fabrication. The development of these robust peptide bundle building block structural units, known formally as coiled coils, provides a new tool for a wide diversity of researchers to impact materials science, physics, chemical engineering, and biomedicine.

The short peptide molecules are amenable to solution assembly and processing associated with materials. Short amino acid

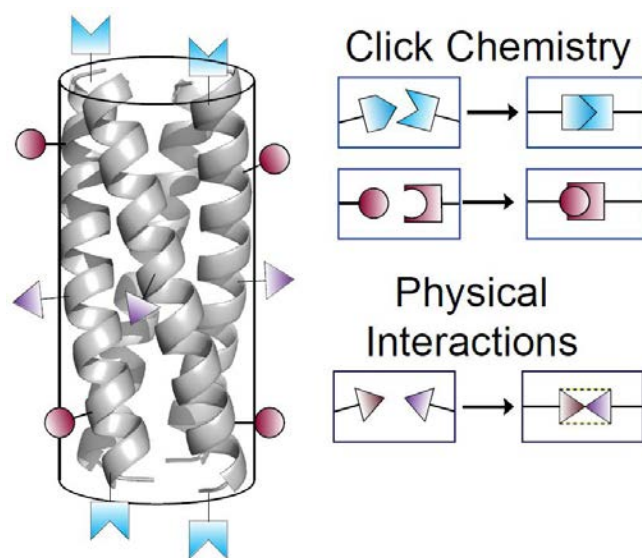


**FIGURE 1:** Schematic of a coiled coil peptide bundle building block designed from the assembly of four helical peptides packed in an antiparallel configuration with each bundle end having two amine and two acid functional groups on the constituent peptides. With computational design, the side chains can consist of any desired natural or non-natural chemical functionality to provide the exact display of chemistry at the bundle periphery.

sequences often are robust with respect to the cycling of temperature and wide variation of solution conditions such as pH, salt, and other added organic or polymer molecules. Such processing provides additional control over the hierarchical assembly and desired morphology of designed peptide materials. A common building block motif that will be used for ongoing materials construction is the interbundle, hierarchical formation of 1-D chains. Through modification of bundle peptide termini, we control the covalent conjugation of bundles in an end-to-end fashion.

<sup>1</sup> Department of Materials Science and Engineering, University of Delaware, Newark, DE 19716

<sup>2</sup> Department of Chemistry, University of Pennsylvania, Philadelphia PA, 19104

<sup>3</sup> Department of Chemical and Biological Engineering, University of Delaware, Newark, DE 19716

Two different bundle-forming peptides were synthesized containing click functional groups at the N-terminus, Figure 2. The single modification to the constituent peptide sequence of a tetrameric bundle results in four total functional groups

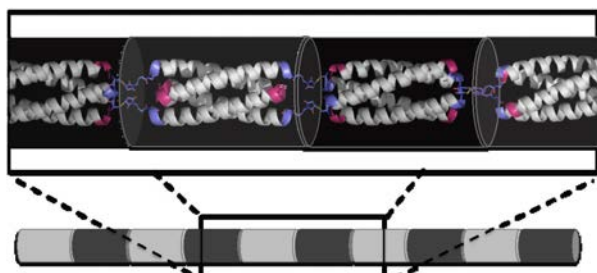


**FIGURE 2:** Schematic of end-to-end conjugation of the N-termini of designed bundles into a 1D chain. The use of the Thiol-Michael ‘click’ reaction, with one bundle having thiol end groups via a cysteine amino acid and another bundle having non-natural maleimide end groups, produces an extremely stiff, rigid rod chain of alternating bundle building blocks [2].

being displayed from the bundle, two click functional groups at each end. This is a direct consequence of using an antiparallel homotetramer coiled-coil as the base bundle monomer. Two separate batches of peptide tetramer bundles were synthesized. One batch had N-terminal maleimides and the other had N-terminal cysteine residues (thiols). The thiol and maleimide functional groups from the ends of each bundle reacted together through a rapid thiol-Michael addition reaction forming an incredibly rigid, high aspect ratio polymer chain. These polybundles had widths consistent with a single bundle as determined by transmission electron microscopy and small-angle neutron scattering and several had lengths  $> 1 \mu\text{m}$ .

Using computational design, stable bundle units can be assembled that possess significant charge density at the exterior, opening the door to the study of the polybundles as model polyelectrolytes. An example is shown in Figure 4 and is

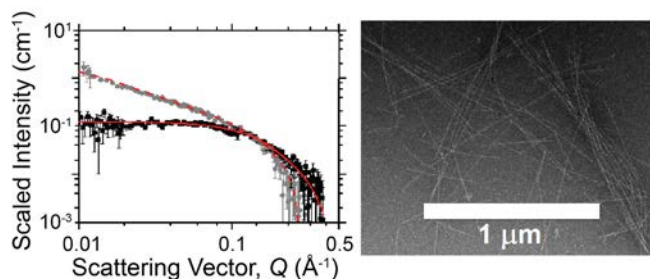


**FIGURE 3:** Left, SANS of individual bundle building blocks (black symbols) with rigid cylinder fit (red solid line) and of rigid rod chains (gray symbols) with rigid cylinder fit (red dashed line). Individual bundles were measured to have  $\approx 4 \text{ nm}$  length and  $\approx 2 \text{ nm}$  diameter as predicted by computational design. Rigid rods have the same  $2 \text{ nm}$  diameter and also display the characteristic  $-1$  scaling of  $\log(I)$  vs  $\log(Q)$  for a rigid 1-D object. Right, negatively stained TEM image of ultrarigid rod chains [3].

published in Sinha et al. [3], where alternating bundles along a rigid rod are highly positively charged at  $\text{pH} = 7$ . With growing concentration of rods, electrostatic repulsion introduces both an inter-rod structure factor correlation peak as well as a correlation hole due to the rods local excluded volume due to the significant charge.

Ongoing work involves the design of rigid rod chains and more flexible chains, with different interbundle linker chemistry and charged patterns to explore the colloidal behavior of the model rods as well as the liquid crystal phases that they produce.

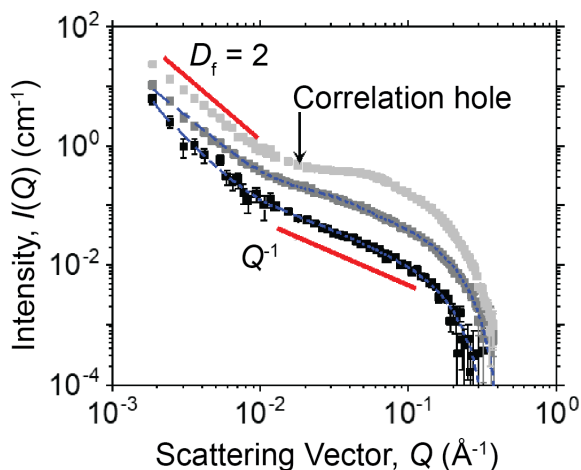


**FIGURE 4:** Rigid rod solution SANS possessing significant positive charge. Low and medium concentrations (black symbols and dark gray symbols) reveal scattering from individual rods. Higher concentration (light gray) reveals an inter-rod structure factor peak as well as the introduction of a correlation hole [3].

## References

- [1] J. B. Bale, S. Gonen, Y. Liu, W. Sheffler, D. Ellis, C. Thomas, D. Cascio, T. O. Yeates, T. Gonen, N. P. King, D. Baker, *Science* **353**, 389 (2016).
- [2] D. D. Wu, N. Sinha, J. Lee, B. P. Sutherland, N. I. Halaszynski, Y. Tian, J. Caplan, H. V. Zhang, J. G. Saven, C. J. Kloxin, D. J. Pochan, D. J., *Nature* **574**, 658 (2019).
- [3] N. J. Sinha, D. D. Wu, C. J. Kloxin, J. G. Saven, G. V. Jensen, D. J. Pochan, *Soft Matter* **15**, 9858 (2019).



# Accelerated local dynamics in matrix-free polymer grafted nanoparticles

M. Jhalaria,<sup>1</sup> M. Tyagi,<sup>2,3</sup> and S. Kumar<sup>1</sup>

The use of polymer membranes is well-established for achieving cost efficient and energy efficient gas separations [1]. Since the separation performance of most membranes is highly dependent on their chemical structure, most improvements to date have been achieved through the synthesis of new polymers. A philosophically different approach is physics-based, employing composite materials, e.g., ones constructed using *only* polymer grafted nanoparticles (GNPs). These hybrid inorganic-organic constructs have been recently shown to have tunable transport characteristics.

In particular, GNP based membranes display enhanced diffusivities of light gases (e.g. CO<sub>2</sub>) when compared to the corresponding ungrafted homopolymer membrane with no added NPs. The degree of this enhancement is dependent on the molecular weight ( $M_n$ ) of the grafted polymer chain at constant grafting density ( $\sigma$ ). In fact, a nonmonotonic behavior is observed with a diffusivity maximum at an intermediate  $M_n$ , one where the  $R_g$  of the chain is close to the radius of the nanoparticle [2]. Diffusivity control in these composites was achieved by varying the grafted chain length at fixed grafting density, meaning that the gas transport properties of such scaffolds are likely controlled by the nanoscale segmental dynamics of the polymer. It is widely accepted that diffusion of gases in polymers proceeds through a jump diffusion mechanism, where gas molecules jump from one “free volume” pocket to another with penetrant jump lengths of  $\approx 1$  nm. This suggests that the use of quasielastic neutron scattering (QENS) would be appropriate, as it allows access to dynamics with spatial ( $< 3$  nm) and temporal ( $< 3$  ns) sensitivity.

Here, we use spherical SiO<sub>2</sub> NPs (14 nm  $\pm$  4 nm diameter) functionalized with poly(methyl acrylate) chains with a series of molecular weights ( $M_n \approx 29$  kg/mol to 136 kg/mol) at  $\sigma \approx 0.47$  chains/nm<sup>2</sup>. To enable comparison, a neat homopolymer with  $M_n = 96$  kg/mol was also studied. For this set of configurations, the expected maximum in diffusivity is when  $M_n \approx 90$  kg/mol. All experiments were done at 420 K, which is much higher than the glass transition temperature ( $T_g$ ) of the polymer and the composites ( $T_g \approx 290$  K).

When we compare representative quasielastic spectra from a composite with  $M_n = 88$  kg/mol and the neat homopolymer at a single wavevector,  $q = 11.1$  nm<sup>-1</sup> in Figure 1A, we observe a

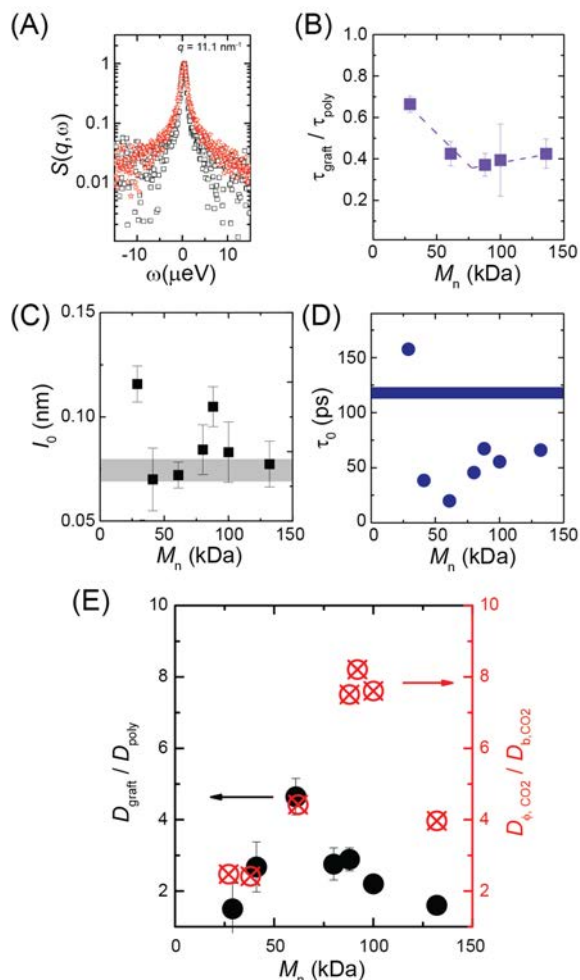


**FIGURE 1:** (A) Dynamic structure factors at  $q = 11.1$  nm<sup>-1</sup> for a composite with  $M_n = 88$  kg/mol (red  $\otimes$ ) and neat homopolymer (black  $\bullet$ ) showing increase in quasielastic broadening for the composite. (B) Normalized relaxation times across averaged across all wavevectors for the composites at different graft  $M_n$  for  $\sigma = 0.47$  chains/nm<sup>2</sup>. All data were normalized with respect to the average relaxation time of the neat homopolymer. (C) Characteristic jump lengths for composites as a function of  $M_n$ . The grey band represents the value for the bulk polymer. (D) Characteristic jump relaxation times for composites as a function of  $M_n$ . The blue band represents the value for the neat homopolymer. (E) Normalized segmental diffusion coefficients (black) for the graft chains. A clear non monotonic trend is observed with a maximum at  $M_n = 61$  kg/mol. Corresponding normalized CO<sub>2</sub> diffusivities at 308 K are also shown for the composites (red).

<sup>1</sup> Department of Chemical Engineering, Columbia University, New York, NY 10027

<sup>2</sup> NIST Center for Neutron Research, National Institute of Standards and Technology, Gaithersburg, MD 20899

<sup>3</sup> Department of Material Science and Engineering, University of Maryland, College Park, MD 20742

larger broadening in the composite relative to the ungrafted homopolymer. This indicates that at this length scale ( $d \approx 2\pi/q \approx 0.5 \text{ nm}$ ) within the largest measurable time (set by the resolution of the instrument), the graft chains are more mobile. To compare all the composites in the time domain, the data was inverse Fourier transformed and deconvolved to calculate the average relaxation times. As shown in Figure 1B, the mean relaxation times of the grafted chains are always lower than that of the neat homopolymer by a factor of five. A weak molecular weight dependence is observed, with the normalized relaxation times beyond 61 kg/mol nearly independent of the grafted chain  $M_n$ .

While we note that the mean relaxation times of the grafted polymers are lower than that of the bulk polymer - to independently analyze both characteristic time and length scales of the motion, we use an anomalous jump diffusion-based model that was proposed for glass forming polymers [3]. The central tenet behind the model is the existence of decaging jumps by polymer segments, with a well-defined length scale (jump length,  $l_0$ ) and frequency (jump frequency,  $1/\tau_0$  or jump relaxation time  $\tau_0$ ). For the graft chains, there is a distinct minimum in  $\tau_0$  at an intermediate  $M_n$  of 61 kg/mol where the relaxation times are 6-7 times smaller than that of the neat polymer (Figure 1D). Changes in the spatial mobility (i.e. the jump length) are much weaker than the frequency of the motion, but a maximum does manifest itself as a maximum at a larger  $M_n = 88 \text{ kg/mol}$ , very close to the expected maximum in the light gas diffusivities (Figure 1C).

We estimate a segmental diffusion constant using the Einstein-Smoluchowski principle as  $D = l_0^2/6\tau$ . This diffusion coefficient is only related to the nanoscale motion of the polymers and likely unrelated to the center of mass diffusion of polymer chains at longer times. Through this approach, we also combine the observed variance in both parameters with molecular weight and easily compare to measured light gas diffusivities in these composites. We observe nonmonotonicity in the segmental diffusion coefficients, qualitatively similar to the observation for light gases, with a maximum at a  $M_n$  of 61 kg/mol; all calculated diffusivities being larger than that of the neat

homopolymer. This behavior is very similar to the measured enhancements in  $\text{CO}_2$  diffusivities (red circles, Figure 1E), albeit with a shift of the segmental diffusion maximum to a lower molecular weight and lower magnitude of the enhancement in the GNPs. A possible reconciliation comes from two facts – a) There need not be a one-to-one correspondence between the gas diffusion and local segmental dynamics, likely because the gas molecule is smaller than the polymer segments and b) the temperature response of the diffusion coefficient is different for different graft  $M_n$ . Nevertheless, the importance of dynamics on the scale of  $\approx 1 \text{ nm}$  for the transport of penetrants in polymer membranes is highlighted through this study.

Thus, GNP based membranes provide a tunable platform for controlling transport of penetrants. Using this platform, we identify dynamics at the scale of  $\approx 1 \text{ nm}$  being the driving force behind the transport with both spatial and temporal aspects of the motion contributing to changes [4]. The major contributor is the frequency of motion at this length scale, with faster dynamics leading to a nonmonotonic degree of enhancement in the segmental diffusion coefficient. More detailed studies can help identify how different GNP parameters ( $\sigma$  and core diameter) modulate the dynamics of the graft chains and develop a better understanding of how these scaffolds control the segmental dynamics.

## References

- [1] M. Galizia, W. S. Chi, Z. P. Smith, T. C. Merkel, R. W. Baker and B. D. Freeman, *Macromolecules* **50** (20), 7809 (2017).
- [2] C. R. Bilchak, E. Buenning, M. Asai, K. Zhang, C. J. Duming, S. K. Kumar, Y. C. Huang, B. C. Benicewicz, D. W. Gidley, S. W. Cheng, A. P. Sokolov, M. Minelli and F. Doghieri, *Macromolecules* **50** (18), 7111 (2017).
- [3] A. Arbe, J. Colmenero, F. Alvarez, M. Monkenbusch, D. Richter, B. Farago and B. Frick, *Phys Rev E* **67** (5), 051802 (2003).
- [4] M. Jhalaria, E. Buenning, Y. Huang, M. Tyagi, R. Zorn, M. Zamponi, V. Garcia-Sakai, J. Jestin, B. C. Benicewicz and S. K. Kumar, *Phys Rev Lett* **123** (15), 158003 (2019).

# Evolution of local and global chain conformation of polymer melts during extensional flow: what happens inside the “tube”?

C. R. López-Barrón,<sup>1</sup> W. R. Burghardt<sup>2</sup> and M. S. Kweon<sup>2</sup>

Strong extensional flows are ubiquitous in industrial polymer processing operations, such as film blowing, thermoforming and foaming. This has motivated a significant amount of research over the last few decades [1] aiming to elucidate the molecular origins of non-linear viscoelastic responses to extensional flow fields. However, a unifying theory that correlates local and global chain conformation with stress flow fields is still lacking. This is, in part, due to the lack of direct measurements of structural evolution during melt flow at all relevant length scales. Such measurements could aid in answering two unresolved fundamental questions of polymer rheology: (1) what is the effect of elongational flows on the local conformation (within the so-called “confining tube” [2]) of polymer chains? and (2) how is the rheological response affected by the local inter-monomer interactions, namely, the chemistry of the monomers?

We present a combined experimental method [3] to directly measure the structural evolution of polymer chains during uniaxial extensional flow on scales ranging from their radius of gyration ( $R_g$ ) down to the monomer conformation. This method combines time-resolved *in-situ* extensional rheo-small-angle neutron and wide-angle X-ray scattering measurements (tEr-SANS and tErWAXS, respectively) using a commercial Sentmanat extensional rheometer (SER) mounted on an ARES G2 strain-controlled rheometer (for tErSANS measurements) or on a custom-made oven (for tErWAXS measurements). Figure 1 shows a schematic representation of these measurements, which were applied in a polystyrene (PS) isotope blend [3]. In both cases, the (X-ray or neutron) beam passes through the center of the molten polymer film that is being uniaxially deformed by the SER, and 2D scattering profiles are collected *in-situ* (i.e., during the deformation) on the detectors. As illustrated in the top panel in Figure 1, the global chain alignment in the range from segmental to single molecule scales is measured with tErSANS [4], whereas local orientation of the backbone-backbone and phenyl-phenyl interactions between adjacent styrene monomers are measured with tErWAXS. The extensional stress is directly measured by the torque transducer in the rheometer.

The chain alignment in the segmental length corresponding to the  $R_g$  about the stretching direction (SD) is quantified by the segmental alignment factor, defined as  $A_f = (\int_0^{2\pi} I(\phi) \cos(2\phi) d\phi / \int_0^{2\pi} I(\phi) d\phi)$  [5], where  $I(\phi)$  is the

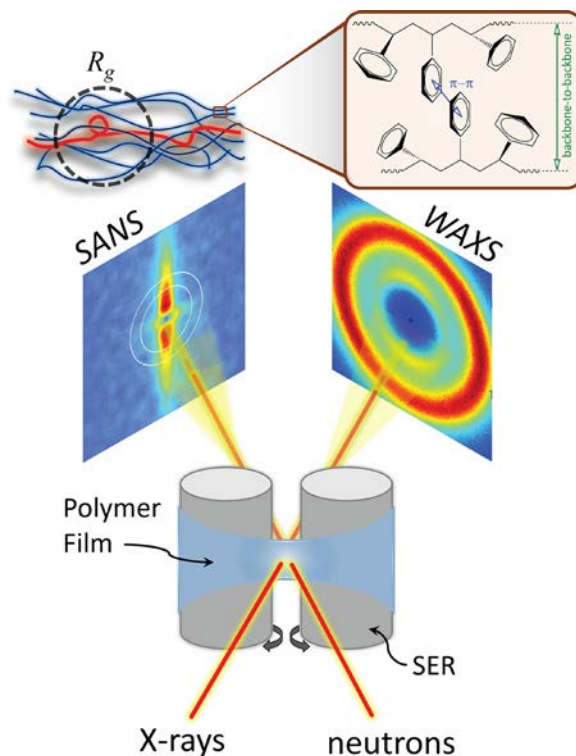


**FIGURE 1:** Schematic representation of the tErSANS and tErWAXS measurements using a commercial SER. The top panel shows a schematic illustration of the global and local chain conformations induced by extensional flow.

SANS intensity (radially-averaged within the annular sector indicated in Figure 2(a)) measured as a function of azimuthal angle ( $\phi$ ), as shown in Figure 2(c). Two new parameters are defined to quantify the strain-induced anisotropic inter-phenyl interactions (also referred as inter-phenyl  $\pi$ - $\pi$  stacking) and the “local” backbone stretching (backbone-to-backbone correlations). These are  $A_{\pi-\pi} = (I_{\pi\pi-SD} - I_{\pi\pi-TD}) / (I_{\pi\pi-SD} + I_{\pi\pi-TD})$  and  $A_{bb} = (I_{bb-TD} - I_{bb-SD}) / (I_{bb-SD} + I_{bb-TD})$ , respectively, where integrated intensities measured in angular sectors (of equal area) along the stretching and transverse directions (SD and TD, respectively), as indicated in Figure 2(b). The alignment factors described above were measured as a function of time and strain during start-up of uniaxial extension of the PS isotope blend at different temperatures and strain rates, which allows us to access a wide range of Weissenberg number (four decades) and extensional stress (0 MPa to 20 MPa) [3].

<sup>1</sup> ExxonMobil Chemical Company, Baytown, TX 77520

<sup>2</sup> Department of Chemical and Biological Engineering, Northwestern University, Evanston, IL 60208



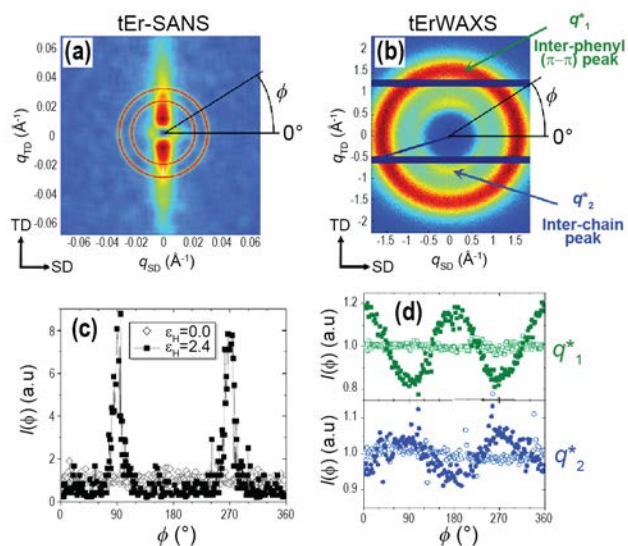


**FIGURE 2:** (a) and (b) show SANS and WAXS 2D data, respectively, of the PS isotope blend measured at Hencky strain of 2.4 during uniaxial extensional flow at 130 °C. (c) Radially-averaged SANS intensity as a function of azimuthal angle measured at strains of 0 and 2.4. (d) Radially-averaged WAXS intensity as a function of azimuthal angle measured at the inter-phenyl ( $q_1^*$ ) and inter-chain ( $q_2^*$ ) peaks, respectively.

We found that single master curves are obtained when all the of time-dependent alignment factors and stress data (measured at different temperatures and deformation rates) are plotted parametrically (Figure 3). This fact led us to propose three empirical rules that relate the bulk extensional stress to the microstructure evolution at different length scales. These are the stress-SANS rule (SSR, given as  $\sigma_E = C_{E,Rg}^{-1} A_f$ ) and two stress-WAXS rules (SWR, given as  $\sigma_E = C_{E,\pi-\pi}^{-1} A_{\pi-\pi}$  and  $\sigma_E = C_{E,bb}^{-1} A_{bb}$ ). Note that these rules resemble the well-known stress-optical rule (SOR), although they are not entirely analogous, as each of them probe different segmental lengths of the polymer chains. The stress-SANS coefficient ( $C_{E,Rg} = 0.69 \text{ MPa}^{-1}$ ) and the stress-WAXS coefficients ( $C_{E,\pi-\pi} = 0.025 \text{ MPa}^{-1}$  and  $C_{E,bb} = 0.074 \text{ MPa}^{-1}$ ) are given by the slopes in the straight lines in Figure 3. The deviation from the linear correlations indicates failure of the SSR and SWRs, which occurs at one order of magnitude larger stress values for the local alignment than for the global alignment. This observation, along with the fact that the SANS coefficient is one order of magnitude larger than the stress-WAXS coefficients, reveals that the global chain conformation is much more sensitive to the stress field than the local chain conformation (inside the tube).

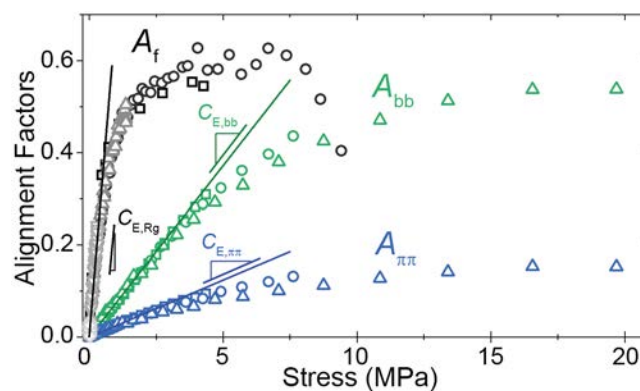


**FIGURE 3:** Segmental alignment factor ( $A_f$ ), anisotropic  $\pi$ - $\pi$  stacking ( $A_{\pi-\pi}$ ), and "local" backbone stretching ( $A_{bb}$ ) versus stress, measured with tErSANS and tErWAXS. Solid lines are fits to the SSR and SWRs.

In summary, this work demonstrates the power of combining in-situ time-resolved SANS with time-resolved X-ray scattering measurements to elucidate the interrelations between viscoelastic response and microstructure in a wide length scale range. This method allowed us to reveal the very important role of the polymer "chemistry" (i.e., the chemical identity of the monomeric units) on the non-linear response of polymer melts to fast flows, which is typically ignored in most studies that consider a polymer chains as a mere one-dimensional strings (i.e., spaghetti-like entities). This study also revealed that the chain conformation on a global scale responds more strongly to extensional flow than does the local conformation (i.e., inside the confining tube), due to the local structure at the monomer level. Therefore, it follows that the application of the methods presented here to other polymeric systems represents an opportunity to gain deep understanding of the effect of specific interaction forces present in different monomeric units (e.g., hydrogen bonding,  $\pi$ - $\pi$  interactions, ionic bonds, etc.).

## References

- [1] S. Q. Wang, *Nonlinear Polymer Rheology: Macroscopic Phenomenology and Molecular Foundation* (Wiley, 2018).
- [2] M. Doi, S. F. Edwards, *The theory of polymer dynamics* (Clarendon Press; Oxford University Press, New York, 1986), p. 391.
- [3] C. R. López-Barrón, W. R. Burghardt, M. S. Kweon, *ACS Macro Lett.* **9**, 26 (2020).
- [4] C. R. López-Barrón, Y. Zeng, J. J. Richards, *J. Rheol.* **61**, 697 (2017).
- [5] L. M. Walker, N. J. Wagner, *Macromolecules* **29**, 2298 (1996).

# Neutron probe for mass transport mechanisms in oil-in-water emulsions

Y.-T. Lee, D. Li, and L. Pozzo

Emulsions are ubiquitous in many consumer products including foods, cosmetics and cleaning products. They are also key components to engineered systems such as lubricants, drug delivery vehicles and micro or nano reactors such as in latex polymerization. A deep understanding of the transport mechanisms that occur in these dynamic and complex microenvironments is critical to the successful design and to control the performance of these systems. In this work we use small angle neutron scattering (SANS) with carefully designed contrast variation, and time-resolved data collection capabilities at the NCNR, to provide fresh insights into the mechanisms of molecular and colloidal mass transport that occur in oil-in-water emulsion systems stabilized by anionic alkyl sulfate surfactants such as sodium dodecyl sulfate or SDS [1, 2].

Figure 1 highlights possible mechanisms of oil exchange that take place in emulsions. Droplets can exchange oil by molecular diffusion processes that depend, among other things, on the solubility and diffusivity of the molecules in the continuous water phase. Alternatively, micelles can also ‘shuttle’ oil between droplets by solubilizing molecules in their hydrophobic core. Colloidal transport mechanisms, which rely on the direct interactions between droplets, may also dominate kinetics of oil exchange. For example, two droplets may coalesce to form a larger ‘mixed’ droplet. Alternatively, droplets may collide or come into close proximity to accelerate transient interfacial transport without undergoing irreversible coalescence. To determine the dominant transport mechanisms, contrast variation time-resolved SANS (CV-SANS) was used to track oil exchange after rapid mixing of identical emulsion systems that differed only in their isotopic H/D oil composition. When these are mixed ( $t = 0$ ) the molecular exchange is initiated and tracked as a function of time by a decrease in scattering intensity due to the loss of contrast with the continuous water phase.

Figure 2 highlights the kinetics of oil exchange that occurs when hexadecane, a water-insoluble oil, is emulsified with SDS at surfactant concentrations above and below the critical micelle concentration (CMC). The kinetics of oil exchange for this system is very slow and it takes several hours to observe an appreciable decrease in contrast. Control experiments monitoring an unmixed emulsion were also performed to demonstrate that they were stable against coalescence and that any intensity decrease was dominated by the change in neutron scattering contrast. The oil exchange kinetics

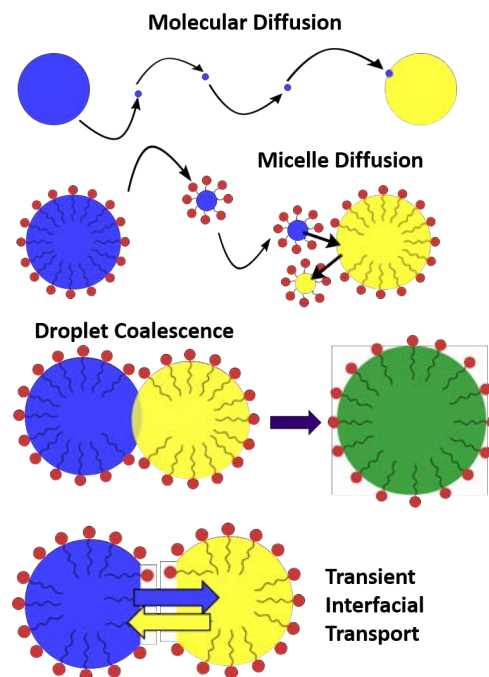


**FIGURE 1:** Potential oil exchange mechanisms in oil-in-water emulsion systems.

were further quantified by the calculation of the relaxation function  $R(t)$  that was then fit to a simple exponential decay. It was noteworthy to find that the decay rate was unaffected by the presence or absence of micelles in the colloidal dispersion. This result suggests that SDS micelles do not play a significant role in regulating the transport of hexadecane molecules between droplets. Moreover, control experiments without any SDS surfactant in the system showed even slower kinetics of exchange. Thus, for SDS-stabilized hexadecane-in-water emulsions, the dominant mechanism of oil exchange was determined to be dependent on interfacial exchange mechanisms due to direct droplet interaction. In contrast, CV-SANS experiments with shorter alkanes (i.e. octane and dodecane) demonstrated that molecular diffusive transport can indeed dominate for oils with increasing solubility in water [1].

Similar CV-SANS experiments were also performed using the same emulsion systems but under the application of an external high-intensity focused ultrasound (HIFU) field using a recently developed sample environment [3]. In these experiments, the droplet size distribution was also determined to be relatively

unchanged for the duration of the experiment. However, Figure 3 shows that the kinetics of exchange for sonicated samples was greatly accelerated and full decay was achieved within just a few minutes of ultrasound activation [2]. Here, the dominant mechanism was determined to be a steady-state balance between mechanically induced droplet coalescence and breakup leading to complete oil-exchange without a net change in size distribution. Importantly, the addition of surfactant (SDS) was shown to reduce the kinetics of oil exchange through the formation of a colloiddally stabilizing interface. CV-SANS experiments performed at variable acoustic pressures also indicated that cavitation processes were essential to the acceleration of oil exchange via droplet coalescence [2].

In conclusion, the use of CV-SANS with time-resolved analysis was demonstrated to be a powerful experimental tool for the quantitative analysis of mass-transport occurring inside complex emulsion systems without the necessary addition of external 'tags' that would undoubtedly influence the systems of interest. The development of new instruments, such as the new CHRNS vSANS instrument at the NCNR, which are capable of simultaneous data acquisition at multiple sample-to-detector distances with neutron beams of increased brightness are key to the success of such kinetic experiments. The extended low- $q$  range of vSANS, though it had not yet been commissioned for use in this specific work, will further enable the analysis of oil exchange rates in emulsions

while simultaneously monitoring changes in droplet size distributions. Finally, developments in sample environments such as shear cells, ultrasound cells, microfluidics and stop-flow will further expand the analysis of transport in complex fluids and emulsions under realistic use situations.

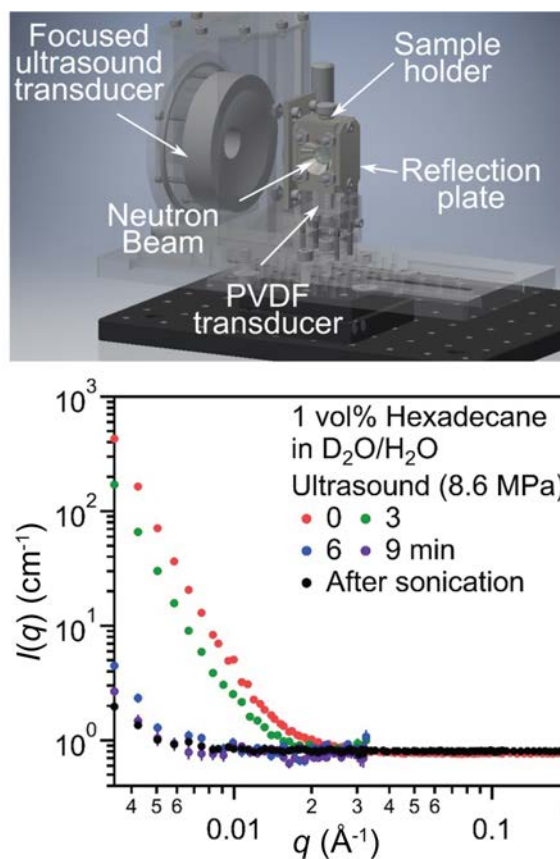


**FIGURE 3:** (Top) Design drawing of in-situ high-intensity focused ultrasound sample environment for SANS or SAXS analysis. (Bottom) Decay rates in SDS-stabilized emulsions are greatly accelerated during ultrasound application.

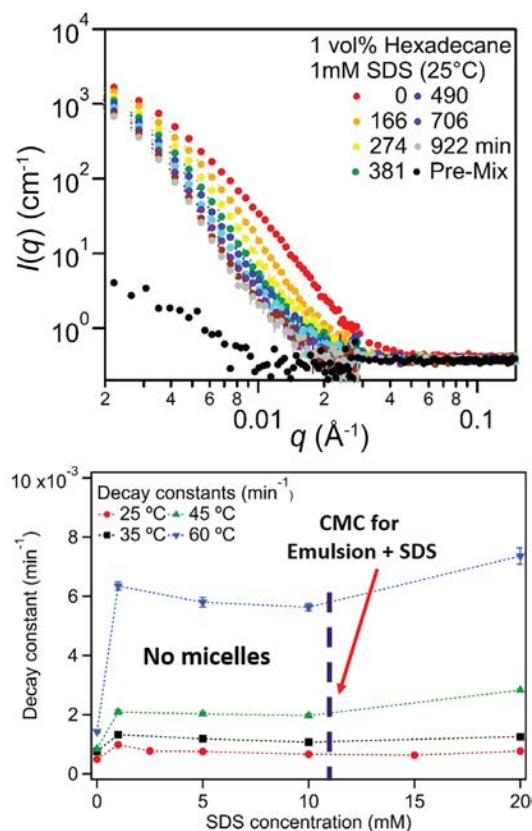


**FIGURE 2:** (Top) Time-resolved SANS analysis of mass exchange between deuterium-enriched and hydrogen-enriched hexadecane emulsions stabilized by sodium dodecyl sulfate (SDS). (Bottom) Decay rates in SDS-stabilized emulsions are insensitive to the presence or absence of micelles in the dispersion.

## References

- [1] Y.T. Lee, L.D. Pozzo, *Langmuir*, **35** (47), 15192 (2019).
- [2] Y.T. Lee, D.S. Li, L.D. Pozzo, *Langmuir*, **35** (47), 15204 (2019).
- [3] D.S. Li, Y.T. Lee, Y. Xi, I. Pelivanov, M. O'Donnell, L.D. Pozzo, *Soft Matter*, **14**, 5283 (2018).



# Techniques for time-resolved SANS measurements

C. Glinka,<sup>1,2</sup> M. Bleuel,<sup>1,3</sup> P. Tsai,<sup>1</sup> D. Základná,<sup>4</sup> D. Honecker,<sup>5</sup> D. Dresen,<sup>6</sup> F. Mees,<sup>6</sup> and S. Disch<sup>6</sup>

Changes in nanoscale structure that occur on time scales in the micro- to millisecond regime in response to a stimulus are critical to the function and performance of materials as varied as muscle tissue, membranes, superconductors, 'smart' gels, electrorheological fluids, domains in ferroelectrics and ferromagnets, and photosensitive macromolecules. The ability to observe nanoscale structural changes in this time regime by SANS requires, due to intensity limitations, collecting data over many response cycles. The time resolution attainable this way on a conventional reactor SANS instrument is ultimately limited by the instrument's wavelength bandwidth (typically  $\Delta\lambda/\lambda \approx 10\%$ ) which typically spreads out the detection times of neutrons scattered by the sample by several milliseconds. However, by employing R. Gähler's time-focusing technique [1] that he termed TISANE (for Time-Involved Small-Angle Neutron Experiments), sub-millisecond time resolution is achievable.

TISANE utilizes counter-rotating high-speed choppers upstream from the instrument's collimation to emit neutron pulses with microsecond burst times. The frequency of these bursts, in relation to the sample stimulus frequency, results in time focusing at the detector independent of the spread in wavelengths. The time resolution achievable by TISANE is largely determined by the chopper burst times. The duty cycle of the choppers (percentage of time the choppers are 'open') does impose a reduction in average beam intensity which is only partially mitigated by the time-focusing. Hence TISANE should only be employed when the resolution achievable with conventional cyclic time binning is insufficient. Recent TISANE resolution measurements [2] have been made under a variety of instrument configurations to serve as a guide to when TISANE measurements provide an advantage over conventional time-binning measurements (Figure 1).

The capability of the TISANE setup on the NG-7 SANS instrument was demonstrated recently in a study of the reorientation dynamics of magnetic nanoparticles [2] in an oscillating magnetic field, with a time resolution as fine as  $150\ \mu\text{s}$ . The enhanced time resolution provided by TISANE allowed tracking of the oscillatory motion of the polar particle axis up to frequencies close to the kHz range, well beyond the limit set by the continuous SANS technique.

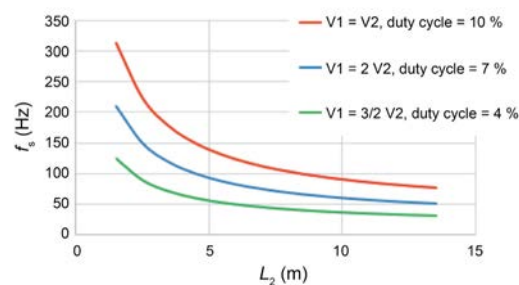


**FIGURE 1:** The curves correspond to values of the sample-to-detector distance,  $L_2$ , and the sample stimulus frequency,  $f_s$ , where the time resolution obtainable with continuous-beam time-resolved measurements matches that obtainable with TISANE. For all values of  $L_2$  and  $f_s$  above a given curve, the TISANE resolution is better, the more so the farther from the curve. For  $L_2$ ,  $f_s$  values below the curves, i.e. at lower frequencies and shorter detector distances (larger  $Q$  measurements), continuous-mode measurements are preferable, due primarily to their 100 % duty cycle. The three curves are for three relative speeds of the two choppers (1:1, 1:2, and 1:1.5) which is another way of improving the TISANE time resolution albeit with a reduction in duty cycle.

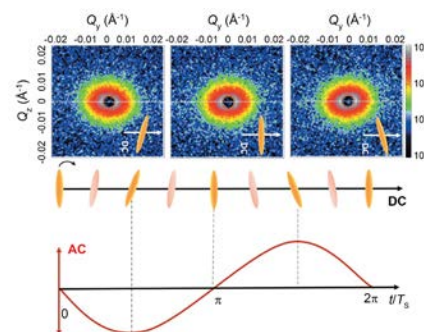


**FIGURE 2:** 2D SANS patterns (upper panel) of the scattering from elongated magnetic nanoparticles [2] at different time frames during the application of a 100 Hz applied magnetic field. The middle panel is a schematic representation of the orientation of the nanoparticles at the corresponding times.

## References

- [1] D. Kipping, R. Gähler, K. Habicht, Phys. Lett. A **372**, 1541 (2008).
- [2] C. J. Glinka et al., J. Appl. Cryst. **53**, 598 (2020).

<sup>1</sup> NIST Center for Neutron Research, National Institute of Standards and Technology, Gaithersburg, MD, 20899

<sup>2</sup> University of Delaware, Newark, DE, 19716

<sup>3</sup> University of Maryland, College Park, MD 20742

<sup>4</sup> Charles University in Prague, Hlavova 2030/8, Prague 2, Czech Republic

<sup>5</sup> University of Luxembourg, 162a, Avenue de la Faïencerie, Grand Duchy of Luxembourg, L-1511, Luxembourg

<sup>6</sup> Universität zu Köln, 116 Luxemburger Str., 50939, Köln, Germany, 50939, Germany

# Measuring structure and viscosity of complex fluids at extreme shear rates

R. P. Murphy,<sup>1</sup> Z. W. Riedel,<sup>1</sup> M. A. Nakatani,<sup>1</sup> P. F. Salipante,<sup>2</sup> J. S. Weston,<sup>3</sup> S. D. Hudson,<sup>2</sup> and K. M. Weigandt<sup>1</sup>

Small-angle neutron scattering continues to be an important tool in measuring multicomponent, complex fluids at the nanoscale. Complex fluids such as protein therapeutics, soaps, paints, and food products are often processed at high fluid velocities in confined geometries. The ratio of fluid velocity to geometry gap size defines the velocity gradient and corresponding shear rate, which can approach values of  $10^6 \text{ s}^{-1}$  during industrially-relevant processes of injection, spraying, or lubrication.

By combining rheology and SANS techniques into a single method, called RheoSANS, it is possible to simultaneously measure the fluid viscosity and nanostructure, providing key insight into how changes in fluid structure lead to changes in viscosity. Until recently, RheoSANS methods were limited to speeds of roughly  $1 \text{ m s}^{-1}$ , corresponding to a shear rate of  $10^3 \text{ s}^{-1}$  using a 1 mm sample gap. To expand the shear rate limitations, a measurement device called Capillary RheoSANS (CRSANS) [1] was developed at the NCNR with support from the *nSoft* consortium and NIST Innovations in Measurement Science (IMS) funding. The CRSANS device consists of a coiled fused silica capillary (Fig. 1) and high-pressure pumps that push fluid at  $50 \text{ m s}^{-1}$  within a confined diameter that can range from  $1 \mu\text{m}$  to  $200 \mu\text{m}$ . The advances in high pressure, fluid velocity, and confinement provide a thousand-fold increase in the shear rate at the capillary wall, which can achieve shear rates in excess of  $10^6 \text{ s}^{-1}$ .

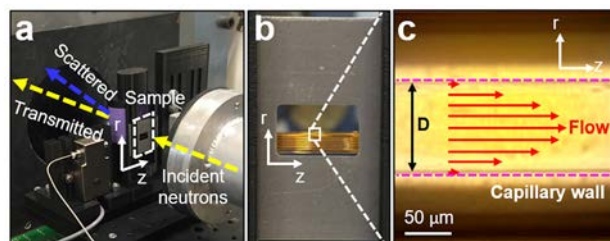


**FIGURE 1:** (a) Capillary RheoSANS device at the *nSoft* NGB-10m SANS. (b) Front view of a single silica capillary that is coiled to increase the sample volume in the beam path. (c) Pressure-driven flow in a capillary ( $D = 100 \mu\text{m}$ ) capable of generating shear rates of  $10^6 \text{ s}^{-1}$  at the wall and fluid velocity of  $50 \text{ m s}^{-1}$  at the center [1].

An example CRSANS measurement is shown in Fig. 2, which demonstrates the viscosity and 2D SANS measurements of worm-like micelle surfactants commonly used in enhanced oil recovery applications. The steady-shear viscosity decreases

strongly with increasing shear rate up to  $10^4 \text{ s}^{-1}$ , which coincides with the growing anisotropy in the SANS as the worm-like micelles align along the flow direction (horizontal direction). Interestingly, the micelle alignment decreases upon increasing the shear rate further above  $10^4 \text{ s}^{-1}$ . This maximum in alignment of micelles coincides with the macroscopic change in the power-law scaling of the viscosity from a slope of  $-2/3$  to  $-1/3$  (dotted lines in Fig. 2a), which is predicted to occur as worm-like micelles break down into shorter rod-like micelles [2].

Using Capillary RheoSANS, scientists can now examine how complex fluids behave at extreme flow conditions. With the combined RheoSANS capabilities at the NCNR, the rheology and nanostructure can be measured over *eight orders* of magnitude in shear rate, opening the door to previously impossible neutron measurements of the microstructure of soft materials and complex fluids.

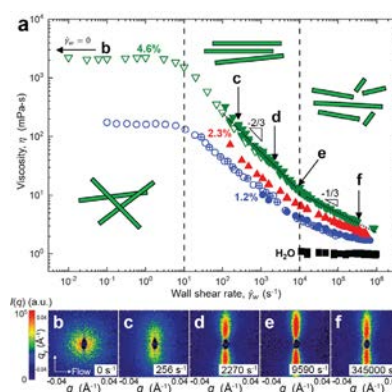


**FIGURE 2:** (a) Steady-shear viscosity of surfactant solution of worm-like micelles at various surfactant concentrations of (green) 4.6%, (red) 2.3%, and (blue) 1.2% by mass. Different measurement geometries are compared for (solid) capillaries, (open) rotating concentric cylinders, and (crossed) rectangular slits. (b-e) Corresponding 2D SANS shows micelle alignment increases up to  $10^4 \text{ s}^{-1}$  but decreases at higher rates [1].

## References

- [1] R. P. Murphy et al., *Soft Matter* **16**, 6285 (2020).
- [2] P. F. Salipante et al., *Journal of Rheology* **64** (3), 481 (2020).

<sup>1</sup> NIST Center for Neutron Research, National Institute of Standards and Technology, Gaithersburg, MD 20899

<sup>2</sup> Material Science and Engineering Division, National Institute of Standards and Technology, Gaithersburg, MD 20899

<sup>3</sup> Russell School of Chemical Engineering, University of Tulsa, Tulsa, OK 74104

# An autonomous liquid-handling platform for industrial formulation discovery

P. A. Beaucage and T. B. Martin

Complex liquid mixtures are the foundation of industries ranging from personal care products to biotherapeutics to specialty chemicals. In many such applications, small variations in composition can produce dramatic variations in performance. While neutron and X-ray scattering methods are workhorse techniques for characterizing model formulations, the large number of components in many real products makes mapping the parameter space impossible due to the sheer number of possible compositions. To enable rational design of these materials, we must leverage machine learning (ML) tools to greatly reduce the expense of creating structure-composition maps (phase diagrams). Applying ML tools requires a platform capable of autonomously creating samples with varying composition and chemistry. While there are numerous examples of robots which perform specific user facility operations, these systems tend to be bespoke and non-adaptable to new tasks. We have developed a highly adaptable sample environment that can be programmed to autonomously prepare and characterize liquid-formulations, which, in addition to ML-assisted search, will be used for *nSoft* consortium mail-in operations and reference dataset generation.

The goal of the system is to prepare samples from stock solutions and characterize their properties using neutron and X-ray scattering. The base platform consists of commercial off-the-shelf components, including an automated pipetting system, syringe pumps, flow selectors, and flow cells / capillaries (Figure 1). While the initial configuration focuses on enabling automated small-angle neutron (SANS) and X-ray (SAXS) measurements, it is designed to accommodate other inline devices (e.g., flow mixers), secondary measurements (e.g., UV-Vis spectroscopy) or even other sample environments (e.g., Capillary  $\mu$ RheoSANS).

The physical design of the robot is supported by a highly extensible Python microservice backend. Each device or group of devices (e.g., syringe pump + flow selectors) is encapsulated in a Python-based server that provides a command language and an interactive webpage showing the command queue. The granularity of the command language for each device server is arbitrary and is defined using simple Python classes. Users can define commands which map directly onto device operations (e.g., move flow selector to port 8) or complex composite commands involving multiple devices (e.g., perform a multi-cycle rinse routine). All of these commands are transmitted as web requests allowing our system to be integrated into existing

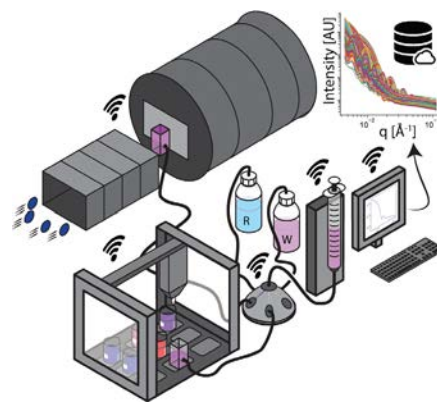


FIGURE 1: Schematic of liquid handling robot.

networks. By separating device groups into different device servers, we allow for asynchronous operations so that rinsing, sample preparation, and sample measurement can occur simultaneously.

Users design experiments on the platform by writing Python scripts or Jupyter notebooks. The user interface is through simple, physical commands such as “load” and “measure” and the user does not interact with communication or operational details; for SANS experiments at the NCNR, the neutron instrument is entirely controlled in the script via the Python interface to NICE. To enable autonomous formulation exploration driven by ML, we further developed a Python library which abstracts the sample preparation process. Users specify the location and composition of stock solutions along with the composition of desired samples. The library then solves the mass balance equations and creates a pipetting protocol. Users can specify desired samples by component mass, volume, or scattering length density, enabling the trivial construction of concentration or contrast-variation series. Most importantly, this sample abstraction will enable future ML algorithms to specify points in composition space without needing user intervention during autonomous phase-space mapping.

While ML-assisted phase mapping is still in development, our system has successfully operated at the NCNR and the Cornell High-Energy Synchrotron Source (CHESS). In both cases, we generated a library of scattering data for surfactant and nanoparticle solutions that will form the foundation of a future public database of small-angle scattering data.



# Annealing and etching away machining damage in a neutron interferometer

B. Heacock,<sup>1</sup> R. W. Haun,<sup>2</sup> K. Hirota,<sup>3</sup> T. Hosobata,<sup>4</sup> M. G. Huber,<sup>1</sup> M. E. Jamer,<sup>5</sup> M. Kitaguchi,<sup>3,6</sup> D. A. Pushin,<sup>7,8</sup> H. Shimizu,<sup>3</sup> I. Taminiau<sup>9</sup>, Y. Yamagata,<sup>4</sup> T. Yamamoto,<sup>3</sup> and A. R. Young<sup>10,11</sup>

Neutron interferometers coherently split and recombine a neutron wave, generating an interference pattern that depends on the neutron's interaction with samples inside of the interferometer. The macroscopic path separation unique to perfect-crystal neutron interferometers is achieved with Bragg scattering, where the neutron beam's wavelength and direction of travel almost perfectly matches the distance between atoms in the interferometer. For the neutron wave to recombine coherently, however, the angular alignment of the crystal lattice across the entire interferometer must be less than 10 nrad ( $2 \times 10^{-3}$  seconds of arc), which in terms of angular resolution would be like aiming for the bullseye of a dart board 1300 km away. Fortunately, the stringent angular alignment requirements may be satisfied without the need of sub-arc-second-precision motion control by constructing an interferometer from a high purity, floating-zone grown silicon ingot, so that the "blades" which diffract the neutron wave protrude from a still-connected base (Fig. 1a). Historically, this has used a notoriously non-reproducible, etching process with some interferometers functioning almost perfectly and others hardly usable. In recent work [1], we have demonstrated a more reliable process where improved machining techniques and post-fabrication annealing of the interferometer reduced the required etching depth by an order of magnitude.

A test-case "two-blade" interferometer was fabricated at the RIKEN Center for Advanced Photonics (Fig 1a). The finish cuts were made using a specialized, ultra-high precision grinding (UHPG) technique that produced a geometry with one micrometer tolerances and relatively small amounts of surface-level machining damage. Such an interferometer is judged in quality by the sharpness of a central interference peak-like structure which is formed as a function of alignment of the two diffracting "blades" at the 10 nrad angular scale. The interferometer was tested at multiple stages in the post-fabrication process: Step N. UHPG only; Steps I and II, annealed at 800 °C for 10 hours and 72 hours,

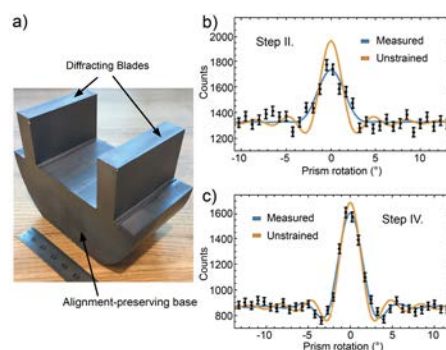


**FIGURE 1:** (a) The "two-blade" interferometer described in the text. Interference structure (a) after annealing (Step II), but before etching and (b) after both etching and annealing (Step IV) compared to a theoretical, unstrained interferometer.

respectively; Step III. 4  $\mu\text{m}$  of material chemically etched away; and Step IV. reannealed at 800 °C for 10 hours.

While no interference structure could be resolved for Step N, the shape of the neutron beam's profile leaving the interferometer indicated surface level strain at the  $10^{-5}$  level extending down approximately 1.5 mm into the crystal blades. After Step I, a weak interference pattern appeared, suggesting a reduction of surface strain by three orders of magnitude. After reannealing (Step II) did not alter the interference pattern (Fig 1b), 4  $\mu\text{m}$  of material was etched away (Step III), reducing strain by another order of magnitude and producing a nearly perfect interference pattern (Fig. 2c). Annealing a third time (Step IV) did not appreciably change the quality of the interference pattern, but a shift of the peak location indicated the relative alignment of the two blades changed by 10 nrad, which suggests continued strain reduction in the interferometer base.

## References

- [1] B. Heacock et al., Acta Cryst. **A75**(6), 833 (2019).

<sup>1</sup> Physical Measurement Laboratory, National Institute of Standards and Technology, Gaithersburg, MD 20899  
<sup>2</sup> Institute for Physical Science and Technology, University of Maryland, College Park, MD 20742  
<sup>3</sup> Department of Physics, Nagoya University, Nagoya 464-8602, Japan  
<sup>4</sup> RIKEN Center for Advanced Photonics, RIKEN, Hirosawa 2-1, Wako, Saitama 351-0198, Japan  
<sup>5</sup> Department of Physics, United State Naval Academy, Annapolis, MD 21402  
<sup>6</sup> Kobayashi-Maskawa Institute, Nagoya University, Nagoya 464-8602, Japan  
<sup>7</sup> Institute for Quantum Computing, University of Waterloo, Waterloo, ON N2L3G1, Canada  
<sup>8</sup> Department of Physics and Astronomy, University of Waterloo, Waterloo, ON N2L3G1, Canada  
<sup>9</sup> Quantum Valley Investments, Waterloo, ON N2L0A9, Canada  
<sup>10</sup> Department of Physics, North Carolina State University, Raleigh, NC 27708  
<sup>11</sup> Triangle Universities Nuclear Laboratory, Durham, NC 27708

# An RF neutron spin flipper for controlling the polarization in large beams with high efficiency

W. C. Chen,<sup>1</sup> R. Erwin,<sup>1</sup> P. Tsai,<sup>1</sup> Md. T. Hassan,<sup>1,2</sup> and C. F. Majkrzak<sup>1</sup>

Neutron polarization analysis using nearly perfect polarizing devices provides excellent sensitivity for distinguishing weak magnetic scattering from strong nuclear scattering. An adiabatic radio-frequency (RF) neutron spin flipper is such a device allowing researchers to flip the spin in a broadband neutron beam [1]. However, existing RF spin flippers are limited to use for a relatively small beam cross section, not suitable for the large incident beam of typically in the range of 5 cm<sup>2</sup> to 10 cm<sup>2</sup>. However, the incident beam on the newly developed polychromatic beam reflectometer, CANDOR, is much larger (90 cm<sup>2</sup>). Simulations showed that these flippers would not provide the required flipping efficiency of higher than 0.995 in the wavelength range from 4 Å to 6 Å. Here, we report the development of an RF spin flipper that provides an efficiency of 0.999 or better over the entire 6 cm x 15 cm beam, and a technique enabling measurements of the flipping efficiency with a precision better than 0.001. This RF flipper includes a neutron guide with either <sup>58</sup>Ni-coating or super-polished glass placed inside the coil which reduces the loss of beam intensity.

In an RF spin flipper, two orthogonal magnetic fields, one stationary ( $B_0$ ) and the other oscillating ( $B_1$ ), are required. The vectorially combined  $B_0$  and  $B_1$  field (effective field) in the rotating frame rotates its direction with a rate of change much slower than the Larmor frequency of the neutron as the neutron passes through the device. The neutron thus “sees” a change in direction of the effective field and the neutron spin flips. The flipper (Fig 1) contains three static magnetic guide-field sections (a), (b) and (c) which are employed to generate a gradient in  $B_0$  in the RF coil and provide the guide field for adiabatic neutron spin transport. The overall length of the flipper is  $\approx$  530 mm in which 250 mm is necessary for the RF coil (f). Sections (a), (b), and (c) are installed on CANDOR, while section (d) was used during testing to mimic the field generated by the magnetic cavity of the double-V supermirror. To increase the current delivered to the RF coil, which thereby raises  $B_1$ , we developed an inexpensive RF circuit using a modified Hartley RF oscillator and mutual coupling of the resonant coil to the excitation coil. This yields a larger flipping ratio than using a conventional 40 W RF power amplifier.

The RF spin flipper was characterized and optimized using the PHADES test station and two opaque <sup>3</sup>He spin filters that have a high opacity such that their resulting neutron polarizations

are close to unity [2]. The adiabatic fast passage (AFP) nuclear magnetic resonance (NMR) technique was employed to flip the <sup>3</sup>He polarization, thus the neutron polarization of the incident beam, thereby establishing the maximum achievable flipping ratio and/or neutron polarization.

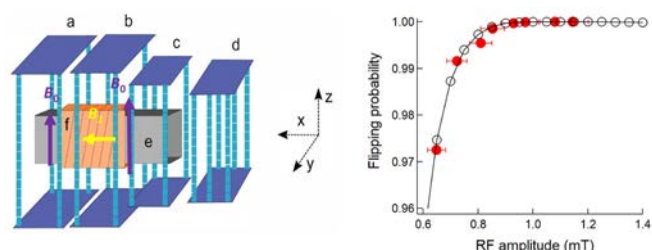


**FIGURE 1:** Left: Schematic of the adiabatic RF neutron spin flipper. The arrow length indicates strength of the static field  $B_0$ . The neutron beam travels from right to left along  $x$ . Right: Dependence of the flipping efficiency on the RF amplitude from both simulation (open circle) and measurements (filled circle) for the <sup>58</sup>Ni-coated neutron guide. The line is a guide to the eye. Error bars represent one standard deviation.

Zimmer *et al.* showed that when the product of opacity and <sup>3</sup>He polarization of an opaque <sup>3</sup>He NSF is larger than 3.8, the resulting neutron polarization is higher than 99.9%. The neutron polarization and the efficiency of a flipper can then be determined to a relative standard error of  $\approx$  0.0002 [2]. Figure 2 shows the flipping efficiency as a function of the RF amplitude using the <sup>58</sup>Ni-coated neutron guide (section (e) in Figure 1). A plateau of the flipping efficiency of 0.9997(3) was observed at an RF amplitude of 0.95 mT, which is consistent with the simulation. The flipping ratio at the plateau was 879(63), which is comparable to that obtained using the <sup>3</sup>He AFP NMR flipper, and confirming that the RF flipper provides a flipping efficiency nearing unity. We also found that the flipping probability changed only slightly with the resonant frequency, indicating that the operation of the RF flipper is not sensitive to small frequency deviations.

## References

- [1] A.I. Egorov *et al.*, Sov. J. Nucl. Phys. **19**, 330 (1974).
- [2] O. Zimmer *et al.*, Phys. Lett. B **455**, 62 (1999).
- [3] W.C. Chen *et al.*, in preparation.

<sup>1</sup> NIST Center for Neutron Research, National Institute of Standards and Technology, Gaithersburg, MD 20899

<sup>2</sup> University of Maryland, College Park, MD 20742

# Restraining molecular simulations with neutron reflection data

B. W. Treece,<sup>1</sup> F. Heinrich,<sup>1,2</sup> and M. Lösche<sup>1,2,3</sup>

Neutron reflectometry (NR) is one of the few techniques in structural biology able to characterize disordered and peripheral membrane-binding proteins under physiologically relevant, fully solvent-immersed conditions. NR reports an ensemble and time average of the structure of a membrane-associated protein as a one-dimensional component volume occupancy profile with an intrinsic resolution of about 1 nm. This is insufficient for many biomedical applications such as drug discovery, which require atomistic detail. Molecular dynamics (MD) simulations have therefore long been considered an optimal complement to NR to provide the two missing dimensions and to obtain a structural model of the protein-membrane complex at high resolution. More often than not, experiment and simulation gave incompatible results, either due to necessary simplifications of the experimental context or computational approximations during the simulation. To fill this gap, we recently implemented two related approaches that constrain MD simulations using NR data, leading to the best-possible agreement between the two and allow to obtain a high-resolution consensus structure.

Within a collaboration with the Roux group from the University of Chicago [1] we adapted the restraint ensemble MD (re-MD) approach, which previously had been successfully applied to other structural techniques such as nuclear magnetic resonance (NMR). The re-MD approach is formally equivalent to the maximum entropy method and minimally perturbs a MD trajectory for the purpose of matching target experimental observables. For a protein-membrane complex investigated with NR, this target observable is the 1-dimensional structural profile of the protein and its relative distance from the lipid membrane obtained from independent modeling of the NR data [2]. It is currently not realistic to use the NR data by itself as the target observable, as this would involve simulating the entire experimental setup and all relevant interactions. The re-MD approach is particularly suited for smaller proteins and peptides, and we have applied it to characterize the membrane-bound structure of the intrinsically disordered SH4-U region of the Hck kinase [1], a signaling protein which regulates many cellular processes relevant in cancer, whose membrane interaction was studied with NR at the NCNR. The re-MD approach led to a convergence of the simulated ensemble with NR data and NMR data collected in Chicago, leading to an atomistically resolved model of SH4-U membrane association. For larger proteins, the re-MD approach quickly reaches a

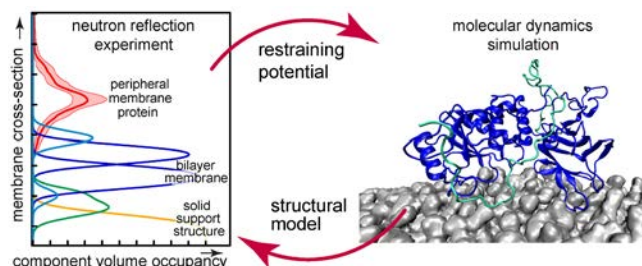


**FIGURE 1:** A restraining potential for the MD simulation is obtained from a model fit to the NR data. In turn, the MD simulation provides a high-resolution structural interpretation of the experimental data.

computational limit due to the system size and the need to perform parallel simulations. In collaboration with Argonne National Laboratory, we have devised a restraint MD simulation method that uses a single MD simulation in combination with time averaging to obtain the structural ensemble [3]. While this approach generally does not reach the optimal compromise between simulation and experiment that is achieved by re-MD, the restraining potential was designed to minimally affect experimental observables other than the target. We have tested this method with NR data of the membrane-bound PTEN lipid phosphatase [4]. The restraint on the configuration space showed a faster equilibration of the simulation compared to an unrestraint simulation and previously unobserved protein configurations were identified, leading to new insights into the role of the auto-inhibitory C-terminus of the protein during membrane-binding (see Figure 1). Future work will apply the method to more disease-relevant proteins and will integrate additional experimental techniques.

## Reference

- [1] M. Pond, R. Eells, B. Treece, et al., *J. Mol. Biol.* **432** (9), 2985 (2020).
- [2] F. Heinrich, M. Lösche, *BBA-Biomembranes* **1838** (9), 2341 (2014).
- [3] B. W. Treece et al., *J. Chem. Theory Comput.* **16** (5), 3408 (2020).
- [4] S. Shenoy, P. Shekhar, F. Heinrich, M. Daou, et al., *PloS one* **7** (4), e32591 (2012)

<sup>1</sup> Department of Physics, Carnegie Mellon University, Pittsburgh, PA 15213

<sup>2</sup> NIST Center for Neutron Research, National Institute of Standards and Technology, Gaithersburg, MD 20899

<sup>3</sup> Department of Biomedical Engineering, Carnegie Mellon University, Pittsburgh, PA 15213



# Neutron Source Operations

## Reliability and availability of the reactor

The reactor operated for 160 days during FY 2020, achieving a reliability of greater than 98%. Operational days were limited due to the temporary suspension of operations as a result of the pandemic.

## Cold source cryostat intermediary quality assurance

The cryostat for the new deuterium cold source is a complex assembly of individual shells machined out of billets of heat-treated aluminum 6061 alloy that are welded together into one structure. To ensure the safety and performance of the actual cryostat, an analysis of the theoretical strength of the final product was carried out, followed by the fabrication of a prototype. The prototype serves several purposes including the manufacturability of the assembly. As the contractor assembled the prototype, it became clear that the design clearances were insufficient to accommodate material movement during the welding process resulting in several thermal shorts after the welded assembly was completed. This led us to make slight alterations to the geometry of the cryostat, which successfully eliminated thermal shorts without affecting the neutron optics.

Due to the issues encountered with manufacturing the prototype, the contractor initiated a special quality assurance

procedure where the components of the cold source were 3D printed at full scale which allowed visual inspection which demonstrated that the required clearances were maintained. The input into the 3D printer was exactly the same as that used to program the CNC machines that are used to fabricate the final aluminum parts. Upon determining that the clearances were adequate in the mock assembly of the 3D printed parts, the design files were used to generate the CNC programs used to machine the actual parts. In the end, this process resulted in a plastic version of the entire cryostat, which can be used for demonstrations.

## New system for testing the air tightness of the NBSR confinement building

The NCNR's confinement building acts as a barrier against unwanted release and as such requires an annual test of the building integrity against air leaks. Whenever a change is made to the structure, systems or components that comprise the confinement building, this test must be repeated. Both the annual test and any design change inspections require the building pressure to be changed to prescribed vacuum and overpressure levels while measuring the rate of gas flow in and out of the building.

The leak rate test system that was delivered with the original building consisted of two fans (one to deliver vacuum and one to deliver overpressure), a very large (washing machine size) gasometer, an inclined manometer and several damper valves to control the fan output. Testing required two operators over a time that spanned multiple operator shifts. This introduced the possibility of communication errors and excluded workers from the confinement building for extended periods of time during testing.

The new system is built on a single skid, occupies only about 40 square feet and can be operated by one operator. Instead of two fans, the system driver is single regenerative blower, which can bring the building to testing pressure in several minutes. The blower is driven by a variable speed motor, which after the building is brought to pressure is dialed back using the building pressure as a control signal in a PID control loop. The new system has been deployed several times, proving to be much faster, so other users of the confinement building are no longer banned from entering for significant amounts of time. Repeat testing is also much quicker, which reduces the risk that a series of testing would impact reactor operations. Overall, the new system has reduced the test/repair/test time cycle by an order of magnitude.



**FIGURE 1:** David Hix of the Cold Source Team inspecting clearances between the 3D printed mock components of the deuterium cold source cryostat.

## Training reactor engineers and health physicists to become licensed reactor operators

During FY 2019 the cadre of licensed NBSR operators had shrunk to a level that could jeopardize the ability of the NCNR to provide 24/7 operations, with an obvious negative impact on neutron availability for science. At the low point, the NCNR was seven operators short of a full complement of 20 licensed reactor operators.

In response, the NCNR undertook an aggressive campaign to fill the seven vacancies. Not knowing ahead of time how fast we would succeed in attracting the necessary talent, the NCNR trained several Health Physics and Reactor Engineering personnel, preparing them for a reactor operator licensing exam by the Nuclear Regulatory Commission (NRC). Four reactor engineers successfully passed the NRC exam given in June/July 2020. We now have four engineers available for occasional shifts as operators. In the process, the NCNR trained a new reactor operator trainer, who is now prepared to instruct the seven newly recruited operators.

Even though this program has involved considerable effort for several months, the entire program was well received by all involved. Besides adding needed reactor operators, it became clear that this training provided reactor engineers and health physicists an enhanced understanding of the rigors of operating a reactor. Thus the NCNR, now has not only more operators, it also has reactor engineers and health physicists who are more closely integrated into reactor operations, hopefully leading to more efficient designs and procedures.



**FIGURE 2:** New building leak test system. During a vacuum test air from the building is directed to the regenerative blower or during a pressure test the flow in the vertical pipe is reversed, while the flows through the other pipe segments remain the same. The building pressure is measured independently with a microprocessor controlled differential pressure transducer.

# Facility Developments 2020

## The *n*Soft Consortium 10m SANS Detector Upgrade

A 10 m SANS is the flagship instrument of the *n*Soft consortium, enabling measurement technique development and rapid access for industrial members. The current detector, a 0.65 m × 0.65 m manufactured by Ordela, has been in service for more than 20 years and is of an obsolete design and Ordela is now defunct. Thus, NIST is replacing it with a new detector which is an array of 1 m Reuter Stokes linear position sensitive tubes each with a diameter of 8 mm. The linear position sensitive tubes are arranged in “8-pack” modules yielding an effective spatial resolution of 8 mm × 6 mm and a sensitivity of 75% for 5 Å neutrons. Additionally, the new detector array is capable of time-stamping neutron events with nanosecond precision using the Precision Time Protocol (IEEE-1588).

The new detector was delivered in July 2020. To accommodate it, the carriage holding it within the SANS vessel is being redesigned along with the beam stop changer and the installation fixture. A compressed air supply line is being installed that will satisfy the more stringent cooling requirements. Parts manufacturing is well underway along with the hardware and software modifications required to operate the detector. The installation is projected to occur in April 2021.

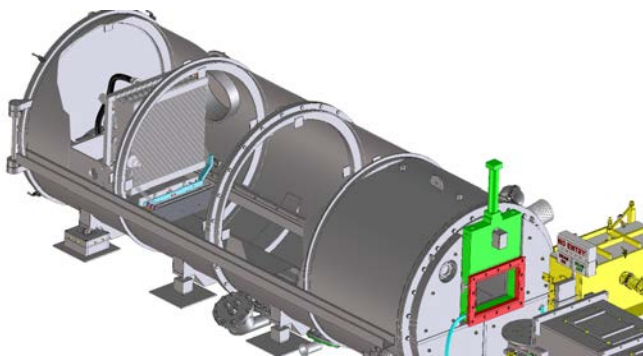


**FIGURE 1:** The 10 m SANS with new detector, carriage and beam stop installed.

## CANDOR Commissioning Update

The CANDOR reflectometer, which is currently being commissioned at the NIST Center for Neutron Research marries the advantages of time-of-flight polychromatic reflectometers, such as those commonly employed at pulsed neutron sources, to the high time-averaged flux of a reactor neutron source. The key component of this instrument is a multiplexed detector consisting of channels each containing 54 graphite crystals

which reflect neutrons of a particular wavelength onto an individual scintillator screen (described in more detail below). The calibration of this energy-dispersive detector system is crucial for reliable data reduction. This was accomplished using Bragg reflection from a pressed germanium single crystal. In Figure 2, each peak represents the response of one of the 54 detectors in a single detector channel as the incident neutron wavelength is swept from 4 Å to 6 Å. Significant efforts have also been made to minimize the background, which sets an absolute limit to the reflectivity that can be measured using the instrument. CANDOR has front-end polarization provided by a double-V cavity and RF flipper, both of which have been commissioned and are functioning well. Back-end polarization options include  $^3\text{He}$  for wide-beam mode and a supermirror in single-bank mode, both of which are awaiting final testing in early 2021. In addition, reduction software for the multiplexed CANDOR data stream was developed and implemented.

At the same angular resolution, CANDOR collects data about 20 times faster than the NCNR's current reflectometers. Figure 3 compares the performance of CANDOR to that of the Polarized Beam Reflectometer (PBR). The results of measurements are identical between the two instruments; however, CANDOR can reach much higher  $Q$ . Figure 4 demonstrates the ability of CANDOR to reach high  $Q$  ( $0.5 \text{ \AA}^{-1}$ ) with low background at both air/solid and liquid/solid interfaces. Due to this exceptional performance, CANDOR is accepting proposals for the first time in November 2020.

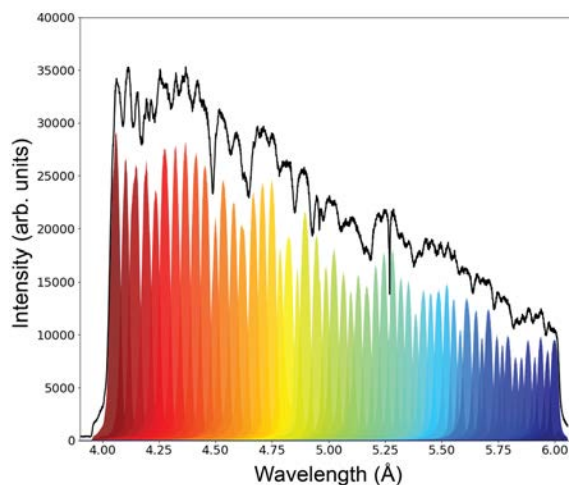


**FIGURE 2:** Wavelength response of the CANDOR detector. Each colored peak represents the response of a single CANDOR detector, while the solid line is the sum of the detector responses.



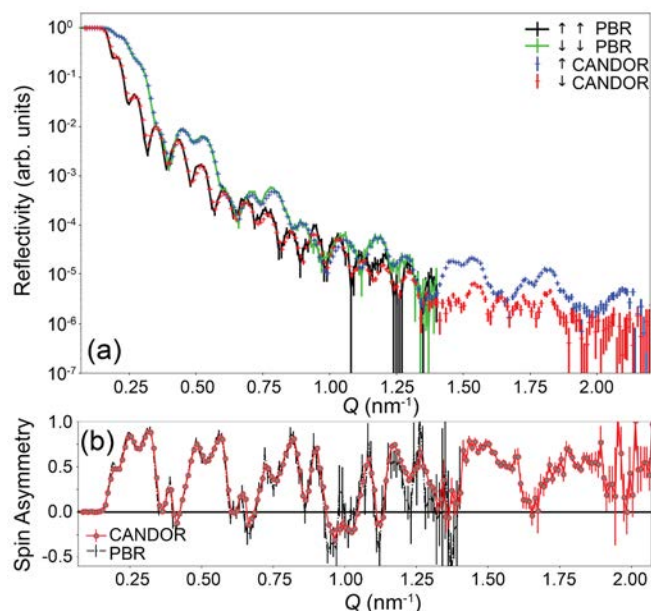


**FIGURE 3:** Demonstration of the polarized neutron reflectometry capabilities of CANDOR and comparison to the PBR instrument. Reflectivity is shown in (a) and the spin asymmetry in (b).

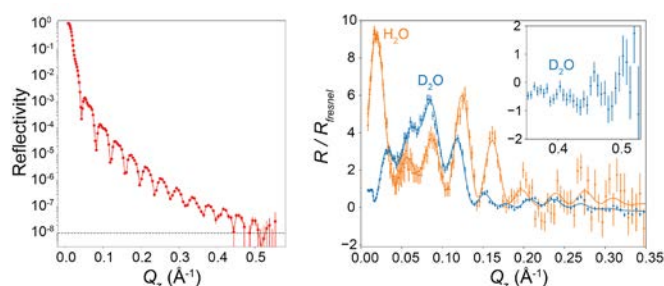


**FIGURE 4:** (Left) Unpolarized specular reflectivity from a platinum-coated silicon wafer showing the ability of CANDOR to resolve features to high  $Q$  and extremely low reflectivities as low as  $10^{-8}$ . (Right) Fresnel-normalized unpolarized specular reflectivity from a lipid bilayer tethered to a gold-coated silicon wafer in a flow cell filled with  $D_2O$  or  $H_2O$ . (Inset) Structure in the reflectivity can be resolved at high  $Q$ .

### CANDOR Data Acquisition Electronics and Firmware

The CANDOR detector bank consists of arrays of neutron sensitive tiles using  $LiFZnS(Ag)$  scintillator read out with wavelength shifting fibers and silicon photomultipliers. Central to the operation of these neutron sensors is the machinery to discriminate neutron events via real time pulse shape analysis. To meet this challenge, the NCNR developed a custom module for data acquisition that includes advanced pulse shape discrimination logic. CANDOR\_DQA is a low cost, 6-layer board design utilizing the ubiquitous USB interface for control and readout. This allows for virtually unlimited scalability, easily handling any future expansion of CANDOR detector system. Each board can handle 32 individual detector channels and process up to  $10^8$  neutron events per second when operating on a 5 Gbps (USB 3.1) link. When installed in a 20 card Eurocard crate, a system can serve 640 detectors and process 2 billion neutron events per second. The set of

front-end cards is managed by an application running on a lightweight Linux operating system. In addition to a custom protocol for readout by instrument control software, the management application sports a web interface for command and configuration. Updated firmware now includes additional code for mitigating silicon photomultiplier (SiPM) thermal noise effects, resulting in better gamma rejection ratio. The new firmware also better compensates for the CANDOR detector's long neutron fluorescence, resulting in shorter deadtimes for the detector.

### Data Acquisition Software

The New Instrument Control Environment (NICE) has been deployed to additional instruments at the NCNR. The CANDOR instrument is completed, and NICE is operating it full-time. NICE is currently in the testing phase on the thermal triple-axis instrument at BT7. Additional code necessary for full deployment on BT7 has been written, including all items required for full-time operations and new items discovered during the test deployment. Planning is underway for the future deployment of NICE on MACS.

### New Cold-Triple Axis Instrument Design Update

The cold triple axis spectrometer, SPINS, has operated continually on the NG-5 beam line for the last three decades. In that time, there have been dramatic developments in guide technology, multiplexed spectrometer analyzers, and numerical planning tools. The NCNR has recently finished an extensive redesign of the front-end relying heavily on Monte-Carlo simulations, aimed to optimize the flux at the sample position. The finalized front-end model for the new instrument consists of a doubly elliptic guide (Fig. 5) with mixed supermirror coating followed by a double focusing monochromator. Compared to the current rectangular  $^{58}Ni$  guide with a vertical (single) focusing monochromator, the new front-end will generate a factor of 7 increase in flux due to the improved optics compared to SPINS (Fig. 6).

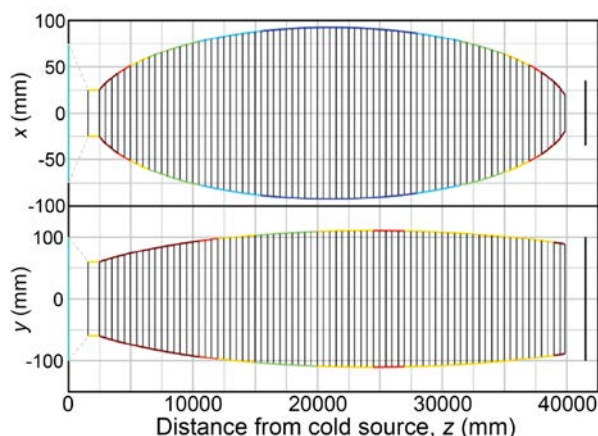


**FIGURE 5:** In-plane and out-of-plane cross-sectional cuts of the guide, vertical lines are individual guide segments. Guide wall color designates optimized  $m$  values (red:  $m = 4$ , blue:  $m = 1.5$ ).

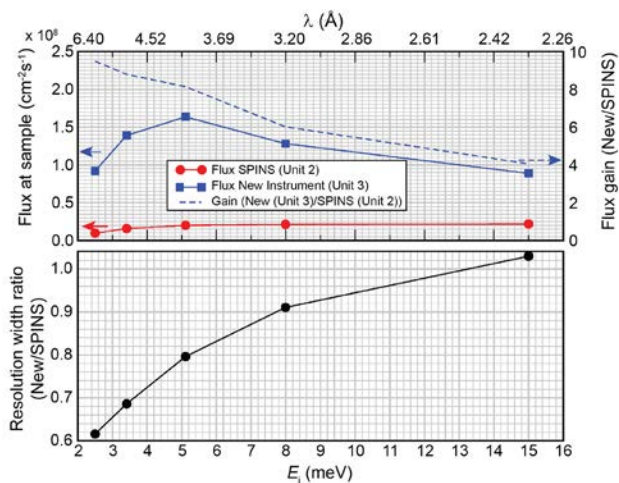


**FIGURE 6:** Expected performance of the replacement for SPINS with the new  $\text{D}_2$  cold source. The blue squares show that the neutron flux on the sample should exceed  $10^8 \text{ n/cm}^2\text{s}$ . The gain over the calculated flux for the current SPINS (red circles) is shown as a function of energy in the blue dashed line. The bottom figure shows that the energy resolution of the new instrument will be better than that of SPINS over most of the energy range.

The continuous elliptical shape optimized via Monte-Carlo was then segmented into half meter polygonal sections and the  $m$ -value varied along the length of the guide to match the changing divergence. This  $m$ -value refinement allowed us to cut the guide cost from \$4M to \$2.5M while still maintaining nearly identical flux. Design and award of guide element contracts began in FY2019 and except for two short sections, all of the guide has been ordered. The two remaining sections are those that may be interchange for a V-cavity polarizer and neutron velocity selector. The first half of the guide will be installed in 2023 while the second half will be installed along with the spectrometer in 2025-2026. The design for the sample table and analyzer portion of the spectrometer is underway but has not been finalized. Our current plan is to build a new SPINS-like multiplexed analyzer, with the PSD as the central detection device that will be fully modeled and optimized by Monte-Carlo. If resources permit, a high-performance analyzer system could be implemented adding an additional order-of-magnitude in detection capability to the new instrument.

### NG-A' Design

The future replacement of guide NG-5 for a new cold triple-axis spectrometer requires relocating the Neutron Depth Profiling (NDP) instrument and creating a new end-position on the cold neutron guide network to accommodate it. NG-A was chosen since the Neutron Spin Echo (NSE) instrument uses only the upper portion of the beam and offers space on the west side of the shielding that can easily accommodate the instrument. To deflect the lower portion of the beam sufficiently to provide clearance for NDP, we will install a bender in the lower portion of NG-A which extracts a 5 cm wide  $\times$  4 cm tall beam. The guide that transmits this beam to NDP is designated NG-A'.

NG-A is strongly curved upstream of the bender entrance, avoiding a direct line of sight to the source. This provides

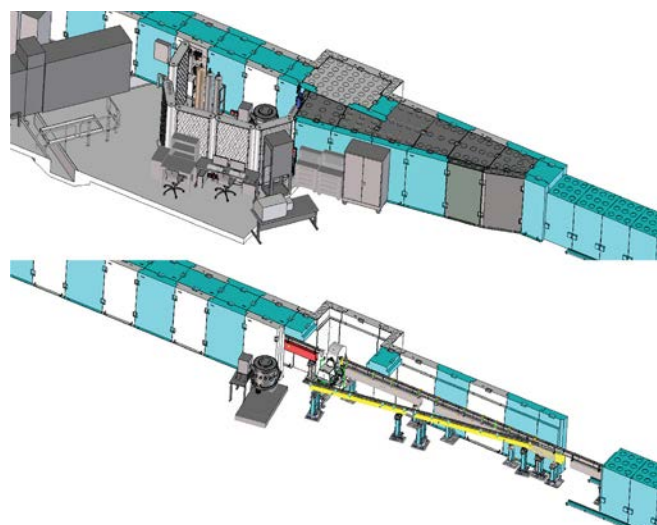


**FIGURE 7:** Upper figure: Illustration of the installed NDP instrument and user area on guide NG-A' with the new shielding. Lower figure: Cutaway showing the NG-A' guide layout and NDP sample chamber position. The guide feeding the NSE instrument and the NSE velocity selector are visible in the background.

a neutron beam largely free of fast neutrons and gamma rays. The bender is 0.8 m long with a radius of curvature of approximately 4.5 m and 23 ( $\approx 1.9 \text{ mm}$  wide) channels with  $m = 3.5$  and  $m = 1.5$  supermirror on the concave and convex surfaces respectively. The bender is followed by a 7 m long section of straight guide. The multiple channels and the ensuing straight section provide spatial uniformity of the beam and the 23 bender channels prove optimal for white beam intensity with 0.3 mm thick substrates (due to the tradeoff of reduced characteristic wavelength against reduced transmitting area and increased number of reflections). The installation of the bender means that approximately 6.4 m of the existing 5 cm(w)  $\times$  12 cm(h) guide preceding the NSE velocity selector will be replaced by 5 cm(w)  $\times$  7 cm(h) cross-section guide, matching that of the guide downstream of the velocity selector. This change has negligible impact on the performance of NSE.

Simulations predict that with the upgraded liquid deuterium cold source, the thermal-equivalent (capture) flux at the exit of NG-A' will be  $\approx 3.7 \times 10^9 \text{ cm}^{-2}\text{s}^{-1}$ , an increase of about 40% compared to that on NG-5. We will install NG-A' and the re-configured NG-A beam delivery systems in October 2020. NDP will then be moved from NG-5 to its new location on NG-A'. It will undergo testing and calibrations during the last reactor cycle of 2020 with the goal of hosting user experiments during the first reactor cycle of 2021.

### Progress on $\text{D}_2$ Cold Source

The extended reactor shutdown planned for 2023 will include the installation of the new  $\text{D}_2$  cold source and the upgrade of neutron guides 5, 6, and 7. Many of the neutron guides required for the outage have already arrived at the NCNR while the remainder of guides have been ordered and will be on-site by the Fall of 2021, well ahead of the 2023 shutdown. Detailed design of components including the new in-pile helium casings

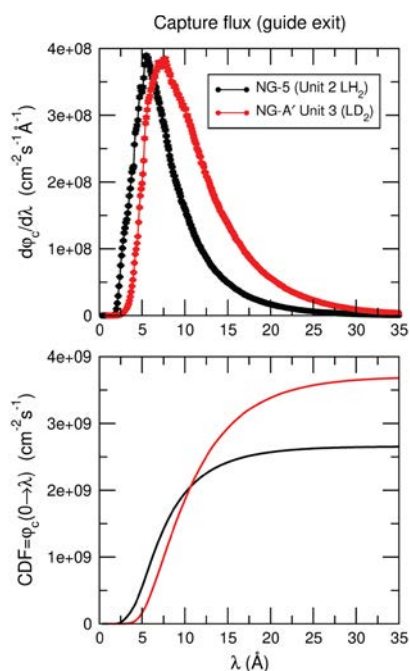


**FIGURE 8:** Simulations of the NDP guide performance comparing fluxes at the current NG-5 guide exit with the Unit 2 liquid hydrogen cold source (black curves) and those on NG-A' with the upgraded Unit 3 liquid deuterium cold source (red curves). The lower figure shows the cumulative distribution functions of the spectra in the upper figures.

for the reactor penetrations called “CTC” and “CTE” are complete and the CTC in-pile casing is already on site and is currently undergoing testing of the alignment mechanism. New shutters for guides 5, 6 and 7 are in development and the detailed design of the NG-7 shutter has recently been released for drafting. Finally, the four vacuum jackets that will house the neutron guides between the in-pile casing and shutters are also in various stages of development. Drafting of the downstream NG-5 vacuum jacket is in final stage and the detailed design is nearly complete of the upstream common casing and the downstream vacuum jacket for NG-6.

A tremendous amount of effort went into developing a comprehensive, resource loaded, project schedule yielding an aggressive, yet realistic plan to achieve an expected outage of less than 12 months. A detailed design of a mock-up assembly representing CTE, CTC, and CTW, along with the reactor bio-shield and features attached to the bio-shield face has been completed. Award of this assembly is expected by the end of the year and delivery expected in the second quarter of 2021. This design has been a collaboration between RFO and ROE as both groups will use the mock-up to practice disassembly of the current liquid H cold source and insertion of the D<sub>2</sub> cold source. Practice assembly on the mock-up is vital to identify potential interference problems and reducing radiation exposure (ALARA) during installation.

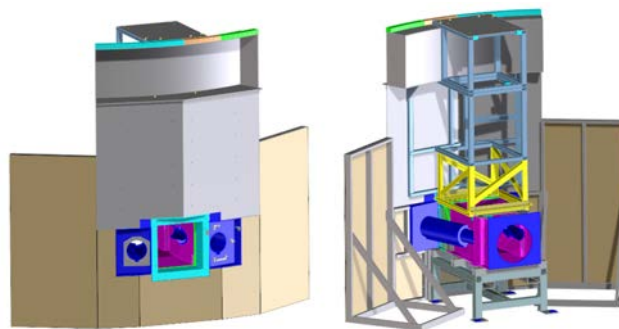


**FIGURE 9:** Mock-up of CTE, CTC, and CTW for practice installation of the new cold source.

## PGAA Secondary Flight Path Upgrade

The PGAA secondary beam flight path was recently upgraded to provide a second sample position increasing the scientific capacity of this instrument. Prior to the final installation, three custom tables tied together by a single tabletop and a fourth table tied into the main three via connecting plates were installed and precision leveled and aligned. During the shutdown, the flight tube sections, and main beam stop were installed. The flight path is made in two sections. The first is attached to the sample box and is under vacuum, and the second is a continuation of the flight path to minimize local scattering downstream and contains the main beam stop. Each section contains two cassette boxes holding collimation plates that can be switched out. The open section between the flight tubes is available for scientific use with either secondary detectors or other equipment. A secondary beam stop will also be positioned in this area, at the end of the first section, when no equipment is being used in this area.



**FIGURE 10:** New table installation at PGAA.



# Serving the Science and Technology Community

The mission of the NIST Center for Neutron Research is to assure the availability of neutron measurement capabilities to meet the needs of U.S. researchers from industry, academia and other U.S. government agencies. To carry out this mission, the NCNR uses several different mechanisms to work with participants from outside NIST, including a competitive proposal process, instrument partnerships, and collaborative research with NIST.

## Proposal System

Most of the beam time on NCNR instruments is made available through a competitive, peer-review CHRNS proposal process. The NCNR issues calls for proposals approximately twice a year. Proposals are reviewed at several different levels. First, expert external referees evaluate each proposal on merit and provide us with written comments and ratings. This is a very thorough process where several different referees review each proposal. Second, the proposals are evaluated on technical feasibility and safety by NCNR staff. Third, we convene our Beam Time Allocation Committee (BTAC) to assess the reviews and to allocate the available instrument time. Using the results of the external peer review and their own judgment, the BTAC makes recommendations to the NCNR Director on the amount of beam time to allocate to each approved experiment. Approved experiments are scheduled by NCNR staff members in consultation with the experimenters.

The current BTAC members are:

- Pinar Akcora (Stevens Institute of Technology)
- Andrew Allen (NIST Ceramics Division)
- Jeffrey Allen (Michigan Technological University)
- Collin Broholm (The Johns Hopkins University)
- Leslie Butler (Louisiana State University)
- Mark Dadmun (University of Tennessee)
- Thomas Epps (University of Delaware)
- Kushol Gupta (University of Pennsylvania)
- John Heron (University of Michigan)
- Hubert King (ExxonMobil)
- Valery Kiryukhin (Rutgers University)
- Ramanan Krishnamoorti (University of Houston)
- Jennifer Lee (National Institutes of Health)
- Kai Liu (Georgetown University)
- Martin Mourigal (Georgia Institute of Technology)
- James Neilson (Colorado State University)
- Lilo Pozzo (University of Washington)
- Stephen Wilson (University of California Santa Barbara)

## Partnerships

The NCNR may form partnerships with other institutions to fund the development and operation of selected instruments. Partnerships are negotiated for a fixed period and may be renewed if there is mutual interest and a continued need. These partnerships have proven to be an important and effective way to expand the research community's access to NCNR capabilities.

## Collaboration with NIST

Some time on all instruments is available to NIST staff in support of our mission. This time is used to work on NIST research needs, instrument development, and promoting the widespread use of neutron measurements in important research areas, particularly by new users. As a result of these objectives, a significant fraction of the time available to NIST staff is used collaboratively by external users, who often take the lead in the research. Access through such collaborations is managed through written beam time requests. In contrast to proposals, beam time requests are reviewed and approved internally by NCNR staff. We encourage users interested in exploring collaborative research opportunities to contact an appropriate NCNR staff member.

## Research Participation and Productivity

The NCNR continued its strong record of serving the U.S. research community this year. Over the 2020 reporting year, the NCNR served 3068 researchers. (Research participants include users who come to the NCNR to use the facility as well as active collaborators, including co-proposers of approved experiments, and co-authors of publications resulting from work performed at the NCNR.) As the number of participants has grown, the number of publications per year has also increased.

## 2020 NCNR Proposal Program

In response to the last two calls for proposals (calls 39 and 40) for instrument time, we received 869 proposals, of which 490 were approved and received beam time. The following table shows the statistics for several instrument classes. The oversubscription, *i.e.*, the ratio of days requested on all proposals to the days available, was 2.3 on average. Proposal demand has grown substantially since the NCNR first began accepting proposals in 1991.

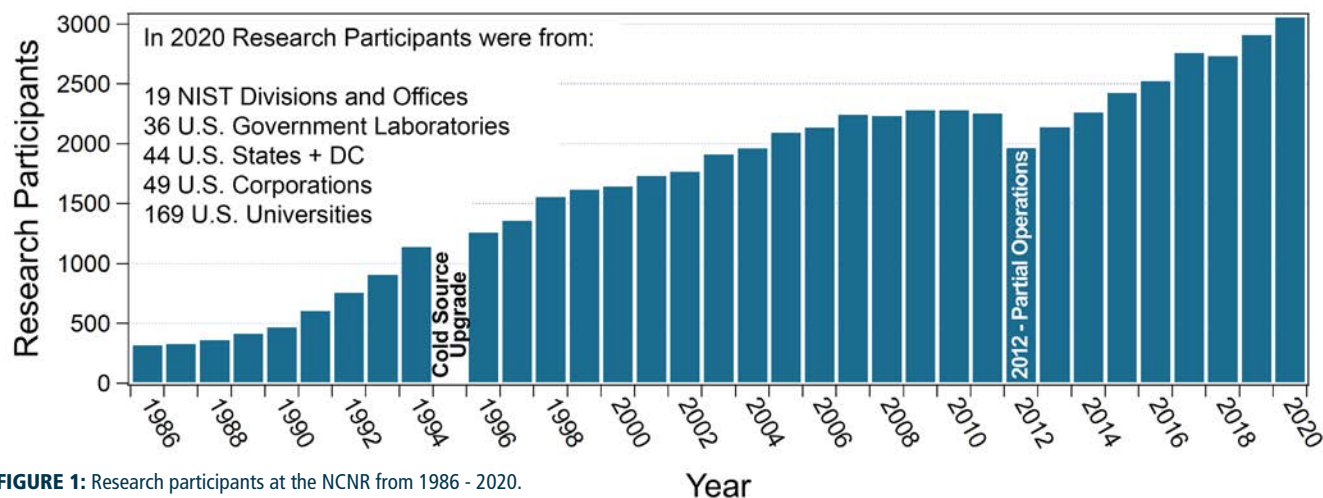


**FIGURE 1:** Research participants at the NCNR from 1986 - 2020.

Instrument class	Proposals	Days requested	Days allocated
SANS	337	1258	615
Reflectometers	116	771	360
Spectrometers	348	2263	900
Diffraction	32	119	66
Imaging	36	186	74
<b>Total</b>	<b>869</b>	<b>4579</b>	<b>2015</b>

### Users Group

The NCNR Users Group (NUG) provides an independent forum for all facility users to raise issues to NCNR management, working through its executive officers to carry out this function. All members of the Executive Committee (EC) are elected by NCNR users. The current members of the NUG Executive Committee are Carlos Lopez-Barron, (Chair, ExxonMobil), Brian Habersberger (The Dow Chemical Company), Michael Hore (Case Western University), Dmitry Reznik, (CHRS Liaison, University of Colorado), Samantha Rhinehart (Student/Postdoc Member, University of Tennessee), Stephen Wilson (University of California Santa Barbara), and Claire White (Princeton University).

The EC regularly solicits user feedback via a variety of means. The User Group held a well-attended meeting at the virtual American Conference on Neutron Scattering (ACNS) in July 2020 and plans to have another meeting at the ACNS in 2022. The EC also administers a brief email survey that is sent to users approximately one week after the completion of their experiment. Issues identified by the EC are regularly discussed with the NCNR and CHRS management teams with a focus on resolving those requiring immediate action. The EC also conducted a comprehensive user survey in the winter of 2020. There were more than 160 responses, the majority of whom are CHRS users. Compilation of the results is in progress. The results from the prior 2015 survey are posted on the NUG website (<https://ceem.indiana.edu/lens/nug/nug.php>). Working

closely with NUG, the NCNR and CHRS management teams developed a comprehensive response/action plan to the 2015 survey designed to make the user experience more productive and enjoyable (Refer to [https://ncnr.nist.gov/news/Response\\_to\\_survey\\_FINAL\\_19jul2016.pdf](https://ncnr.nist.gov/news/Response_to_survey_FINAL_19jul2016.pdf)).

### Panel of Assessment

The major organizational components of NIST are evaluated annually for quality and effectiveness by the National Research Council (NRC), the principal operating agency of both the National Academy of Sciences and the National Academy of Engineering. A panel appointed by the NRC convened at the NCNR on July 10 - 12, 2018. The panel members included Tom C. Lubensky (University of Pennsylvania, chair), Simon Billinge (Columbia University and Brookhaven National Laboratory), Susan Coppersmith (University of Wisconsin, Madison), Aaron Eberle (ExxonMobil Chemical Company), Paul Fleury (Yale University), Dale Klein (University of Texas), Tonya Kuhl (University of California, Davis), Peter Moore (Yale University) and Thomas Russell (University of Massachusetts, Amherst). Their report entitled "An Assessment of the National Institute of Standards and Technology Center for Neutron Research: Fiscal Year 2018" is available at <https://www.nap.edu/catalog/25282/an-assessment-of-the-center-for-neutron-research-at-the-national-institute-of-standards-and-technology>.

### The Center for High Resolution Neutron Scattering (CHRS)

CHRS is a national user facility that is jointly funded by the National Science Foundation and the NCNR. Its primary goal is to maximize access to state-of-the-art neutron scattering instrumentation for the research community. It operates five neutron scattering instruments at the NCNR, enabling users from around the nation to observe dynamical phenomena involving energies from  $\approx 30$  neV to  $\approx 10$  meV, and to obtain structural information on length scales from  $\approx 0.1$  nm to  $\approx 10$   $\mu$ m. A more detailed account of CHRS activities may be found on p. 63 of this report.

## Partnerships for Specific Instruments

### **NG-7 SANS Consortium**

A consortium that includes NIST, the ExxonMobil Research and Engineering Company, and the Industrial Partnership for Research in Interfacial and Materials Engineering (IPRIME) led by the University of Minnesota, operates, maintains, and conducts research at the 30m SANS instrument located on NG7. Twenty-five percent of the beam time on this instrument is allocated to the general scientific community through the NCNR's proposal system. Consortium members conduct independent research programs primarily in the area of large-scale structure in soft matter. For example, ExxonMobil has used this instrument to deepen their understanding of the underlying nature of ExxonMobil's products and processes, especially in the fields of polymers, complex fluids, and petroleum mixtures.

### **The nSoft Consortium**

Formed in August 2012, the nSoft Consortium allows member companies to participate with NIST in the development of advanced measurements of materials and manufacturing processes and develop their own expertise in state-of-the-art measurement technologies to include in their analytical research programs. nSoft develops new neutron-based measurement science for manufacturers of soft materials including plastics, composites, protein solutions, surfactants, and colloidal fluids. Members receive access to leading expertise and training support in neutron technology and soft materials science at NIST. Contact: Ron Jones, nSoft Director, [rljones@nist.gov](mailto:rljones@nist.gov), 301-975-4624.

### **NIST / General Motors – Neutron Imaging**

An ongoing partnership and collaboration between General Motors and NIST, which also includes Honda Motors

through GM's partnership with Honda, continues to yield exciting results using neutron imaging. Neutron imaging has been employed to visualize the operation of fuel cells for automotive vehicle applications. Neutron imaging is an ideal method for visualizing hydrogen, the fuel of electric vehicle engines. These unique, fundamental measurements provide valuable material characterizations that will help improve the performance, increase the reliability, and reduce the time to market introduction of the next generation electric car engines. 25% of the time on the BT-2 Neutron Imaging Facility is made available to the general scientific community through peer-reviewed proposals.

## Interagency Collaborations

The Smithsonian Institution's Nuclear Laboratory for Archaeological Research is part of the Anthropology Department at the National Museum of Natural History. It has had a longstanding and productive partnership with the NCNR, during which time it has chemically analyzed over 43,100 archaeological artifacts by Instrumental Neutron Activation Analysis (INAA), drawing extensively on the collections of the Smithsonian, as well as on those of many other institutions in this country and abroad. Such chemical analyses provide a means of linking these diverse collections together in order to study continuity and change involved in the production of ceramic and other artifacts.

The Center for Food Safety and Applied Nutrition, U.S. Food and Drug Administration (FDA), maintains laboratory facilities at the NCNR providing agency-wide analytical support for food safety and food defense programs. Neutron activation and low-level gamma-ray detection techniques yield multi-element and radiological information about foods and related materials and provide a metrological foundation for FDA's field investigations and for radiological emergency response planning.



# The Center for High Resolution Neutron Scattering (CHRNS)

The Center for High Resolution Neutron Scattering (<https://www.nist.gov/ncnr/chrns>) is a national user facility jointly funded by the National Science Foundation through its Division of Materials Research (grant number DMR-2010792) and by NIST. The primary purpose of this partnership is to maximize access for the scientific community to transformative neutron scattering instrumentation. The mission of CHRNS is fourfold: (i) to develop and operate neutron scattering instrumentation, with broad application in materials research, for use by the general scientific community; (ii) to promote the effective use of the CHRNS instruments by having an identifiable staff whose primary function is to assist users; (iii) to conduct research that advances the capabilities and utilization of CHRNS facilities; and (iv) to contribute to the development of human resources through educational and outreach efforts. A 2½ minute video, *Getting Great Data with CHRNS* ([https://ncnr.nist.gov/staff/dimeo/CHRNS\\_Animation\\_Final.mp4](https://ncnr.nist.gov/staff/dimeo/CHRNS_Animation_Final.mp4)), highlights and summarizes CHRNS' focus on advancing neutron scattering measurement capabilities and its prominent role in expanding, educating, and diversifying the community of researchers who use neutron methods.

The CHRNS agreement was renewed for five years beginning on September 1, 2020. The success of the proposal was based on the demonstrated ability of CHRNS to provide advanced neutron scattering measurement capabilities to the scientific community and its prominent role in expanding, educating, and diversifying the community of researchers who use neutron methods. As part of the new agreement, the portfolio of instruments supported by CHRNS will continue to evolve to ensure that the scientific capabilities exceed or are comparable to the best worldwide.

Over the next five years, CHRNS will pursue a new initiative that aims to provide the scientific community powerful new capabilities for studying the time evolution of the structure of materials subjected to external stimuli. Specifically, CHRNS will implement a systematic methodology for simultaneous time-stamping of instrument and sample environment data. Existing sample environments will be modified, and entirely new ones developed including stopped-flow mixing and electrochemistry experiments optimized for vSANS and CANDOR. Machine learning and AI procedures will be developed to aid in optimizing experiments and to provide real-time reporting of unexpected experimental conditions. Taken together, this program will significantly enhance the nation's capabilities for using neutrons to study the evolution of materials *in operando*,

under processing conditions, etc., such as the charge and discharge cycles of batteries, the non-equilibrium structures of complex fluids under shear, the kinetics of reactions, and the formation of biomolecular complexes.

The scientific community provides essential input for these new directions for CHRNS through a variety of mechanisms including post-experiment feedback and user surveys, the most recent of which was administered by the NCNR User Group Executive Committee (EC) in the winter of 2020. The EC also led a well-attended discussion for neutron users at the recent virtual American Conference on Neutron Scattering (ACNS) held on July 13-16, 2020. Users are also encouraged to provide input by directly contacting the CHRNS Director, Associate Director, NCNR Director, and/or members of the EC.

## Scattering Instruments

During 2020 CHRNS provided robust user operations for five premier neutron scattering instruments: a backscattering spectrometer (HFBS), the Multi-Axis Crystal Spectrometer (MACS), a neutron spin echo (NSE) spectrometer, an ultra-small angle neutron scattering instrument (uSANS), and a very small angle neutron scattering instrument (vSANS). In addition, CHRNS supported the commissioning activities associated with a new innovative white beam neutron reflectometer (CANDOR) with a unique multiplexing detector bank. uSANS, is being phased out of the CHRNS suite in the fall of 2020 as CANDOR completes its commissioning phase. Combined, CHRNS instruments can provide structural information on a length scale of 0.1 nm to  $\approx 10$  microns, and dynamical information on energy scales from  $\approx 30$  neV to  $\approx 10$  meV.

The unique strengths of these premier instruments are complementary by design. Specifically, HFBS can resolve motions with characteristic times of order a few nanoseconds. Since it offers the highest count rate with sub- $\mu$ eV resolution in the US, it is an ideal choice for high resolution, quasi-elastic scattering studies of low-energy dynamics in polymers and biomolecules.

MACS boasts the world's highest monochromatic cold-neutron flux and routinely is featured in transformative investigations of quantum magnetism. With its 20-detector analyzer array, MACS is well suited for surveys of large regions of reciprocal space, leveraging its exceptional polarized beam capabilities that incorporate a unique toroidal  $^3\text{He}$  spin filter. As part of the new initiative in the CHRNS renewal agreement, efforts

are underway to exploit fully the new event mode for data acquisition on MACS. Of note is the ABCD (Always Be Collecting Data) approach on MACS which involves continuous sweeping of various angles and recording the position each time a neutron is counted. Compared with step scanning, this approach will substantially increase the data rate, particularly for strongly scattering samples.

The NSE instrument provides the highest energy resolution of any neutron spectrometer in North America. It relies upon the Larmor precession of neutrons' magnetic moments as an internal "clock" attached to each neutron allowing measurements of the final polarization of the neutrons to be directly correlated with the speed of the neutron. This modality results in data being obtained in the time domain rather than in the frequency domain. Fourier times as long as 300 ns (roughly corresponding to an energy resolution of 0.01  $\mu\text{eV}$ ) have been achieved for investigations of slow diffusive processes in a range of soft materials notably including polymer nanocomposites, biomembranes, and biopharmaceuticals. A complete upgrade of the NSE is underway with funding received by the University of Delaware, in collaboration with NIST, from the NSF Mid-Scale Research Infrastructure program. The new primary coils and detector will increase the maximum Fourier time achievable at a given wavelength by  $> 2.5\times$  and reduce count times by as much as a factor of 10 for a given Fourier time.

For soft matter and magnetic structure characterization, the innovative vSANS instrument is meeting the emerging needs of the CHNRNS user community. vSANS has a variety of front-end optics choices including three choices of wavelength resolution in addition to the traditional velocity selector and slit collimation as well as the standard pinhole geometry. Three separate, adjustable detectors yield an extended  $Q$  range from  $0.002\text{ nm}^{-1}$  to  $7\text{ nm}^{-1}$  in a single instrument setting. The flexible sample area opens possibilities for sophisticated sample environments ranging from capillary rheometers to Peltier temperature blocks to superconducting magnets. The 45m instrument can also be readily configured for GISANS (Grazing Incidence Small Angle Neutron Scattering) experiments. All these features can be used with full polarization analysis. All these elements combined provide unprecedented possibilities not only for structural characterization of materials, but also for time-dependent studies of complex hierarchical structures.

A significant addition to the CHNRNS instrument suite is CANDOR, which will be included in the next Call for Proposals expected in the fall of 2020. The novelty of CANDOR lies in its use of a bank of state-of-the-art "energy-dispersive" detectors, which permits a polychromatic beam to impinge on the sample for measurements of either specular and non-specular reflectivity with or without polarized beams. A gain of  $\approx 20$  compared to the previous generation of neutron reflectometers in service at the NCNR has been realized, and reflectivities as low as  $10^{-8}$  have been measured. Data reduction is provided by *Reductus* which allows users to access and reduce their



**FIGURE 1:** CHNRNS scientist Hannah Burrall shows a  $^3\text{He}$  spin filter to CHNRNS users Rida Atif (left) and Priscilla Glaser (right) from Georgetown University while setting up their vSANS experiment.

data anywhere they have a web connection. This exceptional performance will enable unprecedented structural and kinetic characterization of complex materials from the nanoscale to the mesoscale.

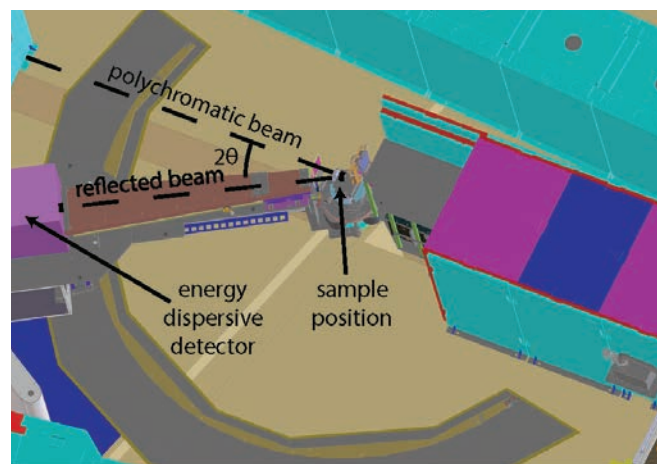


**FIGURE 2:** Engineering schematic of CANDOR and actual instrument in the winter of 2020.

## Research

The wide range of instrument capabilities available in CHRRNS support a very diverse scientific program, allowing researchers in materials science, chemistry, biology, geosciences, and condensed matter physics to investigate materials such as polymers, metals, ceramics, magnetic materials, colloids, fluids and gels, rocks, and biomaterials. The research community can obtain access to the state-of-the-art CHRRNS instrumentation using the NCNR's proposal system. Proposals to use the CHRRNS instruments are critically reviewed on the basis of scientific merit and/or technological importance and broader impacts. In the most recent Call for Proposals, 454 instrument-days were awarded of the 982 days requested on the CHRRNS instruments. Roughly half of the users of neutron scattering techniques at the NCNR use CHRRNS-funded instruments, and approximately one third of NCNR publications (see the "Publications" section on p. 71), are based at least in part on research performed using these instruments. This report contains several highlights of CHRRNS publications. See the labeled highlights in the table of contents.

## Scientific Support Services

CHRRNS provides scientific support in the critical areas of sample environment and chemical laboratories. The accomplishments in each of these areas during FY2020 are summarized below.

CHRRNS offers eight well-equipped and well-supplied user laboratories, including a Guide Hall Laboratory which provides a safe environment for CHRRNS users to handle activated samples. The laboratory staff continues to ensure that the required equipment and/or supplies are available for users for their experiments.

The CHRRNS sample environment staff provides CHRRNS users with the equipment and training needed to make neutron measurements under external conditions of temperature, pressure, magnetic field, humidity, and fluid flow. From mK dilution refrigeration systems to a 1600°C furnace, the equipment spans a large temperature range. Beyond precise temperature control, CHRRNS users have access to a variety of flow systems, rheometers, gas-loading systems, two superconducting magnets with fields of up to 11 Tesla, leak detectors, and other complex equipment to control parameters such as pressure, humidity, and electric fields. During FY2020 the team set up and operated a diverse range of complex sample environment equipment for more than 110 experiments on CHRRNS instruments. This total includes 9 experiments involving rheometers and shear cells, 2 capillary rheosans experiments, 10 pressure experiments, 10 electromagnet experiments including 8 of which made use of neutron polarization capabilities, 11 superconducting magnetic experiments, and 11 experiments that required access to mK temperatures, 7 of which simultaneously required magnetic fields up to 11.5 T.

Single crystal studies of quantum magnetism and lattice dynamics often require that measurements be made in

more than one reciprocal lattice plane. Because many of these studies are performed at low temperatures, the user must warm the sample to room temperature before it can be removed from the sample environment equipment and re-oriented. To nearly eliminate the time lost in this process, CHRRNS designed, constructed, and is commissioning a single crystal holder that provides two degrees of freedom for in-situ sample alignment. This holder provides good thermal conductivity between the sample and the mixing chamber of the dilution fridge, making it useful for many experiments on MACS. CHRRNS also refurbished the high temperature furnace for vSANS, which can now reach temperatures as high as 900 °C. In addition, cylindrical tailpieces capable of accommodating up to three samples have been constructed from single boules of silicon for use on closed-cycle refrigerators. Manufacturing these components from single crystals of silicon, in lieu of aluminum, substantially reduces the background from metallurgical scattering at low  $Q$ . When used with electromagnets, which provide magnetic fields both parallel and perpendicular to the beam, these tail sets allow users to rotate samples relative to the magnetic field. Finally, CHRRNS acquired a new Peltier block, which allows for more efficient temperature changes during vSANS experiments.

## Education and Outreach

CHRRNS sponsors a variety of educational programs and activities tailored to specific student groups and professions. One of the premier outreach activities is the annual neutron summer school for graduate students. The twenty-sixth annual summer school was originally scheduled for early June 2020 but will instead be held virtually in the fall of 2020. It will be entitled "Methods and Applications of Small Angle Neutron Scattering and Neutron Reflectivity." Planning is currently underway.

Since direct outreach has proven to be an effective means to attract users, CHRRNS pursues many avenues for engaging researchers from institutions that serve diverse groups. To that end a partnership with the Interdisciplinary Materials Research and Education Laboratory (IMREL) at Fayetteville State University (FSU) was established in August 2018 through the NSF PREM (Partnerships for Research and Education in Materials) program (Agreement No. DMR-1827731). The PREM supports cutting-edge materials research as the context for producing motivated and skilled members of those groups most underrepresented in materials research as future professional leaders. This partnership is organized around a common theme of structure-processing-property correlations of nanomaterials to support student training in research using neutron scattering. During FY2020 several CHRRNS scientists (Dan Neumann, Julie Borchers and Yun Liu) had the opportunity to visit IMREL to meet with all the PREM students and learn about their research. In summer 2019 CHRRNS staff members were also excited to host two PREM interns, one of whom (Washat Roxanne Ware) received the Best Poster Presentation Award for her PREM-based research at the Emerging Researchers National Conference on February 6-8, 2020. In a similar vein, CHRRNS is launching



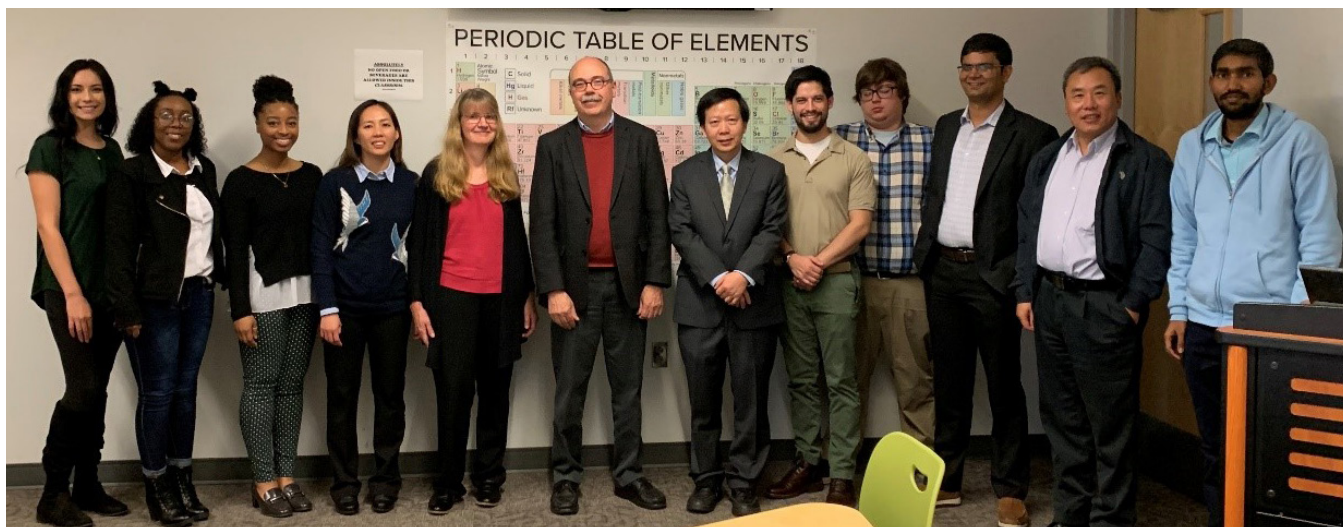


**FIGURE 3:** Visit of CHRNA scientists with PREM researchers at Fayetteville State University in October 2019

a partnership with California State University, San Bernardino within the NSF CREST (Centers of Research Excellence in Science and Technology) program as part of their new Phase II Center for Advanced Functional Materials (HRD-1914777).

CHRNA co-sponsored several workshops throughout the year including the fourth Fundamentals of Quantum Materials Winter school at the University of Maryland (January 6-9, 2020). Presenters from both the University of Delaware and from CHRNA were featured at Neutron Day – 2019, entitled “Solving Grand Challenge Problems in Science & Engineering with Neutrons,” held on October 20, 2019. A related highlight was the NSE Boot Camp organized by Prof. Norman Wagner in early April 2020, featuring CHRNA scientists as lecturers. Other outreach participants included Thomas Gnäupel-Herold who was a co-organizer of a virtual workshop on Stress Analysis held as part of the Annual Denver X-ray Conference on August 3-7, 2020.

CHRNA scientists also participated in teaching courses and giving lectures at nearby universities. In the spring of 2020, Yun Liu taught a graduate course entitled “Advanced Characterization of Soft Matter Materials” at the Material Science Engineering Department in the University of Maryland. The course covered the theories of neutron, x-ray and light scattering with applications in soft matter science.

As part of its expanding education and outreach effort, CHRNA allows university-based research groups with BTAC-approved experimental proposals to request travel support for an additional graduate student to participate in the experiment. This support is intended to enable new graduate students, for example, to acquire first-hand experience with a technique that they may later use in their own research. Announcements of this program are sent to all university groups whose experimental proposals receive beam time from the BTAC. Recipients of the announcement are encouraged to consider graduate students from under-represented groups for this opportunity. The program is also advertised on the NCNR’s

website at <https://www.nist.gov/ncnr/chrna/travel-support>. As a new initiative in the CHRNA renewal, this opportunity will be expanded to include a limited number of travel awards to enable graduate students or post-docs to attend workshops or related CHRNA-sponsored events, once travel to NIST is opened again to users.

Due to NIST-site access restrictions in the summer of 2020, CHRNA was unable to participate in NIST’s Summer Undergraduate Research Fellowship (SURF) program. Recent SURF participants, however, co-authored several significant publications. Mark Zic, a 2019 SURF student, obtained data critical to a publication in the journal *Science*, that announced the discovery of spin-triplet superconductivity in  $\text{UTe}_2$ . This article has already been cited more than 80 times. SURF participant Paul Neves made significant contributions to a related publication in *Nature Physics*, the results of which prompted the nickname of the effect as “Lazarus superconductivity.” These accomplishments, as well as Mr. Neves’ research on skyrmions, culminated in Goldwater Scholarships for both students, as well

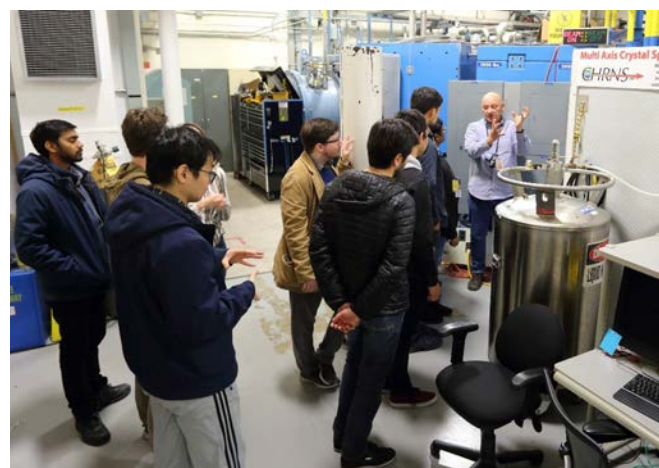


**FIGURE 4:** CHRNA Scientist, Jose Rodriguez, explains MACS to a student tour group Participants from the Fundamentals of Quantum Materials Winter school at the University of Maryland in January 2020.

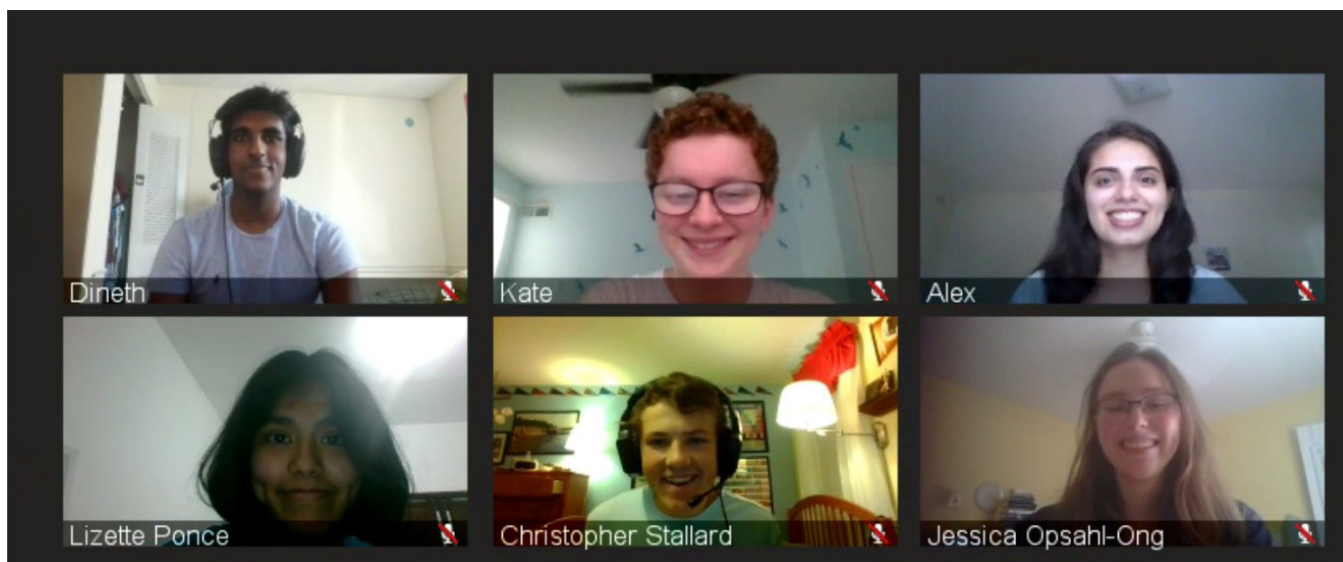


**FIGURE 6:** The 2020 CHNRNS High School Interns

as an NSF Graduate Research Fellowship for Mr. Zic. It is also notable that SURF students Zachary Reidel and Marshall Nakatani contributed to the development of capillary RheoSANS reported recently in *Soft Matter*.

CHNRNS initiated a Research Experiences for Teachers (RET) program in 2010. Unfortunately, CHNRNS was unable to host RET participants on-site during the summer of 2020 due to access restrictions. Based on work done in the summers of 2018 and 2019, Scott Hanna from Winston Churchill High School co-authored an article reporting DCS investigations of diffusion of quantum liquids in bulk and confinement. This is the first RET publication since the CHNRNS RET program was begun.

### Elementary, Middle, and High School Activities

In lieu of the NIST-wide Summer High-school Intern Program (SHIP) in the summer of 2020, CHNRNS remotely hosted six interns from local high schools. The students optimized algorithms for fitting order parameters through reinforcement learning, explored security benchmark implementations for Linux, supplemented an augmented reality training simulation program for the reactor operators, and developed an analysis program for prompt gamma activation spectra. The results of the students' summer investigations were highlighted at a virtual symposium in August.



**FIGURE 5:** Scott Hanna (center) from Winston Churchill High School with his 2019 mentors, Tim Prisk (right) and Richard Azuah (left), in front of DCS.

Many specialized tours and activities for high school and university students were offered throughout the year, including the CUWIP (Conferences for Undergraduate Women in Physics) tour in January, which was attended by 150 female STEM students. In typical years CHNRNS staff members also give science-based talks, participate in Career Days, or lead hands-on demonstrations at local schools, participate in STEM events, and even volunteer as robotics coaches.



# 2020 Awards



**Don Pierce** of the NCNR received the 2019 **NIST Distinguished Career Award** for 30 years of innovative engineering contributions to the design of world-leading neutron instruments and beam delivery systems. This award is granted to employees who made positive, lasting, long-term quality contributions to accomplishing NIST goals.



The NCNR's **Yun Liu** received the 2019 **Department of Commerce Silver Medal**. Yun was recognized for identifying the root cause of a major obstacle preventing the realization of the full potential of promising new monoclonal antibody therapies.



The NCNR's **Wei Zhou** received the 2019 **Samuel Wesley Stratton Award** for neutron measurements and modeling that reveal atomic interactions enabling simpler and cheaper methods of chemical separation and energy storage. Through this annual award, the Institute recognizes outstanding scientific or engineering achievements in support of NIST objectives



**Pieter Mumm** of NIST's Radiation Physics Division and colleagues were awarded the 2019 **Department of Commerce Silver Medal** for advancing nuclear reactor monitoring and nuclear nonproliferation by developing a novel, first-of-a-kind detector for measuring antineutrinos. The entire PROSPECT team also received a 2019 **Director's Science and Technology Award** from Lawrence Livermore National Laboratory for the first above ground detection of reactor anti-neutrinos.



**Muhammad Arif** (1954 – 2018) was inducted into the **NIST Portrait Gallery** for the creation and success of the neutron interferometry and neutron imaging programs at NIST.



The NCNR's **Yamali Hernandez** received an **NSSA Service Award** from the Neutron Scattering Society of America at the 2020 American Conference on Neutron Scattering in July 2020. Yamali was honored "for her contributions to neutron education and outreach, and development of user laboratories for the benefit of the neutron community."



**Sheng Ran** was awarded the 2020 **Lee Osheroff Richardson Science Prize**, presented by Oxford Instruments. Sheng was recognized for his research on unconventional superconductivity and electronic phases, particularly his seminal contributions to the discovery of exotic and extremely high-field re-entrant superconductivity in uranium ditelluride. Sheng was a post-doctoral researcher with the NCNR's Nick Butch and is currently an Assistant Professor of Physics at the Washington University in St. Louis.

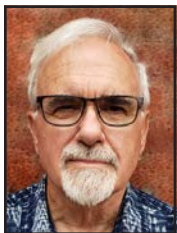


**Craig Brown** of the NCNR has been named a 2020 **NSSA Fellow** "For insightful neutron scattering studies of gas adsorption in metal organic frameworks and other microporous materials."



**Paul Butler** of the NCNR has been named a 2020 **NSSA Fellow** "For outstanding research on the chemistry and physics of complex fluids and biomembranes, and exceptional service to the neutron community, including major contributions to neutron scattering data acquisition and analysis."





**Ronald Bishop**, retired Curator of Mexican and Central American Archaeology at the Smithsonian National Museum of Natural History has been awarded the first ever **Anna O. Shepard Award**. This award is presented by the Art, Archaeology and Conservation Science Division of the American Ceramic Society, recognizing his "outstanding contributions to materials science applied to art, archaeology, architecture, or cultural heritage." Bishop has been a guest researcher at the NCNR since 1983, applying delayed gamma neutron activation analysis to archaeological ceramics, especially from the Maya region of southern Mexico, Guatemala, and Belize.



Prof. **Norm Wagner** from the University of Delaware was awarded the University's highest faculty honor, the 2020 **Francis Alison Award**. This award is bestowed on the faculty member who best characterizes "the scholar-schoolmaster" and recognizes Norm for his many achievements as an engineer, inventor, teacher, and mentor. Norm is and long-time user and associate of the NCNR.



**Thomas H. Epps, III** from the University of Delaware has been awarded the 2020 **Percy L. Julian Award**. This award is presented by the National Organization for the Professional Advancement of Black Chemists and Chemical Engineers (NOBCChE) for significant contributions in pure and/or applied research in science or engineering. Thomas is the Director of the Center for Research in Soft matter & Polymers and the Thomas and Kipp Gutshall Professor of Chemical & Biomolecular Engineering at the University of Delaware and is a frequent user of the NCNR.



**Mike Hore**, an Assistant Professor of Macromolecular Science and Engineering at Case Western University, and a former NCNR post-doc was recognized as a 2019 **Soft Matter Emerging Investigator** by the Journal Soft Matter, in recognition of his potential to influence future directions in the field of soft matter.



**Gary Koenig**, an Associate Professor at the University of Virginia in the Department of Chemical Engineering, was recognized as one of the 2020 **Molecular Systems Design & Engineering Emerging Investigators** for his research in lithium battery technology and his potential to influence future directions in the field. Gary is a frequent user of the neutron imaging facilities at the NCNR.



**Michael Nguyen** was awarded the **Biointerphases Award for Best Student Presentation** at the Biomembrane Symposium at the 257th ACS National Meeting & Exposition held in April 2019. Michael is a graduate student at the University of Windsor who has paid an extended visit at the NCNR.



**Washat Roxanne Ware**, a sophomore chemistry major at Fayetteville State University (FSU) and SURF student at the NCNR, received **first place for her undergraduate poster presentation** titled "Photophysics of Two-Dimensional Organic Inorganic Perovskites". She presented her work at the Emerging Researchers National Conference in Science, Technology, Engineering and Mathematics in February 2020. FSU and CHRNS cooperate in a Partnership for Research and Education in Materials (PREM) to support cutting-edge research that promotes involvement of minorities and female students.



**Mark Zic**, an undergraduate at the University of Maryland's Quantum Materials Center, has received a **National Science Foundation Graduate Research Fellowship**. These fellowships recognize outstanding graduate students in science, technology engineering, and mathematics. Mark is a former NCNR SURF student and was a research intern with the NCNR's Nick Butch.



**Nairiti Sinha** was awarded the **best online presentation** in the oral presentation category for the POLY/PMSE Excellence in Graduate Polymer Research Symposium at the 2020 American Chemical Society Spring National Meeting. Nairiti was a graduate student in the Materials Science and Engineering Department at the University of Delaware who was stationed at the NCNR.



Prof. **Thomas P. Russell**, the Silvio O. Conte Distinguished Professor of Polymer Science and Engineering at the University of Massachusetts at Amherst is the recipient of the 2020 **Clifford G. Shull Prize** of the Neutron Scattering Society of America (NSSA) in recognition of "his pivotal role in the application of neutron reflectivity and small angle neutron scattering to polymer science and his important work on behalf of the neutron scattering community." Tom is a long-time user of the NCNR



Prof. **Timothy P. Lodge**, Regents Professor of Chemical Engineering and Materials Science at the University of Minnesota (and a long-time user of the NCNR) is the recipient of the 2020 **Sustained Research Prize** of the Neutron Scattering Society of America (NSSA) "for his pivotal contributions to the fundamental understanding of polymer structure, thermodynamics, and dynamics through the use of small angle neutron scattering."



**Matthew E. Helgeson**, Associate Professor of Chemical Engineering at the University of California, Santa Barbara is the recipient of the 2020 **Science Prize** of the Neutron Scattering Society of America (NSSA) "For his development and use of neutron scattering methods with application to non-equilibrium thermodynamics and rheology of complex fluids and soft materials." Matt has been a user of the NCNR since he was a graduate student.



**Johnny Ching-Wei Lee**, a graduate student at the University of Illinois at Urbana Champaign is the recipient of the 2020 Prize for **Outstanding Student Research** of the Neutron Scattering Society of America (NSSA) with the citation: "For seminal neutron scattering experiments forming time-resolved structure-property-processing relations of polymeric materials." Most of his award-winning neutron scattering results were obtained at the NCNR.

# Publications: August 1, 2019 to July 31, 2020

- Adamek, E.R., Dewey, M.S., Fomin, N., Gilliam, D.M., Greene, G.L., Hoogerheide, S.F., Mumm, H.P., Nico, J.S., Snow, W.M., "Precision Neutron Flux Measurement using the Alpha-Gamma Device," EPJ Web Conf. **219**, 10004 (2019).
- Ade-Browne, C., Mirzamani, M., Dawn, A., Qian, S., Thompson, R.G., Glenn, R.W., Kumari, H., "Effect of Ethoxylation and Lauryl Alcohol on the Self-Assembly of Sodium Laurylsulfate: Significant Structural and Rheological Transformation," Colloid Surface. A **595**, 124704 (2020).
- Agrawal, N.R., Yue, X., Feng, Y., Raghavan, S.R., "Wormlike Micelles of a Cationic Surfactant in Polar Organic Solvents: Extending Surfactant Self-Assembly to New Systems and Subzero Temperatures," Langmuir **35**(39), 12782 (2019). [CHNRNS]
- Alam, K., Meng, K.-Y., Ponce-Pérez, R., Cocolletzi, G.H., Takeuchi, N., Foley, A., Yang, F., Smith, A.R., "Exchange Bias and Exchange Spring Effects in Fe/CrN Bilayers," J. Phys. D Appl. Phys. **53**(12), 125001 (2020).
- Andersson, M.S., Grinderslev, J.B., Jensen, T.R., García Sakai, V., Häussermann, U., Udovic, T.J., Karlsson, M., "Interplay of  $\text{NH}_4^+$  and  $\text{BH}_4^-$  Reorientational Dynamics in  $\text{NH}_4\text{BH}_4$ ," Phys. Rev. Mater., in press.
- Arenas-Gómez, B., Garza, C., Liu, Y., Castillo, R., "Alignment of Worm-Like Micelles at Intermediate and High Shear Rates," J. Colloid Interf. Sci. **560**, 618 (2020). [CHNRNS]
- Asgari, M., Semino, R., Schouwink, P.A., Kochetygov, I., Tarver, J., Trukhina, O., Krishna, R., Brown, C.M., Ceriotti, M., Queen, W.L., "Understanding How Ligand Functionalization Influences  $\text{CO}_2$  and  $\text{N}_2$  Adsorption in a Sodalite Metal-Organic Framework," Chem. Mater. **32**(4), 1526 (2020).
- Ashenfelter, J., Balantekin, A.B., Band, H.R., Bass, C.D., Bergeron, D.E., Berish, D., Bowden, N.S., Brodsky, J.P., Bryan, C.D., Cherwinka, J.J., Classen, T., Conant, A.J., Dean, D., Deichert, G., Diwan, M.V., Dolinski, M.J., Erickson, A., Febbraro, M., Foust, B.T., Gaison, J.K., Galindo-Uribarri, A., Gilbert, C.E., Hackett, B.T., Hans, S., Hansell, A.B., Heeger, K.M., Insler, J., Jaffe, D.E., Jones, D.C., Kyzlyova, O., Lane, C.E., Langford, T.J., LaRosa, J., Littlejohn, B.R., Lu, X., Martinez Caicedo, D.A., Matta, J.T., McKeown, R.D., Mendenhall, M.P., Mueller, P.E., Mumm, H.P., Napolitano, J., Neilson, R., Nikkel, J.A., Norcini, D., Nour, S., Pushin, D.A., Qian, X., Romero-Romero, E., Rosero, R., Sarenac, D., Surukuchi, P.T., Telles, A.B., Tyra, M.A., Varner, R.L., Viren, B., White, C., Wilhelmi, J., Wise, T., Yeh, M., Yen, Y.-R., Zhang, A., Zhang, C., Zhang, X., "The Radioactive Source Calibration System of the PROSPECT Reactor Antineutrino Detector," Nucl. Instrum. Meth. A **944**, 162465 (2019).
- Ashkar, R., "Selective Dynamics in Polymeric Materials: Insights from Quasi-Elastic Neutron Scattering Spectroscopy," J. Appl. Phys. **127**(15), 151101 (2020). [CHNRNS]
- Astete, C.E., De Mel, J.U., Gupta, S., Noh, Y., Bleuel, M., Schneider, G.J., Sabliov, C.M., "Lignin-Graft-Poly(Lactic-co-Glycolic) Acid Biopolymers for Polymeric Nanoparticle Synthesis," ACS Omega, in press.
- Babu, S.K., Spornjak, D., Mukundan, R., Hussey, D.S., Jacobson, D.L., Chung, H.T., Wu, G., Steinbach, A.J., Litster, S., Borup, R.L., Zelenay, P., "Understanding Water Management in Platinum Group Metal-Free Electrodes using Neutron Imaging," J. Power Sources, in press.
- Bakker, J.H., Washington, A.L., Parnell, S.R., van Well, A.A., Pappas, C., Bouwman, W.G., "Analysis of SESANS Data by Numerical Hankel Transform Implementation in Sas View," J. Neutron Res. **22**(1), 57 (2020). [CHNRNS]



- Balantekin, A.B., Band, H.R., Bass, C.D., Bergeron, D.E., Berish, D., Bowden, N.S., Brodsky, J.P., Bryan, C.D., Classen, T., Conant, A.J., Deichert, G., Diwan, M.V., Dolinski, M.J., Erickson, A., Foust, B.T., Gaison, J.K., Galindo-Uribarri, A., Gilbert, C.E., Hackett, B.T., Hans, S., Hansell, A.B., Heeger, K.M., Heffron, B., Jaffe, D.E., Ji, X., Jones, D.C., Kyzlyova, O., Lane, C.E., Langford, T.J., LaRosa, J., Littlejohn, B.R., Lu, X., Maricic, J., Mendenhall, M.P., Milincic, R., Mitchell, I., Mueller, P.E., Mumm, H.P., Napolitano, J., Neilson, R., Nikkel, J.A., Norcini, D., Nour, S., Palomino-Gallo, J.L., Pushin, D.A., Qian, X., Romero-Romero, E., Rosero, R., Surukuchi, P.T., Tyra, M.A., Varner, R.L., White, C., Wilhelmi, J., Woolverton, A., Yeh, M., Zhang, A., Zhang, C., Zhang, X., "Nonfuel Antineutrino Contributions in the ORNL High Flux Isotope Reactor (HFIR)," *Phys. Rev. C* **101**(5), 054605 (2020).
- Barry, K., Zhang, B., Anand, N., Xin, Y., Vailionis, A., Neu, J., Heikes, C., Cochran, C., Zhou, H., Qiu, Y., Ratcliff, W., Siegrist, T., Beekman, C., "Modification of Spin-Ice Physics in  $\text{Ho}_2\text{Ti}_2\text{O}_7$  Thin Films," *Phys. Rev. Mater.* **3**(8), 084412 (2019). [CHNRNS]
- Bauer, J.J., Rosenberg, E.R., Kundu, S., Mkhoyan, K.A., Quarterman, P., Grutter, A.J., Kirby, B.J., Borchers, J.A., Ross, C.A., "Dysprosium Iron Garnet Thin Films with Perpendicular Magnetic Anisotropy on Silicon," *Adv. Electron. Mater.* **6**(1), 1900820 (2020).
- Bellur, K., Médiçi, E.F., Choi, C.K., Hermanson, J.C., Allen, J.S., "Multiscale Approach to Model Steady Meniscus Evaporation in a Wetting Fluid," *Phys. Rev. Fluids* **5**(2), 024001 (2020).
- Beltran-Villegas, D.J., Wessels, M.G., Lee, J.Y., Song, Y., Wooley, K.L., Pochan, D.J., Jayaraman, A., "Computational Reverse-Engineering Analysis for Scattering Experiments on Amphiphilic Block Polymer Solutions," *J. Am. Chem. Soc.* **141**(37), 14916 (2019). [CHNRNS]
- Bergeron, D.E., Mumm, H.P., Tyra, M.A., La Rosa, J., Nour, S., Langford, T.J., "Optimum Lithium Loading of a Liquid Scintillator for Neutron and Neutrino Detection," *Nucl. Instrum. Meth. A* **953**, 163126 (2020).
- Bernardo, G., Gaspar, H., Pérez, G.E., Shackleford, A.S.D., Parnell, A.J., Bleuel, M., Mendes, A., King, S.M., Parnell, S.R., "Impact of 1,8-Diiodooctane on the Morphology of Organic Photovoltaic (OPV) Devices - A Small Angle Neutron Scattering (SANS) Study," *Polym. Test.* **82**, 106305 (2020).
- Bharati, A., Hudson, S.D., Weigandt, K.M., "Poiseuille and Extensional Flow Small-Angle Scattering for Developing Structure-Rheology Relationships in Soft Matter Systems," *Curr. Opin. Colloid In.* **42**, 137 (2019).
- Black, D.R., Mendenhall, M.H., Brown, C.M., Henins, A., Filliben, J., Cline, J.P., "Certification of Standard Reference Material 660c for Powder Diffraction," *Powder Diff.* **35**(1), 17 (2020).
- Book, A., Kienzle, P.A., "Retrieval of the Complex Reflection Coefficient below the Critical Edge for Neutron Reflectometry," *Physica B* **588**, 412181 (2020).
- Boota, M., Urbankowski, P., Porzio, W., Barba, L., Osti, N.C., Bleuel, M., Keum, J.K., Mamontov, E., "Understanding Functionalization of Titanium Carbide (MXene) with Quinones and their Pseudocapacitance," *ACS Appl. Energy Mater.* **3**(5), 4127 (2020). [CHNRNS]
- Bordelon, M.M., Kenney, E., Liu, C., Hogan, T., Posthuma, L., Kavand, M., Lyu, Y., Sherwin, M., Butch, N.P., Brown, C., Graf, M.J., Balents, L., Wilson, S.D., "Field-Tunable Quantum Disordered Ground State in the Triangular-Lattice Antiferromagnet  $\text{NaYbO}_2$ ," *Nat. Phys.* **15**(10), 1058 (2019).
- Bordelon, M.M., Liu, C., Posthuma, L., Sarte, P.M., Butch, N.P., Pajeroski, D.M., Banerjee, A., Balents, L., Wilson, S.D., "Spin Excitations in the Frustrated Triangular Lattice Antiferromagnet  $\text{NaYbO}_2$ ," *Phys. Rev. B* **101**(22), 224427 (2020).
- Boughton, A.J., Krueger, S., Fushman, D., "Branching via K11 and K48 Bestows Ubiquitin Chains with a Unique Interdomain Interface and Enhanced Affinity for Proteasomal Subunit Rpn1," *Structure* **28**(1), 29 (2020). [CHNRNS]
- Bowerman, S., Curtis, J.E., Clayton, J., Brookes, E.H., Wereszczynski, J., "BEES: Bayesian Ensemble Estimation from SAS," *Biophys. J.* **117**(3), 399 (2019).
- Brubaker, Z.E., Ran, S., Said, A.H., Manley, M.E., Söderlind, P., Rosas, D., Idell, Y., Zieve, R.J., Butch, N.P., Jeffries, J.R., "Phonon Dispersion of Mo-Stabilized  $\gamma$ -U Measured using Inelastic X-ray Scattering," *Phys. Rev. B* **100**(9), 094311 (2019).
- Brubaker, Z.E., Xiao, Y., Chow, P., Kenney-Benson, C., Smith, J.S., Cynn, H., Reynolds, C., Butch, N.P., Zieve, R.J., Jeffries, J.R., "Valence Instability across the Magnetostructural Transition in  $\text{USb}_2$ ," *Phys. Rev. B* **101**(8), 085123 (2020).
- Butch, N.P., Rodriguez-Rivera, J.A., Maple, M.B., "Ungapped Magnetic Excitations beyond Hidden Order in  $\text{URu}_{2-x}\text{Re}_x\text{Si}_2$ ," *Philos. Mag.* **100**(10), 1282 (2020). [CHNRNS]
- Byrne, J., Worcester, D.L., "The Neutron Lifetime Anomaly and Charge Exchange Collisions of Trapped Protons," *J. Phys. G Nucl. Partic.* **46**(8), 085001 (2019).

- Campanella, A.J., Trump, B.A., Gosselin, E.J., Bloch, E.D., Brown, C.M., "Neutron Diffraction Structural Study of CO<sub>2</sub> Binding in Mixed-Metal CPM-200 Metal-Organic Frameworks," *Chem. Commun.* **56**(17), 2574 (2020).
- Carlton, H., Krycka, K., Bleuel, M., Huitink, D., "In Situ Dimensional Characterization of Magnetic Nanoparticle Clusters during Induction Heating," *Part. Part. Syst. Char.* **37**(1), 1900358 (2020). [CHRS]
- Chakraborty, S., Ding, J., Thies, M.C., Kitchens, C.L., "More Elongated Solution Structures in Lignin Precursors Improve Properties of Resultant Carbon Fibers," *ACS Appl. Polym. Mater.* **1**(10), 2561 (2019). [CHRS]
- Chakraborty, S., Kitchens, C.L., "Modifying Ligand Chemistry to Enhance Reusability of pH-Responsive Colloidal Gold Nanoparticle Catalyst," *J. Phys. Chem. C* **123**(43), 26450 (2019). [CHRS]
- Chan, E.P., Frieberg, B.R., Ito, K., Tarver, J., Tyagi, M., Zhang, W., Coughlin, E.B., Stafford, C.M., Roy, A., Rosenberg, S., Soles, C.L., "Insights into the Water Transport Mechanism in Polymeric Membranes from Neutron Scattering," *Macromolecules* **53**(4), 1443 (2020). [CHRS]
- Chapagain, K., Brown, D.E., Kolesnik, S., Lapidus, S., Haberl, B., Molaison, J., Lin, C., Kenney-Benson, C., Park, C., Pietosa, J., Markiewicz, E., Andrzejewski, B., Lynn, J.W., Rosenkranz, S., Dabrowski, B., Chmaissem, O., "Tunable Multiferroic Order Parameters in Sr<sub>1-x</sub>BaxMn<sub>1-y</sub>Ti<sub>y</sub>O<sub>3</sub>," *Phys. Rev. Mater.* **3**(8), 084401 (2019).
- Chattrakun, K., Hoogerheide, D.P., Mao, C., Randall, L.L., King, G.M., "Protein Translocation Activity in Surface-Supported Lipid Bilayers," *Langmuir* **35**(37), 12246 (2019).
- Chaturvedi, V., Walter, J., Paul, A., Grutter, A., Kirby, B., Jeong, J.S., Zhou, H., Zhang, Z., Yu, B., Greven, M., Mkhoyan, K.A., Birol, T., Leighton, C., "Strain-Induced Majority Carrier Inversion in Ferromagnetic Epitaxial LaCoO<sub>3-δ</sub> Thin Films," *Phys. Rev. Mater.* **4**(3), 034403 (2020).
- Chen, S.-H., Corsaro, C., Mallamace, F., Fazio, E., Mallamace, D., "The Proton Density of States in Confined Water (H<sub>2</sub>O)," *Int. J. Mol. Sci.* **20**(21), 5373 (2019).
- Chen, T., Chen, Y., Tam, D.W., Gao, B., Qiu, Y., Schneidewind, A., Radelytskyi, I., Prokes, K., Chi, S., Matsuda, M., Broholm, C., Dai, P., "Anisotropic Effect of a Magnetic Field on the Neutron Spin Resonance in FeSe," *Phys. Rev. B* **101**(14), 140504(R) (2020). [CHRS]
- Chen, Y., Dahal, A., Rodriguez-Rivera, J.A., Xu, G., Heitmann, T.W., Dugaev, V., Ernst, A., Singh, D.K., "Perovskite Magnet with Quantum Mechanical Glassiness," *Mater. Today Phys.* **12**, 100163 (2020). [CHRS]
- Chen, Y., Gaudet, J., Dasgupta, S., Marcus, G.G., Lin, J., Chen, T., Tomita, T., Ikhlas, M., Zhao, Y., Chen, W.C., Stone, M.B., Tchernyshyov, O., Nakatsuji, S., Broholm, C., "Antichiral Spin Order, its Soft Modes, and their Hybridization with Phonons in the Topological Semimetal Mn<sub>3</sub>Ge," *Phys. Rev. B*, in press.
- Chen, Y., Chuang, Y.-W., Lee, S.H., Zhu, Y., Honz, K., Guan, Y., Wang, Y., Wang, K., Mao, Z., Zhu, J., Heikes, C., Quarterman, P., Zajdel, P., Borchers, J.A., Ratcliff, II, W., "Ferromagnetism in van der Waals Compound MnSb<sub>1.8</sub>Bi<sub>0.2</sub>Te<sub>4</sub>," *Phys. Rev. Mater.* **4**(6), 064411 (2020).
- Chen, Y., Yumnam, G., Dahal, A., Rodriguez-Rivera, J.A., Xu, G., Heitmann, T.W., Singh, D.K., "Magnetic Order and Instability in Newly Synthesized CoSeAs Marcasite," *Phys. Rev. Res.* **2**(2), 023168 (2020). [CHRS]
- Chen, Y., Jeong, C., Savelyev, A., Krueger, S., Curtis, J.E., Brookes, E.H., Fushman, D., "ROTDIF-Web and ALTENS: GenApp-Based Science Gateways for Biomolecular Nuclear Magnetic Resonance (NMR) Data Analysis and Structure Modeling," in "Gateways 2019 Proceedings," <https://doi.org/10.17605/OSF.IO/T4GKH> (Sept. 23, 2019, San Diego, CA) (2019).
- Chen, Z., Li, P., Anderson, R., Wang, X., Zhang, X., Robison, L., Redfern, L.R., Moribe, S., Islamoglu, T., Gómez-Gualdrón, D.A., Yildirim, T., Stoddart, J.F., Farha, O.K., "Balancing Volumetric and Gravimetric Uptake in Highly Porous Materials for Clean Energy," *Science* **368**(6488), 297 (2020).
- Chen-Mayer, H.H., Brown, S., Yang, H., "Feasibility Study of Compton Imaging for PGAA," *J. Radioanal. Nucl. Ch.* **322**(3), 1729 (2019).
- Chillal, S., Iqbal, Y., Jeschke, H.O., Rodriguez-Rivera, J.A., Bewley, R., Manuel, P., Khalyavin, D., Steffens, P., Thomale, R., Nazmul Islam, A.T.M., Reuther, J., Lake, B., "Evidence for a Three-Dimensional Quantum Spin Liquid in PbCuTe<sub>2</sub>O<sub>6</sub>," *Nat. Commun.* **11**(1), 2348 (2020). [CHRS]
- Cho, H., Dasari, K.B., Jaćimović, R., Zeisler, R., Sharp, N.E., Kim, S.-H., Sun, G.M., Yim, Y.-H., "Application of the INAA Methods for KRISS Infant Formula CRM Analysis: Standardization of INAA at KRISS," *J. Radioanal. Nucl. Ch.* **322**(3), 1537 (2019).
- Chremos, A., Horkay, F., "Comparison of Neutral and Charged Polyelectrolyte Bottlebrush Polymers in Dilute Salt-Free Conditions," *MRS Adv.* **5**(17), 899 (2020).
- Chremos, A., Horkay, F., "Disappearance of the Polyelectrolyte Peak in Salt-Free Solutions," *Phys. Rev. E* **102**(1), 012611 (2020).

- Christovam, D.S., Giles, C., Mendonça-Ferreira, L., Leão, J., Ratcliff, W., Lynn, J.W., Ramos, S., Hering, E.N., Hidaka, H., Baggio-Saitovich, E., Fisk, Z., Pagliuso, P.G., Adriano, C., "Spin Rotation Induced by Applied Pressure in the Cd-Doped  $\text{Ce}_2\text{RhIn}_8$  Intermetallic Compound," *Phys. Rev. B* **100**(16), 165133 (2019).
- Chu, S., Lin, K., Yang, T., Yu, C., Cao, Y., Zhang, Y., Sun, Y., Li, Z., Jiang, X., Lin, Z., Li, Q., Chen, J., Kato, K., Wu, H., Huang, Q., Xing, X., "Large Nonlinear Optical Effect in Tungsten Bronze Structures via Li/Na Cross-Substitutions," *Chem. Commun.*, in press.
- Colman, R.H., Okur, H.E., Kockelmann, W., Brown, C.M., Sans, A., Felser, C., Jansen, M., Prassides, K., "Elusive Valence Transition in Mixed-Valence Sesquioxide  $\text{Cs}_4\text{O}_6$ ," *Inorg. Chem.* **58**(21), 14532 (2019).
- Comert, F., Greenwood, A., Maramba, J., Acevedo, R., Lucas, L., Kulasinghe, T., Cairns, L.S., Wen, Y., Fu, R., Hammer, J., Blazyk, J., Sukharev, S., Cotten, M.L., Mihailescu, M., "The Host-Defense Peptide Piscidin P1 Reorganizes Lipid Domains in Membranes and Decreases Activation Energies in Mechanosensitive Ion Channels," *J. Biol. Chem.* **294**(49), 18557 (2019).
- Cui, Z., Grutter, A.J., Zhou, H., Cao, H., Dong, Y., Gilbert, D.A., Wang, J., Liu, Y.-S., Ma, J., Hu, Z., Guo, J., Xia, J., Kirby, B.J., Shafer, P., Arenholz, E., Chen, H., Zhai, X., Lu, Y., "Correlation-Driven Eightfold Magnetic Anisotropy in a Two-Dimensional Oxide Monolayer," *Sci. Adv.* **6**(15), eaay0114 (2020).
- Dai, J., Xie, D., Liu, Y., Zhang, Z., Yang, Y., Yang, Q., Ren, Q., Bao, Z., "Supramolecular Metal-Organic Framework for  $\text{CO}_2/\text{CH}_4$  and  $\text{CO}_2/\text{N}_2$  Separation," *Ind. Eng. Chem. Res.* **59**(16), 7866 (2020).
- Dally, R.L., Ratcliff, II, W.D., Zhang, L., Kim, H.-S., Bleuel, M., Kim, J.W., Haule, K., Vanderbilt, D., Cheong, S.-W., Lynn, J.W., "Magnetic Phase Transitions and Spin Density Distribution in the Molecular Multiferroic System  $\text{GaV}_4\text{S}_8$ ," *Phys. Rev. B* **102**(1), 014410 (2020).
- Dally, R.L., Heng, A.J.R., Keselman, A., Bordelon, M.M., Stone, M.B., Balents, L., Wilson, S.D., "Three-Magnon Bound State in the Quasi-One-Dimensional Antiferromagnet  $\alpha\text{-NaMnO}_2$ ," *Phys. Rev. Lett.* **124**(19), 197203 (2020).
- Danielsen, S.P.O., Davidson, E.C., Fredrickson, G.H., Segalman, R.A., "Absence of Electrostatic Rigidity in Conjugated Polyelectrolytes with Pendant Charges," *ACS Macro Lett.* **8**(9), 1147 (2019). [CHRN]
- De Mel, J.U., Gupta, S., Perera, R.M., Ngo, L., Zolnierczuk, P., Bleuel, M., Pingali, S.V., Schneider, G.J., "Influence of External NaCl Salt on Membrane Rigidity of Neutral DOPC Vesicles," *Langmuir*, in press. [CHRN]
- Decker, G.E., Lorz, G.R., Deegan, M.M., Bloch, E.D., "MOF-Mimetic Molecules: Carboxylate-Based Supramolecular Complexes as Molecular Metal-Organic Framework Analogues," *J. Mater. Chem. A* **8**, 4217 (2020).
- Dergunov, S.A., Richter, A.G., Kim, M.D., Pingali, S.V., Urban, V.S., Pinkhassik, E., "Deciphering and Controlling Structural and Functional Parameters of the Shells in Vesicle-Templated Polymer Nanocapsules," *Langmuir* **35**(40), 13020 (2019).
- Desautels, R.D., DeBeer-Schmitt, L., Montoya, S.A., Borchers, J.A., Je, S.-G., Tang, N., Im, M.-Y., Fitzsimmons, M.R., Fullerton, E.E., Gilbert, D.A., "Realization of Ordered Magnetic Skyrmions in Thin Films at Ambient Conditions," *Phys. Rev. Mater.* **3**(10), 104406 (2019). [CHRN]
- DiPasquale, M., Nguyen, M.H.L., Rikeard, B.W., Cesca, N., Tannous, C., Castillo, S.R., Katsaras, J., Kelley, E.G., Heberle, F.A., Marquardt, D., "The Antioxidant Vitamin E as a Membrane Raft Modulator: Tocopherols do not Abolish Lipid Domains," *BBA - Biomembranes*, in press. [CHRN]
- Dimitrievska, M., Wu, H., Stavila, V., Babanova, O.A., Skoryunov, R.V., Solonin, A.V., Zhou, W., Trump, B.A., Andersson, M.S., Skripov, A.V., Udovic, T.J., "Structural and Dynamical Properties of Potassium Dodecahydro-Monocarbonyl-Dodecaborate:  $\text{KCB}_{11}\text{H}_{12}$ ," *J. Phys. Chem. C*, in press. [CHRN]
- Dimitrievska, M., Chong, M., Bowden, M.E., Wu, H., Zhou, W., Nayyar, I., Ginovska, B., Gennett, T., Autrey, T., Jensen, C.M., Udovic, T.J., "Structural and Reorientational Dynamics of Tetrahydroborate ( $\text{BH}_4^-$ ) and Tetrahydrofuran (THF) in a  $\text{Mg}(\text{BH}_4)_2 \cdot 3\text{THF}$  Adduct: Neutron-Scattering Characterization," *Phys. Chem. Chem. Phys.* **22**(1), 368 (2020). [CHRN]
- Domhoff, A., Balwani, A., Martin, T.B., Davis, E.M., "Leveraging Nanoparticle Dispersion State to Tune Vanadium Ion Selectivity of Nanophase-Segregated Ionomer Nanocomposites for Redox Flow Batteries," *ACS Appl. Energy Mater.* **2**(12), 8535 (2019).
- Domhoff, A., Davis, E.M., "Influence of Casting Substrate on Bulk Morphology and Vanadium Ion Transport in Ionomer Nanocomposites," *J. Appl. Phys.* **127**(17), 174701 (2020).
- Duell, B.A., Li, J., Subramanian, M.A., "Hibonite Blue: A New Class of Intense Inorganic Blue Colorants," *ACS Omega* **4**(26), 22114 (2019).
- Dumont, J.H., Spears, A.J., Hjelm, R.P., Hawley, M., Maurya, S., Li, D., Yuan, G., Watkins, E.B., Kim, Y.S., "Unusually High Concentration of Alkyl Ammonium Hydroxide in the Cation-Hydroxide-Water Coadsorbed Layer on Pt," *ACS Appl. Mater. Interfaces* **12**(1), 1825 (2020).



- Dwivedi, G.D., Wu, C.-M., Chen, B.-Y., Lin, S.T., Qiu, W.-Z., Sun, S.J., Xu, G., Lynn, J.W., Chiou, J.W., Lee, C.-H., Li, W.-H., Yano, S., Chou, H., "Magnon Profile on SrRuO<sub>3</sub> Films Studied by Inelastic Neutron Scattering," *Phys. Rev. B* **101**(5), 054403 (2020).
- Eckberg, C., Campbell, D.J., Metz, T., Collini, J., Hodovanets, H., Drye, T., Zavalij, P., Christensen, M.H., Fernandes, R.M., Lee, S., Abbamonte, P., Lynn, J.W., Paglione, J., "Sixfold Enhancement of Superconductivity in a Tunable Electronic Nematic System," *Nat. Phys.* **16**(3), 346 (2020).
- Edwards, A.T., Javidialesaadi, A., Weigandt, K.M., Stan, G., Eads, C.D., "Structure and Dynamics of Spherical and Rodlike Alkyl Ethoxylate Surfactant Micelles Investigated using NMR Relaxation and Atomistic Molecular Dynamics Simulations," *Langmuir* **35**(43), 13880 (2019).
- El-Khatib, S., Bhatti, K.P., Srivastava, V., James, R.D., Leighton, C., "Nanoscale Magnetic Phase Competition throughout the Ni<sub>50-x</sub>Co<sub>x</sub>Mn<sub>40</sub>Sn<sub>10</sub> Phase Diagram: Insights from Small-Angle Neutron Scattering," *Phys. Rev. Mater.* **3**(10), 104413 (2019).
- Evans, H.A., Wu, Y., Seshadri, R., Cheetham, A.K., "Perovskite-Related ReO<sub>3</sub>-Type Structures," *Nat. Rev. Mater.* **5**, 196 (2020).
- Fan, Y., Quartermann, P., Finley, J., Han, J., Zhang, P., Hou, J.T., Stiles, M.D., Grutter, A.J., Liu, L., "Manipulation of Coupling and Magnon Transport in Magnetic Metal-Insulator Hybrid Structures," *Phys. Rev. Appl.* **13**(6), 061002 (2020).
- Farmer, T.O., Guo, E.-J., Desautels, R.D., DeBeer-Schmitt, L., Chen, A., Wang, Z., Jia, Q., Borchers, J.A., Gilbert, D.A., Holladay, B., Sinha, S.K., Fitzsimmons, M.R., "Nanoscale Magnetization Inhomogeneity within Single Phase Nanopillars," *Phys. Rev. Mater.* **3**(8), 081401(R) (2019). [CHNRNS]
- Felder, J.B., Wong-Ng, W., Qabbani, R.A., Roth, R.S., Toby, B.H., Chan, J.Y., "Structural Investigation of the 'Tripled -Tetragonal-Tungsten-Bronze' Phases Sr<sub>2</sub>M<sub>10-x</sub>O<sub>27-y</sub> (M = Nb, Ta)," *Polyhedron* **170**, 359 (2019).
- Feng, X., Wang, X., Wang, H., Wu, H., Liu, Z., Zhou, W., Lin, Q., Jiang, J., "Elucidating J-Aggregation Effect in Boosting Singlet-Oxygen Evolution using Zirconium-Porphyrin Frameworks: A Comprehensive Structural, Catalytic, and Spectroscopic Study," *ACS Appl. Mater. Interfaces* **11**(48), 45118 (2019).
- Frielinghaus, H., Butler, P.D., Pauw, B.R., Rennie, A.R., "Eleventh canSAS Meeting: International Cooperation and Collaboration in Small-Angle Scattering," *Synchrotron Radiat. News* **32**(6), 48 (2019).
- Frischknecht, A.L., Paren, B.A., Middleton, L.R., Koski, J.P., Tarver, J.D., Tyagi, M., Soles, C.L., Winey, K.I., "Chain and Ion Dynamics in Precise Polyethylene Ionomers," *Macromolecules* **52**(20), 7939 (2019).
- Gao, J., Qian, X., Lin, R.-B., Krishna, R., Wu, H., Zhou, W., Chen, B., "Mixed Metal-Organic Framework with Multiple Binding Sites for Efficient C<sub>2</sub>H<sub>2</sub>/CO<sub>2</sub> Separation," *Angew. Chem. Int. Edit.* **59**(11), 4396 (2020).
- Gao, K.W., Loo, W.S., Snyder, R.L., Abel, B.A., Choo, Y., Lee, A., Teixeira, S.C.M., Garetz, B.A., Coates, G.W., Balsara, N.P., "Miscible Polyether/Poly(Ether-Acetal) Electrolyte Blends," *Macromolecules* **53**(14), 5728 (2020).
- Gao, Q., Sun, Y., Shi, N., Milazzo, R., Pollastri, S., Olivi, L., Huang, Q., Liu, H., Sanson, A., Sun, Q., Liang, E., Xing, X., Chen, J., "Large Isotropic Negative Thermal Expansion in Water-Free Prussian Blue Analogues of ScCo(CN)<sub>6</sub>," *Scripta Mater.*, in press.
- Gardner, J.S., Ehlers, G., Faraone, A., García Sakai, V., "High-Resolution Neutron Spectroscopy using Backscattering and Neutron Spin-Echo Spectrometers in Soft and Hard Condensed Matter," *Nat. Rev. Phys.* **2**, 103 (2020). [CHNRNS]
- Garg, S., Liu, Y., Perez-Salas, U., Porcar, L., Butler, P.D., "Anomalous Inter-Membrane Cholesterol Transport in Fluid Phase Phosphoserine Vesicles Driven by Headgroup Ordered to Disordered Entropic Transition," *Chem. Phys. Lipids* **223**, 104779 (2019). [CHNRNS]
- Gehring, P., Hallas, A., Helgeson, M., Josey, B., Louca, D., Page, K., Ross, K.A., Ross, N., "The 9th American Conference on Neutron Scattering," *Neutron News* **30**(2-3), 4 (2019).
- Gentile, T.R., Huber, M.G., Koetke, D.D., Peshkin, M., Arif, M., Dombeck, T., Hussey, D.S., Jacobson, D.L., Nord, P., Pushin, D.A., Smither, R., "Direct Observation of Neutron Spin Rotation in Bragg Scattering due to the Spin-Orbit Interaction in Silicon," *Phys. Rev. C* **100**(3), 034005 (2019).
- Giannakis, I., Leshen, J., Kawai, M., Ran, S., Kang, C.-J., Saha, S.R., Zhao, Y., Xu, Z., Lynn, J.W., Miao, L., Wray, L.A., Kotliar, G., Butch, N.P., Aynajian, P., "Orbital-Selective Kondo Lattice and Enigmatic f Electrons Emerging from Inside the Antiferromagnetic Phase of a Heavy Fermion," *Sci. Adv.* **5**(10), eaaw9061 (2019).
- Glinka, C., Bleuel, M., Tsai, P., Zákutná, D., Honecker, D., Dresen, D., Mees, F., Disch, S., "Sub-Millisecond Time-Resolved Small-Angle Neutron Scattering Measurements at NIST," *J. Appl. Crystallogr.* **53**(3), 598 (2020). [CHNRNS]
- Gnewuch, S., Rodriguez, E.E., "Distinguishing the Intrinsic Antiferromagnetism in Polycrystalline LiCoPO<sub>4</sub> and LiMnPO<sub>4</sub> Olivines," *Inorg. Chem.* **59**(9), 5883 (2020).

- Gray, I., Moriyama, T., Sivadas, N., Stiehl, G.M., Heron, J.T., Need, R., Kirby, B.J., Low, D.H., Nowack, K.C., Schlom, D.G., Ralph, D.C., Ono, T., Fuchs, G.D., "Spin Seebeck Imaging of Spin-Torque Switching in Antiferromagnetic Pt/NiO Heterostructures," *Phys. Rev. X* **9**(4), 041016 (2019).
- Gu, X., Mavko, G., Ma, L., Oakley, D., Accardo, N., Carr, B.J., Nyblade, A.A., Brantley, S.L., "Seismic Refraction Tracks Porosity Generation and Possible CO<sub>2</sub> Production at Depth under a Headwater Catchment," *P. Natl. A. Sci. USA*, in press. [CHNRNS]
- Gu, X., Rempe, D.M., Dietrich, W.E., West, A.J., Lin, T.-C., Jin, L., Brantley, S.L., "Chemical Reactions, Porosity, and Microfracturing in Shale during Weathering: The Effect of Erosion Rate," *Geochim. Cosmochim. Ac.* **269**, 63 (2020). [CHNRNS]
- Gupta, S., Schneider, G.J., "Modeling the Dynamics of Phospholipids in the Fluid Phase of Liposomes," *Soft Matter* **16**(13), 3245 (2020). [CHNRNS]
- Hadad, N., Adler, D., Pierce, D., Ogg, B., Anderson, D., Sutton, I., Desert, S., Olsen, S., "Design and Engineering of Neutron Instruments Meeting (DENIM)-8th Annual Meeting," *Neutron News* **30**(4), 9 (2020).
- Haddock, C.C., Hiromoto, M., Hirota, K., Ino, T., Kitaguchi, M., Mishima, K., Oi, N., Shima, T., Shimizu, H.M., Snow, W.M., Yoshioka, T., "Measurement of the Total Neutron-Scattering Cross-Section Ratios of Noble Gases of Natural Isotopic Composition using a Pulsed Neutron Beam," *Phys. Rev. C* **100**(6), 064002 (2019).
- Halter, D.P., Klein, R.A., Boreen, M.A., Trump, B.A., Brown, C.M., Long, J.R., "Self-Adjusting Binding Pockets Enhance H<sub>2</sub> and CH<sub>4</sub> Adsorption in a Uranium-Based Metal–Organic Framework," *Chem. Sci.* **11**(26), 6709 (2020).
- Hao, J., Hu, F., Wang, J.-T., Shen, F.-R., Yu, Z., Zhou, H., Wu, H., Huang, Q., Qiao, K., Wang, J., He, J., He, L., Sun, J.-R., Shen, B., "Large Enhancement of Magnetocaloric and Barocaloric Effects by Hydrostatic Pressure in La(Fe<sub>0.92</sub>Co<sub>0.08</sub>)<sub>11.9</sub>Si<sub>1.1</sub> with a NaZn<sub>13</sub>-Type Structure," *Chem. Mater.* **32**(5), 1807 (2020).
- Hassan, M.T., Chen, W.C., "Optimization of a Magnetostatic Cavity for a <sup>3</sup>He Spin Analyzer on the CANDOR Polychromatic Reflectometer," *J. Phys.: Conf. Ser.* **1316**, 012017 (2019). [CHNRNS]
- Haun, R., Wietfeldt, F.E., Arif, M., Huber, M.G., Black, T.C., Heacock, B., Pushin, D.A., Shahi, C.B., "Precision Measurement of the Neutron Scattering Length of <sup>4</sup>He using Neutron Interferometry," *Phys. Rev. Lett.* **124**(1), 012501 (2020).
- Heacock, B., Sarenac, D., Cory, D.G., Huber, M.G., Hussey, D.S., Kapahi, C., Miao, H., Wen, H., Pushin, D.A., "Angular Alignment and Fidelity of Neutron Phase-Gratings for Improved Interferometer Fringe Visibility," *AIP Adv.* **9**(8), 085115 (2019).
- Heacock, B., Haun, R., Hirota, K., Hosobata, T., Huber, M.G., Jamer, M.E., Kitaguchi, M., Pushin, D.A., Shimizu, H., Taminiau, I., Yamagata, Y., Yamamoto, T., Young, A.R., "Measurement and Alleviation of Subsurface Damage in a Thick-Crystal Neutron Interferometer," *Acta Crystallogr. A* **75**(6), 833 (2019).
- Heinrich, F., Kienzle, P.A., Hoogerheide, D.P., Lösche, M., "Information Gain from Isotopic Contrast Variation in Neutron Reflectometry on Protein-Membrane Complex Structures," *J. Appl. Crystallogr.* **53**(3), 800 (2020).
- Heinrich, F., Salyapongse, A., Kumagai, A., Dupuy, F.G., Shukla, K., Penk, A., Huster, D., Ernst, R.K., Pavlova, A., Gumbart, J.C., Deslouches, B., Di, Y.P., Tristram-Nagle, S., "Synergistic Biophysical Techniques Reveal Structural Mechanisms of Engineered Cationic Antimicrobial Peptides in Lipid Model Membranes," *Chem.-Eur. J.* **26**(28), 6247 (2020).
- Helton, J.S., Butch, N.P., Pajerowski, D.M., Barilo, S.N., Lynn, J.W., "Three-Dimensional Magnetism and the Dzyaloshinskii-Moriya Interaction in  $S = 3/2$  Kagome Staircase Co<sub>3</sub>V<sub>2</sub>O<sub>8</sub>," *Sci. Adv.* **6**(18), eaay9709 (2020).
- Herrera Diez, L., Liu, Y.T., Gilbert, D.A., Belmeguenai, M., Vogel, J., Pizzini, S., Martinez, E., Lamperti, A., Mohammedi, J.B., Laborieux, A., Roussigné, Y., Grutter, A.J., Arenholtz, E., Quarterman, P., Maranville, B., Ono, S., Salah El Hadri, M., Tolley, R., Fullerton, E.E., Sanchez-Tejerina, L., Stashkevich, A., Chérif, S.M., Kent, A.D., Querlioz, D., Langer, J., Ocker, B., Ravelosona, D., "Nonvolatile Ionic Modification of the Dzyaloshinskii-Moriya Interaction," *Phys. Rev. Appl.* **12**(3), 034005 (2019).
- Hirscher, M., Yartys, V.A., Baricco, M., Bellosta von Colbe, J., Blanchard, D., Bowman, Jr., R.C., Broom, D.P., Buckley, C.E., Chang, F., Chen, P., Cho, Y.W., Crivello, J.-C., Cuevas, F., David, W.I.F., de Jongh, P.E., Denys, R.V., Dornheim, M., Felderhoff, M., Filinchuk, Y., Froudakis, G.E., Grant, D.M., Gray, E.M., Hauback, B.C., He, T., Humphries, T.D., Jensen, T.R., Kim, S., Kojima, Y., Latroche, M., Li, H.-W., Lototsky, M.V., Makepeace, J.W., Møller, K.T., Naheed, L., Ngene, P., Noréus, D., Nygård, M.M., Orimo, S.-I., Paskevicius, M., Pasquini, L., Ravnsbæk, D.B., Sofianos, M.V., Udovic, T.J., Vegge, T., Walker, G.S., Webb, C.J., Weidenthaler, C., Zlotea, C., "Materials for Hydrogen-Based Energy Storage - Past, Recent Progress and Future Outlook," *J. Alloy Compd.* **827**, 153548 (2020).

- Hoogerheide, D.P., "PPDiffuse: A Quantitative Prediction Tool for Diffusion of Charged Polymers in a Nanopore," *J. Res. Natl. Inst. Stan.* **125**, 125018 (2020).
- Hoogerheide, D.P., Forsyth, V.T., Brown, K.A., "Neutron Scattering for Structural Biology," *Phys. Today* **73**(6), 36 (2020).
- Hoogerheide, D.P., Heinrich, F., Maranville, B.B., Majkrzak, C.F., "Accurate Background Correction in Neutron Reflectometry Studies of Soft Condensed Matter Films in Contact with Fluid Reservoirs," *J. Appl. Crystallogr.* **53**(1), 15 (2020).
- Hoogerheide, D.P., Gurnev, P.A., Rostovtseva, T.K., Bezrukov, S.M., "Effect of a Post-Translational Modification Mimic on Protein Translocation through a Nanopore," *Nanoscale* **12**(20), 11070 (2020).
- Hoogerheide, S.F., Caylor, J., Adamek, E.R., Anderson, E.S., Biswas, R., Chavali, S.M., Crawford, B., DeAngelis, C., Dewey, M.S., Formin, N., Gilliam, D.M., Grammer, K.B., Greene, G.L., Haun, R.W., Ivanov, J.A., Li, F., Mulholland, J., Mumm, H.P., Nico, J.S., Snow, W.M., Valette, D., Wietfeldt, F.E., Yue, A.T., "Progress on the BL2 Beam Measurement of the Neutron Lifetime," *EPJ Web Conf.* **219**, 03002 (2019).
- Horkay, F., Basser, P.J., Geissler, E., "Static and Dynamic Behavior of Aggrecan Solutions," *MRS Adv.* **5**(17), 891 (2019). [CHNRNS]
- Horkay, F., Chremos, A., Douglas, J.F., Jones, R.L., Lou, J., Xia, Y., "Systematic Investigation of Synthetic Polyelectrolyte Bottlebrush Solutions by Neutron and Dynamic Light Scattering Osmometry, and Molecular Dynamics Simulation," *J. Chem. Phys.* **152**(19), 194904 (2020).
- Hu, J., Zeng, H., Chen, X., Wang, Z., Wang, H., Wang, R., Wu, L., Huang, Q., Kong, L., Zheng, J., Xiao, Y., Zhang, W., Pan, F., "Revealing Insights into  $\text{Li}_x\text{FePO}_4$  Nanocrystals with Magnetic Order at Room Temperature Resulting in Trapping of Li Ions," *J. Phys. Chem. Lett.* **10**(17), 4794 (2019).
- Hu, X., Zhang, D., Chen, T., Chen, A.Z., Holmgren, E.N., Zhang, Q., Pajerowski, D.M., Yoon, M., Xu, G., Choi, J.J., Lee, S.-H., "Crystal Structures and Rotational Dynamics of a Two-Dimensional Metal Halide Perovskite  $(\text{OA})_2\text{PbI}_4$ ," *J. Chem. Phys.* **152**(1), 014703 (2020).
- Huang, A., Yao, H., Olsen, B.D., "SANS Partial Structure Factor Analysis for Determining Protein-Polymer Interactions in Semidilute Solution," *Soft Matter* **15**(37), 7350 (2019). [CHNRNS]
- Huang, G.-R., Wang, Y., Do, C., Shinohara, Y., Egami, T., Porcar, L., Liu, Y., Chen, W.-R., "Orientational Distribution Function of Aligned Elongated Molecules and Particulates Determined from their Scattering Signature," *ACS Macro Lett.* **8**(10), 1257 (2019). [CHNRNS]
- Huber, M.G., Hoogerheide, S.F., Arif, M., Haun, R.W., Wietfeldt, F.E., Black, T.C., Shahi, C.B., Heacock, B., Young, A.R., Taminiau, I.A.J., Sarenac, D., Cory, D.G., Pushin, D.A., "Overview of Neutron Interferometry at NIST," *EPJ Web Conf.* **219**, 06001 (2019).
- Hutanu, V., Deng, H., Ran, S., Fuhrman, W.T., Thoma, H., Butch, N.P., "Low-Temperature Crystal Structure of the Unconventional Spin-Triplet Superconductor  $\text{UTe}_2$  from Single-Crystal Neutron Diffraction," *Acta Crystall. B-Stru.* **76**(1), 137 (2020).
- Jau, Y.-Y., Chen, W.C., Gentile, T.R., Hussey, D.S., "Sensitive Neutron Transverse Polarization Analysis using a  $^3\text{He}$  Spin Filter," *Rev. Sci. Instrum.* **91**(7), 073303 (2020).
- Jhalaria, M., Buenning, E., Huang, Y., Tyagi, M., Zorn, R., Zamponi, M., Garcia-Sakai, V., Jestin, J., Benicewicz, B.C., Kumar, S.K., "Accelerated Local Dynamics in Matrix-Free Polymer Grafted Nanoparticles," *Phys. Rev. Lett.* **123**(15), 158003 (2019). [CHNRNS]
- Jiang, P., Neuefeind, J.C., Avdeev, M., Huang, Q., Yue, M., Yang, X., Cong, R., Yang, T., "Unprecedented Lattice Volume Expansion on Doping Stereochemically Active  $\text{Pb}^{2+}$  into Uniaxially Strained Structure of  $\text{CaBa}_{1-x}\text{Pb}_x\text{Zn}_2\text{Ga}_2\text{O}_7$ ," *Nat. Commun.* **11**, 1303 (2020).
- Jiang, T., Hall, A., Eres, M., Hemmatian, Z., Qiao, B., Zhou, Y., Ruan, Z., Couse, A.D., Heller, W.T., Huang, H., de la Cruz, M.O., Rolandi, M., Xu, T., "Single-Chain Heteropolymers Transport Protons Selectively and Rapidly," *Nature* **577**, 216 (2020).
- Jo, K.-I., Oh, Y., Sung, B.J., Kim, T.-H., Um, M.S., Choi, W.J., Bang, J., Yuan, G., Satija, S.K., Koo, J., "Enhanced Dynamics of Confined Polymers near the Immiscible Polymer-Polymer Interface: Neutron Reflectivity Studies," *ACS Macro Lett.* **9**(2), 210 (2020).
- Jones, J., Phuoc, V.T., del Campo, L., Massa, N.E., Brown, C.M., Pagola, S., "Accessing New Charge-Transfer Complexes by Mechanochemistry: A Tetrathiafulvalene Chloranilic Acid Polymorph Containing Segregated Tetrathiafulvalene Stacks," *Cryst. Growth Des.* **19**(9), 4970 (2019).
- Jørgensen, M., Shea, P.T., Tomich, A.W., Varley, J.B., Berckx, M., Lovera, S., Černý, R., Zhou, W., Udovic, T.J., Lavallo, V., Jensen, T.R., Wood, B.C., Stavila, V., "Understanding Superionic Conductivity in Lithium and Sodium Salts of Weakly Coordinating *Closo*-Hexahalocarborate Anions," *Chem. Mater.* **32**(4), 1475 (2020).
- Josey, B.P., Heinrich, F., Silin, V., Lösche, M., "Association of Model Neurotransmitters with Lipid Bilayer Membranes," *Biophys. J.* **118**(5), 1044 (2020).



- Jurns, J., Middleton, M., Williams, R., "Progress Towards Operation of a Deuterium Cold Neutron Source at the NCNR," IOP Conf. Ser.: Mater. Sci. Eng. **755**, 012025 (2020).
- Kim, D., Sihm, M.R., Jeon, M.-G., Yuan, G., Satija, S.K., Kim, Y., Choi, J., "Non-Equilibrium Phase Behavior of Immiscible Polymer-Grafted Nanoparticle Blends," *Macromolecules* **52**(15), 5811 (2019).
- Kim, M., Heinrich, F., Haugstad, G., Yu, G., Yuan, G., Satija, S.K., Zhang, W., Seo, H.S., Metzger, J.M., Azarin, S.M., Lodge, T.P., Hackel, B.J., Bates, F.S., "Spatial Distribution of PEO-PPO-PEO Block Copolymer and PEO Homopolymer in Lipid Bilayers," *Langmuir* **36**(13), 3393 (2020).
- Kim, Y., Kim, D., Lee, S., Kim, J., Hussey, D.S., Lee, S.W., "Neutron Grating Interferometer with an Analyzer Grating Based on a Light Blocker," *Opt. Express*, in press.
- Kline, S.R., "2019 NCNR Annual Report," NIST Spec. Publ. **1242**, 1 (2019).
- Knott, R., Dutta, N.K., Choudhury, N.R., "Molecular Structure Development in Silsesquioxane-Urethane Thin Film Hybrids: A Small-Angle Neutron Scattering Investigation," *J. Appl. Polym. Sci.*, in press.
- Kons, C., Phan, M.-H., Srikanth, H., Arena, D.A., Nemati, Z., Borchers, J.A., Krycka, K.L., "Investigating Spin Coupling Across a Three-Dimensional Interface in Core/Shell Magnetic Nanoparticles," *Phys. Rev. Mater.* **4**(3), 034408 (2020). [CHNRNS]
- Kosco, J., Bidwell, M., Cha, H., Martin, T., Howells, C.T., Sachs, M., Anjum, D.H., Gonzalez Lopez, S., Zou, L., Wadsworth, A., Zhang, W., Zhang, L., Tellam, J., Sougrat, R., Laquai, F., DeLongchamp, D.M., Durrant, J.R., McCulloch, I., "Enhanced Photocatalytic Hydrogen Evolution from Organic Semiconductor Heterojunction Nanoparticles," *Nat. Mater.* **19**(5), 559 (2020).
- Krzysko, A.J., Nakouzi, E., Zhang, X., Graham, T.R., Rosso, K.M., Schenter, G.K., Ilavsky, J., Kuzmenko, I., Frith, M.G., Ivory, C.F., Clark, S.B., Weston, J.S., Weigandt, K.M., De Yoreo, J.J., Chun, J., Anovitz, L.M., "Correlating Inter-Particle Forces and Particle Shape to Shear-Induced Aggregation/Fragmentation and Rheology for Dilute Anisotropic Particle Suspensions: A Complementary Study via Capillary Rheometry and *In-Situ* Small and Ultra-Small Angle X-ray Scattering," *J. Colloid Interf. Sci.*, in press.
- Ku, A.Y., Khan, A.S., Gnäupel-Herold, T., "Quasi-Static and Dynamic Response, and Texture Evolution of Two Overaged Al 7056 Alloy Plates in T761 and T721 Tempered: Experiments and Modeling," *Int. J. Plasticity* **130**, 102679 (2020).
- Kumari, H., Eisenhart, A., Pajoubpong, J., Heinrich, F., Beck, T.L., "Investigating Partitioning of Free *Versus* Macrocyclic Bound Guest into a Model POPC Lipid Bilayer," *RSC Adv.* **10**(26), 15148 (2020).
- Kupwade-Patil, K., Bumajdad, A., Littrell, K.C., Büyüköztürk, O., "In Situ Examination of Engineered Local Additives in Cement Paste via Neutron Based Scattering Techniques," *Constr. Build. Mater.* **243**, 118175 (2020).
- Kupwade-Patil, K., Boul, P.J., Rasner, D.K., Lapidus, S.H., Leao, J.B., Johnson, K.D., Thaemlitz, C.J., Büyüköztürk, O., "In Situ Investigation of Phosphonate Retarder Interaction in Oil Well Cements at Elevated Temperature and Pressure Conditions," *J. Am. Ceram. Soc.*, in press.
- Kushan, E., Demir, C., Senses, E., "Surfactant Driven Liquid to Soft Solid Transition of Cellulose Nanocrystal Suspensions," *Langmuir*, in press. [CHNRNS]
- LaManna, J.M., Aaron, D.S., Mench, M.M., "Architecture-Based Control of Temperature Gradient-Driven Water Transport in Polymer Electrolyte Fuel Cells," *J. Electrochem. Soc.* **167**(10), 104504 (2020).
- Lee, C.-H., Ma, M.-H., Li, W.-H., Wei, P.-C., Chen, Y.-Y., Zhao, Y., Lynn, J.W., "Extremely Space and Time Restricted Thermal Transport in the High Temperature *Cmcm* Phase of Thermoelectric SnSe," *Mater. Today Phys.* **11**, 100171 (2019).
- Lee, C., Lee, J.K., Zhao, B., Fahy, K.F., LaManna, J.M., Baltic, E., Hussey, D.S., Jacobson, D.L., Schulz, V.P., Bazylak, A., "Temperature-Dependent Gas Accumulation in Polymer Electrolyte Membrane Electrolyzer Porous Transport Layers," *J. Power Sources* **446**, 227312 (2020).
- Lee, C., Lee, J.K., George, M.G., Fahy, K.F., LaManna, J.M., Baltic, E., Hussey, D.S., Jacobson, D.L., Bazylak, A., "Reconciling Temperature-Dependent Factors Affecting Mass Transport Losses in Polymer Electrolyte Membrane Electrolyzers," *Energ. Convers. Manage.* **213**, 112797 (2020).
- Lee, J., Zhao, T., Peeler, D.J., Lee, D.C., Pichon, T.J., Li, D., Weigandt, K.M., Horner, P.J., Pozzo, L.D., Sellers, D.L., Pun, S.H., "Formulation of Thrombin-Inhibiting Hydrogels via Self-Assembly of Ionic Peptides with Peptide-Modified Polymers," *Soft Matter* **16**(15), 3762 (2020).
- Lee, J.C.-W., Hong, Y.-T., Weigandt, K.M., Kelley, E.G., Kong, H., Rogers, S.A., "Strain Shifts under Stress-Controlled Oscillatory Shearing in Theoretical, Experimental, and Structural Perspectives: Application to Probing Zero-Shear Viscosity," *J. Rheol.* **63**(6), 863 (2019). [CHNRNS]

- Lee, S., Oh, O., Kim, Y., Kim, D., Hussey, D.S., Wang, G., Lee, S.W., "Deep Learning for High-Resolution and High-Sensitivity Interferometric Phase Contrast Imaging," *Sci. Rep.* **10**, 9891 (2020).
- Lee, S.H., Zhu, Y., Wang, Y., Miao, L., Pillsbury, T., Yi, H., Kempinger, S., Hu, J., Heikes, C.A., Quarterman, P., Ratcliff, W., Borchers, J.A., Zhang, H., Ke, X., Graf, D., Alem, N., Chang, C.-Z., Samarth, N., Mao, Z., "Spin Scattering and Noncollinear Spin Structure-Induced Intrinsic Anomalous Hall Effect in Antiferromagnetic Topological Insulator  $\text{MnBi}_2\text{Te}_4$ ," *Phys. Rev. Res.* **1**(1), 012011(R) (2019).
- Lee, Y.-T., Li, D.S., Pozzo, L.D., "Kinetic Analysis of Ultrasound-Induced Oil Exchange in Oil-in-Water Emulsions through Contrast Variation Time-Resolved Small-Angle Neutron Scattering," *Langmuir* **35**(47), 15204 (2019). [CHNRS]
- Lee, Y.-T., Pozzo, L.D., "Contrast-Variation Time-Resolved Small-Angle Neutron Scattering Analysis of Oil-Exchange Kinetics between Oil-in-Water Emulsions Stabilized by Anionic Surfactants," *Langmuir* **35**(47), 15192 (2019). [CHNRS]
- Li, L., Cheng, X., Blum, T., Huyan, H., Zhang, Y., Heikes, C., Yan, X., Gadre, C., Aoki, T., Xu, M., Xie, L., Hong, Z., Adamo, C., Schlom, D.G., Chen, L.-Q., Pan, X., "Observation of Strong Polarization Enhancement in Ferroelectric Tunnel Junctions," *Nano Lett.* **19**(10), 6812 (2019).
- Li, Q., Yi, T., Wang, X., Pan, H., Quan, B., Liang, T., Guo, X., Yu, X., Wang, H., Huang, X., Chen, L., Li, H., "In-Situ Visualization of Lithium Plating in All-Solid-State Lithium-Metal Battery," *Nano Energy* **63**, 103895 (2019).
- Li, W.M., Zhao, J.F., Cao, L.P., Hu, Z., Huang, Q.Z., Wang, X.C., Liu, Y., Zhao, G.Q., Zhang, J., Liu, Q.Q., Yu, R.Z., Long, Y.W., Wu, H., Lin, H.J., Chen, C.T., Li, Z., Gong, Z.Z., Guguchia, Z., Kim, J.S., Stewart, G.R., Uemura, Y.J., Uchida, S., Jin, C.Q., "Reply to Yamamoto: A Cuprate Superconductor with Unconventional Features," *P. Natl. A. Sci. USA* **116**(37), 18166 (2019).
- Li, W.M., Zhao, J.F., Cao, L.P., Hu, Z., Huang, Q.Z., Wang, X.C., Yu, R.Z., Long, Y.W., Wu, H., Lin, H.J., Chen, C.T., Gong, Z.Z., Guguchia, Z., Kim, J.S., Stewart, G.R., Uemura, Y.J., Uchida, S., Jin, C.Q., "The Unconventional Copper Oxide Superconductor with Conventional Constitution," *J. Supercond. Nov. Magn.* **33**(1), 81 (2020).
- Li, Y., Liu, Z., Xu, Z., Song, Y., Huang, Y., Shen, D., Ma, N., Li, A., Chi, S., Frontzek, M., Cao, H., Huang, Q., Wang, W., Xie, Y., Zhang, R., Rong, Y., Shelton, W.A., Young, D.P., DiTusa, J.F., Dai, P., "Flat-Band Magnetism and Helical Magnetic Order in Ni-Doped  $\text{SrCo}_2\text{As}_2$ ," *Phys. Rev. B* **100**(9), 094446 (2019).
- Lima, T.A., Paschoal, V.H., Freitas, R.S., Faria, L.F.O., Li, Z., Tyagi, M., Z, Y., Ribeiro, M.C.C., "An Inelastic Neutron Scattering, Raman, Far-Infrared, and Molecular Dynamics Study of the Intermolecular Dynamics of Two Ionic Liquids," *Phys. Chem. Chem. Phys.* **22**(16), 9074 (2020).
- Lin, B., Zhou, X., Zhao, H., Yuan, J., Zhou, K., Chen, K., Wu, H., Guo, R., Scheel, M.A., Chumakov, A., Roth, S.V., Mao, Y., Wang, L., Tang, Z., Müller-Buschbaum, P., Ma, W., "Balancing the Pre-Aggregation and Crystallization Kinetics Enables High Efficiency Slot-Die Coated Organic Solar Cells with Reduced Non-Radiative Recombination Losses," *Energ. Environ. Sci.*, in press.
- Lin, K., Gong, P., Chu, S., Li, Q., Lin, Z., Wu, H., Wang, Q., Wang, J., Kim, M.J., Kato, K., Wang, C.-W., Liu, X., Huang, Q., Chen, J., Zhu, H., Deng, J., Xing, X., "Strong Second Harmonic Generation in a Tungsten Bronze Oxide by Enhancing Local Structural Distortion," *J. Am. Chem. Soc.* **142**(16), 7480 (2020).
- Lin, R.-B., Xiang, S., Zhou, W., Chen, B., "Microporous Metal-Organic Framework Materials for Gas Separation," *Chem* **6**(2), 337 (2020).
- Liu, C., Wang, T., Ji, J., Wang, C., Wang, H., Jin, P., Zhou, W., Jiang, J., "The Effect of Pore Size and Layer Number of Metal-Porphyrin Coordination Nanosheets on Sensing DNA," *J. Mater. Chem. C* **7**(33), 10240 (2019).
- Liu, Q., Febbraro, M., deBoer, R.J., Boeltzig, A., Chen, Y., Cerjan, C., Couder, M., Frentz, B., Görres, J., Henry, E.A., Lamere, E., Macon, K.T., Manukyan, K.V., Morales, L., O'Malley, P.D., Pain, S.D., Peters, W.A., Schneider, D., Seymour, C., Seymour, G., Temanson, E., Toomey, R., Vande Kolk, B., Weaver, J., Wiescher, M., "Measurement of the  $^{10}\text{B}(\alpha, n_0) ^{13}\text{N}$  Cross Section for  $2.2 < E_\alpha < 4.9$  MeV and its Application as a Diagnostic at the National Ignition Facility," *Phys. Rev. C* **100**(3), 034601 (2019).
- Liu, Q., Febbraro, M., deBoer, R.J., Aguilar, S., Boeltzig, A., Chen, Y., Couder, M., Görres, J., Lamere, E., Lyons, S., Macon, K.T., Manukyan, K., Morales, L., Pain, S., Peters, W.A., Seymour, C., Seymour, G., Toomey, R., Vande Kolk, B., Weaver, J., Wiescher, M., "Low-Energy Cross-Section Measurement of the  $^{10}\text{B}(\alpha, n)^{13}\text{N}$  Reaction and its Impact on Neutron Production in First-Generation Stars," *Phys. Rev. C* **101**(2), 025808 (2020).
- Liu, S., Tyagi, M., Akcora, P., "Polymer-Coupled Local Dynamics Enhances Conductivity of Ionic Liquids," *Macromolecules*, in press. [CHNRS]
- Liu, T., Gautam, S., Cole, D.R., Patankar, S., Tomasko, D., Zhou, W., Rother, G., "Structure and Dynamics of Ethane Confined in Silica Nanopores in the Presence of  $\text{CO}_2$ ," *J. Chem. Phys.* **152**(8), 084707 (2020).

- Liu, T., Dai, A., Lu, J., Yuan, Y., Xiao, Y., Yu, L., Li, M., Gim, J., Ma, L., Liu, J., Zhan, C., Li, L., Zheng, J., Ren, Y., Wu, T., Shahbazian-Yassar, R., Wen, J., Pan, F., Amine, K., "Correlation between Manganese Dissolution and Dynamic Phase Stability in Spinel-Based Lithium-Ion Battery," *Nat. Commun.* **10**(1), 4721 (2019).
- Liu, X., Singh, S., Kirby, B.J., Zhong, Z., Cao, Y., Pal, B., Kareev, M., Middey, S., Freeland, J.W., Shafer, P., Arenholz, E., Vanderbilt, D., Chakhalian, J., "Emergent Magnetic State in (111)-Oriented Quasi-Two-Dimensional Spinel Oxides," *Nano Lett.* **19**(12), 8381 (2019).
- Liu, Y., Kelley, E.G., Batchu, K.C., Porcar, L., Perez-Salas, U., "Creating Asymmetric Phospholipid Vesicles via Exchange with Lipid-Coated Silica Nanoparticles," *Langmuir*, in press. [CHNRNS]
- Liu, Y., "Short-Time Dynamics of Proteins in Solutions Studied by Neutron Spin Echo," *Curr. Opin. Colloid In.* **42**, 147 (2019). [CHNRNS]
- Liu, Z., Yang, C., Zhang, L., Yu, Y., Yu, M., García Sakai, V., Tyagi, M., Yamada, T., He, L., Zhang, X., Hong, L., "Heterogeneity of Water Molecules on the Free Surface of Thin Reduced Graphene Oxide Sheets," *J. Phys. Chem. C* **124**(20), 11064 (2020). [CHNRNS]
- Loo, W.S., Faraone, A., Grundy, L.S., Gao, K.W., Balsara, N.P., "Polymer Dynamics in Block Copolymer Electrolytes Detected by Neutron Spin Echo," *ACS Macro Lett.* **9**(5), 639 (2020). [CHNRNS]
- Loo, W.S., Mongcopa, K.I., Gribble, D.A., Faraone, A.A., Balsara, N.P., "Investigating the Effect of Added Salt on the Chain Dimensions of Poly(Ethylene Oxide) through Small-Angle Neutron Scattering," *Macromolecules* **52**(22), 8724 (2019). [CHNRNS]
- Lopez, C.G., Horkay, F., Mussel, M., Jones, R.L., Richtering, W., "Screening Lengths and Osmotic Compressibility of Flexible Polyelectrolytes in Excess Salt Solutions," *Soft Matter*, in press. [CHNRNS]
- López-Barrón, C.R., Burghardt, W.R., Kweon, M.S., "Local and Global Stretching of Polymer Chains during Startup of Extensional Flow," *ACS Macro Lett.* **9**(1), 26 (2020).
- Lorzing, G.R., Balto, K.P., Antonio, A.M., Trump, B.A., Brown, C.M., Bloch, E.D., "Elucidating the Structure of the Metal-Organic Framework Ru-HKUST-1," *Chem. Mater.*, in press.
- Lowe, A., Tsyryn, N., Chorążewski, M., Zajdel, P., Mierzwa, M., Leão, J.B., Bleuel, M., Feng, T., Luo, D., Li, M., Li, D., Stoudenets, V., Pawlus, S., Faik, A., Grosu, Y., "Effect of Flexibility and Nanotriboelectrification on the Dynamic Reversibility of Water Intrusion into Nanopores: Pressure-Transmitting Fluid with Frequency-Dependent Dissipation Capability," *ACS Appl. Mater. Interfaces* **11**(43), 40842 (2019). [CHNRNS]
- Luo, Y., Marcus, G.G., Trump, B.A., Kindervater, J., Stone, M.B., Rodriguez-Rivera, J.A., Qiu, Y., McQueen, T.M., Tchernyshyov, O., Broholm, C., "Low-Energy Magnons in the Chiral Ferrimagnet  $\text{Cu}_2\text{OSeO}_3$ : A Coarse-Grained Approach," *Phys. Rev. B* **101**(14), 144411 (2020). [CHNRNS]
- Lussier, J.A., Richtik, B.N., Mauws, C., Lynn, J.W., Wiebe, C.R., "Absence of Magnetic Ordering in the Spin Liquid Candidate  $\text{Ca}_3\text{Cu}_2\text{GeV}_2\text{O}_{12}$ ," *J. Phys.: Condens. Mat.* **32**(13), 134001 (2020).
- Luzin, V., Spiridonov, P., Spencer, K., Gnaupel-Herold, T., "Neutron Diffraction Study of Macrostress and Microstress in  $\text{Al-Al}_2\text{O}_3$ -Based Corrosion Protection Coating Obtained by Cold Spray (Dynamic Metallization)," *J. Therm. Spray Techn.*, in press.
- Lyu, Y., Gu, X., Mao, Y., "Green Composite of Instant Coffee and Poly(Vinyl Alcohol): An Excellent Transparent UV-Shielding Material with Superior Thermal-Oxidative Stability," *Ind. Eng. Chem. Res.* **59**(18), 8640 (2020).
- Mach, J., Gales, C., Park, J.-S., Okasinski, J., Budrow, C., Beaudoin, A., Swartz, K., Miller, M., Gnaupel-Herold, T., "FD&E Total Life T-Sample Residual Stress Analytical Predictions and Measured Results," *SAE Tech.* **2019**(1), 0528 (2019).
- Mai, T.T., McCreary, A., Lampen-Kelley, P., Butch, N., Simpson, J.R., Yan, J.-Q., Nagler, S.E., Mandrus, D., Hight Walker, A.R., Valdés Aguilar, R., "Polarization-Resolved Raman Spectroscopy of  $\alpha\text{-RuCl}_3$  and Evidence of Room-Temperature Two-Dimensional Magnetic Scattering," *Phys. Rev. B* **100**(13), 134419 (2019).
- Majcher, M.J., McInnis, C.L., Himbert, S., Alsop, R.J., Kinio, D., Bleuel, M., Rheinstädter, M.C., Smeets, N.M.B., Hoare, T., "Photopolymerized Starchstarch Nanoparticle (SNP) Network Hydrogels," *Carbohydr. Polym.* **236**, 115998 (2020). [CHNRNS]
- Mallamace, F., Corsaro, C., Mallamace, D., Chen, S.-H., Fratini, E., Baglioni, P., "The Boson Peak Interpretation and Evolution in Confined Amorphous Water," *Sci. China Phys. Mech.* **62**(10), 107004 (2019).
- Mamontov, E., Osti, N.C., Tyagi, M., "Temperature Dependence of Nanoscale Dynamic Processes Measured in Living Millipedes by High Resolution Inelastic and Elastic Neutron Scattering," *Sci. Rep.* **9**(1), 11646 (2019). [CHNRNS]



- Manandhar, K., Ren, Y., Stasak, D., Hou, H., Kirsch, D., Sarker, S., Mehta, A., Sardar, S., Xiao, M., Weaver, J.L., León, C., Hart, G., Sunaoshi, T., Lemmon, J.P., Takeuchi, I., "High-Throughput Exploration of Lithium-Alloy Protection Layers for High-Performance Lithium-Metal Batteries," *ACS Appl. Energy Mater.* **3**(3), 2547 (2020).
- Manley, M.E., Hellman, O., Shulumba, N., May, A.F., Stonaha, P.J., Lynn, J.W., Garlea, V.O., Alatas, A., Hermann, R.P., Budai, J.D., Wang, H., Sales, B.C., Minnich, A.J., "Intrinsic Anharmonic Localization in Thermoelectric PbSe," *Nat. Commun.* **10**(1), 1928 (2019)
- Mao, Y., Hsiao, B.S., Chu, B., "Static and Dynamic Light Scattering," in "World Scientific Series in Nanoscience and Nanotechnology Handbook of Synthetic Methodologies and Protocols of Nanomaterials, Vol. 4," edited by Zhu, Y., Han, Y. (World Scientific Co. Pte. Ltd., Singapore) Chap. **8**, 335 (2019).
- Marques, M.P.M., Batista de Carvalho, A.L.M., Mamede, A.P., Dopplapudi, A., Rudić, S., Tyagi, M., Garcia Sakai, V., Batista de Carvalho, L.A.E., "A New Look into the Mode of Action of Metal-Based Anticancer Drugs," *Molecules* **25**(2), 246 (2020). [CHNRS]
- Martys, N.S., George, W.L., Murphy, R.P., Weigandt, K.M., "Pipe Flow of Sphere Suspensions having a Power-Law-Dependent Fluid Matrix," *J. Rheol.* **64**(2), 445 (2020).
- Marx, D.C., Leblanc, M.J., Plummer, A.M., Krueger, S., Fleming, K.G., "Domain Interactions Determine the Conformational Ensemble of the Periplasmic Chaperone SurA," *Protein Sci.*, in press. [CHNRS]
- Matsuda, M., Dissanayake, S.E., Abernathy, D.L., Qiu, Y., Copley, J.R.D., Kumada, N., Azuma, M., "Frustrated Magnetic Interactions in an  $S = 3/2$  Bilayer Honeycomb Lattice Compound  $\text{Bi}_3\text{Mn}_4\text{O}_{12}(\text{NO}_3)$ ," *Phys. Rev. B* **100**(13), 134430 (2019).
- McCreary, A., Simpson, J.R., Mai, T.T., McMichael, R.D., Douglas, J.E., Butch, N., Dennis, C., Valdés Aguilar, R., Hight Walker, A.R., "Quasi-Two-Dimensional Magnon Identification in Antiferromagnetic  $\text{FePS}_3$  via Magneto-Raman Spectroscopy," *Phys. Rev. B* **101**(6), 064416 (2020).
- McDermott, A.G., DesLauriers, P.J., Fodor, J.S., Jones, R.L., Snyder, C.R., "Measuring Tie Chains and Trapped Entanglements in Semicrystalline Polymers," *Macromolecules* **53**(13), 5614 (2020).
- Medina, E., Pathirana, V.H., Li, J., Ramirez, A.P., Subramanian, M.A., "Tetrahedral  $\text{Mn}^{4+}$  as Chromophore in Sillenite-Type Compounds," *J. Solid State Chem.*, in press.
- Mekuria, T., Khalid, S., Krycka, K., Bleuel, M., Verma, H., Hong, H., Karna, S.P., Seifu, D., "Cobalt Ferrite Nanoparticle Intercalated Carbon Nanotubes for a Nanomagnetic Ultrasensitive Sensor for Cr-VI in Water," *AIP Adv.* **10**(6), 065134 (2020). [CHNRS]
- Metz, T., Bae, S., Ran, S., Liu, I.-L., Eo, Y.S., Fuhrman, W.T., Agterberg, D.F., Anlage, S.M., Butch, N.P., Paglione, J., "Point-Node Gap Structure of the Spin-Triplet Superconductor  $\text{UTe}_2$ ," *Phys. Rev. B* **100**(22), 220504(R) (2019).
- Miao, L., Liu, S., Xu, Y., Kotta, E.C., Kang, C.-J., Ran, S., Paglione, J., Kotliar, G., Butch, N.P., Denlinger, J.D., Wray, L.A., "Low Energy Band Structure and Symmetries of  $\text{UTe}_2$  from Angle-Resolved Photoemission Spectroscopy," *Phys. Rev. Lett.* **124**(7), 076401 (2020).
- Minnaar, C., De Beer, F., Bessarabov, D., "Current Density Distribution of Electrolyzer Flow Fields: In Situ Current Mapping and Neutron Radiography," *Energ. Fuel.* **34**(1), 1014 (2020).
- Mkam Tsengam, I.K., Omarova, M., Shepherd, L., Sandoval, N., He, J., Kelley, E., John, V., "Clusters of Nanoscale Liposomes Modulate the Release of Encapsulated Species and Mimic the Compartmentalization Intrinsic in Cell Structures," *ACS Appl. Nano Mater.* **2**(11), 7134 (2019).
- Mohapatra, S.S., Frisina, R.D., Mohapatra, S., Sneed, K.B., Markoutsas, E., Wang, T., Dutta, R., Damjanovic, R., Phan, M.-H., Denmark, D.J., Biswal, M.R., McGill, A.R., Green, R., Howell, M., Ghosh, P., Gonzalez, A., Ahmed, N.T., Borresen, B., Farmer, M., Gaeta, M., Sharma, K., Bouchard, C., Gamboni, D., Martin, J., Tolve, B., Singh, M., Judy, J.W., Li, C., Santra, S., Daunert, S., Zeynalov, E., Gelfand, R.M., Lenhart, S., McLamore, E.S., Xiang, D., Morgan, V., Friedersdorf, L.E., Lal, R., Webster, T.J., Hoogerheide, D.P., Nguyen, T.D., D'Souza, M.J., Çulha, M., Kondiah, P.P.D., Martin, D.K., "Advances in Translational Nanotechnology: Challenges and Opportunities," *Appl. Sci.* **10**(14), 4881 (2020).
- Mongcopa, K.I.S., Gribble, D.A., Loo, W.S., Tyagi, M., Mullin, S.A., Balsara, N.P., "Segmental Dynamics Measured by Quasi-Elastic Neutron Scattering and Ion Transport in Chemically Distinct Polymer Electrolytes," *Macromolecules* **53**(7), 2406 (2020). [CHNRS]
- Morris, M.A., Sung, S.H., Ketkar, P.M., Dura, J.A., Nieuwendaal, R.C., Epps, III, T.H., "Enhanced Conductivity via Homopolymer-Rich Pathways in Block Polymer-Blended Electrolytes," *Macromolecules* **52**(24), 9682 (2019).
- Moseley, D.H., Stavretis, S.E., Zhu, Z., Guo, M., Brown, C.M., Ozerov, M., Cheng, Y., Daemen, L.L., Richardson, R., Knight, G., Thirunavukkuarasu, K., Ramirez-Cuesta, A.J., Tang, J., Xue, Z.-L., "Inter-Kramers Transitions and Spin-Phonon Couplings in a Lanthanide-Based Single-Molecule Magnet," *Inorg. Chem.* **59**(7), 5218 (2020).

- Mozur, E.M., Hope, M.A., Trowbridge, J.C., Halat, D.M., Daemen, L.L., Maughan, A.E., Prisk, T.R., Grey, C.P., Neilson, J.R., "Cesium Substitution Disrupts Concerted Cation Dynamics in Formamidinium Hybrid Perovskites," *Chem. Mater.* **32**(14), 6266 (2020). [CHRSN]
- Mozur, E.M., Trowbridge, J.C., Maughan, A.E., Gorman, M.J., Brown, C.M., Prisk, T.R., Neilson, J.R., "Dynamical Phase Transitions and Cation Orientation-Dependent Photoconductivity in  $\text{CH}(\text{NH}_2)_2\text{PbBr}_3$ ," *ACS Mater. Lett.* **1**(2), 260 (2019). [CHRSN]
- Murakami, T., Nambu, Y., Koretsune, T., Xiangyu, G., Yamamoto, T., Brown, C.M., Kageyama, H., "Realization of Interlayer Ferromagnetic Interaction in  $\text{MnSb}_2\text{Te}_4$  toward the Magnetic Weyl Semimetal State," *Phys. Rev. B* **100**(19), 195103 (2019).
- Murphy, R.P., Riedel, Z.W., Nakatani, M.A., Salipante, P.F., Weston, J.S., Hudson, S.D., Weigandt, K.M., "Capillary RheoSANS: Measuring the Rheology and Nanostructure of Complex Fluids at High Shear Rates," *Soft Matter* **16**(27), 6285 (2020). [CHRSN]
- Murphy, R.P., Hatch, H.W., Mahynski, N.A., Shen, V.K., Wagner, N.J., "Dynamic Arrest of Adhesive Hard Rod Dispersions," *Soft Matter* **16**(5), 1279 (2020). [CHRSN]
- Murray, P.D., Gilbert, D.A., Grutter, A.J., Kirby, B.J., Hernández-Maldonado, D., Varela, M., Brubaker, Z.E., Liyanage, W.L.N.C., Chopdekar, R.V., Taufour, V., Zieve, R.J., Jeffries, J.R., Arenholz, E., Takamura, Y., Borchers, J.A., Liu, K., "Interfacial-Redox-Induced Tuning of Superconductivity in  $\text{YBa}_2\text{Cu}_3\text{O}_{7-\delta}$ ," *ACS Appl. Mater. Interfaces* **12**(4), 4741 (2020).
- Musicó, B., Wright, Q., Ward, T.Z., Grutter, A., Arenholz, E., Gilbert, D., Mandrus, D., Keppens, V., "Tunable Magnetic Ordering through Cation Selection in Entropic Spinel Oxides," *Phys. Rev. Mater.* **3**(10), 104416 (2019).
- Naidjonoka, P., Hernandez, M.A., Pålsson, G.K., Heinrich, F., Stålbrand, H., Nylander, T., "On the Interaction of Softwood Hemicellulose with Cellulose Surfaces in Relation to Molecular Structure and Physicochemical Properties of Hemicellulose," *Soft Matter*, in press.
- Nayem, J., Zhang, Z., Tomlinson, A., Zarraga, I.E., Wagner, N.J., Liu, Y., "Micellar Morphology of Polysorbate 20 and 80 and their Ester Fractions in Solution via Small-Angle Neutron Scattering," *J. Pharm. Sci.* **109**(4), 1498 (2020).
- Need, R.F., Bac, S.-K., Liu, X., Lee, S., Kirby, B.J., Dobrowolska, M., Kossut, J., Furdyna, J.K., "Magnetic Properties and Electronic Origin of the Interface between Dilute Magnetic Semiconductors with Orthogonal Magnetic Anisotropy," *Phys. Rev. Mater.* **4**(5), 054410 (2020).
- Need, R.F., Lauzier, J., Sutton, L., Kirby, B.J., de la Venta, J., "Using Structural Phase Transitions to Enhance the Coercivity of Ferromagnetic Films," *APL Mater.* **7**(10), 101115 (2019).
- Neil, C.W., Hjelm, R.P., Hawley, M.E., Watkins, E.B., Cockreham, C., Wu, D., Mao, Y., Fischer, T.B., Stokes, M.R., Xu, H., "Small-Angle Neutron Scattering (SANS) Characterization of Clay- and Carbonate-Rich Shale at Elevated Pressures," *Energ. Fuel.* **34**(7), 8178 (2020). [CHRSN]
- Nguyen, N.A., Shen, H., Liu, Y., Mackay, M.E., "Kinetics and Mechanism of Poly(3-Hexylthiophene) Crystallization in Solution under Shear-flow," *Macromolecules* **53**(14), 5795 (2020).
- Nguyen, T., Han, F., Andrejevic, N., Pablo-Pedro, R., Apte, A., Tsurimaki, Y., Ding, Z., Zhang, K., Alatas, A., Alp, E.E., Chi, S., Fernandez-Baca, J., Matsuda, M., Tennant, D.A., Zhao, Y., Xu, Z., Lynn, J.W., Huang, S., Li, M., "Topological Singularity Induced Chiral Kohn Anomaly in a Weyl Semimetal," *Phys. Rev. Lett.* **124**(23), 236401 (2020).
- Ni, X., He, Y., Wang, H., "Expanding the Metrology of Coulombic Efficiency using Neutron Depth Profiling," *Radiat. Eff. Defect. S.* **175**(3-4), 356 (2020).
- Nico, J.S., Jacobson, D.L., "Muhammad Arif (1954-2018)," *Neutron News* **31**(1), 6 (2020).
- Nie, Z., Ong, S., Hussey, D.S., LaManna, J.M., Jacobson, D.L., Koenig, Jr., G.M., "Probing Transport Limitations in Thick Sintered Battery Electrodes with Neutron Imaging," *Mol. Sys. Des. Eng.* **5**(1), 245 (2020).
- Noferini, D., Faraone, A., Rossi, M., Mamontov, E., Fratini, E., Baglioni, P., "Disentangling Polymer Network and Hydration Water Dynamics in Polyhydroxyethyl Methacrylate Physical and Chemical Hydrogels," *J. Phys. Chem. C* **123**(31), 19183 (2019). [CHRSN]
- Noh, H.-J., Im, Y.-K., Yu, S.-Y., Seo, J.-M., Mahmood, J., Yildirim, T., Baek, J.-B., "Vertical Two-Dimensional Layered Fused Aromatic Ladder Structure," *Nat. Commun.* **11**(1), 2021 (2020).
- Odette, G.R., Yamamoto, T., Williams, T.J., Nanstad, R.K., English, C.A., "On the History and Status of Reactor Pressure Vessel Steel Ductile to Brittle Transition Temperature Shift Prediction Models," *J. Nucl. Mater.* **526**, 151863 (2019).
- Oktawiec, J., Jiang, H.Z.H., Vitillo, J.G., Reed, D.A., Darago, L.E., Trump, B.A., Bernales, V., Li, H., Colwell, K.A., Furukawa, H., Brown, C.M., Gagliardi, L., Long, J.R., "Negative Cooperativity upon Hydrogen Bond-Stabilized  $\text{O}_2$  Adsorption in a Redox-Active Metal-Organic Framework," *Nat. Chem.* **11**(1), 3087 (2020).

- Ortiz, B.R., Gomes, L.C., Morey, J.R., Winiarski, M., Bordelon, M., Mangum, J.S., Oswald, I.W.H., Rodriguez-Rivera, J.A., Neilson, J.R., Wilson, S.D., Ertekin, E., McQueen, T.M., Toberer, E.S., "New Kagome Prototype Materials: Discovery of  $KV_3Sb_5$ ,  $RbV_3Sb_5$ , and  $CsV_3Sb_5$ ," *Phys. Rev. Mater.* **3**(9), 094407 (2019). [CHRS]
- Osti, N.C., Matsumoto, R.A., Thompson, M.W., Cummings, P.T., Tyagi, M., Mamontov, E., "Microscopic Dynamics in an Ionic Liquid Augmented with Organic Solvents," *J. Phys. Chem. C* **123**(32), 19354 (2019).
- Pajerowski, D.M., Escanhoela, Jr., C.A., Haskel, D., Prisk, T.R., Frontzek, M.D., Phelan, D., Mihalik, Jr., M., Mihalik, M., "Nd Ordering, Cluster Formation, and the Origin of Negative Magnetization in  $NdMn_{0.8}Fe_{0.2}O_{3+\delta}$ ," *J. Magn. Magn. Mater.* **497**, 165968 (2020). [CHRS]
- Pajerowski, D.M., Krayner, L.A., Jeon, H., Borchers, J.A., Biswas, A., Ravel, B., "Correlation of Cation Deficiency and Nanostructure to Decreased Magnetism in a Ferroelectric  $BiMnO_3$  Film," *J. Appl. Phys.* **126**(8), 085303 (2019). [CHRS]
- Pajerowski, D.M., Pratt, D.K., Hahn, S.E., Tian, W., Granroth, G.E., Kolesnikov, A.I., Taskin, A.A., Ando, Y., McQueeney, R.J., "Spin Waves Above and Below the Verwey Transition in  $TbBaFe_2O_5$ ," *Phys. Rev. B* **101**(6), 064418 (2020).
- Pan, L., Grutter, A., Zhang, P., Che, X., Nozaki, T., Stern, A., Street, M., Zhang, B., Casas, B., He, Q.L., Choi, E.S., Disseler, S.M., Gilbert, D.A., Yin, G., Shao, Q., Deng, P., Wu, Y., Liu, X., Kou, X., Masashi, S., Han, X., Binek, C., Chambers, S., Xia, J., Wang, K.L., "Observation of Quantum Anomalous Hall Effect and Exchange Interaction in Topological Insulator/Antiferromagnet Heterostructure," *Adv. Mater.*, in press.
- Pandey, A., Miao, P., Klemm, M., He, H., Wang, H., Qian, X., Lynn, J.W., Aronson, M.C., "Correlations and Incipient Antiferromagnetic Order within the Linear Mn Chains of Metallic  $Ti_4MnBi_2$ ," *Phys. Rev. B* **102**(1), 014406 (2020).
- Papachristodoulou, M., Douth, J., Leung, H.S.B., Church, A., Charleston, T., Clifton, L.A., Butler, P.D., Roberts, C.J., Bracewell, D.G., "In Situ Neutron Scattering of Antibody Adsorption during Protein A Chromatography," *J. Chromatogr. A* **1617**, 460842 (2020). [CHRS]
- Pei, J., Wang, J.-X., Shao, K., Yang, Y., Cui, Y., Wu, H., Zhou, W., Li, B., Qian, G., "Engineering Microporous Ethane-Trapping Metal-Organic Frameworks for Boosting Ethane/Ethylene Separation," *J. Mater. Chem. A* **8**(7), 3613 (2020).
- Pei, W.-Y., Yang, J., Wu, H., Zhou, W., Yang, Y.-W., Ma, J.-F., "A Calix[4]Resorcinarene-Based Giant Coordination Cage: Controlled Assembly and Iodine Uptake," *Chem. Commun.* **56**(16), 2491 (2020).
- Peng, J., Cantillo, N.M., Nelms, K.M., Roberts, L.S., Goenaga, G., Imel, A., Barth, B.A., Dadmun, M., Heroux, L., Hayes, D.G., Zawodzinski, T., "Electron Transfer in Microemulsion-Based Electrolytes," *ACS Appl. Mater. Interfaces*, in press.
- Peng, X., Kulkarni, D., Huang, Y., Omasta, T.J., Ng, B., Zheng, Y., Wang, L., LaManna, J.M., Hussey, D.S., Varcoe, J.R., Zhenyuk, I.V., Mustain, W.E., "Using Operando Techniques to Understand and Design High Performance and Stable Alkaline Membrane Fuel Cells," *Nat. Commun.* **11**(1), 3561 (2020).
- Phan, M.D., Korotych, O.I., Brady, N.G., Davis, M.M., Satija, S.K., Ankner, J.F., Bruce, B.D., "X-ray and Neutron Reflectivity Studies of Styrene-Maleic Acid Copolymer Interactions with Galactolipid-Containing Monolayers," *Langmuir* **36**(14), 3970 (2020).
- Phan, M.D., Lee, K.Y., Lee, J., Satija, S.K., Shin, K., "The Effect of Cholesterol on Membrane Binding and Self-Assembly of Collagen Fibrils," *Langmuir* **36**(26), 7259 (2020).
- Phan, T.Q., Strantza, M., Hill, M.R., Gnaupel-Herold, T.H., Heigel, J., D'Elia, C.R., DeWald, A.T., Clausen, B., Pagan, D.C., Ko, J.Y.P., Brown, D.W., Levine, L.E., "Elastic Residual Strain and Stress Measurements and Corresponding Part Deflections of 3D Additive Manufacturing Builds of IN625 AM-Bench Artifacts using Neutron Diffraction, Synchrotron X-ray Diffraction, and Contour Method," *Integr. Mater. Manuf. Innovat.* **8**(3), 318 (2019).
- Ping, W., Wang, C., Lin, Z., Hitz, E., Yang, C., Wang, H., Hu, L., "Reversible Short-Circuit Behaviors in Garnet-Based Solid-State Batteries," *Adv. Energy Mater.* **10**(25), 2000702 (2020).
- Piva, M.M., Tartaglia, R., Freitas, G.S., Souza, J.C., Christovam, D.S., Thomas, S.M., Leão, J.B., Ratcliff, W., Lynn, J.W., Lane, C., Zhu, J.-X., Thompson, J.D., Rosa, P.F.S., Adriano, C., Granado, E., Pagliuso, P.G., "Electronic and Magnetic Properties of Stoichiometric  $CeAuBi_2$ ," *Phys. Rev. B* **101**(21), 214431 (2020).
- Plymale, A.E., Wells, J.R., Pearce, C.I., Brislawn, C.J., Graham, E.B., Cheeke, T.E., Allen, J.L., Fansler, S.J., Arey, B.W., Bowden, M.E., Saunders, D.L., Danna, V.G., Tyrrell, K.J., Weaver, J.L., Sjöblom, R., Paul, R., McCloy, J.S., Hjärthner-Holdar, E., Englund, M., Ogenhall, E., Peeler, D.K., Kruger, A.A., "Niche Partitioning of Microbial Communities at an Ancient Vitified Hillfort: Implications for Vitified Radioactive Waste Disposal," *Geomicrobiol. J.*, in press.
- Podlesnyak, A., Prokhnenko, O., Nikitin, S.E., Kolesnikov, A.I., Matsuda, M., Dissanayake, S.E., Prisk, T.R., Nojiri, H., Diaz-Ortega, I.F., Kidder, M.K., Anovitz, L.M., "Magnetic Ground State and Magnetic Excitations in Black Dioptase  $Cu_6Si_6O_{18}$ ," *Phys. Rev. B* **100**(18), 184401 (2019).



- Pokorski, J.K., Hore, M.J.A., "Structural Characterization of Protein-Polymer Conjugates for Biomedical Applications with Small-Angle Scattering," *Curr. Opin. Colloid In.* **42**, 157 (2019). [CHNRNS]
- Poling-Skutvik, R., Slim, A.H., Narayanan, S., Conrad, J.C., Krishnamoorti, R., "Soft Interactions Modify the Diffusive Dynamics of Polymer-Grafted Nanoparticles in Solutions of Free Polymer," *ACS Macro Lett.* **8**(8), 917 (2019).
- Pond, M.P., Eells, R., Treece, B.W., Heinrich, F., Lösche, M., Roux, B., "Membrane Anchoring of Hck Kinase via the Intrinsically Disordered SH4-U and Length Scale Associated with Subcellular Localization," *J. Mol. Biol.* **432**(9), 2985 (2020).
- Popov, I., Sacchi, R.L., Sanders, N.C., Matsumoto, R.A., Thompson, M.W., Osti, N.C., Kobayashi, T., Tyagi, M., Mamontov, E., Pruski, M., Cummings, P.T., Sokolov, A.P., "Critical Role of Anion-Solvent Interactions for Dynamics of Solvent-in-Salt Solutions," *J. Phys. Chem. C* **124**(16), 8457 (2020). [CHNRNS]
- Porter, Z., Need, R.F., Ahadi, K., Zhao, Y., Xu, Z., Kirby, B.J., Lynn, J.W., Stemmer, S., Wilson, S.D., "Correlating Magnetic Structure and Magnetotransport in Semimetal Thin Films of  $\text{Eu}_{1-x}\text{Sm}_x\text{TiO}_3$ ," *Phys. Rev. Mater.* **4**(5), 054411 (2020).
- Potashnikov, D., Caspi, E.N., Pesach, A., Kota, S., Sokol, M., Hanner, L.A., Barsoum, M.W., Evans, H.A., Eyal, A., Keren, A., Rivin, O., "Magnetic Properties of  $(\text{Fe}_{1-x}\text{Mn}_x)_2\text{AlB}_2$  and the Impact of Substitution on the Magnetocaloric Effect," *Phys. Rev. Mater.*, in press.
- Poudel, L., Lawrence, J.M., Wu, L.S., Ehlers, G., Qiu, Y., May, A.F., Ronning, F., Lumsden, M.D., Mandrus, D., Christianson, A.D., "Multicomponent Fluctuation Spectrum at the Quantum Critical Point in  $\text{CeCu}_{6-x}\text{Ag}_x$ ," *Npj Quantum Mater.* **4**(1), 52 (2019). [CHNRNS]
- Prabhu, V.M., Ali, S., Bleuel, M., Mao, Y., Ma, Y., "Ultra-Small Angle Neutron Scattering to Study Droplet Formation in Polyelectrolyte Complex Coacervates," in "Methods in Enzymology," edited by Chenoweth, D.M. (Elsevier, Amsterdam, Netherlands), in press. [CHNRNS]
- Prisk, T.R., Kolesnikov, A.I., Granroth, G.E., Lin, J.-L., Heuser, B.J., "Vibrational Modes and Quantum Zero-Point Energy of Hydrogen in  $\text{ZrH}_{0.0155}$  and  $\text{ZrH}_2$ ," *J. Alloy Compd.* **818**, 152832 (2020).
- Prisk, T.R., Hanna, S., Azuah, R.T., "Self-Diffusion of Liquid Hydrogen: A Quasi-Elastic Neutron Scattering Study," *J. Low Temp. Phys.*, in press.
- Pritchard, K., Osovitzky, A., Ziegler, J., Binkley, E., Tsai, P., Hadad, N., Jackson, M., Hurlbut, C., Baltic, G.M., Majkrzak, C.F., Maliszewskyj, N.C., " $^6\text{LiF:ZnS(Ag)}$  Neutron Detector Performance Optimized using Waveform Recordings and ROC Curves," *IEEE T. Nucl. Sci.* **67**(1), 414 (2020).
- Puster, L.O., Stanley, C.B., Uversky, V.N., Curtis, J.E., Krueger, S., Chu, Y., Peterson, C.B., "Characterization of an Extensive Interface on Vitronectin for Binding to Plasminogen Activator Inhibitor-1: Adoption of Structure in an Intrinsically Disordered Region," *Biochemistry-US* **58**(51), 5117 (2019).
- Qavi, S., Foudazi, R., "Rheological Characteristics of Mesophases of Block Copolymer Solutions," *Rheol. Acta* **58**(8), 483 (2019).
- Qiu, B., Zhang, M., Lee, S.-Y., Liu, H., Wynn, T.A., Wu, L., Zhu, Y., Wen, W., Brown, C.M., Zhou, D., Liu, Z., Meng, Y.S., "Metastability and Reversibility of Anionic Redox-Based Cathode for High-Energy Rechargeable Batteries," *Cell Rep. Phys. Sci.* **1**(3), 100028 (2020).
- Quarterman, P., Satchell, N., Kirby, B.J., Loloee, R., Burnell, G., Birge, N.O., Borchers, J.A., "Distortions to the Penetration Depth and Coherence Length of Superconductor/Normal-Metal Superlattices," *Phys. Rev. Mater.* **4**(7), 074801 (2020).
- Ran, S., Eckberg, C., Ding, Q.-P., Furukawa, Y., Metz, T., Saha, S.R., Liu, I.-L., Zic, M., Kim, H., Paglione, J., Butch, N.P., "Nearly Ferromagnetic Spin-Triplet Superconductivity," *Science* **365**(6454), 684 (2019). [CHNRNS]
- Ran, S., Kim, H., Lin, I.-L., Saha, S.R., Hayes, I., Metz, T., Eo, Y.S., Paglione, J., Butch, N.P., "Enhancement and Reentrance of Spin Triplet Superconductivity in  $\text{UTe}_2$  under Pressure," *Phys. Rev. B* **101**(14), 140503(R) (2020).
- Ran, S., Liu, I.-L., Eo, Y.S., Campbell, D.J., Neves, P.M., Fuhrman, W.T., Saha, S.R., Eckberg, C., Kim, H., Graf, D., Balakirev, F., Singleton, J., Paglione, J., Butch, N.P., "Extreme Magnetic Field-Boosted Superconductivity," *Nat. Phys.* **15**, 1250 (2019). [CHNRNS]
- Richards, J.J., Riley, J.K., "Dielectric RheoSANS: A Mutual Electrical and Rheological Characterization Technique using Small-Angle Neutron Scattering," *Curr. Opin. Colloid In.* **42**, 110 (2019).
- Rickeard, B.W., Nguyen, M.H.L., DiPasquale, M., Yip, C.G., Baker, H., Heberle, F.A., Zuo, X., Kelley, E.G., Nagao, M., Marquardt, D., "Transverse Lipid Organization Dictates Bending Fluctuations in Model Plasma Membranes," *Nanoscale* **12**(3), 1438 (2020). [CHNRNS]

- Rinehart, S.J., Nguyen, B.N., Viggiano, R.P., Meador, M.A.B., Dadmun, M.D., "Quantitative Evaluation of the Hierarchical Porosity in Polyimide Aerogels and Corresponding Solvated Gels," *ACS Appl. Mater. Interfaces* **12**(27), 30457 (2020).
- Rinehart, S.J., Smart, T., Dougherty, J., Dadmun, M.D., "Impact of Substrate Rigidity on the Structure of Multilayer Nanoscale ITO Films: Implications for Flexible Electronic Devices," *ACS Appl. Nano Mater.* **3**(3), 2383 (2020).
- Rinehart, S.J., Yuan, G., Dadmun, M.D., "The Interplay of Thermodynamics and Kinetics: Imparting Hierarchical Control Over Film Formation of Self-Stratified Blends," *Soft Matter* **16**(5), 1287 (2020).
- Rippy, G., Trinh, L., Kane, A.M., Ionin, A.L., Lee, M.S., Chopdekar, R.V., Christiansen-Salameh, J.M., Gilbert, D.A., Grutter, A.J., Murray, P.D., Holt, M.V., Cai, Z., Liu, K., Takamura, Y., Kukreja, R., "X-ray Nanodiffraction Studies of Ionically Controlled Nanoscale Phase Separation in Cobaltites," *Phys. Rev. Mater.* **3**(8), 082001(R) (2019).
- Rostom, S., White, B.T., Yuan, G., Saito, T., Dadmun, M.D., "Polymer Chain Diffusion in All-Polymer Nanocomposites: Confinement vs. Chain Acceleration," *J. Phys. Chem. C*, in press.
- Rubinson, K.A., Mountain, R.D., "Ion and Water Transport Reasonably Involves Rotation and Pseudorotation: Measurement and Modeling the Temperature Dependence of Small-Angle Neutron Scattering of Aqueous  $\text{SrI}_2$ ," *Phys. Chem. Chem. Phys.* **22**(24), 13479 (2020).
- Rus, E.D., Dura, J.A., "In Situ Neutron Reflectometry Study of Solid Electrolyte Interface (SEI) Formation on Tungsten Thin-Film Electrodes," *ACS Appl. Mater. Interfaces* **11**(50), 47553 (2019).
- Rytting, B.M., Harper, M.R., Edmond, K.V., Zhang, Y., Kilpatrick, P.K., "High-Purity Vanadyl Porphyrins: Their Aggregation and Effect on the Aggregation of Asphaltenes," *Energ. Fuel* **34**(1), 164 (2020).
- Saini, A., Borchers, J.A., George, S., Maranville, B.B., Krycka, K.L., Dura, J.A., Theis-Bröhl, K., Wolff, M., "Layering of Magnetic Nanoparticles at Amorphous Magnetic Templates with Perpendicular Anisotropy," *Soft Matter*, in press. [CHRS]
- Samant, S., Basutkar, M., Singh, M., Masud, A., Grabowski, C.A., Kisslinger, K., Strzalka, J., Yuan, G., Satija, S., Apata, I., Raghavan, D., Durstock, M., Karim, A., "Effect of Molecular Weight and Layer Thickness on the Dielectric Breakdown Strength of Neat and Homopolymer Swollen Lamellar Block Copolymer Films," *ACS Appl. Polym. Mater.*, in press.
- Sanchez-Fernandez, A., Leung, A.E., Kelley, E.G., Jackson, A.J., "Complex by Design: Hydrotrope-Induced Micellar Growth in Deep Eutectic Solvents," *J. Colloid Interf. Sci.*, in press. [CHRS]
- Sarapas, J.M., Martin, T.B., Chremos, A., Douglas, J.F., Beers, K.L., "Bottlebrush Polymers in the Melt and Polyelectrolytes in Solution Share Common Structural Features," *P. Natl. A. Sci. USA* **117**(10), 5168 (2020).
- Sarenac, D., Kapahi, C., Chen, W., Clark, C.W., Cory, D.G., Huber, M.G., Taminiau, I., Zhernenkov, K., Pushin, D.A., "Generation and Detection of Spin-Orbit Coupled Neutron Beams," *P. Natl. A. Sci. USA* **116**(41), 20328 (2019).
- Sarsour, M., Amadio, J., Anderson, E., Barrón-Palos, L., Crawford, B., Crawford, C., Esposito, D., Fox, W., Francis, I., Fry, J., Gardiner, H., Haddock, C., Holly, A., Hoogerheide, S.F., Korsak, K., Lieers, J., Magers, S., Maldonado-Velázquez, M., Mayorov, D., Mumm, H.P., Nico, J.S., Okudaira, T., Paudel, C., Santra, S., Shimizu, H.M., Snow, W.M., Sprow, A., Steen, K., Swanson, H.E., Töveßson, F., Vanderwerp, J., Yergeau, P.A., "Neutron Spin Rotation Measurements," *EPJ Web Conf.* **219**, 06002 (2019).
- Säubert, S., Scheie, A., Duvinage, C., Kindervater, J., Zhang, S., Changlani, H.J., Xu, G., Koohpayeh, S.M., Tchernyshyov, O., Broholm, C.L., Pfeleiderer, C., "Orientation Dependence of the Magnetic Phase Diagram of  $\text{Yb}_2\text{Ti}_2\text{O}_7$ ," *Phys. Rev. B* **101**(17), 174434 (2020).
- Scheie, A., Ross, K., Stavropoulos, P.P., Seibel, E., Rodriguez-Rivera, J.A., Tang, J.A., Li, Y., Kee, H.-Y., Cava, R.J., Broholm, C., "Counterrotating Magnetic Order in the Honeycomb Layers of  $\text{NaNi}_2\text{BiO}_{6-\delta}$ ," *Phys. Rev. B* **100**(21), 214421 (2019). [CHRS]
- Schneider, K., Verkoyen, P., Krappel, M., Gardiner, C., Schweins, R., Frey, H., Sottmann, T., "Efficiency Boosting of Surfactants with Poly(Ethylene Oxide)-Poly(Alkyl Glycidyl Ether)s - A New Class of Amphiphilic Polymers," *Langmuir*, in press. [CHRS]
- Schorr, S., Gurieva, G., Guc, M., Dimitrievska, M., Pérez-Rodríguez, A., Izquierdo-Roca, V., Schnohr, C.S., Kim, J., Jo, W., Merino, J.M., "Point Defects, Compositional Fluctuations, and Secondary Phases in Non-Stoichiometric Kesterites," *J. Phys. Energy* **2**(1), 012002 (2020).
- Schroeder, A., Bhattarai, S., Gebretsadik, A., Adawi, H., Lussier, J.-G., Krycka, K.L., "Magnetic Correlations in the Disordered Ferromagnetic Alloy Ni-V Revealed with Small Angle Neutron Scattering," *AIP Adv.* **10**(1), 015036 (2020). [CHRS]

- Schueller, E.C., Kitchaev, D.A., Zuo, J.L., Bocarsly, J.D., Cooley, J.A., Van der Ven, A., Wilson, S.D., Seshadri, R., "Structural Evolution and Skyrmonic Phase Diagram of the Lacunar Spinel  $\text{GaMo}_4\text{Se}_8$ ," *Phys. Rev. Mater.* **4**(6), 064402 (2020).
- Scott, D., Tullman, J., Kelman, Z., Marino, J., Silin, V., "Enzyme-Mediated Assembly of Chimeric Membrane Proteins at Phospholipid Bilayers," *Eng. Rep.* **1**(2), e212040 (2019).
- Scott, H.L., Skinkle, A., Kelley, E.G., Waxham, M.N., Levental, I., Heberle, F.A., "On the Mechanism of Bilayer Separation by Extrusion, or Why Your LUVs are not Really Unilamellar," *Biophys. J.* **117**(8), 1381 (2019). [CHNRNS]
- Seidel, Z.P., Lee, Jr., C.T., "Enhanced Activity of the Cellulase Enzyme  $\beta$ -Glucosidase upon Addition of an Azobenzene-Based Surfactant," *ACS Sustain. Chem. Eng.* **8**(4), 1751 (2020). [CHNRNS]
- Senses, E., Darvishi, S., Tyagi, M.S., Faraone, A., "Entangled Polymer Dynamics in Attractive Nanocomposite Melts," *Macromolecules* **53**(12), 4982 (2020). [CHNRNS]
- Sepulveda-Medina, P.I., Wang, C., Li, R., Fukuto, M., Weiss, R.A., Vogt, B.D., "Kinetically Controlled Morphology in Copolymer-Based Hydrogels Crosslinked by Crystalline Nanodomains Determines Efficacy of Ice Inhibition," *Mol. Sys. Des. Eng.* **5**(3), 645 (2020). [CHNRNS]
- Shan, L., Xie, R., Wagner, N.J., He, H., Liu, Y., "Microstructure of Neat and SBS Modified Asphalt Binder by Small-Angle Neutron Scattering," *Fuel* **253**, 1589 (2019). [CHNRNS]
- Shao, K., Pei, J., Wang, J.-X., Yang, Y., Cui, Y., Zhou, W., Yildirim, T., Li, B., Chen, B., Qian, G., "Tailoring the Pore Geometry and Chemistry in Microporous Metal-Organic Frameworks for High Methane Storage Working Capacity," *Chem. Commun.* **55**(76), 11402 (2019).
- Sharma, V.K., Nagao, M., Rai, D.K., Mamontov, E., "Membrane Softening by Nonsteroidal Anti-Inflammatory Drugs Investigated by Neutron Spin Echo," *Phys. Chem. Chem. Phys.* **21**(36), 20211 (2019). [CHNRNS]
- Sharma, V.K., Mamontov, E., Tyagi, M., "Effects of NSAIDs on the Nanoscopic Dynamics of Lipid Membrane," *BBA - Biomembranes* **1862**(2), 183100 (2020). [CHNRNS]
- Shen, F.-R., Hu, F.-X., Yu, Z.-B., Zhou, H.-B., Wu, H., Huang, Q.-Z., Hao, J.-Z., Gao, Y.-H., Qiao, K.-M., Li, J., Zhang, C., Liang, W.-H., He, L.-H., Wang, J., Liang, T.-J., Sun, J.-R., Shen, B.-G., "Neutron Diffraction Study on Hydrostatic Pressure Regulated Magnetostructural Transition and Magnetocaloric Effect in  $\text{MnNi}_{1-x}\text{Fe}_x\text{Si}_{1-y}\text{Ge}_y$  Alloys," *J. Appl. Phys.* **127**(13), 133905 (2020).
- Shen, F., Zhou, H., Hu, F., Wang, J.-T., Deng, S., Wang, B., Wu, H., Huang, Q., Wang, J., Chen, J., He, L., Hao, J., Yu, Z., Liang, F., Liang, T., Sun, J., Shen, B., "Cone-Spiral Magnetic Ordering Dominated Lattice Distortion and Giant Negative Thermal Expansion in Fe-Doped  $\text{MnNiGe}$  Compounds," *Mater. Horiz.* **7**(3), 804 (2020).
- Shi, N., Sanson, A., Gao, Q., Sun, Q., Ren, Y., Huang, Q., Oliveira de Souza, D., Xing, X., Chen, J., "Strong Negative Thermal Expansion in a Low-Cost and Facile Oxide of  $\text{Cu}_2\text{P}_2\text{O}_7$ ," *J. Am. Chem. Soc.* **142**(6), 3088 (2020).
- Shi, Q., Zhang, D.-X., Yin, H., Qiu, Y.-P., Zhou, L.-L., Chen, C., Wu, H., Wang, P., "Noble-Metal-Free Ni-W-O-Derived Catalysts for High-Capacity Hydrogen Production from Hydrazine Monohydrate," *ACS Sustain. Chem. Eng.* **8**(14), 5595 (2020).
- Shih, K.-C., Su, C.-Y., Chang, S.-Y., Jensen, G., Hua, C.-C., Nieh, M.-P., Lai, H.-M., "Correlation of the Hierarchical Structure with Rheological Behavior of Polypseudorotaxane Gel Composed of Pluronic and  $\beta$ -Cyclodextrin," *Soft Matter* **16**(21), 4990 (2020). [CHNRNS]
- Shim, J., Bates, F.S., Lodge, T.P., "Bicontinuous Microemulsions in Partially Charged Ternary Polymer Blends," *ACS Macro Lett.* **8**(9), 1166 (2019).
- Shim, J., Xie, S., Bates, F.S., Lodge, T.P., "Effect of Ion Concentration on the Formation of Bicontinuous Microemulsions in Partially Charged Ternary Polymer Blends," *Macromolecules* **52**(23), 9416 (2019).
- Shoup, J.E., Arena, D.A., Borchers, J.A., Kirby, B.J., Caruana, A.J., Kinane, C.J., Langridge, S., Rogers, M., Cespedes, O., "Structural Studies of Magnetic  $\text{C}_{60}/\text{Cu}$  Multilayers," *AIP Adv.* **10**(2), 025312 (2020).
- Shrestha, U.M., Vailonis, K.M., Jenkins, D.M., Dadmun, M.D., "Investigating the Copolymerization of Ligands into Metal-Organic Nanotubes using Small-Angle Neutron Scattering: Implications for Nanostraws," *ACS Appl. Nano Mater.* **3**(6), 5605 (2020).
- Sinha, N.J., Wu, D., Kloxin, C.J., Saven, J.G., Jensen, G.V., Pochan, D.J., "Polyelectrolyte Character of Rigid Rod Peptide Bundlemer Chains Constructed via Hierarchical Self-Assembly," *Soft Matter* **15**(48), 9858 (2019). [CHNRNS]
- Skorupskii, G., Trump, B.A., Kasel, T.W., Brown, C.M., Hendon, C.H., Dincă, M., "Efficient and Tunable One-Dimensional Charge Transport in Layered Lanthanide Metal-Organic Frameworks," *Nat. Chem.* **12**(2), 131 (2020).



- Skripov, A.V., Dimitrievska, M., Babanova, O.A., Skoryunov, R.V., Soloninin, A.V., Morelle, F., Filinchuk, Y., Faraone, A., Wu, H., Zhou, W., Udovic, T.J., "Low-Temperature Rotational Tunneling of Tetrahydroborate Anions in Lithium Benzimidazolate-Borohydride  $\text{Li}_2(\text{blm})\text{BH}_4$ ," *J. Phys. Chem. C* **123**(34), 20789 (2019). [CHRS]
- Smaha, R.W., He, W., Jiang, J.M., Wen, J., Jiang, Y.-F., Shekelton, J.P., Titus, C.J., Wang, S.G., Chen, Y.-S., Teat, S.J., Aczel, A.A., Zhao, Y., Xu, G., Lynn, J.W., Jiang, H.-C., Lee, Y.S., "Materializing Rival Ground States in the Barlowite Family of Kagome Magnets: Quantum Spin Liquid, Spin Ordered, and Valence Bond Crystal States," *Npj Quantum Mater.* **5**, 23 (2020).
- Snow, W.M., Apanavicius, J., Dickerson, K.A., Devaney, J.S., Drabek, H., Reid, A., Shen, B., Woo, J., Haddock, C., Alexeev, E., Peters, M., "Internal Consistency of Neutron Coherent Scattering Length Measurements from Neutron Interferometry and from Neutron Gravity Reflectometry," *Phys. Rev. D* **101**(6), 062004 (2020).
- Snow, W.M., Dickerson, K.A., Devaney, J.S., Haddock, C., "Calculations of Neutron Reflectivity in the eV Energy Range from Mirrors made of Heavy Nuclei with Neutron-Nucleus Resonances," *Phys. Rev. A* **100**(2), 023612 (2019).
- Soles, C.L., Burns, A.B., Ito, K., Chan, E., Liu, J., Yee, A.F., Tyagi, M.S., "Importance of Sub-Nanosecond Fluctuations on the Toughness of Polycarbonate Glasses," *Macromolecules*, in press. [CHRS]
- Soloninin, A.V., Skoryunov, R.V., Babanova, O.A., Skripov, A.V., Dimitrievska, M., Udovic, T.J., "Comparison of Anion and Cation Dynamics in a Carbon-Substituted *Closo*-Hydroborate Salt:  $^1\text{H}$  and  $^{23}\text{Na}$  NMR Studies of Solid-Solution  $\text{Na}_2(\text{CB}_9\text{H}_{10})(\text{CB}_{11}\text{H}_{12})$ ," *J. Alloy Compd.* **800**, 247 (2019).
- Song, B.-Q., Yang, Q.-Y., Wang, S.-Q., Vandichel, M., Kumar, A., Crowley, C., Kumar, N., Deng, C.-H., GasconPerez, V., Lusi, M., Wu, H., Zhou, W., Zaworotko, M.J., "Reversible Switching between Nonporous and Porous Phases of a New SIFSIX Coordination Network Induced by a Flexible Linker Ligand," *J. Am. Chem. Soc.* **142**(15), 6896 (2020).
- Song, Y., Yuan, D., Lu, X., Xu, Z., Bourret-Courchesne, E., Birgeneau, R.J., "Strain-Induced Spin-Nematic State and Nematic Susceptibility Arising from  $2 \times 2$  Fe Clusters in  $\text{KFe}_{0.8}\text{Ag}_{1.2}\text{Te}_2$ ," *Phys. Rev. Lett.* **123**(24), 247205 (2019).
- Song, Y., Wang, W., Van Dyke, J.S., Pouse, N., Ran, S., Yazici, D., Schneidewind, A., Čermák, P., Qiu, Y., Maple, M.B., Morr, D.K., Dai, P., "Nature of the Spin Resonance Mode in  $\text{CeCoIn}_5$ ," *Comm. Phys.* **3**(1), 98 (2020). [CHRS]
- Song, Y., Hao, Y., Wang, S., Zhang, J., Huang, Q., Xing, X., Chen, J., "Complicated Magnetic Structure and its Strong Correlation with the Anomalous Hall Effect in  $\text{Mn}_3\text{Sn}$ ," *Phys. Rev. B* **101**(14), 144422 (2020).
- Song, Y., Huang, R., Liu, Y., Zhang, Z., Huang, Q., Jiang, Y., Wang, S., Li, L., Xing, X., Chen, J., "Magnetic-Field-Induced Strong Negative Thermal Expansion in  $\text{La}(\text{Fe},\text{Al})_{13}$ ," *Chem. Mater.*, in press.
- Song, Y., Sun, Q., Xu, M., Zhang, J., Hao, Y., Qiao, Y., Zhang, S., Huang, Q., Xing, X., Chen, J., "Negative Thermal Expansion in  $(\text{Sc},\text{Ti})\text{Fe}_2$  Induced by an Unconventional Magnetovolume Effect," *Mater. Horiz.* **7**(1), 275 (2020).
- Song, Y., Sun, Q., Yokoyama, T., Zhu, H., Li, Q., Huang, R., Ren, Y., Huang, Q., Xing, X., Chen, J., "Transforming Thermal Expansion from Positive to Negative: The Case of Cubic Magnetic Compounds of  $(\text{Zr},\text{Nb})\text{Fe}_2$ ," *J. Phys. Chem. Lett.* **11**(5), 1954 (2020).
- Songvilay, M., Giles-Donovan, N., Bari, M., Ye, Z.-G., Minns, J.L., Green, M.A., Xu, G., Gehring, P.M., Schmalzl, K., Ratcliff, W.D., Brown, C.M., Chernyshov, D., van Beek, W., Cochran, S., Stock, C., "Common Acoustic Phonon Lifetimes in Inorganic and Hybrid Lead Halide Perovskites," *Phys. Rev. Mater.* **3**(9), 093602 (2019).
- Songvilay, M., Wang, Z., Garcia Sakai, V., Guidi, T., Bari, M., Ye, Z.-G., Xu, G., Brown, K.L., Gehring, P.M., Stock, C., "Decoupled Molecular and Inorganic Framework Dynamics in  $\text{CH}_3\text{NH}_3\text{PbCl}_3$ ," *Phys. Rev. Mater.* **3**(12), 125406 (2019).
- Sonnenschein, J., Balz, C., Tutsch, U., Lang, M., Ryll, H., Rodriguez-Rivera, J.A., Nazmul Islam, A.T.M., Lake, B., Reuther, J., "Signatures for Spinons in the Quantum Spin Liquid Candidate  $\text{Ca}_{10}\text{Cr}_7\text{O}_{28}$ ," *Phys. Rev. B* **100**(17), 174428 (2019). [CHRS]
- Stock, C., Johnson, R.D., Giles-Donovan, N., Songvilay, M., Rodriguez-Rivera, J.A., Lee, N., Xu, X., Radaelli, P.G., Chapon, L.C., Bombardi, A., Cochran, S., Niedermayer, C., Schneidewind, A., Husges, Z., Lu, Z., Meng, S., Cheong, S.-W., "Spin-Wave Directional Anisotropies in Antiferromagnetic  $\text{Ba}_3\text{NbFe}_3\text{Si}_2\text{O}_{14}$ ," *Phys. Rev. B* **100**(13), 134429 (2019). [CHRS]
- Stock, C., Songvilay, M., Gehring, P.M., Xu, G., Roessli, B., "Broadband Critical Dynamics in Disordered Lead-Based Perovskites," *J. Phys.: Condens. Mat.* **32**(37), 374012 (2020).
- Sun, H., Li, X., Zhou, Y., Yu, J., Frandsen, B.A., Wu, S., Xu, Z., Jiang, S., Huang, Q., Bourret-Courchesne, E., Sun, L., Lynn, J.W., Birgeneau, R.J., Wang, M., "Nonsuperconducting Electronic Ground State in Pressurized  $\text{BaFe}_2\text{S}_3$  and  $\text{BaFe}_2\text{S}_{2.5}\text{Se}_{0.5}$ ," *Phys. Rev. B* **101**(20), 205129 (2020).

- Sun, R., Jin, S., Gu, L., Zhang, Q., Huang, Q., Ying, T., Peng, Y., Deng, J., Yin, Z., Chen, X., "Intercalating Anions between Terminated Anion Layers: Unusual Ionic S-Se Bonds and Hole-Doping Induced Superconductivity in  $\text{S}_{0.24}(\text{NH}_3)_{0.26}\text{Fe}_2\text{Se}_2$ ," *J. Am. Chem. Soc.* **141**(35), 13849 (2019).
- Sun, W., Wang, H.-W., Vlcek, L., Peng, J., Brady, A.B., Osti, N.C., Mamontov, E., Tyagi, M., Nanda, J., Greenbaum, S.G., Kent, P.R.C., Naguib, M., "Multiscale and Multimodal Characterization of 2D Titanium Carbonitride MXene," *Adv. Mater. Interfaces* **7**(11), 1902207 (2020). [CHNRS]
- Sundar, S., Gheidi, S., Akintola, K., Côté, A.M., Dunsiger, S.R., Ran, S., Butch, N.P., Saha, S.R., Paglione, J., Sonier, J.E., "Coexistence of Ferromagnetic Fluctuations and Superconductivity in the Actinide Superconductor  $\text{UTe}_2$ ," *Phys. Rev. B* **100**(14), 140502(R) (2019).
- Sunday, D.F., Chremos, A., Martin, T.B., Chang, A.B., Burns, A.B., Grubbs, R.H., "Concentration Dependence of the Size and Symmetry of a Bottlebrush Polymer in a Good Solvent," *Macromolecules*, in press.
- Sunday, D.F., Martin, T.B., Chang, A.B., Burns, A.B., Grubbs, R.H., "Addressing the Challenges of Modeling the Scattering from Bottlebrush Polymers in Solution," *J. Polym. Sci.* **58**(7), 988 (2020).
- Tan, K.C., Yu, Y., Chen, R., He, T., Jing, Z., Pei, Q., Wang, J., Chua, Y.S., Wu, A., Zhou, W., Wu, H., Chen, P., "Metallo-N-Heterocycles - A New Family of Hydrogen Storage Material," *Energy Storage Mater.* **26**, 198 (2020).
- Tardy, E., Courtois, F., Chandresis, M., Poirot-Crouvezier, J.-P., Morin, A., Bultel, Y., "Investigation of Liquid Water Heterogeneities in Large Area PEM Fuel Cells using a Pseudo-3D Multiphysics Model," *Int. J. Mass Tran.* **145**, 118720 (2019).
- Tein, Y.S., Zhang, Z., Wagner, N.J., "Competitive Surface Activity of Monoclonal Antibodies and Nonionic Surfactants at the Air-Water Interface Determined by Interfacial Rheology and Neutron Reflectometry," *Langmuir* **36**(27), 7814 (2020).
- Teixeira, S.C.M., "High-Pressure Small-Angle Neutron Scattering for Food Studies," *Curr. Opin. Colloid In.* **42**, 99 (2019).
- Theis-Bröhl, K., Saini, A., Wolff, M., Dura, J.A., Maranville, B.B., Borchers, J.A., "Self-Assembly of Magnetic Nanoparticles in Ferrofluids on Different Templates Investigated by Neutron Reflectometry," *Nanomaterials* **10**(6), 1231 (2020).
- Thompson, B.R., Zarket, B.C., Lauten, E.H., Amin, S., Muthukrishnan, S., Raghavan, S.R., "Liposomes Entrapped in Biopolymer Hydrogels can Spontaneously Release into the External Solution," *Langmuir* **36**(26), 7268 (2020).
- Tosado, J., Chen, W., Rodriguez, E.E., "A Strategy for Handling Aberration in Spherical Neutron Polarimetry," *J. Phys.: Conf. Ser.* **1316**, 012015 (2019).
- Tranquada, J.M., Xu, G., Zaliznyak, I.A., "Magnetism and Superconductivity in  $\text{Fe}_{1+y}\text{Te}_{1-x}\text{Se}_x$ ," *J. Phys.: Condens. Mat.* **32**(37), 374003 (2020).
- Trappen, R., Grutter, A.J., Huang, C.-Y., Penn, A., Mottaghi, N., Yousefi, S., Haertter, A., Kumari, S., LeBeau, J., Kirby, B.J., Holcomb, M.B., "Effect of Oxygen Stoichiometry on the Magnetization Profiles and Negative Magnetization in LSMO Thin Films," *J. Appl. Phys.* **126**(10), 105301 (2019).
- Trastoy, J., Camjayi, A., del Valle, J., Kalcheim, Y., Crocombette, J.-P., Gilbert, D.A., Borchers, J.A., Villegas, J.E., Ravelosona, D., Rozenberg, M.J., Schuller, I.K., "Magnetic Field Frustration of the Metal-Insulator Transition in  $\text{V}_2\text{O}_3$ ," *Phys. Rev. B* **101**(24), 245109 (2020).
- Treece, B.W., Heinrich, F., Ramanathan, A., Lösche, M., "Steering Molecular Dynamics Simulations of Membrane-Associated Proteins with Neutron Reflection Results," *J. Chem. Theory Comput.* **16**(5), 3408 (2020).
- Usuda, H., Hishida, M., Kelley, E.G., Yamamura, Y., Nagao, M., Saito, K., "Interleaflet Coupling of *n*-Alkane Incorporated Bilayers," *Phys. Chem. Chem. Phys.* **22**(10), 5418 (2020). [CHNRS]
- Uzan, L., Leão, J.B., Brocker, C., Mattes, D., Dax, T., "Heat Transfer Analysis Study for the Design of the New Polychromatic Beam Neutron Reflectometer CANDOR (Chromatic Analysis Neutron Diffractometer Or Reflectometer)," *J. Neutron Res.*, in press. [CHNRS]
- Vedmedenko, E.Y., Kawakami, R.K., Sheka, D.D., Gambardella, P., Kirilyuk, A., Hirohata, A., Binek, C., Chubykalo-Fesenko, O., Sanvito, S., Kirby, B.J., Grollier, J., Everschor-Sitte, K., Kampfrath, T., You, C.Y., Berger, A., "The 2020 Magnetism Roadmap," *J. Phys. D Appl. Phys.*, in press.
- Venkataraman, S., Wei, G., Mineart, K.P., Hedrick, J.L., Prabhu, V.M., Yang, Y.Y., "The Effect of Solvent Quality on Pathway-Dependent Solution-State Self-Assembly of an Amphiphilic Diblock Copolymer," *J. Appl. Phys.* **127**(12), 125104 (2020).
- Vogt, B.D., Weiss, R.A., "Hydrophobically Associating Hydrogels with Microphase-Separated Morphologies," in "Advanced Polymer Science," (Springer Nature, Switzerland), in press. [CHNRS]
- Wade, M.A., Walsh, D., Lee, J.C.-W., Kelley, E., Weigandt, K., Guirionnet, D., Rogers, S.A., "Color, Structure, and Rheology of a Diblock Bottlebrush Copolymer Solution," *Soft Matter* **16**(21), 4919 (2020). [CHNRS]

- Wang, B.-X., Zheng, H., Krivyakina, E., Chmaissem, O., Lopes, P.P., Lynn, J.W., Gallington, L.C., Ren, Y., Rosenkranz, S., Mitchell, J.F., Phelan, D., "Synthesis and Characterization of Bulk  $\text{Nd}_{1-x}\text{Sr}_x\text{NiO}_2$  and  $\text{Nd}_{1-x}\text{Sr}_x\text{NiO}_3$ ," *Phys. Rev. Mater.*, in press.
- Wang, B., Zhang, X., Huang, H., Zhang, Z., Yildirim, T., Zhou, W., Xiang, S., Chen, B., "A Microporous Aluminum-Based Metal-Organic Framework for High Methane, Hydrogen, and Carbon Dioxide Storage," *Nano Res.*, in press.
- Wang, C., Deitrick, K., Seo, J., Cheng, Z., Zacharia, N.S., Weiss, R.A., Vogt, B.D., "Manipulating the Mechanical Response of Hydrophobically Cross-Linked Hydrogels with Ionic Associations," *Macromolecules* **52**(16), 6055 (2019). [CHRS]
- Wang, C., Ping, W., Bai, Q., Cui, H., Hensleigh, R., Wang, R., Brozena, A.H., Xu, Z., Dai, J., Pei, Y., Zheng, C., Pastel, G., Gao, J., Wang, X., Wang, H., Zhao, J.-C., Yang, B., Zheng, X., Luo, J., Mo, Y., Dunn, B., Hu, L., "A General Method to Synthesize and Sinter Bulk Ceramics in Seconds," *Science* **368**(6490), 521 (2020).
- Wang, J.-Y., Chen, W., Nagao, M., Shelat, P., Hammer, B.A.G., Tietjen, G.T., Cao, K.D., Henderson, J.M., He, L., Lin, B., Akgun, B., Meron, M., Qian, S., Ward, S., Marks, J.D., Emrick, T., Lee, K.Y.C., "Tailoring Biomimetic Phosphorylcholine-Containing Block Copolymers as Membrane-Targeting Cellular Rescue Agents," *Biomacromolecules* **20**(9), 3385 (2019). [CHRS]
- Wang, J., Yin, H., Chen, Z., Cao, G., Xu, N., Wu, H., Wang, P., "A Core-Shell Structured  $\text{CoMoO}_4 \cdot n\text{H}_2\text{O} @ \text{Co}_{1-x}\text{Fe}_x\text{OOH}$  Nanocatalyst for Electrochemical Evolution of Oxygen," *Electrochim. Acta* **345**, 136125 (2020).
- Wang, J., Li, L., Guo, L., Zhao, Y., Xie, D., Zhang, Z., Yang, Q., Yang, Y., Bao, Z., Ren, Q., "Adsorptive Separation of Acetylene from Ethylene in Isostructural Gallate-Based Metal-Organic Frameworks," *Chem.-Eur. J.* **25**(68), 15516 (2019).
- Wang, M., Yi, M., Frandsen, B.A., Yin, J., Sun, H., Xu, Z., Cao, H., Bourret-Courchesne, E., Lynn, J.W., Birgeneau, R.J., "Observation of a C-Type Short-Range Antiferromagnetic Order in Layer Spacing Expanded  $\text{FeS}$ ," *Phys. Rev. Mater.* **4**(3), 034802 (2020).
- Wang, S., Zeng, Q., Liu, D., Zhang, H., Ma, L., Xu, G., Liang, Y., Zhang, Z., Wu, H., Che, R., Han, X., Huang, Q., "Giant Topological Hall Effect and Superstable Spontaneous Skyrmions below 330 K in a Centrosymmetric Complex Noncollinear Ferromagnet  $\text{NdMn}_2\text{Ge}_2$ ," *ACS Appl. Mater. Interfaces* **12**(21), 24125 (2020).
- Wang, Y., Zhu, Y., Zhang, R., Anovitz, L.M., Bleuel, M., Liu, S., Chen, S., "SANS Coupled with Fluid Invasion Approaches for Characterization of Overall Nanopore Structure and Mesopore Connectivity of Organic-Rich Marine Shales in China," *Int. J. Coal Geol.* **217**, 103343 (2020).
- Wang, Z., Faraone, A., Yin, P., Porcar, L., Liu, Y., Do, C., Hong, K., Chen, W.-R., "Dynamic Equivalence between Soft Star Polymers and Hard Spheres," *ACS Macro Lett.* **8**(11), 1467 (2019). [CHRS]
- Waschk, M., Sarkar, A., Barthel, J., Voigt, J., Schröder, S., Zakalek, P., Schmitz, M., Kirby, B.J., Pütter, S., Schubert, J., Brückel, T., "Impact of Growth Kinetics on the Interface Morphology and Magnetization in  $\text{La}_{1/3}\text{Sr}_{2/3}\text{FeO}_3/\text{La}_{2/3}\text{Sr}_{1/3}\text{MnO}_3$  Heterostructures," *J. Phys.: Condens. Mat.* **32**(16), 165801 (2020).
- Waddock, N.J., Gehring, P.M., Gold-Parker, A., Smith, I.C., Karunadasa, H.I., Toney, M.F., "Testing the Hypothesis of Dynamic Domains and Critical Scattering in Cubic Methylammonium Lead Triiodide," *Phys. Rev. Lett.*, in press.
- Weber, J., Cheshire, M.C., Distefano, V.H., Littrell, K.C., Ilavsky, J., Bleuel, M., Bozell-Messerschmidt, J.K., Ievlev, A.V., Stack, A.G., Anovitz, L.M., "Controls of Microstructure and Chemical Reactivity on the Replacement of Limestone by Fluorite Studied using Spatially Resolved Small Angle X-ray and Neutron Scattering," *ACS Earth Space Chem.* **3**(9), 1998 (2019). [CHRS]
- Wegner, A., Zhao, J., Li, J., Yang, J., Anikin, A.A., Karapetrov, G., Esfarjani, K., Louca, D., Chatterjee, U., "Evidence for Pseudo-Jahn-Teller Distortions in the Charge Density Wave Phase of  $1\text{T-TiSe}_2$ ," *Phys. Rev. B* **101**(19), 195145 (2020).
- Weston, J.S., Chun, J., Schenter, G., Weigandt, K., Zong, M., Zhang, X., Rosso, K.M., Anovitz, L.M., "Connecting Particle Interactions to Agglomerate Morphology and Rheology of Boehmite Nanocrystal Suspensions," *J. Colloid Interf. Sci.* **572**, 328 (2020).
- Wietfeldt, F.E., Byron, W.A., Collett, B., Darius, G., DeAngelis, C.R., Dewey, M.S., Hassan, M.T., Jones, G., Komives, A., Mendenhall, M.P., Nico, J.S., Stephenson, E.J., "aCORN: Measuring the Electron-Antineutrino Correlation in Neutron Beta Decay," *EPJ Web Conf.* **219**, 04008 (2019).
- Wilfong, B., Zhou, X., Zheng, H., Babra, N., Brown, C.M., Lynn, J.W., Taddei, K.M., Paglione, J., Rodriguez, E.E., "Long-Range Magnetic Order in Hydroxide-Layer-Doped  $(\text{Li}_{1-x}\text{Fe}_x\text{Mn}_y\text{OD})\text{FeSe}$ ," *Phys. Rev. Mater.* **4**(3), 034803 (2020).
- Winslow, S.W., Liu, Y., Swan, J.W., Tisdale, W.A., "Quantification of a  $\text{PbCl}_x$  Shell on the Surface of  $\text{PbS}$  Nanocrystals," *ACS Mater. Lett.* **1**(2), 209 (2019).



- Wisser, J.J., Emori, S., Riddiford, L., Altman, A., Li, P., Mahalingam, K., Urwin, B.T., Howe, B.M., Page, M.R., Grutter, A.J., Kirby, B.J., Suzuki, Y., "Ultrathin Interfacial Layer with Suppressed Room Temperature Magnetization in Magnesium Aluminum Ferrite Thin Films," *Appl. Phys. Lett.* **115**(13), 132404 (2019).
- Wisser, J.J., Grutter, A.J., Gilbert, D.A., N'Diaye, A.T., Klewe, C., Shafer, P., Arenholz, E., Suzuki, Y., Emori, S., "Damping Enhancement in Coherent Ferrite-Insulating-Paramagnet Bilayers," *Phys. Rev. Appl.* **12**(5), 054044 (2019).
- Wong-Ng, W., Laws, W., Huang, Q., Hou, J., Lapidus, S.H., Ribaud, L., Kaduk, J.A., "Crystal Chemistry and Phase Equilibria of the  $\text{CaO-1/2Ho}_2\text{O}_3\text{-CoO}_2$  System at 885 °C in Air," *Solid State Sci.*, in press.
- Worthington, P., Drake, K.M., Li, Z., Napper, A.D., Pochan, D.J., Langhans, S.A., "Implementation of a High-Throughput Pilot Screen in Peptide Hydrogel-Based Three-Dimensional Cell Cultures," *SLAS Discovery* **24**(7), 714 (2019). [CHNRS]
- Wu, D., Sinha, N., Lee, J., Sutherland, B.P., Halaszynski, N.I., Tian, Y., Caplan, J., Zhang, H.V., Saven, J.G., Kloxin, C.J., Pochan, D.J., "Polymers with Controlled Assembly and Rigidity made with Click-Functional Peptide Bundles," *Nature* **574**(7780), 658 (2019). [CHNRS]
- Wu, H., Wang, Z., Zhang, Y., Mo, W., Bai, P., Song, K., Zhang, Z., Wang, Z., Hussey, D.S., Liu, Y., Wang, Z., Wang, X., "Demonstration of Small-Angle Neutron Scattering Measurements with a Nested Neutron-Focusing Supermirror Assembly," *Nucl. Instrum. Meth. A*, in press.
- Wu, H., Yang, Y., Hussey, D.S., Wang, Z., Song, K., Zhang, Z., Wang, Z., Wang, Z., Wang, X., "Study of a Nested Neutron-Focusing Supermirror System for Small-Angle Neutron Scattering," *Nucl. Instrum. Meth. A* **940**, 380 (2019).
- Wu, S., Frandsen, B.A., Wang, M., Yi, M., Birgeneau, R., "Iron-Based Chalcogenide Spin Ladder  $\text{BaFe}_2\text{X}_3$  (X = Se, S)," *J. Supercond. Nov. Magn.* **33**(1), 143 (2020).
- Wu, Y., Yin, G., Pan, L., Grutter, A.J., Pan, Q., Lee, A., Gilbert, D.A., Borchers, J.A., Ratcliff, II, W., Li, A., Han, X.-D., Wang, K.L., "Large Exchange Splitting in Monolayer Graphene Magnetized by an Antiferromagnet," *Nat. Electron.*, in press.
- Xie, S., Meyer, D.J., Wang, E., Bates, F.S., Lodge, T.P., "Structure and Properties of Bicontinuous Microemulsions from Salt-Doped Ternary Polymer Blends," *Macromolecules* **52**(24), 9693 (2019). [CHNRS]
- Xie, S., Zhang, B., Mao, Y., He, L., Hong, K., Bates, F.S., Lodge, T.P., "Influence of Added Salt on Chain Conformations in Poly(Ethylene Oxide) Melts: SANS Analysis with Complications," *Macromolecules*, in press. [CHNRS]
- Xu, A.Y., Castellanos, M.M., Mattison, K., Krueger, S., Curtis, J.E., "Studying Excipient Modulated Physical Stability and Viscosity of Monoclonal Antibody Formulations using Small-Angle Scattering," *Mol. Pharmaceut.* **16**(10), 4319 (2019).
- Xu, A.Y., Castellanos, M.M., Mattison, K., Krueger, S., Curtis, J.E., "Correction to 'Studying Excipient Modulated Physical Stability and Viscosity of Monoclonal Antibody Formulations using Small-Angle Scattering,'" *Mol. Pharmaceut.* **17**(5) 1758 (2020).
- Xu, H., Grutter, A.J., Cui, Z., Wang, Z., Zhai, X., Lu, Y., "Charge Carrier Transport with Low-Temperature Anomalies in Engineered  $4d/5d$  Oxide Superlattices of  $(\text{Sr}_2\text{IrO}_4)_4/(\text{Sr}_3\text{Ru}_2\text{O}_7)_N$ ," *Phys. Rev. B* **101**(15), 155151 (2020).
- Yang, C.-Y., Pan, L., Grutter, A.J., Wang, H., Che, X., He, Q.L., Wu, Y., Gilbert, D.A., Shafer, P., Arenholz, E., Wu, H., Yin, G., Deng, P., Borchers, J.A., Ratcliff, II, W., Wang, K.L., "Termination Switching of Antiferromagnetic Proximity Effect in Topological Insulator," *Sci. Adv.*, in press.
- Yang, L., Zhou, W., Li, H., Alsalmeh, A., Jia, L., Yang, J., Li, J., Li, L., Chen, B., "Reversed Ethane/Ethylene Adsorption in Metal-Organic Framework via Introduction of Oxygen," *Chinese J. Chem. Eng.* **28**(2), 593 (2020).
- Yang, W., Zhou, W., Chen, B., "A Flexible Microporous Hydrogen-Bonded Organic Framework," *Cryst. Growth Des.* **19**(9), 5184 (2019).
- Yang, X., Zhao, S., Geng, S., Yang, L., Huang, Q., Kuang, X., Luo, J., Xing, X., "Structural Origin of Thermally Induced Second Harmonic Generation Enhancement in  $\text{RbNaMgP}_2\text{O}_7$ ," *Chem. Mater.* **31**(23), 9843 (2019).
- Yao, Y., Huang, Z., Li, T., Wang, H., Liu, Y., Stein, H.S., Mao, Y., Gao, J., Jiao, M., Dong, Q., Dai, J., Xie, P., Xie, H., Lacey, S.D., Takeuchi, I., Gregoire, J.M., Jiang, R., Wang, C., Taylor, A.D., Shahbazian-Yassar, R., Hu, L., "High-Throughput, Combinatorial Synthesis of Multimetallic Nanoclusters," *P. Natl. A. Sci. USA* **117**(12), 6316 (2020).
- Yao, Y., Liu, Z., Xie, P., Huang, Z., Li, T., Morris, D., Finck, Z., Zhou, J., Jiao, M., Gao, J., Mao, Y., Miao, J., Zhang, P., Shahbazian-Yassar, R., Wang, C., Wang, G., Hu, L., "Computationally Aided, Entropy-Driven Synthesis of Highly Efficient and Durable Multi-Elemental Alloy Catalysts," *Sci. Adv.* **6**(11), eaaz0510 (2020).
- Ye, J., Book, A., Mayr, S., Gabold, H., Meng, F., Schäfferer, H., Need, R., Gilbert, D., Saerbeck, T., Stahn, J., Böni, P., Kreuzpaintner, W., "Design and Realization of a Sputter Deposition System for the *In Situ* and *In Operando* use in Polarized Neutron Reflectometry Experiments: Novel Capabilities," *Nucl. Instrum. Meth. A* **964**, 163710 (2020).

- Ye, Y., Lin, R.-B., Cui, H., Alsalmeh, A., Zhou, W., Yildirim, T., Zhang, Z., Xiang, S., Chen, B., "A Microporous Metal-Organic Framework with Naphthalene Diimide Groups for High Methane Storage," *Dalton T.* **49**(12), 3658 (2020).
- Yi, D., Wang, Y., van 't Erve, O.M.J., Xu, L., Yuan, H., Veit, M.J., Balakrishnan, P.P., Choi, Y., N'Diaye, A.T., Shafer, P., Arenholz, E., Grutter, A., Xu, H., Yu, P., Jonker, B.T., Suzuki, Y., "Emergent Electric Field Control of Phase Transformation in Oxide Superlattices," *Nat. Commun.* **11**(1), 902 (2020).
- Yoshimune, W., Harada, M., "Impact of Nonadsorbed Ionomer on Viscosity of Catalyst Inks for Polymer Electrolyte Fuel Cells," *B. Chem. Soc. Jpn.* **93**(2), 302 (2020).
- Yoshimune, W., Harada, M., Akimoto, Y., "Small-Angle Neutron Scattering Studies on the Distribution of Polytetrafluoroethylene within Microporous Layers for Polymer Electrolyte Fuel Cells," *Compos. Part C*, in press.
- Yu, J., Wang, M., Frandsen, B.A., Sun, H., Yin, J., Liu, Z., Wu, S., Yi, M., Xu, Z., Acharya, A., Huang, Q., Bourret-Courchesne, E., Lynn, J.W., Birgeneau, R.J., "Structural, Magnetic, and Electronic Evolution of the Spin-Ladder System  $\text{BaFe}_2\text{S}_{3-x}\text{Se}_x$  with Isoelectronic Substitution," *Phys. Rev. B* **101**(23), 235134 (2020).
- Yu, J., Mao, J., Nagao, M., Bu, W., Lin, B., Hong, K., Jiang, Z., Liu, Y., Qian, S., Tirrell, M., Chen, W., "Structure and Dynamics of Lipid Membranes Interacting with Antiviral End-Phosphorylated Polyethylene Glycol Block Copolymers," *Soft Matter* **16**(4), 983 (2020). [CHRS]
- Yu, M.-H., Space, B., Franz, D., Zhou, W., He, C., Li, L., Krishna, R., Chang, Z., Li, W., Hu, T.-L., Bu, X.-H., "Enhanced Gas Uptake in a Microporous Metal-Organic Framework via a Sorbate Induced-Fit Mechanism," *J. Am. Chem. Soc.* **141**(44), 17703 (2019).
- Yumnam, G., Chen, Y., Zhao, Y., Thamizhavel, A., Dhar, S.K., Singh, D.K., "Microscopic Nature of Magnetic Ground State in  $\text{CeAuSb}_2$ ," *Phys. Status Solidi RRL* **13**(10), 1900304 (2019).
- Zhang, C., Yang, S., Padmanabhan, V., Akcora, P., "Solution Rheology of Poly(Acrylic Acid)-Grafted Silica Nanoparticles," *Macromolecules* **52**(24), 9594 (2019). [CHRS]
- Zhang, M., Chen, C., Shi, Z., Huang, K., Fu, W., Zhou, W., "Inserting Amide into NOTT-101 to Sharply Enhance Volumetric and Gravimetric Methane Storage Working Capacity," *Inorg. Chem.* **58**(20), 13782 (2019).
- Zhang, X., Lin, R.-B., Wang, J., Wang, B., Liang, B., Yildirim, T., Zhang, J., Zhou, W., Chen, B., "Optimization of the Pore Structures of MOFs for Record High Hydrogen Volumetric Working Capacity," *Adv. Mater.* **32**(17), 1907995 (2020).
- Zhang, X., Mao, Y., Tyagi, M., Jiang, F., Henderson, D., Jiang, B., Lin, Z., Jones, R.L., Hu, L., Briber, R.M., Wang, H., "Molecular Partitioning in Ternary Solutions of Cellulose," *Carbohydr. Polym.* **220**, 157 (2019). [CHRS]
- Zhang, X., Li, L., Wang, J.-X., Wen, H.-M., Krishna, R., Wu, H., Zhou, W., Chen, Z.-N., Li, B., Qian, G., Chen, B., "Selective Ethane/Ethylene Separation in a Robust Microporous Hydrogen-Bonded Organic Framework," *J. Am. Chem. Soc.* **142**(1), 633 (2020).
- Zhang, Y., Barber, T.J., Hu, Q., Bleuel, M., El-Sobky, H.F., "Complementary Neutron Scattering, Mercury Intrusion and SEM Imaging Approaches to Micro- and Nano-Pore Structure Characterization of Tight Rocks: A Case Study of the Bakken Shale," *Int. J. Coal Geol.* **212**, 103252 (2019). [CHRS]
- Zhang, Y., Hu, Q., Barber, T.J., Bleuel, M., Anovitz, L.M., Littrell, K., "Quantifying Fluid-Wettable Effective Pore Space in the Utica and Bakken Oil Shale Formations," *Geophys. Res. Lett.* **47**(14), e2020GL087896 (2020). [CHRS]
- Zheng, B., Zheng, B., Carr, A.J., Yu, X., McClements, D.J., Bhatia, S.R., "Emulsions Stabilized by Inorganic Nanoclays and Surfactants: Stability, Viscosity, and Implications for Applications," *Inorg. Chim. Acta*, in press. [CHRS]
- Zheng, J., Barpaga, D., Trump, B.A., Shetty, M., Fan, Y., Bhattacharya, P., Jenks, J.J., Su, C.-Y., Brown, C.M., Maurin, G., McGrail, B.P., Motkuri, R.K., "Molecular Insight into Fluorocarbon Adsorption in Pore Expanded Metal-Organic Framework Analogs," *J. Am. Chem. Soc.* **142**(6), 3002 (2020).
- Zhong, W., Shen, S., Feng, S., Liu, Y., Xu, A., Ye, X., Chen, D., "Distorted  $\text{FeSe}_4$  Unit in Ammonium Ion Intercalated  $\text{FeSe}$  Superconductor," *Inorg. Chem. Commun.* **111**, 107605 (2020).
- Zhou, L., Han, Y., Yin, C., Wang, Y., Yang, X., Allix, M., Huang, Q., Xiong, J., Wang, B., Li, G., Kuang, X., Xing, X., "Trigonal-Planar Low-Spin  $\text{Co}^{2+}$  in a Layered Mixed-Polyhedral Network from Topotactic Reduction," *Inorg. Chem.* **58**(20), 14193 (2019).

# Instruments and Contacts

(name, tel. 301-975-xxxx, email)

## High resolution powder diffractometer (BT-1):

- H. Wu, 2387, hui.wu@nist.gov
- Q. Z. Huang, 6164, qing.huang@nist.gov
- C. M. Brown, 5134, craig.brown@nist.gov

## Engineering diffractometer (BT-8):

- T. Gnäupel-Herold, 5380, thomas.gnaeupel-herold@nist.gov

## vSANS instrument (NG-3) (CHRS):

- E. Kelley, 8584, elizabeth.kelley@nist.gov
- Y. Liu, 6235, yun.liu@nist.gov
- K. Krycka, 8685, kathryn.krycka@nist.gov
- R. P. Murphy, 8544, ryan.murphy@nist.gov
- C. Gagnon, 2020, cedric.gagnon@nist.gov

## 30-m SANS instrument (NG-B):

- P. D. Butler, 2028, paul.butler@nist.gov
- S. Krueger, 6734, susan.krueger@nist.gov
- Y. Mao, 6017, yimin.mao@nist.gov
- M. Zhang, 5513, zhenhuan.zhang@nist.gov

## 10-m SANS instrument (NG-B) (nSoft):

- R. Jones, 4624, ronald.jones@nist.gov
- K. Weigandt, 8396, kathleen.weigandt@nist.gov
- T. Martin, 8866, tyler.martin@nist.gov

## uSANS, Perfect Crystal SANS (BT-5):

- M. Bleuel, 5165, markus.bleuel@nist.gov
- P. D. Butler, 2028, paul.butler@nist.gov

## 30-m SANS instrument (NG-7):

- S. Teixeira, 4404, susana.marujoteixeira@nist.gov
- J. G. Barker, 6732, john.barker@nist.gov
- K. Krycka, 8685, kathryn.krycka@nist.gov
- J. R. Krzywón, 6650, jkrzywón@nist.gov

## Polarized Beam Reflectometer/Diffractometer (NG-D):

- B. J. Kirby, 8395, brian.kirby@nist.gov
- J. A. Borchers, 6597, julie.borchers@nist.gov
- C. F. Majkrzak, 5251, cmajkrzak@nist.gov

## MAGIK, Off-Specular Reflectometer (NG-D):

- J. A. Dura, 6251, joseph.dura@nist.gov
- F. Heinrich, 4507, frank.heinrich@nist.gov
- C. F. Majkrzak, 5251, cmajkrzak@nist.gov

## Neutron reflectometer-horizontal sample (NG-7):

- S. K. Satija, 5250, satija@nist.gov
- G. Yuan, 5098, guangcui.yuan@nist.gov

## CANDOR, White-beam reflectometer/diffractometer (CHRS):

- A. Grutter, 4198, alexander.grutter@nist.gov
- D. Hoogerheide, 8839, david.hoogerheide@nist.gov
- B. Maranville, 6034, brian.maranville@nist.gov
- C. F. Majkrzak, 5251, charles.majkrzak@nist.gov

## HFBS, High-flux backscattering spectrometer (NG-2) (CHRS):

- M. Tyagi, 2046, madhusudan.tyagi@nist.gov

## NSE, Neutron spin echo spectrometer (NG-A) (CHRS):

- A. Faraone, 5254, antonio.faraone@nist.gov
- M. Nagao, 5505, michihiro.nagao@nist.gov

## MACS, Multi-angle crystal spectrometer (BT-9) (CHRS):

- J. A. Rodriguez-Rivera, 6019, jose.rodriguez@nist.gov
- Y. Qiu, 3274, yiming.qiu@nist.gov

## Double-focusing triple-axis Spectrometer (BT-7):

- Y. Zhao, 2164, yang.zhao@nist.gov
- Z. Xu, 8097, zhijun.xu@nist.gov
- J. W. Lynn, 6246, jeff.lynn@nist.gov

## SPINS, Spin-polarized triple-axis spectrometer (NG-5):

- G. Xu, 4144, guangyong.xu@nist.gov

## Triple-axis spectrometer (BT-4):

- W. Ratcliff, 4316, william.ratcliff@nist.gov

## FANS, Filter-analyzer neutron spectrometer (BT-4):

- C. M. Brown, 5134, craig.brown@nist.gov

## DCS, Disk-chopper time-of-flight spectrometer (NG-4):

- N. Butch, 4863, nicholas.butch@nist.gov
- W. Zhou, 8169, wei.zhou@nist.gov

## Cold neutron depth profiling (NG-A):

- J. Weaver, 6311, jamie.weaver@nist.gov

## Cold-neutron prompt-gamma neutron activation analysis (NG-D):

- R. L. Paul, 6287, rpaul@nist.gov
- H. H. Chen-Mayer, 5595, heather.chen-mayer@nist.gov



**Thermal-neutron prompt-gamma activation analysis (VT-5):**

- R. L. Paul, 6287, rpaul@nist.gov

**Other activation analysis facilities:**

- N. Sharp, 3926, nicholas.sharp@nist.gov
- R. L. Paul, 6287, rpaul@nist.gov

**Thermal Neutron Imaging Station (BT-2):**

- J. LaManna, 6809, jacob.lamanna@nist.gov
- D. Jacobson, 6207, david.jacobson@nist.gov
- E. Baltic, 4842, eli.baltic@nist.gov
- D. Hussey, 6465, daniel.hussey@nist.gov

**Cold Neutron Imaging Station (NG-6):**

- D. Hussey, 6465, daniel.hussey@nist.gov
- E. Baltic, 4842, eli.baltic@nist.gov
- D. Jacobson, 6207, david.jacobson@nist.gov
- J. LaManna, 6809, jacob.lamanna@nist.gov

**Neutron interferometer (NG-7):**

- M. Huber, 5641, michael.huber@nist.gov
- D. Pushin, 4792, dmitry.pushin@nist.gov
- S. Hoogerheide, 8582, shannon.hoogerheide@nist.gov

**Quantum-based neutron interferometer facility (NG-7):**

- M. Huber, 5641, michael.huber@nist.gov
- S. Hoogerheide, 8582, shannon.hoogerheide@nist.gov
- D. Pushin, 4792, dmitry.pushin@nist.gov

**Fundamental neutron physics station (NG-C):**

- S. Hoogerheide, 8582, shannon.hoogerheide@nist.gov
- H. P. Mumm, 8355, hans.mumm@nist.gov
- M. S. Dewey, 4843, maynard.dewey@nist.gov
- J. Nico, 4663, jeffrey.nico@nist.gov

**Dowser: Advanced Neutron Detector Development (NG-6a):**

- H. P. Mumm, 8355, hans.mumm@nist.gov
- C. B. Shahi, 8194, chandra.shahi@nist.gov

 **$\alpha$ - $\gamma$ : absolute neutron counter (NG-6m):**

- M. S. Dewey, 4843, maynard.dewey@nist.gov
- H. P. Mumm, 8355, hans.mumm@nist.gov
- C. Haddock, 5761, christopher.haddock@nist.gov

**Grating interferometer for fundamental physics (NG-6u):**

- M. G. Huber, 5641, michael.huber@nist.gov
- D. Hussey, 6465, daniel.hussey@nist.gov

**Theory and modeling:**

- J. E. Curtis, 3959, joseph.curtis@nist.gov
- T. Yildirim, 6228, taner@nist.gov

**Neutron test station (PHADES):**

- R. Erwin, 6245, ross.erwin@nist.gov
- S. Watson, 6232, shannon.watson@nist.gov
- K. Krycka, 8685, kathryn.krycka@nist.gov

**Instruments under development:****SPINS-II:**

- L. Harriger, 8360, leland.harriger@nist.gov

# NIST Center for Neutron Research Contacts

Copies of annual reports, facility information, user information, and research proposal guidelines are available electronically.

Please visit our website: <http://www.ncnr.nist.gov>

## **For a paper copy of this report:**

Steve Kline  
301-975-6243  
[steven.kline@nist.gov](mailto:steven.kline@nist.gov)

## **For general information on the facility:**

Rob Dimeo  
301-975-6210  
[robert.dimeo@nist.gov](mailto:robert.dimeo@nist.gov)

Dan Neumann  
301-975-5252  
[dan.neumann@nist.gov](mailto:dan.neumann@nist.gov)

## **For information on visiting the facility and/or user access questions:**

Julie Keyser  
301-975-8200  
[julie.keyser@nist.gov](mailto:julie.keyser@nist.gov)

Mary Ann FitzGerald  
301-975-8200  
[maryann.fitzgerald@nist.gov](mailto:maryann.fitzgerald@nist.gov)

Becky Ogg  
301-975-8200  
[rebecca.ogg@nist.gov](mailto:rebecca.ogg@nist.gov)

## **For information on performing research at the facility:**

Yamali Hernandez  
301-975-5295  
[yamali.hernandez@nist.gov](mailto:yamali.hernandez@nist.gov)

## **Facility address:**

NIST Center for Neutron Research  
National Institute of Standards and Technology  
100 Bureau Drive, Mail Stop 6100  
Gaithersburg, MD 20899-6100 USA



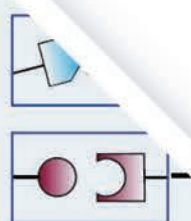
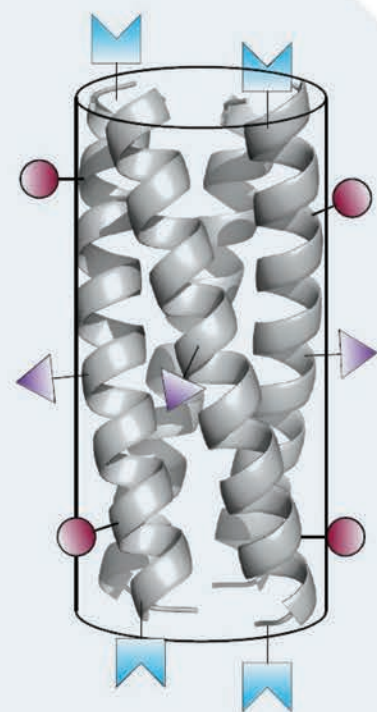
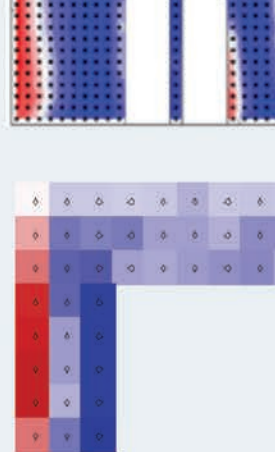
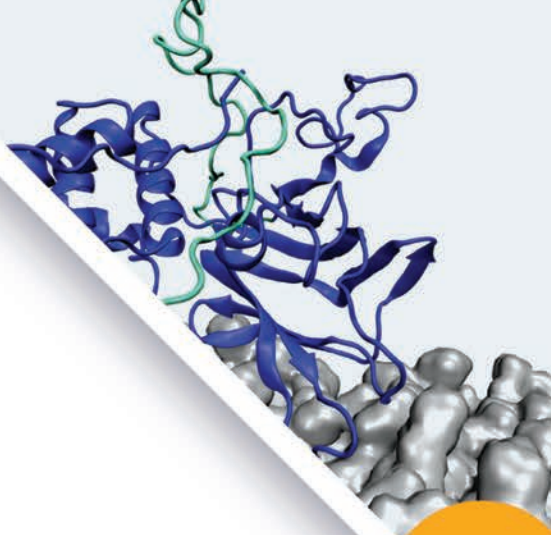


## NIST CENTER FOR NEUTRON RESEARCH

National Institute of Standards  
and Technology

100 Bureau Drive, MS 6100  
Gaithersburg, MD 20899-6100

[www.ncnr.nist.gov](http://www.ncnr.nist.gov)



Physical  
Interactions

